Ferumoxytol MRI for the *in vivo* Identification of Placental Pathology: Investigation in Preparation for Potential Clinical Applications

by:

Sydney Nguyen

A dissertation submitted in partial fulfillment

of the requirements for the degree of

Doctor of Philosophy

(Endocrinology and Reproductive Physiology)

at the

University of Wisconsin-Madison

2020

Date of final oral examination: 06/15/2020

The dissertation is approved by the following members of the Final Oral Committee:

Ian Bird, Professor and Vice Chair of Research, Department of Obstetrics & Gynecology
Oliver Wieben, Professor and Vice Chair of Research, Department of Medical Physics
Leticia Reyes, Assistant Professor, Department of Pathobiological Sciences
Aleksandar Stanic-Kostic, Assistant Professor, Department of Obstetrics & Gynecology
Pamela Kling, Professor, Department of Pediatrics
Thaddeus Golos, Professor and Chair, Department of Comparative Biosciences

Contents

Abbreviations

Abs – Antibodies
ASL – Arterial Spin Labeling
BPD – Biparietal Diameter
CBC – Complete Blood Count
CNS – Central Nervous System
DCE – Dynamic Contrast Enhanced
DPI – Days Post-Infection
EHR – Electronic Health Record
FL – Femur Length
GBCA – Gadolinium-Based Contrast Agent
GD – Gestational Day
HC – Head Circumference
H&E - Hematoxylin and Eosin
IACUC - Institutional Animal Care and Use Committee
MFI – Maternal-Fetal Interface
MRI – Magnetic Resonance Imaging
nAb – Neutralizing Antibodies
NK – Natural Killer
NMR – Nuclear Magnetic Resonance
PBMCs – Peripheral Blood Mononuclear Cells
PFA – Paraformaldehyde
pGA – Predicted Gestational Age
PMA - Phorbol-12-Myristate-13-Acetate
$PRNT_{90}$ - 90% Plaque Reduction Neutralizing Antibody Test
qRT-PCR - Quantitative Reverse Transcription Polymerase Chain Reaction
RBC – Red Blood Cell
SD – Standard Deviation
SLA – Stereolithographic
SPF - Specific Pathogen Free
SPION - Superparamagnetic Iron Oxide Nanoparticle
SRA - Sequence Read Archive
SRV – Simian Retrovirus Type D
SSFSE - Single Shot Fast Spin Echo
STLV - Simian T-Lymphotropic Virus Type 1
TBST – Tris-Buffered Saline and Tween 20
vRNA – Viral Ribonucleic Acid
WBC – White Blood Count
WNPRC - Wisconsin National Primate Research Center
ZIKV – Zika Virus

Figures

Chapter 1

Chapter 2

Chapter 3

Chapter 4

Chapter 5

Chapter 6

Appendix A

Appendix B

Tables

Acknowledgements

I am so deeply thankful to have had the company of so many wonderful humans on this journey:

Thank you to my thesis committee, lab mates, colleagues, and collaborators for giving me the support and guidance I needed to sharpen my skills and produce something I am extremely proud of. You helped make this work possible.

Thank you to my husband, Alex, for keeping me grounded, teaching me how to be kind to myself, and helping me grow (and growing with me) through this process. You always lift me up and for that, I am forever grateful.

Thank you to my parents, Debra and Demetri, for teaching to value myself at a young age, for sparking my love for science, and for imbuing me with that fire that keeps me fighting --
and to my in-laws, Marcia and Tuan, for adopting me as one of their own and providing unyielding support as I perused my education.

Thank you to my sister, Lyra, for showing me strength in difficult times and helping me smile in the face of obstacles.

Thank you to my friends near and far, for the coffee talks, nacho dates, and skype sessions that provided so much warmth and joy along the way.

Finally, thank you to my cats. Your very soft, very goofy moral support has been indispensable.

Chapter 1:

Introduction

1 The Placenta: Form, Function, and Value

The placenta is a temporary specialized organ that supports the developing fetus throughout mammalian pregnancy. Connected to the fetus by the umbilical cord, the placenta has the crucial role of providing life-sustaining oxygen and nutrients directly to the fetal bloodstream to support the miraculous growth of the fetus during gestation [1-3]. Following oocyte fertilization, the resulting zygote undergoes rapid cell division and differentiation. The outermost layer of cells, called the trophectoderm, adhere to the uterine wall and the ensuing trophoblasts migrate into the maternal tissue to secure the connection for placental formation and maintenance throughout fetal development [4]. This process spurs changes to the uterine wall cells, including uterine vasculature. Uterine spiral arteries, vessels that cyclically supply blood to the endometrial mucosa of the non-pregnant uterus, undergo extensive remodeling. Trophoblasts invade uterine spiral arteries, replacing vascular smooth muscle with fibrinoid deposits and establishing a connection between the developing placenta and the maternal bloodstream and turning these low flow, high resistance vessels into the high flow, low resistance vessels required for adequate blood flow to the placenta [5,6].

In humans, the fully-formed maternal-fetal interface is composed of the decidua -- the name for the modified uterine wall during pregnancy, the placenta, and the fetal membranes -- the thin membranes that extend around the amniotic fluid that surrounds the fetus, creating the amniotic sac [7,8] (Figure 1). The placenta directly contacts the decidua on the maternal side and the amniotic and chorionic extension from fetal membranes on the fetal side, referred to as the

chorionic plate. The placenta itself is a tissue of layers. On the maternal side, uterine arteries extend through decidual tissue and into the intervillous space -- a cavity of pooled maternal blood. The intervillous space is separated into functional groups called cotyledons, each fed by a different artery. The cotyledon structure is similar to bubble wrap, fed by the incoming maternal blood flow and its intervillous space, with other communication minimized or non-existent between cotyledons [9,10]. Fetal placental villi lie adjacent to the cotyledon intervillous space. Fetal vessels originating from the umbilical cord perfuse the mesenchymal core of these villi. Within each cotyledon, maternal blood bathes the interface to the placental villi and across the trophoblast surface of the villi, exchanges oxygen and nutrients with the fetal vessels (Figure 2). Waste from the fetal blood is also transported to the maternal blood through the villi. Normally, the maternal and fetal blood never come in direct contact. Following extraction of oxygen, maternal blood circulates out of the intervillous space and to the maternal circulation.

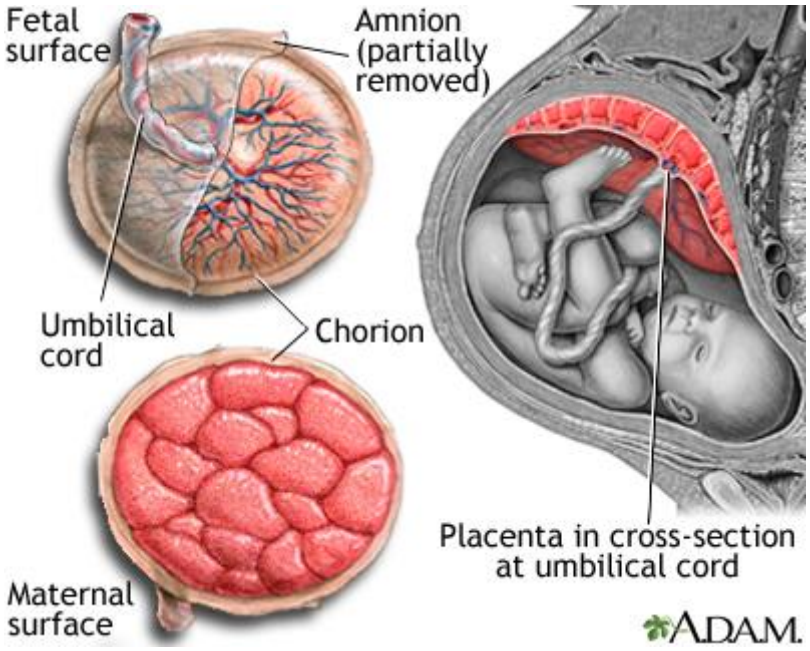

Figure 1. The Maternal-Fetal Interface: Where Maternal and Fetal Tissues Meet. Diagram displaying the maternal-fetal interface with the side of the placenta that faces the fetus (top left),

the side of the placenta adhered to the uterus (bottom left), and the placental connection to the fetus by the umbilical cord within the amniotic sac (right).

Credit: Animated Dissection of Anatomy for Medicine (A.D.A.M.), Ebix Inc., Copyright 1997-2020

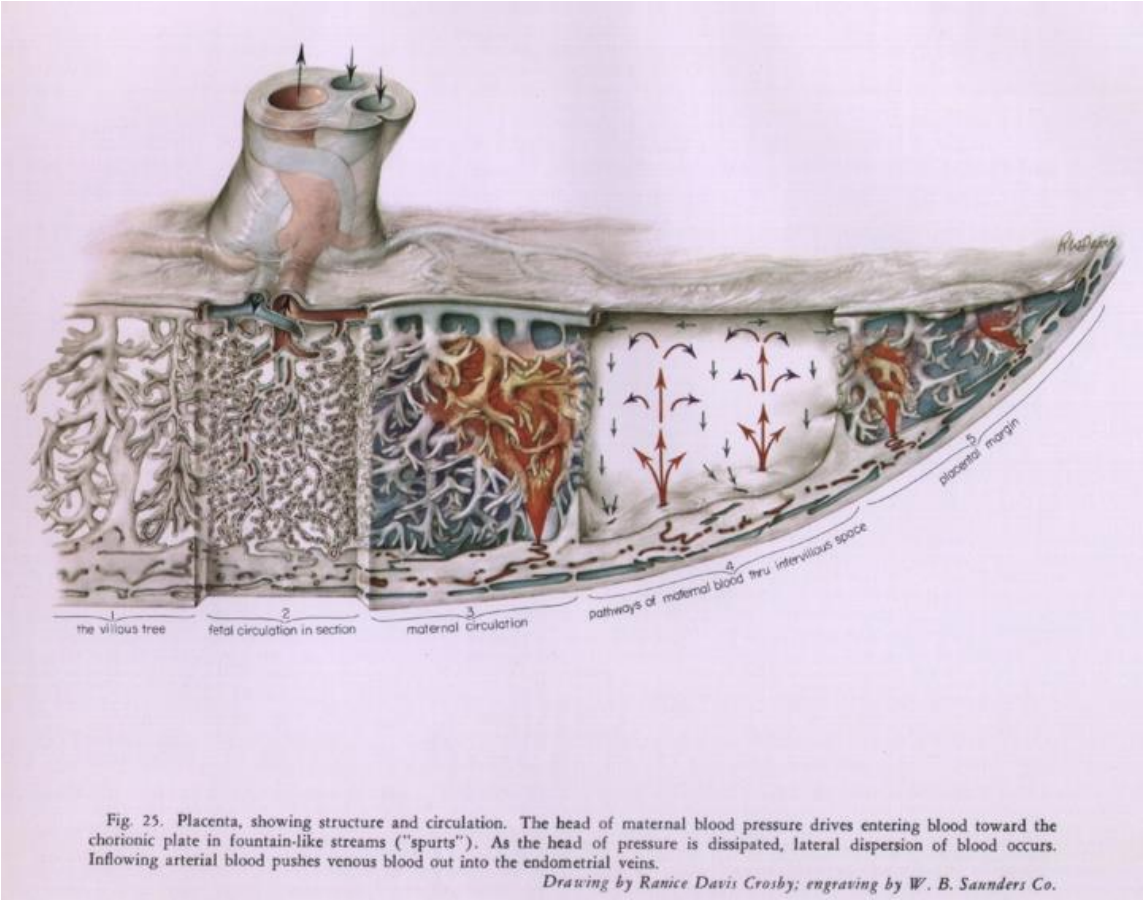

Fig. 25. Placenta, showing structure and circulation. The head of maternal blood pressure drives entering blood toward the chorionic plate in fountain-like streams ("spurts"). As the head of pressure is dissipated, lateral dispersion of blood occurs. Inflowing arterial blood pushes venous blood out into the endometrial veins.

Drawing by Ranice Davis Crosby; engraving by W. B. Saunders Co.

Figure 2. Structure and Circulation of the Placenta. Diagram depicting the structure of the placental villous tree (1) containing fetal blood vessels (2), and the movement of maternal blood into (3) and out of (4) the intervillous space.

Credit: John W S Harris and Elizabeth Mapelsden Ramsey, 1996. Contributions to embryology, v. 38, no. 260: The morphology of human uteroplacental vasculature. Carnegie Institution of Washington.

Changes that prevent normal placenta function can be detrimental to pregnancy success. Insufficient oxygen, nutrient, and waste exchange can restrict fetal growth or lead to pregnancy

loss [11-14]. Placental insufficiency could be caused by structural placental abnormalities that prevent efficient transport of materials, fetal abnormalities that prevent the absorption of oxygen and nutrients, or diminished maternal blood flow into the placenta due to incomplete placental implantation to the uterus [13]. Additionally, otherwise normal placental tissue can become infected by a spectrum of pathogens, directly disrupting tissue morphology or through immune cell infiltration into the maternal-fetal interface. Risk for an infection event is higher with pre-existing maternal disease or abnormal maternal or fetal blood flow rate or pressure [13,15]. Placenta pathology caused by bacterial and viral infection is often focal -- specific to particular cotyledons rather than affecting the entire tissue [16-19]. Thus, pathology can result in normal outcome [20] or inadequately support the growing fetus when affecting many cotyledons. Placental infarctions, for example, are regions of tissue that undergo ischemic necrosis -- tissue death due to deprivation of oxygen-rich blood. Infarcted placental villi become non-functioning and unable to participate in nutrient exchange [15,21]. While small infarctions are common in healthy pregnancies, necrosis in 10-15% of the placenta is associated with high rates of fetal death. Fibrin deposition, involved in blood clotting, may occur in the intervillous space usually reserved for blood pooling, reducing delivering the nutrient-rich maternal blood or in within fetal vessels to prevent fetal blood flow to and/or from placental villi, thus preventing nutrient exchange.

Early identification of placental pathology, evidence of infection or otherwise abnormal function, prior to maternal symptoms of problematic pregnancy could have immense value. If identified early, appropriate enhanced monitoring could take place to minimize maternal and fetal risk, perhaps even enabling the development of new interventions for the prevention of miscarriages or severe maternal consequences, including death. The use of cutting-edge medical

imaging may hold the key to achieving this. Currently, ultrasound is the most common clinical method to monitor pregnancy. Doppler ultrasound can detect umbilical and placental total blood flow, but lacks detailed image resolution to identify focal pathology [22-25]. Magnetic resonance imaging (MRI) can however provide high-resolution anatomic and functional data including blood velocities and flow, perfusion, and oxygenation to characterize the placental implantation site, visualize maternal pelvic anatomy, and diagnose abnormally aggressive trophoblast invasion or placental abruption [26-31].

Currently, MRI is not commonly employed in normal human pregnancy. Research in an appropriate animal model can determine potential risks prior to proposing specific MRI protocols in clinical human placental assessment. The rhesus macaque (a non-human primate) placenta has many similarities to that of humans, making it an excellent model for the study of pregnancy for application in human healthcare [32-34]. Like humans, the macaque trophoblasts invade the maternal decidua to attach the placenta to the uterine wall and initiate maternal vessel migration. The internal placental structure is also villous, where fetal villi serve as the site of oxygen, nutrient, and waste exchange. The intervillous space is segmented into the cotyledon functional groups as well. Macaque placentas are discoid, as in humans, though macaques most often have two disks, with the umbilical cord connecting the primary disk to the fetus, and peripheral inter-placental vessels connecting the primary and secondary disks. Human gestation averages 280 days while rhesus macaques gestate average 165 days [35], although fetal development by trimester is well-aligned. No lower animal has these placental similarities. While the ethics of utilizing a non-human primate model for research is hotly debated [36-38], as these higher mammals have complex thoughts and emotions, the value of pregnancy research utilizing monkeys cannot be otherwise achieved. Only usage of non-human primates can lay the

groundwork for preliminary clinical safety of placental MRI in normal pregnancy, prior to FDA approval [33-34]. Monitoring animal care and use committees ensures careful consideration to provide laboratory primates with safe, comfortable, and enriching environments, minimizing unnecessary stress and discomfort [37]. The minimal number of primates necessary to complete research are used and the resulting tissues are shared among a variety of projects and researchers to ensure maximum data extraction with minimal lives lost.

2 Dynamic Contrast Enhanced Magnetic Resonance Imaging: The Basics

Magnetic resonance imaging (MRI) has been used in medicine since the 1970s and has revolutionized diagnostics, treatment plans, and patient monitoring [1,2]. Based on the concept of nuclear magnetic resonance (NMR) discovered independently by both Felix Bloch and Edward Purcell in 1946, MRI involves the detection of the absorption and emission of radio waves, called NMR signal, of particular atoms, most often hydrogen. Hydrogen atoms have an NMR signal, and are abundant in fat and water -- the primary components of the human body. MRI scanners are composed of a patient bed within a large, tube-shaped magnet that produces a strong magnetic field, forcing molecules within that field to align, moving to an "excited" state [1-4]. The NMR signal of the hydrogen atoms is impacted in a predictable and measurable way, exciting the molecule for a specific period of time before the molecule "relaxes" into its natural state. This relaxation rate is referred to as T1 relaxation. The MRI machine measures these relaxation rates to produce images that are telling of hydrogen atom composition within the subject. Resulting images are tomographic -- slices of a certain thickness through the imaging subject, similar to slices in a loaf of bread. These slices can then be reconstructed, stacking with one another to produce a 3D model of the entire imaging region. These image slices are composed of voxels, volumetric pixels -- a 3D version of the standard picture element used to produce electronic images and text on the screens we use every day. Each voxel serves as a visual representation of the molecule relaxation rate data being processed by the MRI machine, translating recorded relaxation rates to a color scale. The concentration and distribution of hydrogen atoms in different tissues and the body's blood space varies, which means the NMR signal relaxation rate will change with the type of tissue captured in each voxel. Similarly, tissue abnormalities such as tumors, inflammations, and degeneration affect the NMR signal relaxation

rate, affecting how the voxels in that region of tissue are displayed on the images, denoting important clinical value [5-9].

Dynamic contrast enhanced (DCE) MRI utilizes contrast agents to affect the T1 relaxation rate of hydrogen molecules, in order to produce an NMR signal relaxation rate map that reflects body function [10-12]. The subject is imaged during the administration of the contrast agent, which substantially shortens the NMR signal T1 relaxation rate within voxels containing the contrast agent, making the voxel a bright white against the grayscale anatomical scan. Resolution quality is sacrificed to quickly collect images a few seconds apart. When the image slices are reconstructed at all timepoints, the resulting 3D images create a video showcasing the movement of the bright contrast agent signal through the body. The passage of the contrast agent delivered as a bolus into tissues can be used to calculate the perfusion rate of blood into an organ [13,14]. The standard non-contrast MRI modality called Arterial Spin Labeling (ASL) uses the powerful MR magnet to “excite” all of the molecules in a region of the subject, then records the entrance of non-excited molecules into that region [15-17]. This allows monitoring of blood perfusing into the region of interest from other non-excited regions of the body. Although ASL has been shown to be feasible in study of the rhesus macaque placenta [18], blood perfusing cotyledons does not fill to completion before the regional excitation dissipates. This may result in failure to identify slower cotyledonary perfusion or delayed filling due to tissue pathology. Therefore, DCE MRI holds an advantage in assessment of placental function. An example DCE image of the uneroplacental region of a pregnant rhesus macaque is seen in Figure 3.

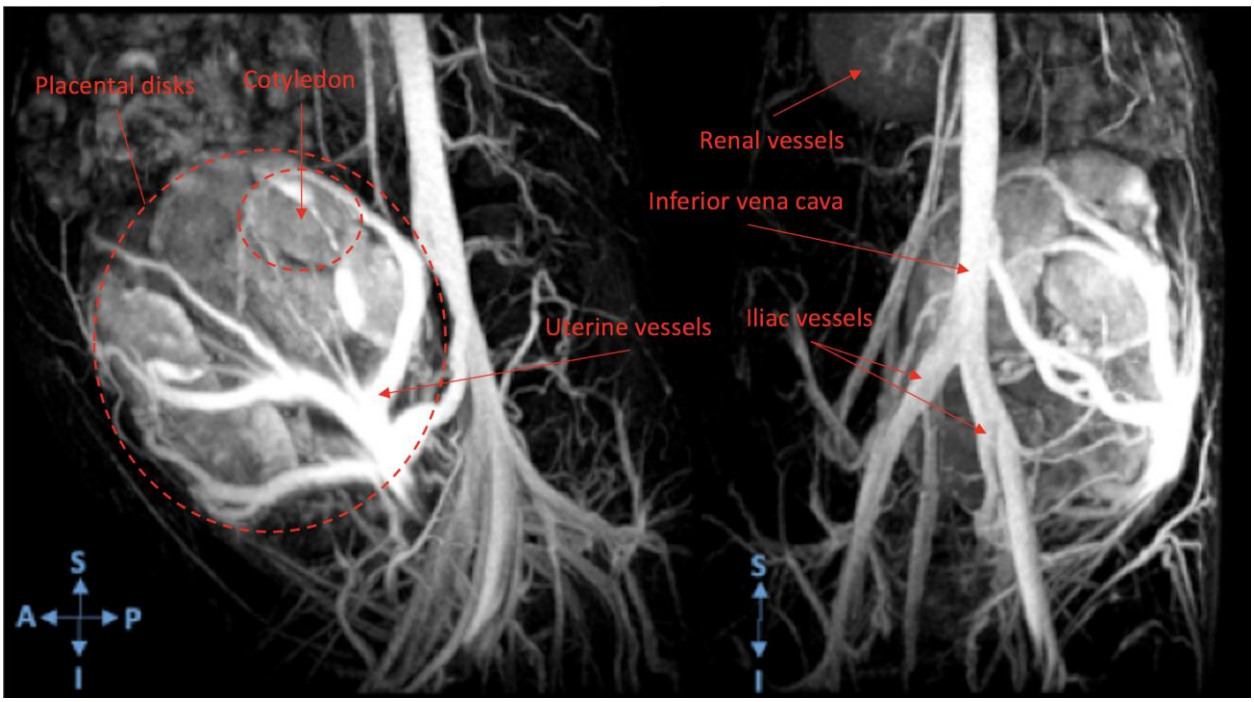

Figure 3. Ferumoxytol Dynamic Contrast Enhanced MRI of the Rhesus Macaque Uteroplacental Region. Depiction of the uteroplacental region of a pregnant rhesus macaque where white signal signifies the location of ferumoxytol following its introduction to the maternal circulation. The two placental disks (large dashed circle) with individual cotyledons (small dashed circle) are visible. Large maternal vessels are annotated to aid in orientation, including uterine vessels, iliac vessels, renal vessels, and inferior vena cava.

Traditionally, gadolinium-based contrast agents (GBCAs) are used for clinical DCE MRI [10,19,20]. However, GBCAs cross the placenta into the fetus with uncertain long-term consequences of in utero GBCA exposure [21,22]. Although without specific evidence that it causes teratogenic or chromosomal damage [23-25], the risk to the fetus of gadolinium-based MR contrast agent administration remains unknown and should not be routinely provided to pregnant patients [26]. Ferumoxytol, approved by the FDA to treat anemia in adults with renal insufficiency who cannot receive oral iron therapy, is an alternative to oral iron therapy for iron

deficiency anemias [27]. Ferumoxytol is an iron oxide nanoparticle, coated completely in polyglucose sorbitol carboxymethyl ether [28] with success as an off-label MRI contrast agent at much lower dosage than for therapeutics [29,30] (comparison with GBCAs summarized in Table 1). The carbohydrate coat prevents the bioactive iron core from reacting in the bloodstream and is designed to minimize allergic responses to the coating material [28]. Immune cells called macrophages are involved in iron trafficking and recycling. To release the bioreactive iron from its carbohydrate coat macrophages must phagocytose and "digest" the ferumoxytol in specialized organelles called lysosomes, which breaks down the coat and exposes the iron [31-33]. At this point, the macrophage recognizes the iron nanoparticles and will contribute it to the body iron pool where it will be recycled through the reticuloendothelial system for later use [28]. Ferumoxytol is considered by obstetricians to be safe and effective for treatment of iron deficiency anemia refractory to oral iron therapy in pregnant women [34].

After contrast injection, both gadolinium and ferumoxytol sustain a dynamic phase when the perfusion of contrast-laden blood entering the organ of interest can be measured [29]. Following the dynamic phase, the contrast agents are incorporated into the entire blood pool circulating through the body. Gadolinium quickly becomes extravascular as well, entering tissues. Ultimately, gadolinium is measurable by MRI in the body for a short time, with a plasma half-life of only about 1 hour, meaning that half of the volume of gadolinium that is injected is cleared from the blood by 1-hour post-injection. Ferumoxytol, on the other hand, has a long plasma half-life of 14-21 hours because ultrasmall superparamagnetic iron oxide nanoparticles are not immediately recognized for clearance by the reticuloendothelial system [28,29]. This extended plasma half-life introduces the benefit of two additional phases following the dynamic injection, which grant opportunity for other non-DCE imaging. First, ferumoxytol enters the

blood pool phase where the contrast agent is entirely intravascular. Less than half an hour following injection, the contrast agent is fully incorporated into the blood space, and an MR angiogram can be taken showcasing the entire vascular network [29,35,36]. Unlike the DCE scan which requires many low-resolution image-captures, the angiogram is taken in one snapshot at high resolution, so detailed vessel maps can be created. Next, the delayed phase takes place [29]. During this phase, macrophages, a major component of the reticuloendothelial system stationed in tissues, will pull the ferumoxytol from the vascular network and into tissues during normal clean-up processes as ferumoxytol-laden blood circulates through the body [28]. In the days following initial injection, the ferumoxytol levels in the blood will fall while levels in tissue macrophages will rise. The ferumoxytol signal will move from the blood to tissue macrophages. If there is an active tissue immune response, the macrophages (and other immune cell) numbers in tissue are higher. Ferumoxytol is retained in the particular tissue where available macrophages help clear the contrast agent. This translates into bright T1 signal in tissues in the days following the initial injection, highlighting regions of potential infection, inflammation, or otherwise non-normal function [37-39]. Ferumoxytol has been utilized in the diagnosis of type 1 diabetes [35], showing that a particular T1 signal pattern displays in the pancreas of affected people. These additional opportunities for imaging coupled with the potentially more pregnancy-safe profile make ferumoxytol an excellent candidate for use in placental imaging.

	GBCAs	Ferumoxytol
Molecule makeup	Gadolinium ion bound to a stable ligand to prevent tissue interactions and enable renal clearance	Bioactive iron oxide nanoparticle core with a polyglucose sorbitol carboxymethyl ether coat – coating prevents reactivity to iron and is meant to minimize allergic reaction
Traditionally used as a DCE MRI contrast agent?	Yes	Treatment for anemia, found to be useful as an off-label contrast agent at a much lower dose
Approved for use in pregnant women?	Yes, but long-term effects are unknown so not routinely provided	As a treatment for anemia – yes As a contrast agent – under investigation
Safe for the fetus?	A small amount is found to cross the placenta to the fetus, long-term effects are unknown	Additional research must be completed to determine if it crosses the placenta to the fetus – initial findings (Chapter 3) suggest no detectable amount
Plasma half-life	1 hour	14-21 hours
Imaging Capabilities	Dynamic Phase – perfusion rates, movement of blood into organs Short window for angiograms, though GBCAs quickly become extravascular	Dynamic Phase – perfusion rates, movement of blood into organs Blood Pool Phase – detailed angiograms Delayed Phase – immune cell homing

Table 1. GBCAs vs Ferumoxytol as Contrast Agents. Comparison of the major factors of these contrast agents relevant to use for placental imaging.

3 The State of Placental MRI

Non-contrast MRI has been successfully applied to human pregnancy to identify common placental disorders. During trophoblast invasion of the uterine wall, trophoblasts can sometimes over-invade the tissue, remaining on the wall of the uterus following labor [1,2] -- a disorder labeled placenta accreta. The placenta normally sheds from the wall of the uterus within 30 minutes following birth, allowing the uterine vessels that fed the placenta to contract to prevent bleeding into the empty uterus. When the placenta does not detach, the uterus cannot contract properly and there is a risk of severe hemorrhage and uterine tissue scarring. Postpartum hemorrhage is the leading cause of maternal morbidity worldwide [1]. Abnormal invasion can be more severe, breaching the uterine myometrium or even surrounding organs (placenta percreta). The degree of anatomical detail afforded by MRI, due to tissue relaxation rate differences between the uterus and placenta, allow for identification of this excessive trophoblast invasion, enabling delivery procedure planning for the prevention of maternal death [2-6]. Other uses of non-contrast MRI in human pregnancy includes 3D mapping of the placenta volume in early gestation for the identification of evidence of growth restriction [7], measurement of blood flow in early gestation to identify placentas with insufficient maternal blood flow [8], and mapping of oxygen-bound blood versus non-oxygen bound blood in relation to blood perfusion rate for use in study of disease [9]. 3D models of non-contrast MRI data are also being used to guide tissue sampling for study following labor, based on the differing relaxation rate of abnormal placental tissue [10].

In the rhesus macaque model, additional progress has been made in an effort to expand possible uses of MRI in pregnancy and develop protocols appropriate for use in humans. Non-contrast MRI is feasible for measuring velocity of individual hydrogen molecules in the blood

over a short time period [11]. When the data is reconstructed, 3D models of maternal and fetal vessels are created, including inflow and outflow of blood to the placenta, allowing confirmation of adequate blood flow to support pregnancy by associated vessels. Additionally, non-contrast MRI has been used to assess blood oxygenation -- the proportion of blood hemoglobin bound versus not bound to oxygen, or blood oxygen level-dependent (BOLD) MRI-- within placental cotyledons [12,13]. Oxygenation measurements of placenta blood can be used to assess sufficient delivery of oxygen to the placenta, and to measure oxygen transport at the placental villi -- both crucial to fetal health.

Study in the rhesus macaque allows examination of the use of contrast agents in pregnancy. DCE MRI with gadolinium in macaques has investigated location of maternal arteries that feed the placenta and their respective cotyledons [14]. These data have been used to quantify placental blood volume, as well as calculate the perfusion rate of blood moving into each cotyledon. These data reflect the relative health of each cotyledon, and may identify the presence of pathology if perfusion rate or blood volume quantification at a particular cotyledon is abnormal. This method was coupled with non-contrast analysis of blood oxygenation in a ZIKV infection model, showing increased rate of blood coming from maternal vessels and higher blood oxygenation in placentas of infected animals [14]. These findings reflect abnormal maternal vessel function and imply reduced oxygen transport to the fetal blood via the placental villi. In the following chapters, I will describe additional progress in placental DCE MRI in a macaque model utilizing ferumoxytol, a drug already approved for treatment of anemia in pregnant women with potential for a more pregnancy-friendly safety profile.

4 Thesis Overview

This thesis reviews the steps taken to appropriately examine ferumoxytol DCE MRI as a method for assessing placental function and the non-invasive identification of tissue pathology during gestation (experimental design outlined in Figure 4). Described first is the development of the infection model used to induce placental pathology. Infection with ZIKV in rhesus macaque pregnancy has been shown to induce a robust inflammatory response at the maternal-fetal interface (MFI) [1-3]. ZIKV virus was originally discovered in Uganda in 1947 in a rhesus macaque [4]. Since then, numerous outbreaks of ZIKV were reported, but severe cases were rare [5-6] until in 2015, when an outbreak in South America associated ZIKV with adverse pregnancy outcomes [7,8]. While adults are generally asymptomatic, infection during pregnancy can result in fetal microcephaly, ocular dysmorphogenesis, brain anomalies, musculoskeletal contractures, neurologic sequelae, and pregnancy loss [9-11]. In related studies,-primates infected with ZIKV have been seen to miscarry or have stillbirth at higher rates than seen in the non-infected colony, and the placentas in infected animals have demonstrated severe infarction with hemorrhage or advanced calcification [2]. ZIKV, Asian-lineage strain H.sapiens-tc/FRA/2013/FrenchPolynesia-01_v1c1, closely related to the strain circulating in the Americas during the 2015 outbreak, was used in establishment of the infection model for this thesis due to its current clinical relevance (2016-2020) and the evidence tied to dramatic placental tissue changes. This granted the opportunity to prospectively image pathological placentas. Our study confirmed efficient transmission of ZIKV to the fetus and placenta resulting from maternal infection, including expected placental pathology. The Puerto Rican ZIKV H.sapiens-tc/PUR/2015/PRVABC59_v3c2 isolate later replaced the Asian-lineage isolate in our experiments when it became available, as it was a more contemporary isolate of the virus.

Prior to applying ferumoxytol DCE MRI to the ZIKV infection model, we first explored and optimized the methods of injecting ferumoxytol into a non-infected rhesus macaque and completing MRI imaging on pregnant animals in order to document that these procedures alone do not introduce pathology. First, seven pregnant macaques were imaged with and without ferumoxytol. Pregnancies delivered at term and the infants were followed for 1 year, all of which showed normal growth and no developmental effects of MRI alone or with ferumoxytol. Next, four pregnant macaques received ferumoxytol DCE MRI. Placental, maternal, and fetal biopsies were collected to identify possible cellular effects of ferumoxytol DCE MRI. When compared to biopsies from macaques that did not receive ferumoxytol or MRI, no impact of ferumoxytol administration or MRI was found. Given this promising safety profile of ferumoxytol MRI, we proceeded with the analysis of ZIKV infected pregnancies by this imaging modality.

The analysis of ferumoxytol DCE MRI data involved an intensive placental dissection and the manual matching of tissue samples to the MRI data, based on placental shape and the layout of cotyledons. For that reason, the methods for dissecting and data matching are presented in a separate chapter, with a description of how the MRI data can be 3D printed and used to streamline research tissue analysis. Placental pathology is often focal and difficult to identify when collecting research biopsies. Placental researchers would benefit from a procedure developed for matching MRI data to the placental tissue -- regions of abnormal blood flow could be identified in advance and those locations could be chosen for biopsy to ensure collection of pathological tissue, rather than taking random biopsies and risking missing all pathology. Our proposed method was found to be feasible in a single non-infected macaque, then applied to all MRI examined ZIKV-infected pregnancies.

Finally, the results of the DCE MRI imaging of rhesus macaques infected with ZIKV virus in the first trimester are described. 14 pregnant macaques were imaged with ferumoxytol, with or without infection, and the resulting data were developed into maps of perfusion domain volume and flow. Placental cotyledon tissue was graded for pathology and matched to these maps to investigate possible correlations between high pathology and abnormal blood movement or placental blood space volume. When individual cotyledons were assessed at term, there was no significant difference in flow or volume between pathological and non-pathological cotyledons within the same placenta. However, when average cotyledon flow and volume was assessed between animals at term, it was found that placentas with a higher number of infarctions and placentas with overall higher relative pathology had significantly varied flow and volume. While our results suggest that DCE MRI may not be sensitive enough to locate pathological vs non-pathological cotyledons in a single placenta, we do see a detectable difference in functional information in overall pathological vs non-pathological placentas in our ZIKV model. This data prompts future studies utilizing infections with varied pathology, as well as studies with infection at different timepoints in gestation, or with different inducers of placental pathology and dysfunction.

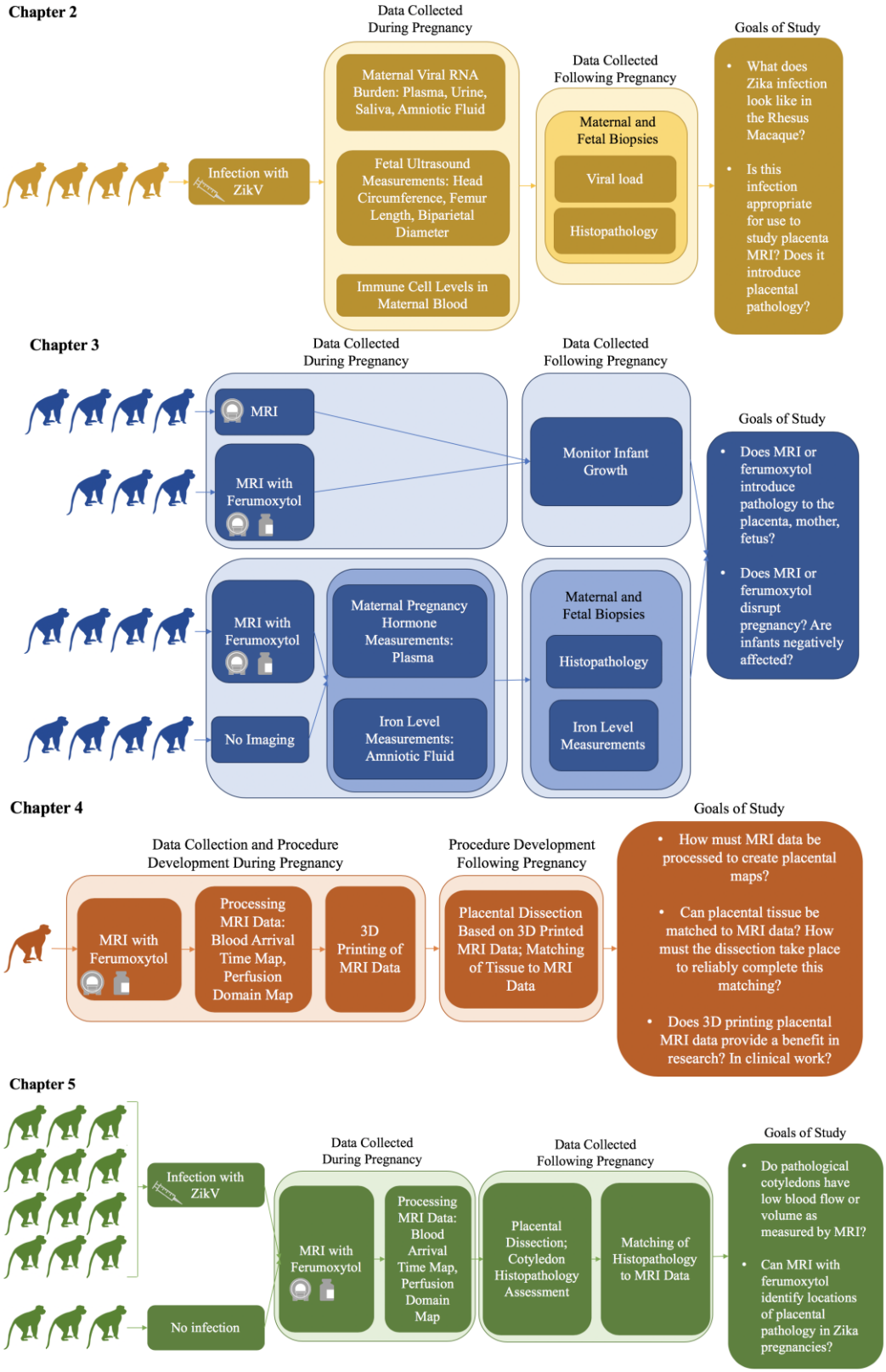

Figure 4. Experimental Design. Experimental design for each chapter of this thesis. Monkeys on the left of each diagram represent each animal utilized per chapter. Chapter 2 establishes an

infection model, ZIKV virus in a pregnant rhesus macaque, for later use in investigation of the abilities of DCE MRI with ferumoxytol. Chapter 3 assesses the safety profile of ferumoxytol MRI in non-infected rhesus macaques, to confirm that use of ferumoxytol or the imaging process does not promote placental dysfunction or pathology. Chapter 4 describes the processing of collected DCE MRI data, the dissection method used when collecting placental tissue, and proposes the benefit of using MRI data to guide placental tissue collection. Chapter 5 analyzes the ability of DCE MRI to predict pathology in the placenta by comparing MRI placental perfusion data to region-matched placental tissue.

Significance

This work furthers our understanding of the use of DCE MRI in the study of placental function and pathology, while also assessing the current limitations on the abilities of the imaging modality and contrast agent. These are important first steps towards applying these imaging methods in humans, where they may hold potential as a diagnostic tool early in pregnancy. It was demonstrated that ferumoxytol DCE MRI is feasible in our rhesus macaque model with low risk of maternal or fetal harm. We provided evidence that imaging is sensitive enough to identify changes in flow and volume in placentas with a higher number of infarctions or higher general pathology severity in a ZIKV model. While only a single infection model is studied here, and placental pathology can vary significantly by infection model, this work sets the stage for further investigation into placental DCE MRI and its potential applications in healthcare.

Limitations

As our studies utilize a single infection model that is known to cause severe placental infection, the scientific investigation completed can only truly make conclusions about the monitoring of similarly severe pathology. There are many conditions that can prevent normal placental function and further investigation should be completed to determine how sensitive DCE MRI is in monitoring less severe pathology. Additionally, due to the expense and availability, the cohorts described here are much smaller than one would see with other animal models.

References

1.1 The Placenta: Form, Function, and Value

1. Gude NM, Roberts CT, Kalionis B, King RG. Growth and function of the normal human placenta. Thrombosis Research 2004; 114:397–407.
2. Burton GJ, Jauniaux E. What is the placenta? American Journal of Obstetrics and Gynecology 2015; 213:S6.E1–S6.E4.
3. Jensen OE, Chernyavsky IL. Blood Flow and Transport in the Human Placenta. Annual Review of Fluid Mechanics 2019; 51:25–47.
4. Turco MY, Moffett A. Development of the human placenta. Development 2019; 146.
5. Lyall F, Robson SC, Bulmer JN. Spiral Artery Remodeling and Trophoblast Invasion in Preeclampsia and Fetal Growth Restriction. Hypertension 2013; 62:1046-1054.
6. Tessier DR, Yockell-Lelièvre J, Gruslin A. Uterine Spiral Artery Remodeling: The Role of Uterine Natural Killer Cells and Extravillous Trophoblasts in Normal and High-Risk Human Pregnancies. American Journal of Reproductive Immunology 2015; 74:1-11.
7. Yang F, Zheng Q, Jin L. Dynamic Function and Composition Changes of Immune Cells During Normal and Pathological Pregnancy at the Maternal-Fetal Interface. Frontiers in Immunology 2019; 10.
8. Jensen OE, Chernyavsky IL. Blood Flow and Transport in the Human Placenta. Annual Review of Fluid Mechanics 2019; 51:25–47.
9. Benirschke K, Kaufman P, Baergen R. Pathology of the Human Placenta. 5th ed. New York, NY: Springer Verlag; 2006.
10. Barker D, Osmond C, Grant S, Thornburg K, Cooper C, Ring S, Davey-Smith G.

Maternal cotyledons at birth predict blood pressure in childhood. Placenta 2013; 34:672–675.

11. Alexander BT. Placental insufficiency leads to development of hypertension in growth-restricted offspring. Hypertension 2003; 41:457-462.
12. Brosens I, Pijnenborg R, Vercruysse L, Romero R. The "Great Obstetrical Syndromes" are associated with disorders of deep placentation. American Journal of Obstetrics and Gynecology 2011; 204:193-201.
13. Krishna U, Bhalerao S. Placental insufficiency and fetal growth restriction. Journal of Obstetrics and Gynaecology India 2011; 61:505-511.
14. Roberts DJ, Post MD. The placenta in pre-eclampsia and intrauterine growth restriction. Journal of Clinical Pathology 2008; 61:1254-1260.
15. Fox H. The histopathology of placental insufficiency. Journal of Clinical Pathology 1976; 29:1–8.
16. Vázquez-Boland JA, Krypotou E, Scortti M. Listeria Placental Infection. MBio 2017; 8.
17. Tabata T, Petitt M, Fang-Hoover J, Zydek M, Pereira L. Persistent Cytomegalovirus Infection in Amniotic Membranes of the Human Placenta. The American Journal of Pathology 2016; 186:2970–2986.
18. Mcdonagh S, Maidji E, Ma W, Chang HT, Fisher S, Pereira L. Viral and Bacterial Pathogens at the Maternal-Fetal Interface. The Journal of Infectious Diseases 2004; 190:826–834.
19. Hirsch AJ, Roberts VHJ, Grigsby PL, Haese N, Schabel MC, Wang X, Lo JO, Liu Z, Kroenke CD, Smith JL, Kelleher M, Broeckel R, et al. Zika virus infection in pregnant

rhesus macaques causes placental dysfunction and immunopathology. Nature Communications 2018; 9.

20. Romero R, Kim YM, Pacora P, Kim CJ, Benshalom-Tirosh N, Jaiman S, Bhatti G, Kim J-S, Qureshi F, Jacques SM, Jung EJ, Yeo L, et al. The frequency and type of placental histologic lesions in term pregnancies with normal outcome. Journal of Perinatal Medicine 2018; 46:613–630.
21. Roberts DJ. Placenta Pathology, a Survival Guide. Archives of Pathology & Laboratory Medicine 2008; 132:641–651.
22. Newnham JP, O'dea MR-A, Reid KP, Diepeveen DA. Doppler flow velocity waveform analysis in high risk pregnancies: a randomized controlled trial. BJOG: An International Journal of Obstetrics and Gynaecology 1991; 98:956–963.
23. Kofinas AD, Penry M, Nelson LH, Meis PJ, Swain M. Uterine and Umbilical Artery Flow Velocity Waveform Analysis in Pregnancies Complicated by Chronic Hypertension or Preeclampsia. Southern Medical Journal 1990; 83:150–155.
24. Fadl S, Moshiri M, Fligner CL, Katz DS, Dighe M. Placental Imaging: Normal Appearance with Review of Pathologic Findings. RadioGraphics 2017; 37:979–998.
25. Hashem LB, Salem DS, Hamed ST, Hussein AM. Role of MRI versus ultrasound in the assessment of placental abnormalities and diseases. The Egyptian Journal of Radiology and Nuclear Medicine 2016; 47:641–658.
26. Chalouhi GE, Deloison B, Siauve N, Aimot S, Balvay D, Cuenod CA, Ville Y, Clément O, Salomon LJ. Dynamic contrast-enhanced magnetic resonance imaging: definitive imaging of placental function?. Seminars in Fetal and Neonatal Medicine 2011; 16:22-28.
27. Frias AE, Schabel MC, Roberts VHJ, Tudorica A, Grigsby PL, Oh KY, Kroenke CD.

Using dynamic contrast-enhanced MRI to quantitatively characterize maternal vascular organization in the primate placenta. Magnetic Resonance in Medicine 2014; 73:1570–1578.

28. Hirsch AJ, Roberts VHJ, Grigsby PL, Haese N, Schabel MC, Wang X, Lo JO, Liu Z, Kroenke CD, Smith JL, Kelleher M, Broeckel R, et al. Zika virus infection in pregnant rhesus macaques causes placental dysfunction and immunopathology. Nature Communications 2018; 9.

29. Ludwig KD, Fain SB, Nguyen SM, Golos TG, Reeder SB, Bird IM, Shah DM, Wieben OE, Johnson KM. Perfusion of the placenta assessed using arterial spin labeling and ferumoxytol dynamic contrast enhanced magnetic resonance imaging in the rhesus macaque. Magnetic Resonance in Medicine 2018; 81:1964–1978.

30. Zhu A, Reeder SB, Johnson KM, Nguyen SM, Golos TG, Shimakawa A, Muehler MR, Francois CJ, Bird IM, Fain SB, Shah DM, Wieben O, et al. Evaluation of a motion-robust 2D chemical shift-encoded technique for R2* and field map quantification in ferumoxytol-enhanced MRI of the placenta in pregnant rhesus macaques. Journal of Magnetic Resonance Imaging 2019; 51:580–592.

31. Zhu A, Reeder SB, Johnson KM, Nguyen SM, Fain SB, Bird IM, Golos TG, Wieben O, Shah DM, Hernando D. Quantitative ferumoxytol-enhanced MRI in pregnancy: A feasibility study in the nonhuman primate. Magnetic Resonance Imaging 2020; 65:100–108.

32. De Rijk EPCT, Esch EV. The Macaque Placenta—A Mini-Review. Toxicologic Pathology 2008; 36:108S–118S.

33. Stouffer RL, Woodruff TK. Nonhuman Primates: A Vital Model for Basic and Applied

Research on Female Reproduction, Prenatal Development, and Women's Health. ILAR Journal 2017; 58:281–294.

34. Weatherall DJ. The use of non-human primates in research: a working group report. London: Academy of Medical Sciences; 2006.

35. Joffe TH, Tarantal AF, Rice K, Leland M, Oerke A-K, Rodeck C, Geary M, Hindmarsh P, Wells JC, Aiello LC. Fetal and infant head circumference sexual dimorphism in primates. American Journal of Physical Anthropology 2004; 126:97–110.

36. Carvalho C, Gaspar A, Knight A, Vicente L. Ethical and Scientific Pitfalls Concerning Laboratory Research with Non-Human Primates, and Possible Solutions. Animals 2018; 9:12.

37. Coleman K. Caring for nonhuman primates in biomedical research facilities: scientific, moral and emotional considerations. American Journal of Primatology 2011; 73:220–225.

38. Quigley M. Non-human primates: the appropriate subjects of biomedical research? Journal of Medical Ethics 2007; 33:655–658.

1.2 Dynamic Contrast Enhanced Magnetic Resonance Imaging: The Basics

1. Hornak JP. The Basics of MRI. Rochester, NY: Rochester Institute of Technology; 2019.

2. Grover VP, Tognarelli JM, Crossey MM, Cox IJ, Taylor-Robinson SD, Mcphail MJ. Magnetic Resonance Imaging: Principles and Techniques: Lessons for Clinicians. Journal of Clinical and Experimental Hepatology 2015; 5:246–255.

3. Pooley RA. Fundamental Physics of MR Imaging. RadioGraphics 2005; 25:1087–1099.

4. Villanueva-Meyer JE, Mabray MC, Cha S. Current Clinical Brain Tumor Imaging. Neurosurgery 2017; 81:397–415.

5. Chan WP. Magnetic resonance imaging of soft-tissue tumors of the extremities: A practical approach. World Journal of Radiology 2013; 5:455–459.

6. Donahue MJ, Blakeley JO, Zhou J, Pomper MG, Laterra J, Zijl PCV. Evaluation of human brain tumor heterogeneity using multipleT1-based MRI signal weighting approaches. Magnetic Resonance in Medicine 2008; 59:336–344.

7. Kim PK, Hong YJ, Im DJ, Suh YJ, Park CH, Kim JY, Chang S, Lee H-J, Hur J, Kim YJ, Choi BW. Myocardial T1 and T2 Mapping: Techniques and Clinical Applications. Korean Journal of Radiology 2017; 18:113–131.

8. Hanrahan CJ, Shah LM. MRI of Spinal Bone Marrow: Part 2, T1-Weighted Imaging-Based Differential Diagnosis. American Journal of Roentgenology 2011; 197:1309–1321.

9. Taylor AJ, Salerno M, Dharmakumar R, Jerosch-Herold M. T1 Mapping. JACC: Cardiovascular Imaging 2016; 9:67–81.

10. O'connor JPB, Tofts PS, Miles KA, Parkes LM, Thompson G, Jackson A. Dynamic contrast-enhanced imaging techniques: CT and MRI. The British Journal of Radiology 2011; 84:S112–S120.

11. Cuenod C, Balvay D. Perfusion and vascular permeability: Basic concepts and measurement in DCE-CT and DCE-MRI. Diagnostic and Interventional Imaging 2013; 94:1187–1204.

12. Gordon Y, Partovi S, Muller-Eschner M, Amarteifio E, Bauerle T, Marc-Andre, Kauczor H-U, Rengier F. Dynamic contrast-enhanced magnetic resonance imaging: fundamentals and application to the evaluation of the peripheral perfusion. Cardiovascular Diagnosis & Therapy 2014; 4:147–164.

13. Nam J, Kang K, Choi S, Lim W, Yoo R-E, Kim J-H, Yun T, Sohn C-H. Comparison between the Prebolus T1 Measurement and the Fixed T1 Value in Dynamic Contrast-Enhanced MR Imaging for the Differentiation of True Progression from Pseudoprogression in Glioblastoma Treated with Concurrent Radiation Therapy and Temozolomide Chemotherapy. American Journal of Neuroradiology 2017; 38:2243–2250.

14. Baxter S, Wang ZJ, Joe BN, Qayyum A, Taouli B, Yeh BM. Timing bolus dynamic contrast-enhanced (DCE) MRI assessment of hepatic perfusion: Initial experience. Journal of Magnetic Resonance Imaging 2009; 29:1317–1322.

15. Pollock JM, Tan H, Kraft RA, Whitlow CT, Burdette JH, Maldjian JA. Arterial Spin-Labeled MR Perfusion Imaging: Clinical Applications. Magnetic Resonance Imaging Clinics of North America 2009; 17:315–338.

16. Borogovac A, Asllani I. Arterial Spin Labeling (ASL) fMRI: Advantages, Theoretical Constraints and Experimental Challenges in Neurosciences. International Journal of Biomedical Imaging 2012; 2012.

17. Haller S, Zaharchuk G, Thomas DL, Lovblad K-O, Barkhof F, Golay X. Arterial Spin Labeling Perfusion of the Brain: Emerging Clinical Applications. Radiology 2016; 281:337–356.

18. Ludwig KD, Fain SB, Nguyen SM, Golos TG, Reeder SB, Bird IM, Shah DM, Wieben OE, Johnson KM. Perfusion of the placenta assessed using arterial spin labeling and ferumoxytol dynamic contrast enhanced magnetic resonance imaging in the rhesus macaque. Magnetic Resonance in Medicine 2018; 81:1964–1978.

19. Lohrke J, Frenzel T, Endrikat J, Alves FC, Grist TM, Law M, Lee JM, Leiner T, Li K-C,

Nikolaou K, Prince MR, Schild HH, et al. 25 Years of Contrast-Enhanced MRI: Developments, Current Challenges and Future Perspectives. Advances in Therapy 2016; 33:1–28.

20. Gaddikeri S, Gaddikeri R, Tailor T, Anzai Y. Dynamic Contrast-Enhanced MR Imaging in Head and Neck Cancer: Techniques and Clinical Applications. American Journal of Neuroradiology 2015; 37:588–595.
21. Ray JG, Vermeulen MJ, Bharatha A, Montanera WJ, Park AL. Association Between MRI Exposure During Pregnancy and Fetal and Childhood Outcomes. Jama 2016; 316:952–961.
22. Siauve N, Chalouhi GE, Deloison B, Alison M, Clement O, Ville Y, Salomon LJ. Functional imaging of the human placenta with magnetic resonance. American Journal of Obstetrics and Gynecology 2015; 213.
23. Rogosnitzky M, Branch S. Gadolinium-based contrast agent toxicity: a review of known and proposed mechanisms. BioMetals 2016; 29:365–376.
24. Oh KY, Roberts VHJ, Schabel MC, Grove KL, Woods M, Frias AE. Gadolinium Chelate Contrast Material in Pregnancy: Fetal Biodistribution in the Nonhuman Primate. Radiology 2015; 276:110–118.
25. Prola-Netto J, Woods M, Roberts VHJ, Sullivan EL, Miller CA, Frias AE, Oh KY. Gadolinium Chelate Safety in Pregnancy: Barely Detectable Gadolinium Levels in the Juvenile Nonhuman Primate after in Utero Exposure. Radiology 2018; 286:122–128.
26. Kanal E, Barkovich AJ, Bell C, Borgstede JP, Bradley WG, Froelich JW, Gimbel JR,

Gosbee JW, Kuhni-Kaminski E, Larson PA, Lester JW, Nyenhuis J, et al. ACR guidance document on MR safe practices: 2013. Journal of Magnetic Resonance Imaging 2013; 37:501–530.

27. AMAG Pharmaceuticals. Feraheme: Highlights of Prescribing Information; 2018. https://www.accessdata.fda.gov/drugsatfda_docs/label/2009/022180lbl.pdf. Accessed August 2, 2020.

28. Pai AB, Garba AO. Ferumoxytol: a silver lining in the treatment of anemia of chronic kidney disease or another dark cloud? Journal of Blood Medicine 2012; 3:77–85.

29. Toth GB, Varallyay CG, Horvath A, Bashir MR, Choyke PL, Daldrup-Link HE, Dosa E, Finn JP, Gahramanov S, Harisinghani M, Macdougall I, Neuwelt A, et al. Current and potential imaging applications of ferumoxytol for magnetic resonance imaging. Kidney International 2017; 92:47–66.

30. Vasanawala SS, Nguyen K-L, Hope MD, Bridges MD, Hope TA, Reeder SB, Bashir MR. Safety and technique of ferumoxytol administration for MRI. Magnetic Resonance in Medicine 2016; 75:2107–2111.

31. Corot C, Robert P, Idee J, Port M. Recent advances in iron oxide nanocrystal technology for medical imaging. Advanced Drug Delivery Reviews 2006; 58:1471–1504.

32. Raynal I, Prigent P, Peyramaure S, Najid A, Rebuzzi C, Corot C. Macrophage Endocytosis of Superparamagnetic Iron Oxide Nanoparticles. Investigative Radiology 2004; 39:56–63.

33. Feng Q, Liu Y, Huang J, Chen K, Huang J, Xiao K. Uptake, distribution, clearance, and toxicity of iron oxide nanoparticles with different sizes and coatings. Scientific Reports 2018; 8.

34. Auerbach M, Landy HJ. Anemia in pregnancy; 2019. https://www.uptodate.com/contents/anemia-in-pregnancy?topicRef=7148&source=see_link. Accessed August 2, 2020.

35. Macdonald JA, Corrado PA, Nguyen SM, Johnson KM, Francois CJ, Magness RR, Shah DM, Golos TG, Wieben O. Uteroplacental and Fetal 4D Flow MRI in the Pregnant Rhesus Macaque. Journal of Magnetic Resonance Imaging 2018; 49:534–545.

36. Stoumpos S, Hennessy M, Vesey AT, Radjenovic A, Kasthuri R, Kingsmore DB, Mark PB, Roditi G. Ferumoxytol-enhanced magnetic resonance angiography for the assessment of potential kidney transplant recipients. European Radiology 2017; 28:115–123.

37. Gaglia JL, Harisinghani M, Aganj I, Wojtkiewicz GR, Hedgire S, Benoist C, Mathis D, Weissleder R. Noninvasive mapping of pancreatic inflammation in recent-onset type-1 diabetes patients. Proceedings of the National Academy of Sciences 2015; 112:2139–2144.

38. Iv M, Samghabadi P, Holdsworth S, Gentles A, Rezaii P, Harsh G, Li G, Thomas R, Moseley M, Daldrup-Link HE, Vogel H, Wintermark M, et al. Quantification of Macrophages in High-Grade Gliomas by Using Ferumoxytol-enhanced MRI: A Pilot Study. Radiology 2019; 290:198–206.

39. Stirrat CG, Alam SR, Macgillivray TJ, Gray CD, Dweck MR, Raftis J, Jenkins WS, Wallace WA, Pessotto R, Lim KH, Mirsadraee S, Henriksen PA, et al. Ferumoxytol-enhanced magnetic resonance imaging assessing inflammation after myocardial infarction. Heart 2017; 103:1528–1535.

1.3 The State of Placental MRI

1. Urner F, Zimmermann R, Krafft A. Manual Removal of the Placenta after Vaginal

Delivery: An Unsolved Problem in Obstetrics. Journal of Pregnancy 2014; 2014:1–5.

2. Kilcoyne A, Shenoy-Bhangle AS, Roberts DJ, Sisodia RC, Gervais DA, Lee SI. MRI of Placenta Accreta, Placenta Increta, and Placenta Percreta: Pearls and Pitfalls. American Journal of Roentgenology 2017; 208:214–221.
3. Varghese B, Singh N, George R, Gilvaz S. Magnetic resonance imaging of placenta accreta. Indian Journal of Radiology and Imaging 2013; 23:379–385.
4. Cuthbert F, Vinas MT, Whitby E. The MRI features of placental adhesion disorder—a pictorial review. The British Journal of Radiology 2016; 89.
5. Fadl S, Moshiri M, Fligner CL, Katz DS, Dighe M. Placental Imaging: Normal Appearance with Review of Pathologic Findings. RadioGraphics 2017; 37:979–998.
6. Hashem LB, Salem DS, Hamed ST, Hussein AM. Role of MRI versus ultrasound in the assessment of placental abnormalities and diseases. The Egyptian Journal of Radiology and Nuclear Medicine 2016; 47:641–658.
7. Armstrong T, Liu D, Martin T, Masamed R, Janzen C, Wong C, Chanlaw T, Devaskar SU, Sung K, Wu HH. 3D R2* mapping of the placenta during early gestation using free-breathing multiecho stack-of-radial MRI at 3T. Journal of Magnetic Resonance Imaging 2018; 49:291–303.
8. Liu D, Shao X, Danyalov A, Chanlaw T, Masamed R, Wang DJ, Janzen C, Devaskar SU, Sung K. Human Placenta Blood Flow During Early Gestation With Pseudocontinuous Arterial Spin Labeling MRI. Journal of Magnetic Resonance Imaging 2019; 51:1247–1257.
9. Hutter J, Harteveld AA, Jackson LH, Franklin S, Bos C, Osch MJP, O'muircheartaigh J, Ho A, Chappell L, Hajnal JV, Rutherford M, Vita ED. Perfusion and apparent

oxygenation in the human placenta (PERFOX). Magnetic Resonance in Medicine 2019; 83:549–560.

10. Roberts VH, Gaffney JE, Lewandowski KS, Schabel MC, Morgan TK, Frias AE. A standardized method for collection of human placenta samples in the age of functional magnetic resonance imaging. BioTechniques 2019; 67:45–49.
11. Macdonald JA, Corrado PA, Nguyen SM, Johnson KM, Francois CJ, Magness RR, Shah DM, Golos TG, Wieben O. Uteroplacental and Fetal 4D Flow MRI in the Pregnant Rhesus Macaque. Journal of Magnetic Resonance Imaging 2018; 49:534–545.
12. Schabel MC, Roberts VHJ, Lo JO, Platt S, Grant KA, Frias AE, Kroenke CD. Functional imaging of the nonhuman primate Placenta with endogenous blood oxygen level-dependent contrast. Magnetic Resonance in Medicine 2015; 76:1551–1562.
13. Hirsch AJ, Roberts VHJ, Grigsby PL, Haese N, Schabel MC, Wang X, Lo JO, Liu Z, Kroenke CD, Smith JL, Kelleher M, Broeckel R, et al. Zika virus infection in pregnant rhesus macaques causes placental dysfunction and immunopathology. Nature Communications 2018; 9.
14. Frias AE, Schabel MC, Roberts VHJ, Tudorica A, Grigsby PL, Oh KY, Kroenke CD. Using dynamic contrast-enhanced MRI to quantitatively characterize maternal vascular organization in the primate placenta. Magnetic Resonance in Medicine 2014; 73:1570–1578.

1.4 Thesis Overview

1. Abbink P, Larocca RA, Barrera RADL, Bricault CA, Moseley ET, Boyd M, Kirilova M,

Li Z, Nganga D, Nanayakkara O, Nityanandam R, Mercado NB, et al. Protective efficacy of multiple vaccine platforms against Zika virus challenge in rhesus monkeys. Science 2016; 353:1129–1132.

2. Dudley DM, Aliota MT, Mohr EL, Weiler AM, Lehrer-Brey G, Weisgrau KL, Mohns MS, Breitbach ME, Rasheed MN, Newman CM, Gellerup DD, Moncla LH, et al. A rhesus macaque model of Asian-lineage Zika virus infection. Nature Communications 2016; 7.

3. Nguyen SM, Antony KM, Dudley DM, Kohn S, Simmons HA, Wolfe B, Salamat MS, Teixeira LBC, Wiepz GJ, Thoong TH, Aliota MT, Weiler AM, et al. Highly efficient maternal-fetal Zika virus transmission in pregnant rhesus macaques. PLOS Pathogens 2017; 13.

4. Dick G, Kitchen S, Haddow A. Zika Virus (I). Isolations and serological specificity. Transactions of the Royal Society of Tropical Medicine and Hygiene 1952; 46:509–520.

5. Duffy MR, Chen T-H, Hancock WT, Powers AM, Kool JL, Lanciotti RS, Pretrick M, Marfel M, Holzbauer S, Dubray C, Guillaumot L, Griggs A, et al. Zika Virus Outbreak on Yap Island, Federated States of Micronesia. New England Journal of Medicine 2009; 360:2536–2543.

6. Hayes EB. Zika Virus Outside Africa. Emerging Infectious Diseases 2009; 15:1347–1350.

7. Chan JF, Choi GK, Yip CC, Cheng VC, Yuen K-Y. Zika fever and congenital Zika syndrome: An unexpected emerging arboviral disease. Journal of Infection 2016; 72:507–524.

8. Meaney-Delman D, Oduyebo T, Polen KN, White JL, Bingham AM, Slavinski SA,

Heberlein-Larson L, George KS, Rakeman JL, Hills S, Olson CK, Adamski A, et al. Prolonged Detection of Zika Virus RNA in Pregnant Women. Obstetrics & Gynecology 2016; 128:724–730.

9. Melo ASDO, Aguiar RS, Amorim MMR, Arruda MB, Melo FDO, Ribeiro STC, Batista AGM, Ferreira T, Santos MPD, Sampaio VV, Moura SRM, Rabello LP, et al. Congenital Zika Virus Infection. JAMA Neurology 2016; 73:1407–1416.
10. Driggers RW, Ho C-Y, Korhonen EM, Kuivanen S, Jääskeläinen AJ, Smura T, Rosenberg A, Hill DA, Debiasi RL, Vezina G, Timofeev J, Rodriguez FJ, et al. Zika Virus Infection with Prolonged Maternal Viremia and Fetal Brain Abnormalities. New England Journal of Medicine 2016; 374:2142–2151.
11. Honein MA, Dawson AL, Petersen EE, Jones AM, Lee EH, Yazdy MM, Ahmad N, Macdonald J, Evert N, Bingham A, Ellington SR, Shapiro-Mendoza CK, et al. Birth Defects Among Fetuses and Infants of US Women With Evidence of Possible Zika Virus Infection During Pregnancy. Jama 2017; 317:59–68.

Chapter 2:

Highly Efficient Maternal-Fetal Zika Virus Transmission in Pregnant Rhesus Macaques

Publication: Sydney M. Nguyen, Kathleen M. Antony, Dawn M. Dudley, Sarah Kohn, Heather A. Simmons, Bryce Wolfe, M. Shahriar Salamat, Leandro B. C. Teixeira, Gregory J. Wiepz, Troy H. Thoong, Matthew T. Aliota, Andrea M. Weiler, Gabrielle L. Barry, Kim L. Weisgrau, Logan J. Vosler, Mariel S. Mohns, Meghan E. Breitbach, Laurel M. Stewart, Mustafa N. Rasheed, Christina M. Newman, Michael E. Graham, Oliver E. Wieben, Patrick A. Turski, Kevin M. Johnson, Jennifer Post, Jennifer M. Hayes, Nancy Schultz-Darken, Michele L. Schotzko, Josh A. Eudailey, Sallie R. Permar, Eva G. Rakasz, Emma L. Mohr, Saverio Capuano III, Alice F. Tarantal, Jorge E. Osorio, Shelby L. O'Connor, Thomas C. Friedrich, David H. O'Connor, and Thaddeus G. Golos. 2017. Highly Efficient Maternal-Fetal Zika Virus Transmission in Pregnant Rhesus Macaques. PLOS Path. doi: 10.1371/journal.ppat.1006378.

ABSTRACT

Infection with Zika virus (ZIKV) is associated with human congenital fetal anomalies. To model fetal outcomes in nonhuman primates, we administered Asian-lineage ZIKV subcutaneously to four pregnant rhesus macaques. While non-pregnant animals in a previous study contemporary with the current report clear viremia within 10-12 days, maternal viremia was prolonged in 3 of 4 pregnancies. Fetal head growth velocity in the last month of gestation determined by ultrasound assessment of head circumference was decreased in comparison with biparietal diameter and femur length within each fetus, both within normal range. ZIKV RNA

was detected in tissues from all four fetuses at term cesarean section. In all pregnancies, neutrophilic infiltration was present at the maternal-fetal interface (decidua, placenta, fetal membranes), in various fetal tissues, and in fetal retina, choroid, and optic nerve (first trimester infection only). Consistent vertical transmission in this primate model may provide a platform to assess risk factors and test therapeutic interventions for interruption of fetal infection. The results may also suggest that maternal-fetal ZIKV transmission in human pregnancy may be more frequent than currently appreciated.

INTRODUCTION

Zika Virus (ZIKV; *Flaviviridae, Flavivirus*) is spread by *Aedes* mosquitoes [1, 2] and sexual contact [3-9]. ZIKV, first detected in the Americas in early 2015, is now endemic. *In utero* infection with ZIKV circulating in Oceania and the Americas has been associated with increased incidence of fetal microcephaly [10, 11]. Fetal findings include placental calcifications, growth restriction, arthrogryposis, severe central nervous system (CNS) malformations [11-16], intraocular calcifications, cataracts [17, 18] and skeletal [19, 20], and sensory [20] disorders. The constellation of developmental abnormalities observed following ZIKV infection during pregnancy is termed “congenital Zika syndrome” [21-23]. Prolonged viremia (>14 days) during pregnancy compared to nonpregnant individuals (7-10 days [24]) has been noted [24-26]; however, the potential association between prolonged maternal viremia and congenital Zika syndrome is not clear at this time.

Nonhuman primates are important models for human infectious disease, and ZIKV infection in rhesus macaques (*Macaca mulatta*) has been established [27-29]. Viremia in nonpregnant Indian rhesus macaques has been shown to persist for 7-10 days, similar to human

infection [27-29]. Nonhuman primate pregnancy has salient similarities to human pregnancy, including hemochorial placentation with extensive trophoblast invasion and remodeling of decidual spiral arteries [30-32] and prolonged gestation with a similar trajectory of fetal development [33]. Maternal infection with a high dose (5000-fold higher than our current study) of an Asian viral strain (strain FSS13025, Cambodia 2010) in a single pigtail macaque (*Macaca nemestrina*) resulted in maternal viremia and severe fetal neurodevelopmental abnormalities as well as fetal and placental infection [34].

It was previously reported that while moderate infectious doses of ZIKV are cleared promptly in nonpregnant macaques, initial data from two pregnant macaques infected in the first trimester showed prolonged viremia, similar to reports of human pregnancies [28]. Here we report that the fetuses of these two first trimester ZIKV pregnancies, as well as two additional late second/early third trimester infections, had maternal-fetal ZIKV transmission with vRNA and pathology in fetal tissues as well as at the maternal-fetal interface.

RESULTS

Maternal ZIKV in blood and other body fluids

Four pregnant macaques were infected by subcutaneous injection of $1x10^4$ PFU of the Asian-lineage ZIKV strain H.sapiens-tc/FRA/2013/FrenchPolynesia-01_v1c1 [28], which is closely related to strains circulating in the Americas. Animals 827577 and 680875 were infected at 31 or 38 days gestation, respectively (mid-first trimester) (term 165±10 days). Animals 598248 and 357676 were infected at 103 or 118 days gestation, respectively (late second/early third trimester). ZIKV RNA was measured in plasma, urine, saliva, and amniotic fluid, and ultrasound imaging of the fetus was performed following infection through ~155 days gestation

(Figs. 1A, S1). All monkeys had detectable plasma viremia for 11 to 70 days post-inoculation (dpi) (Figs. 1B, 2A) and at least one day of detectable vRNA in urine. Two macaques had detectable vRNA in saliva, and one macaque infected at the beginning of the third trimester had detectable vRNA in amniotic fluid on 15, 22, and 36 dpi (118, 125, and 139 days gestation, respectively) (Fig. 1B).

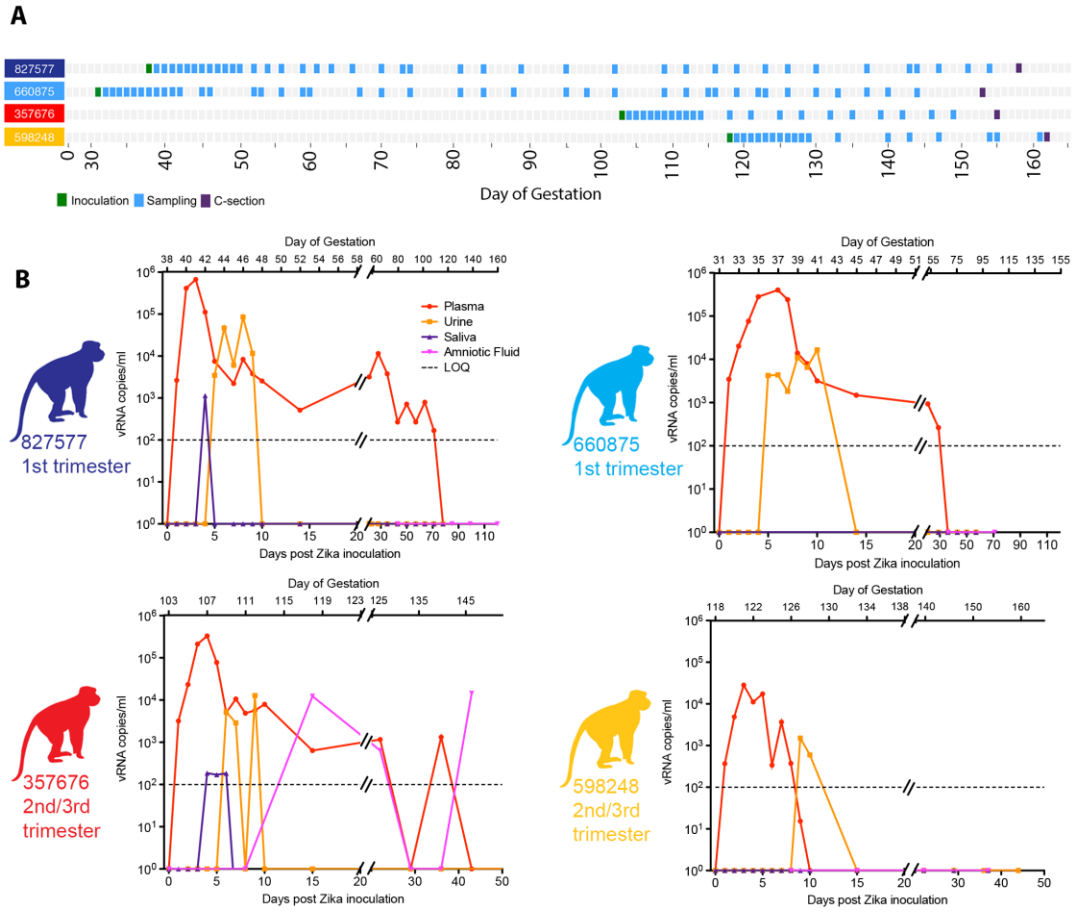

Figure 1. Study layout and viral RNA burden in pregnant rhesus fluids. (**A**) Schematic representation of the timeline of infection, sampling for maternal viral burden, and experimental cesarean section, for all animals in the study. Animals received a ZIKV challenge in the first or late second/early third trimesters of pregnancy, and blood and other fluid samples were collected according to the schedule indicated in detail in supplementary Fig. S1. (**B**) ZIKV viral load in

pregnant macaque fluids. Viral RNA loads (vRNA copies/ml) measured in plasma, urine, saliva, and amniotic fluid presented individually for the four pregnant animals. The day post-inoculation is indicated below each graph, and gestational age (days) for each animal is indicated above (term = 165±10 days). Limit of assay quantification is 100 copies/mL. Limit of detection is 33 copies/mL. Colors for individual animals are continued through the rest of the Figures, including the Supplementary Figures.

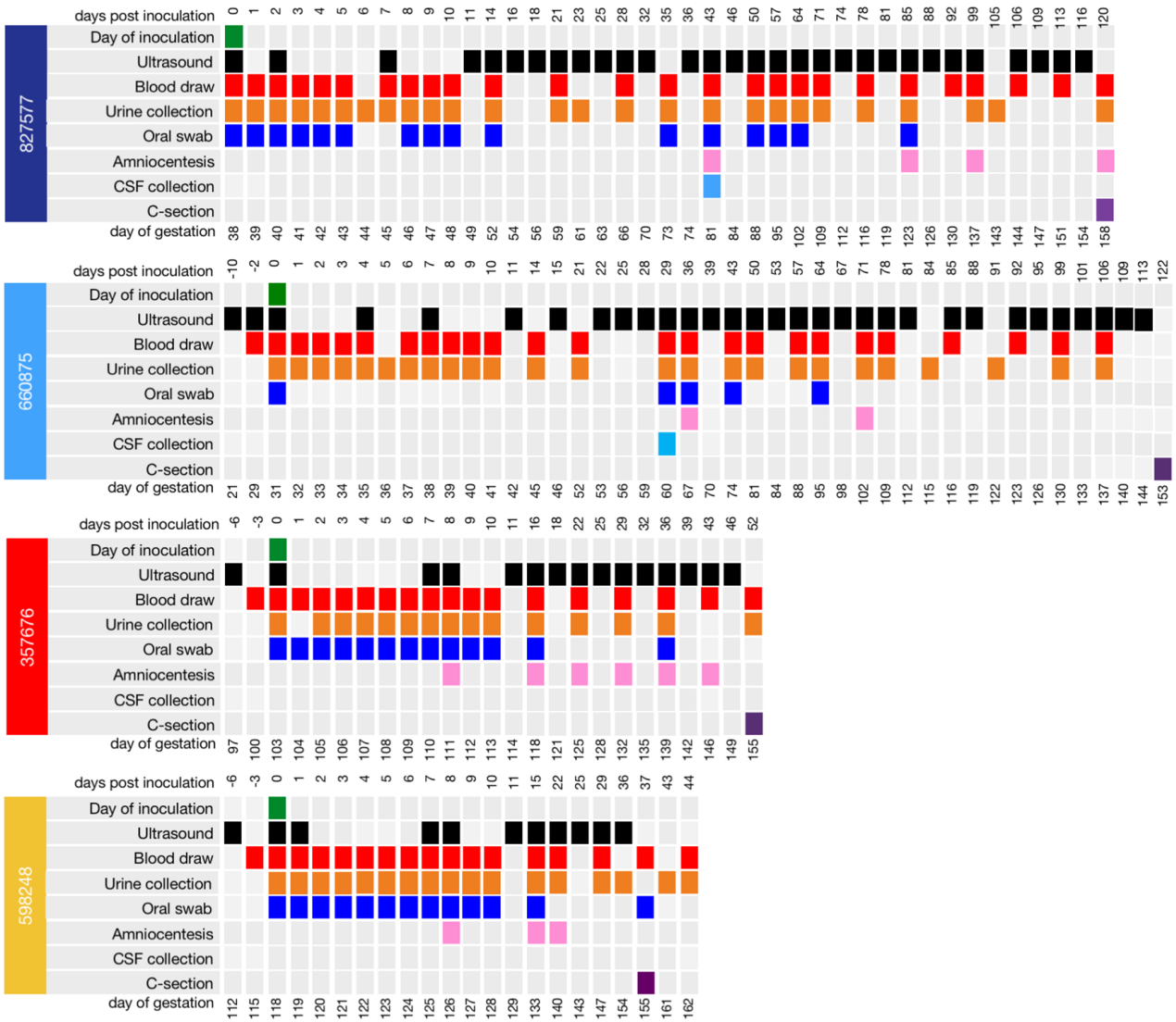

Supplementary Figure S1. Comprehensive sampling experimental timeline for pregnant

animals in the current study. Each animal in the study is indicated at the left, color blocks represent when specific samples were collected (e.g., CSF on 43 dpi (81 days gestation) for animal 827577).

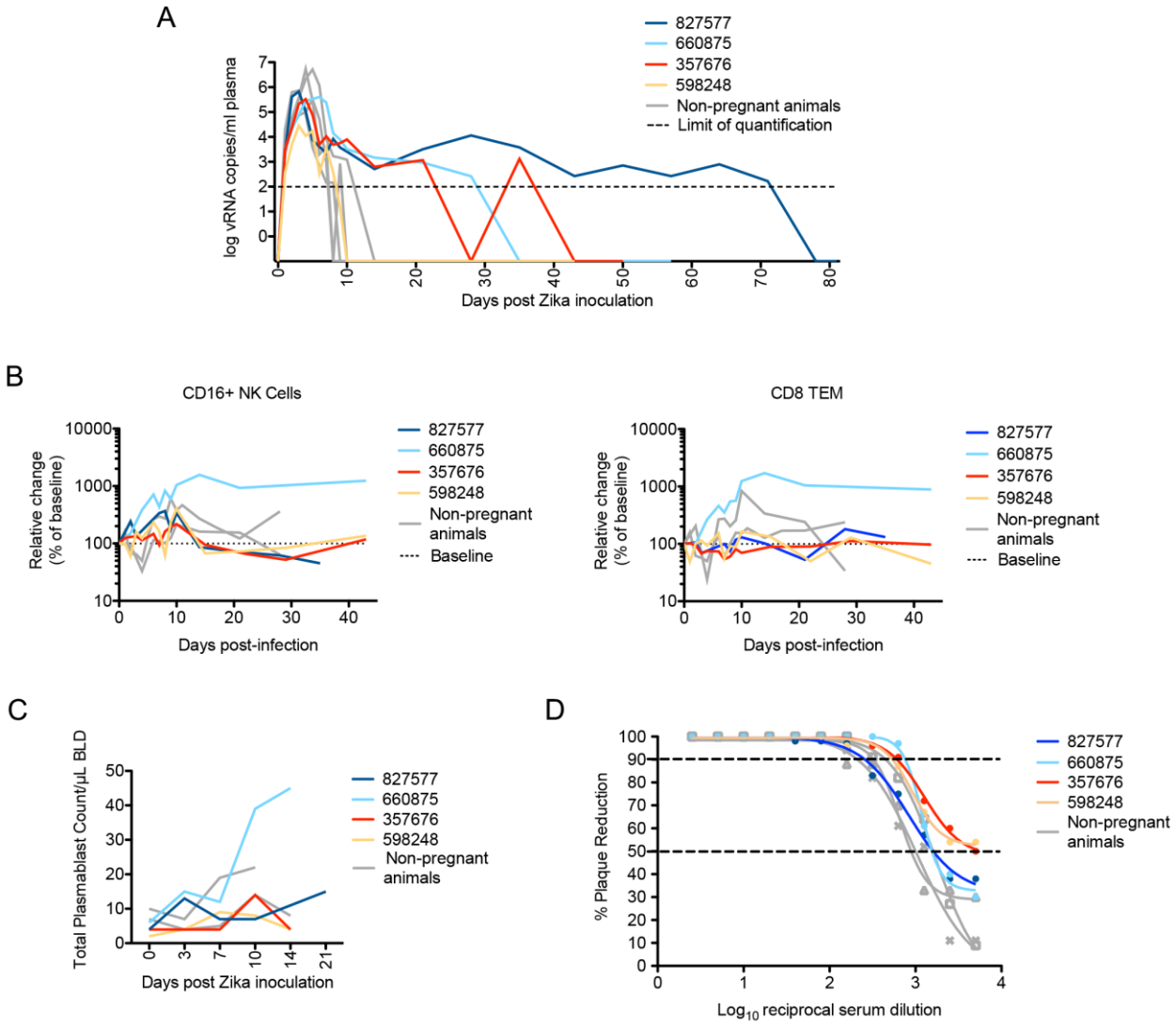

Figure 2. Maternal viral control and immune responses to ZIKV inoculation. (**A**) Peripheral blood plasma viremia in pregnant macaques infected with ZIKV. Results are shown for animals infected at 38 days gestation (animal 827577, dark blue), 31 days gestation (animal 660875, light blue), 103 days gestation (animal 357676, red) or 118 days gestation (animal 598248, yellow).

The day of gestation is estimated +/- 2 days. Grey tracings represent viremia in nonpregnant/male rhesus monkeys infected with the identical dose and strain of ZIKV in a previous study [28]. The horizontal line indicates the quantitative limit of detection. (**B)** Peripheral blood cell response to infection. Absolute numbers of Ki67+ NK cells (left) or CD8+TEM cells (right) are presented as a percentage relative to baseline set at 100% (dashed line), with first trimester and third trimester animals represented in the same colors as presented in Fig. 1A. (**C)** Plasmablast expansion over time from each pregnant animal. The plasmablast expansions of two nonpregnant animals from Dudley *et al* [28] are shown as grey lines. (**D)** Neutralization by ZIKV immune sera from pregnant and nonpregnant ZIKV-infected macaques. Immune sera from macaques infected with ZIKV in either the first trimester (dark or light blue), third trimester (red or yellow), or nonpregnant contemporary controls (gray) from Dudley *et al* [28] were tested for their capacity to neutralize ZIKV-FP. Infection was measured by plaque reduction neutralization test (PRNT) and is expressed relative to the infectivity of ZIKV-FP in the absence of serum. The concentration of sera indicated on the x-axis is expressed as $\log_{10}$ (dilution factor of serum). The EC90 and EC50, estimated by non-linear regression analysis, are also indicated by a dashed line. Neutralization curves for each animal at 28 dpi are shown.

Innate and adaptive immune responses to ZIKV

The duration of viremia was prolonged in three of four pregnant macaques in comparison to non-pregnant animals infected by the same route, dose, and strain of ZIKV in a previous study [28] (Fig. 2A; compare colored and gray lines). Those animals were infected contemporaneously (within 4 weeks) with the monkeys in the current study. To evaluate maternal immune responses, peripheral blood CD16+ natural killer (NK) cell and CD95+CD28- CD8 effector T cell

proliferation were monitored by flow cytometry for Ki-67 expression. Although responses were variable, there was generally higher proliferation relative to baseline in peripheral blood CD16+ NK cells than in CD95+CD28- CD8+ effector T cells (Fig. 2B), and these responses were not qualitatively different from nonpregnant animals (Fig. 2B, grey tracings). The numbers of circulating plasmablasts tended to increase more slowly in third-trimester infections; however, the response did not distinctly differ between the first and third trimesters (Fig. 2C). Sera from macaques that were infected with ZIKV in the first or third trimesters neutralized ZIKV-FP across a range of serum dilutions. Indeed, neutralization curves prepared using sera from all 4 animals revealed a similar profile as compared to sera from ZIKV-infected nonpregnant animals (Fig. 2D). All animals developed neutralizing antibodies (nAb) with a 90% plaque reduction neutralizing antibody test ($PRNT_{90}$) titer of 1:160 (827577 and 598248) or 1:640 (660875 and 357676) by 28 dpi. Interestingly, animal 660875 (first trimester infection) had more vigorous and prolonged NK, T cell, and plasmablast responses to infection compared to the other three pregnancies. ZIKV infection was not associated with consistent changes in complete blood cell counts or serum chemistry in pregnant animals (Fig. 3).

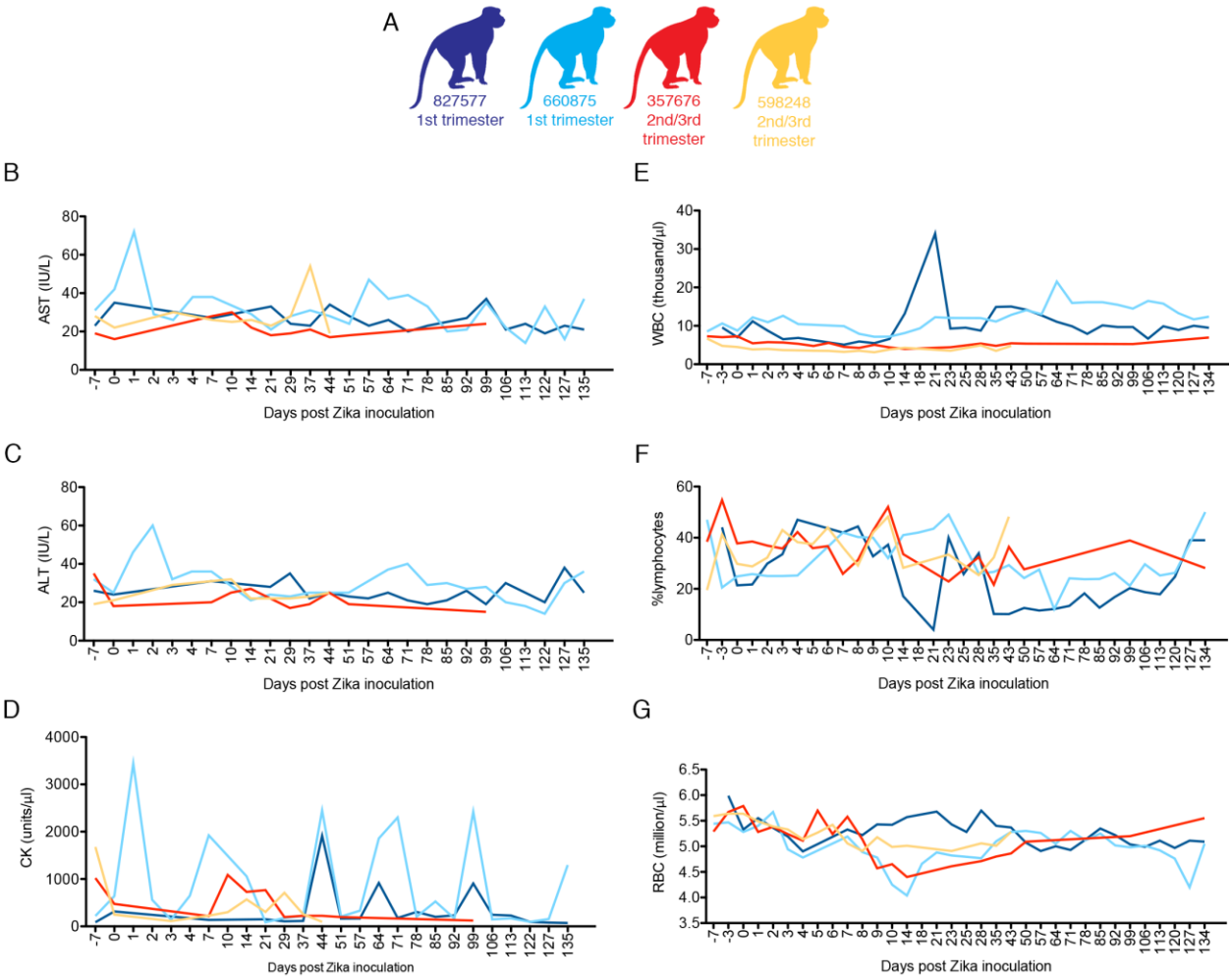

Figure 3. Complete blood counts (CBCs) and serum chemistries for pregnant macaques infected with ZIKV. Animals were infected with 10^4 PFU of ZIKV. Animals infected in the first or third trimesters are represented by color coding (**A**) as presented in Fig. 1. All animals had CBC analysis performed on EDTA blood and chemistry analysis performed on serum at -7, -3, 0, 1-10 and additional indicated dpi. **B.** AST blood chemistries, **C.** ALT serum chemistries, **D.** CK serum chemistries**, E.** WBC counts, **F.** % lymphocytes, **G.** red blood cell (RBC) counts.

Assessment of fetal growth

Sonographic images (e.g., Fig. 4) were obtained approximately weekly to monitor fetal

growth and viability. No significant fetal or placental abnormalities were observed. Fetal femur length (FL) was typically within one standard deviation (SD) of mean database values for fetal rhesus macaques across gestation [35], suggesting absence of symmetrical growth restriction (Fig. 4A). The biparietal diameter (BPD) was within two SD of expected values across gestation (Fig. 4B). However, during the last month of pregnancy, head circumference (HC) in all animals was between one and three SD below the mean (Fig. 4C).

To discern changes in fetal growth trajectories, we extrapolated the predicted gestational ages (pGA) by mapping the observed fetal biometric measures in individual pregnancies onto normative growth curves for BPD, FL, and HC [35, 36]. Figs. 5A-D compare within each animal the pGA estimated by an average of BPD and FL with that estimated by HC. In 3 of 4 pregnancies, pGA as estimated by HC lagged 16.5 to 19 days behind the pGA estimated by an average of BPD and FL. HC reflects both BPD and occipitofrontal diameters. Human fetuses and infants affected by severe microcephaly in congenital ZIKV infection have vermis agenesis (growth failure of the cerebellum) and reduced frontal cortex growth [11, 15, 18, 37]: regions of the brain where growth deficits will give rise to a reduced occipitofrontal diameter. Fetal Magnetic Resonance Imaging (MRI) was also performed for the dams infected in the first trimester (827577, imaged at 102 dpi [140 days gestation], and 660875, imaged at 60 dpi [91 days gestation]). These images provided evidence of normal volume, cortical thickness, sulcation, and ventricular and extra-axial spaces (Supplementary Fig. S2). However, it has been reported that human infants whose mothers were infected with ZIKV during pregnancy have been born with normal cranial anatomy, but developed microcephaly within 6 months [19, 38]. Thus, further studies focused on macaque postnatal development are warranted.

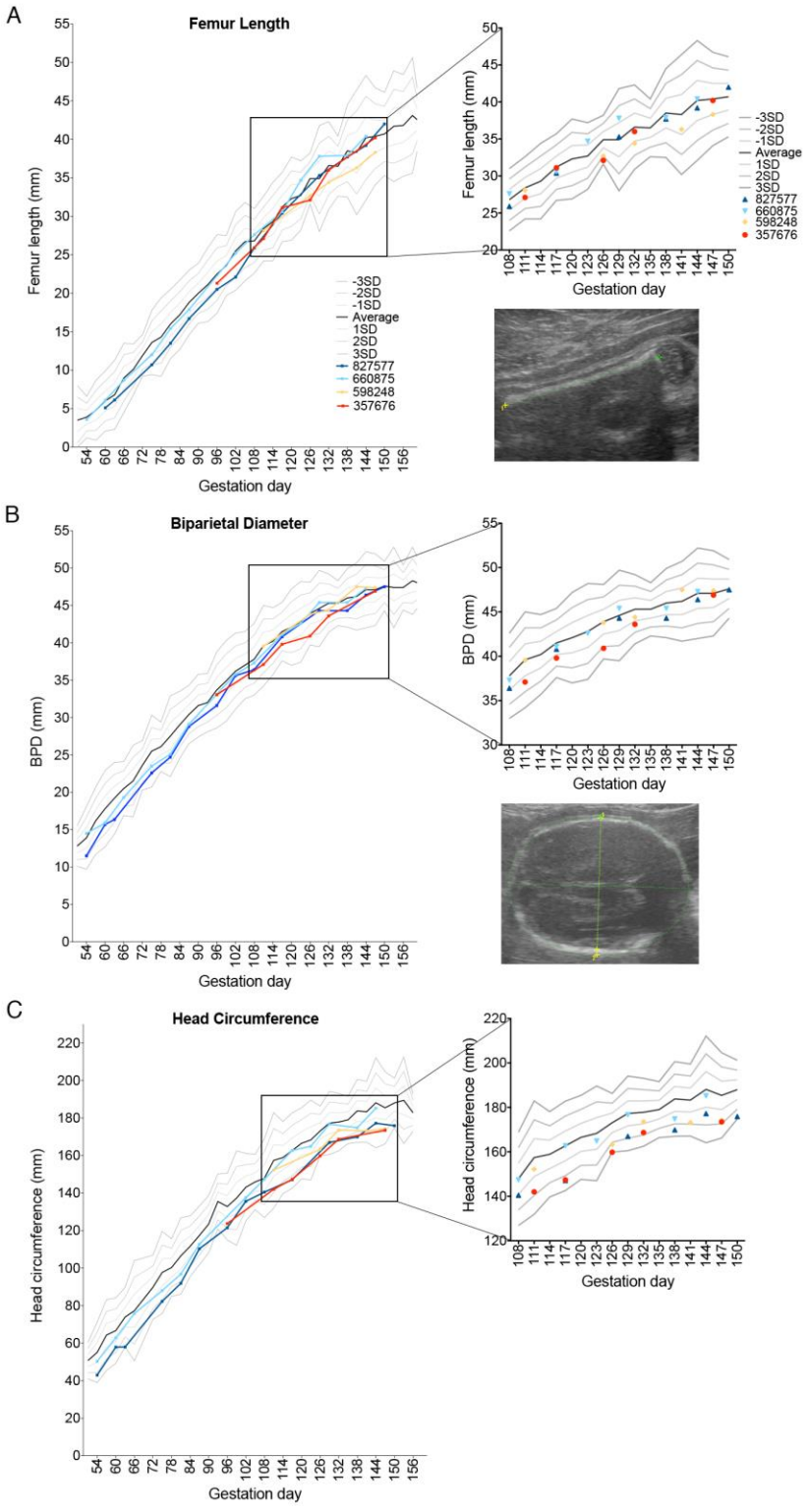

Figure 4. Fetal growth following ZIKV infection. Growth curves of femur length (FL), biparietal diameter (BPD), and head circumference (HC) obtained from fetal ultrasound images

throughout gestation are presented as individual lines or symbols with specific colors as in Fig. 1. (**A**) FL, (**B**) BPD (**C**) and HC were determined for the fetuses in this study and plotted against data from Tarantal [35], which is presented as the mean (solid black line) and 1, 2, and 3 standard deviations from the mean as grey lines above and below the mean. The data from the last month of pregnancy are also presented as a magnified view of the scatter of individual data points on the right. Representative ultrasound images of FL, BPD, and HC are also shown at the right.

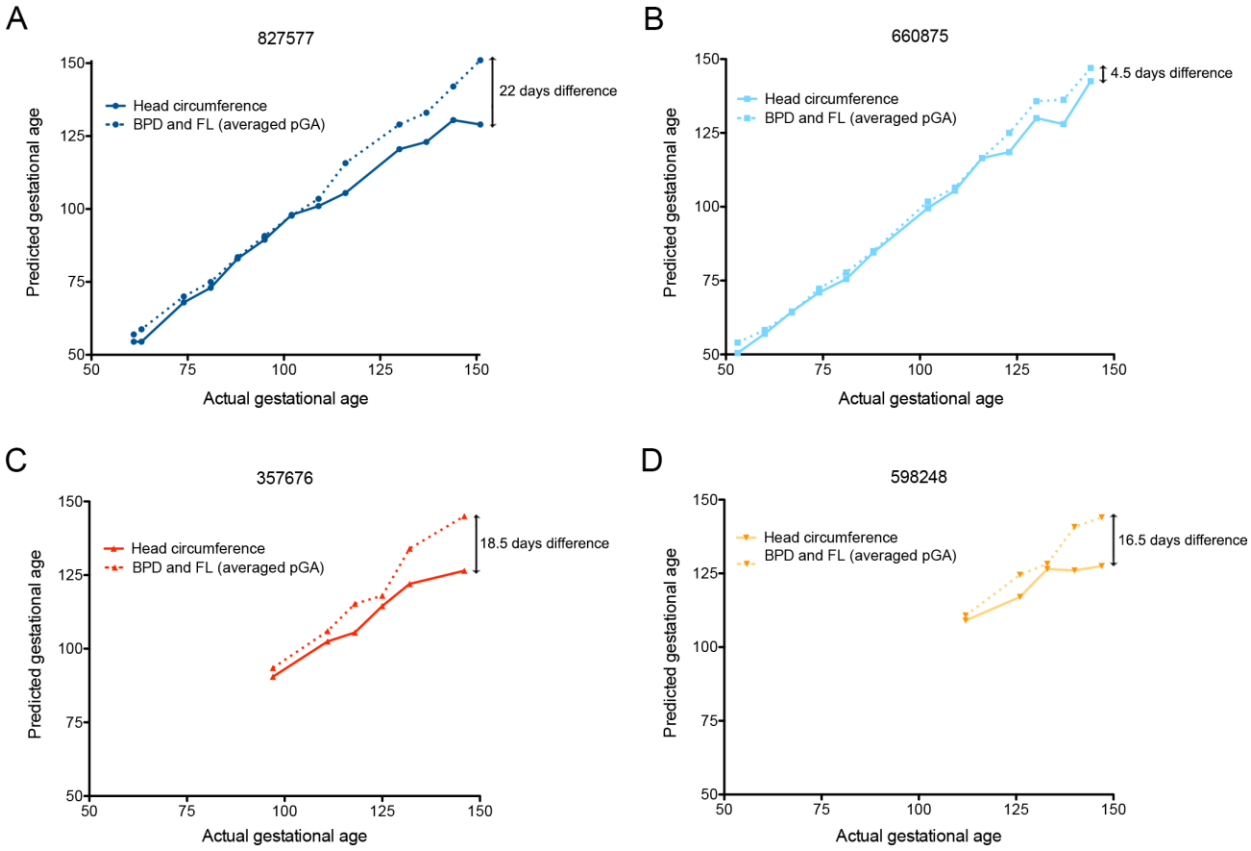

Figure 5. Fetal growth as assessed by predicted gestational ages. The predicted gestational age (pGA) as described by Tarantal [35] from each of the pregnancies is plotted against the actual day of gestation estimated from breeding activity and animal menstrual records. The pGA

was derived from the average of BPD+FL (dashed lines), or the HC (solid lines). **A** (animal 827577) and **B** (animal 660875), first trimester infection. **C** (animal 357676) and **D** (animal 598248), late second/early third trimester infection.

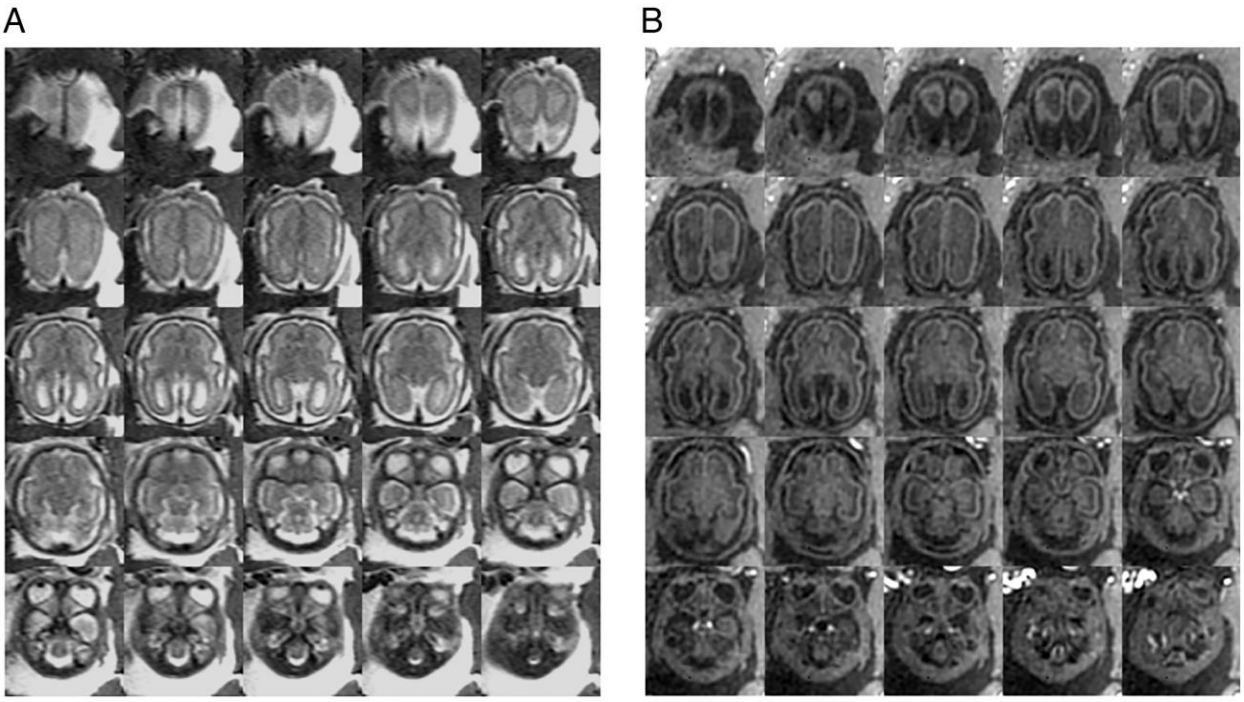

Supplementary Figure S2. Fetal brain imaged by MRI in ZIKV-infected pregnancies. (**A**) T2-weighted axial images of the fetus from dam 660875 at 60 dpi (91 days gestation) acquired with a single shot fast spin echo (SSFSE) sequence. Fluids such as the intraocular fluid, CSF, and amniotic fluid as well as fat appear bright on these images. The brain anatomy appears normal. **(B**) The same fetus acquired with a multiecho spoiled gradient echo sequence.

Fetal viral burden and histopathology

All ZIKV pregnancies progressed without overt adverse outcomes. At 153-158 days gestation, fetuses were surgically delivered, euthanized, and tissues collected. None of the

fetuses had evidence of microcephaly or other abnormalities upon gross examination. Approximately 50 fetal and maternal tissues (Supplementary Fig. S3) were collected from each pregnancy for histopathology and vRNA by qRT-PCR. Results are summarized in Fig 6. ZIKV RNA was detected in all four fetuses, albeit in different tissues in individual fetuses, and in some maternal tissues including spleen, liver, lymph node, and decidua (Fig. 6A). Notably, the pregnancy with the longest duration of viremia (827577; 70 days viremia (39-109 days gestation) had fetal tissues (optic nerve, axillary lymph node) with the highest vRNA burden. However, the fetus from the short (9 day) duration maternal viremia (119-127 days gestation) also had vRNA in fetal lymph node, pericardium, and lung (Fig. 6A).

Pathologists were blinded to vRNA and trimester of infection findings for histology evaluation and scoring (Fig. 6B; see Supplementary Data S1 for a full listing of pathology findings). The maternal-fetal interface in all four ZIKV infections presented minimal to moderate suppurative placentitis with variable mineralization and necrosis, as well as minimal to moderate suppurative deciduitis (Fig. 7). Three of four pregnancies had suppurative amnionitis and three of four dams had mild to moderate suppurative splenitis. Histology confirmed normal CNS structures and absence of encephalitis (inflammation) in all four fetuses. Morphologic fetal diagnoses included: suppurative splenitis, suppurative to lymphoplasmacytic hepatitis, suppurative alveolitis (pneumonia), and suppurative lymphadenitis (Supplementary Data S1). The duration of viremia or trimester of maternal infection did not generally correlate with the severity or distribution of scored fetal pathologies (Table 1), however it is significant that both fetuses infected during the first trimester, but not the third trimester, had ocular pathology: inflammation of retina, choroid, and optic nerve (Fig. 8, Supplementary Data S1). A segment of the fetal axillary lymph node with the highest vRNA burden was immunostained for ZIKV. ZIKV NS2B-positive cells were observed

in lymph node medullary cords, a subset of which were CD163-positive macrophages (Fig. 9).

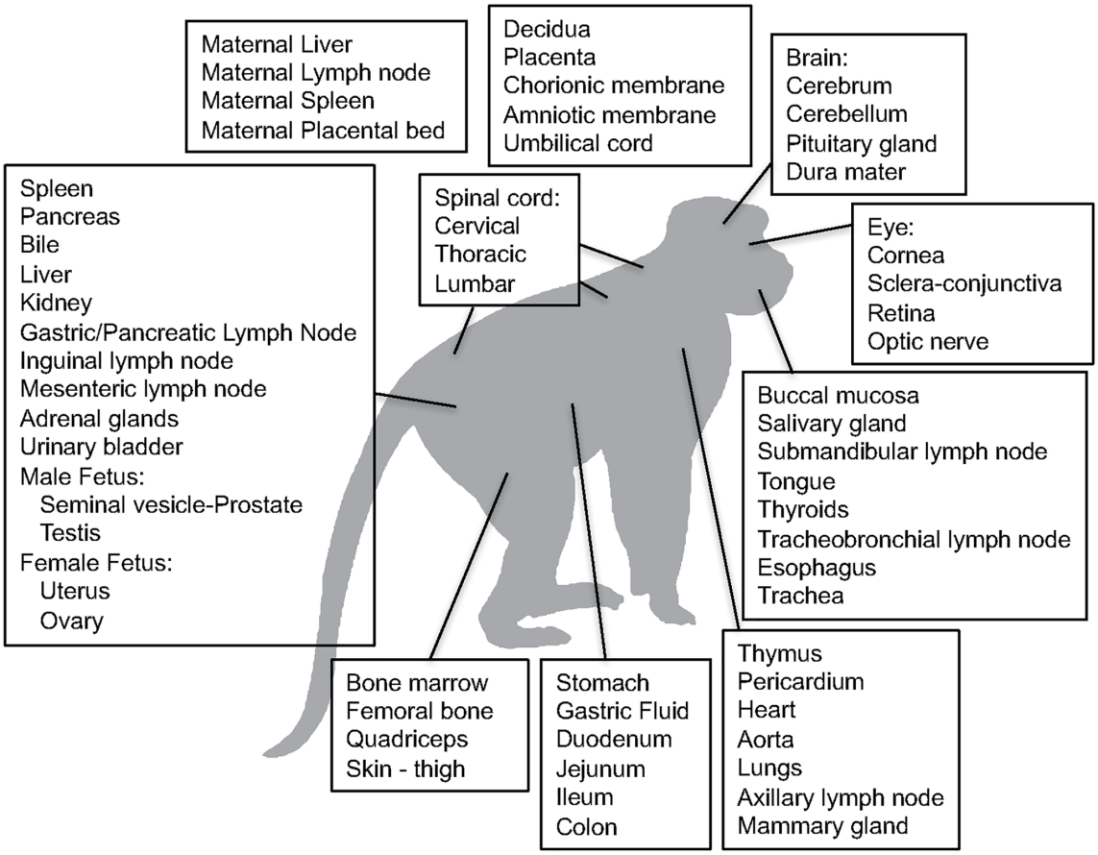

Supplementary Figure S3. Descriptive diagram showing all maternal and fetal tissues that were sampled at collection.

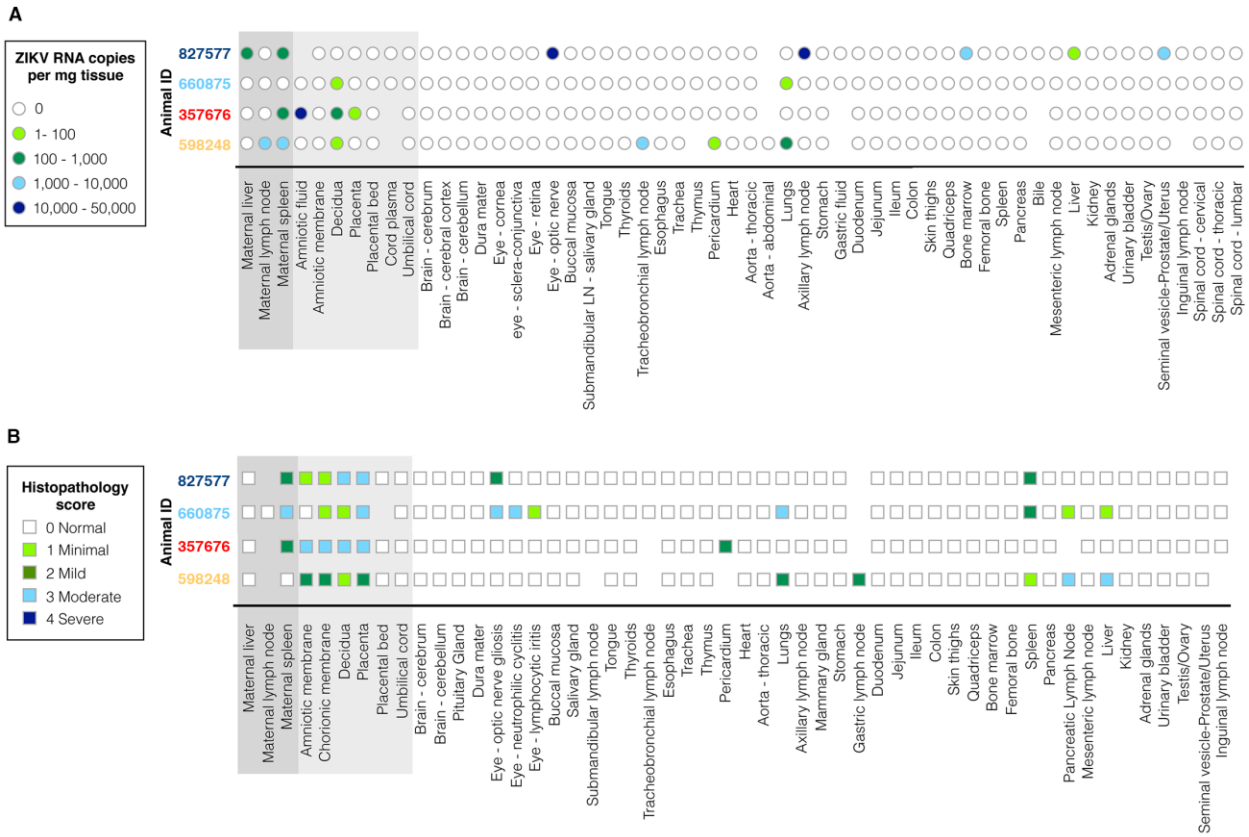

Figure 6. Charts summarizing (A) ZIKV RNA copy numbers, and (B) histologic evaluation and semiquantitative scoring of all normal and lesioned tissues, presenting all maternal and fetal tissues analyzed. Keys for ZIKV RNA copy number burden per mg of tissue, and description of histopathology scores ("Normal" to "Severe") appear at the left. Animal numbers are color coded as introduced in Fig. 1.

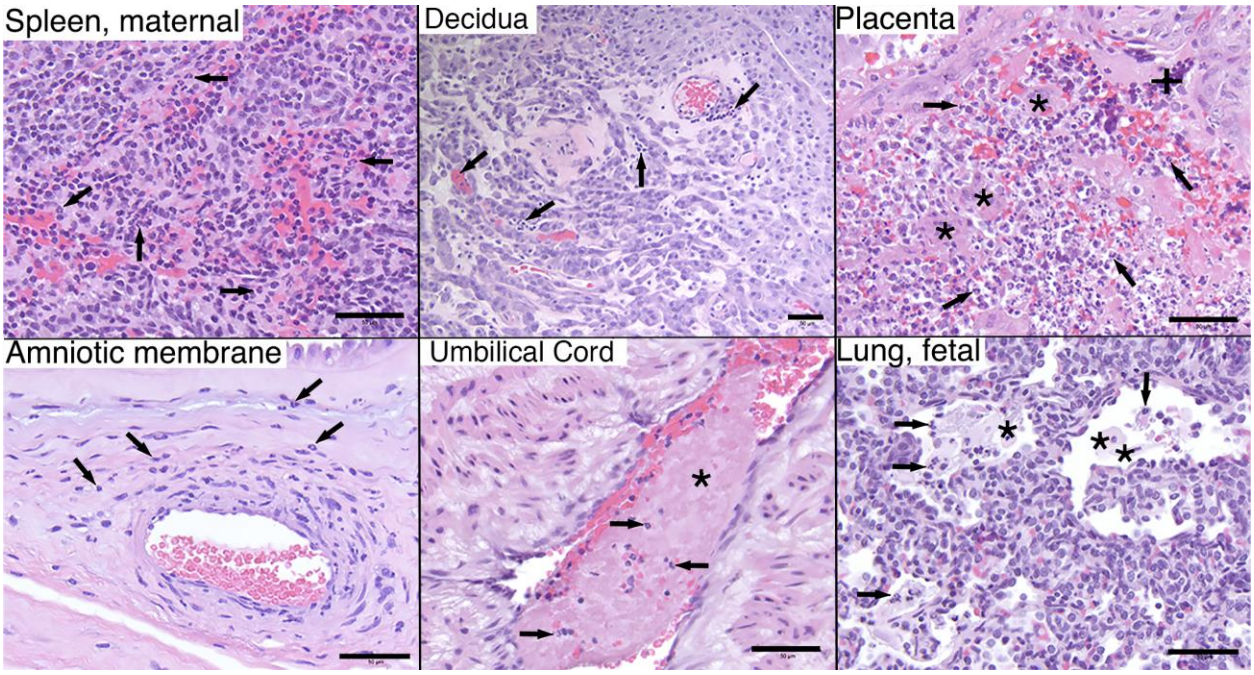

Figure 7. Maternal and fetal histopathology analyses: hematoxylin and eosin (H&E) staining of selected tissues. Maternal spleen, 660875: increased neutrophils (arrows) throughout splenic sinusoids. Maternal decidua, 827577: multifocal stromal, intravascular, and perivascular inflammation (arrows). Placenta, 660875: moderate multifocal necrosis and loss of trophoblastic epithelium (+) with viable and degenerative neutrophils (arrows) between villi (*) and throughout the intervillous space. Chorionic membrane, 598248: diffuse suppurative inflammation throughout the chorionic membrane (ch) with rare single neutrophils (arrows) within the overlying amnion. Amniotic membrane, 598248: scattered neutrophils within the amniotic basement membrane and underlying perivascular stroma. Umbilical cord, 660875: segmental thrombosis (*) with entrapped neutrophils (arrows). Fetal lung, 660875: fetal squamous cells (*) and neutrophils (arrows) admixed with fibrin within alveolar spaces.

ID	Trimester of infection	duration of viremia (days)	Peak plasma viremia	Amn. Fluid*	Saliva	Difference in BPD+FL vs. HC (days)	Score of maternal path	Score of maternal RNA*	Score of MFI path	MFI RNA*	Fetal path	Fetal RNA*	Fetal ocular path
598248	3	11	17,400	0	-	16.5	0	6	7	1	11	6	0
357676	3	28	329,000	4	+	18.5	2	2	12	7	2	0	0
827577	1	71	668,000	0	+	19	2	4	8	0	4	15	2
660875	1	39	402,000	0	-	4.5	3	0	5	1	14	1	7

Table 1. Summary of maternal observations and maternal and fetal pathology and vRNA burden. Summary of all maternal and fetal outcomes for each individual pregnancy, including quantitative vRNA burden and semiquantitative histopathology scores.

Scores are summed scoring for either vRNA levels or histopathology:

*RNA copies/mg tissue scoring: 0 = 0; 1-100 = 1; 100-1000 = 2, 1000-10000 = 3, 10000-50000 = 4.

Histopathology scoring: 0 = normal; 1 = minimal; 2 = mild; 3 = moderate; 4 = severe.

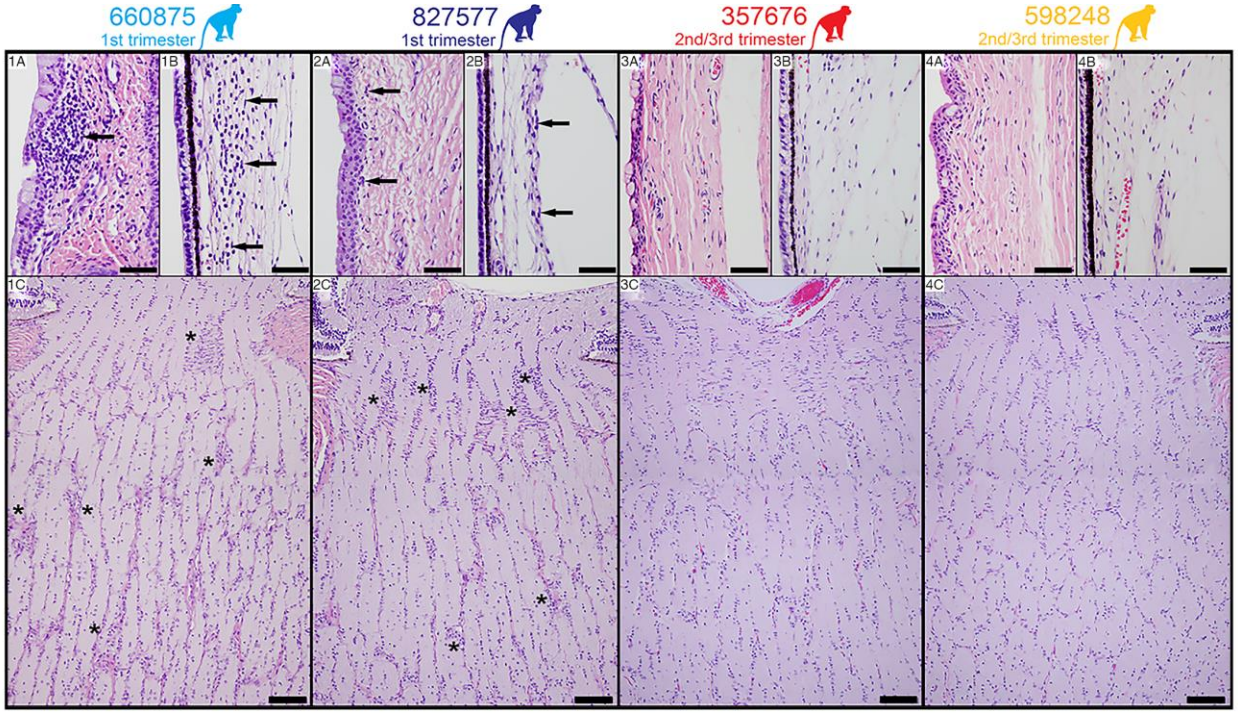

Figure 8. **H&E Staining of fetal tissues of the visual system. Panels 1A-C, animal 660875.** Panel 1A: Mild infiltration of lymphocytes in the bulbar conjunctival substantia propria (arrow). Panel 1B: Moderate neutrophilic infiltration in the ciliary body stroma (arrows). Panel 1C: Moderate gliosis of the laminar and post-laminar optic nerve characterized by overall hypercellularity of the neuropil especially as indicated by asterisks. **Panels 2A-C, animal 827577.** Panel 2A: Minimal infiltration of lymphocytes in the bulbar conjunctival substantia propria (arrows). Panel 2B: Normal ciliary body stroma. Panel 2C: Moderate gliosis of the laminar and post-laminar optic nerve characterized by overall hypercellularity of the neuropil especially as indicated by asterisks. **Panels 3A-C, animal 357676, and Panels 4A-C, animal 598248.** Panels 3A and 4A: Normal bulbar conjunctival substantia propria. Panels 3B and 4B: Normal ciliary body stroma. Panels 3C and 4C: Normal optic nerve.

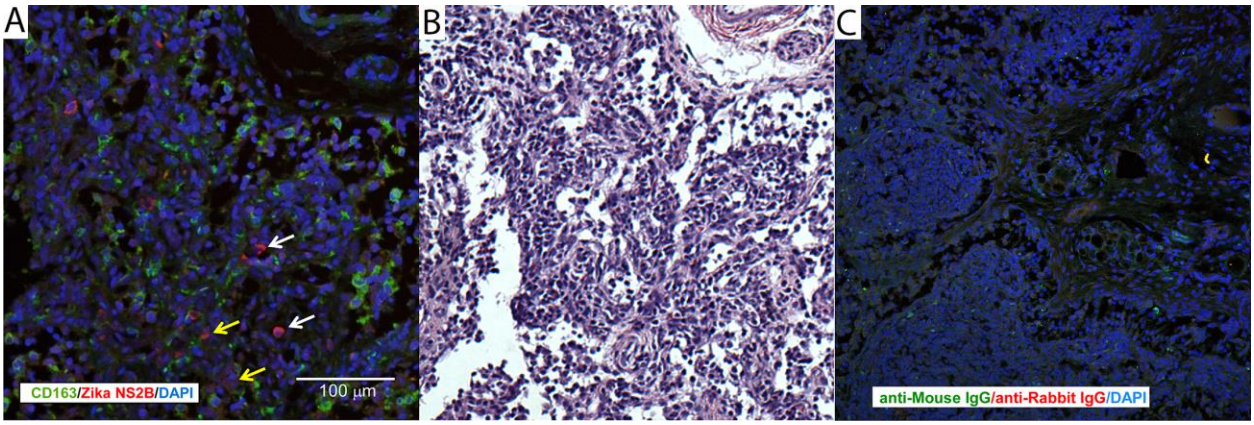

Figure 9. Immunohistochemical localization of ZIKV in fetal [and maternal] tissues. (**A**) Immunofluorescent staining for ZIKV NS2B (red) and macrophage marker CD163 (green) in fetal axillary lymph node with a high vRNA burden. The white scale bar = 100 µm. (**B**) H&E stained near section of the tissue presented in 9A. (**C**) Nonspecific immunostaining with control isotypes for ZIKV NS2B and CD163.

DISCUSSION

This study demonstrates that similar to human pregnancy, Indian rhesus macaque fetuses are susceptible to congenital infection following maternal subcutaneous infection with a moderate infectious dose of Asian-lineage ZIKV during the first or late second/early third trimesters. Maternal-fetal transmission in the rhesus macaque is highly efficient: 4 of 4 maternal infections resulted in infected fetuses, and all pregnancies demonstrated pathology at the maternal-fetal interface and in the fetus, with variable fetal vRNA distribution. Fetal infection was accompanied by an apparent reduced trajectory of fetal HC in the last month of gestation, without overall fetal growth restriction. While we hypothesize that the duration of maternal viremia correlates with risk for fetal impact, pathology at the maternal-fetal interface and fetal vRNA in the pregnancy with the shortest duration of viremia following third trimester infection

suggests that the fetus is at risk even with a brief exposure to circulating maternal virus, as reported in human pregnancy [12]. Indeed, our findings are consistent with the emerging picture of congenital Zika syndrome, in which microcephaly is the most severe of a range of potential sequelae. Given the high rate of vertical transmission in our model in the absence of severe developmental defects, it seems possible that there is a higher rate of human fetal *in utero* ZIKV exposure than is currently appreciated, exposures which do not result in malformations obvious at birth, but may manifest later in postnatal development.

Models of vertical ZIKV transmission have been developed in mice [39, 40, 41, 42]. Mice are generally not susceptible to ZIKV infection because ZIKV cannot subvert the interferon response in mice as it does in humans [43]. However, studies have now been conducted with mouse strains carrying deletions of the IFNAR or pattern recognition receptor genes (e.g., IRF3, IRF7) [40, 41]. In these models, placental infection and pathology is revealed, and there is maternal-fetal transmission and fetal growth defects, loss and brain injury [39, 40, 41]. More recently, an alternate approach in which virus is directly injected into the uterine wall adjacent to the conceptuses has been reported in immunocompetent mice, and this model also results in placental infection and transmission of the virus to the fetus [42]. However, neither immunodeficient nor uterine injection models are directly relevant to the mode of transmission by which the human fetus is exposed to ZIKV. While murine genetic models allow mechanistic investigation of ZIKV pathophysiology that cannot be explored with samples from human clinical patients, the murine maternal-fetal interface, placental structure, and pace and complexity of fetal brain development are quite different from humans, whereas nonhuman primate pregnancy is very similar to human pregnancy in these critical areas for understanding the impact of ZIKV on the fetus.

The NHP has previously been used to model TORCH infections (e.g., cytomegalovirus, toxoplasma**)** on fetal infection and neuropathology [44-46], and listeriosis and other bacterial infections on fetal loss and stillbirth [47, 48] and preterm labor [49]. Congenital ZIKV infection in macaques provides a tractable and translational model of human disease. While it has previously been reported that infection of a pregnant pigtail macaque with a Cambodian ZIKV strain resulted in severe fetal malformations of the central nervous system [34], we did not observe this outcome in our study. It is theoretically possible that the lack of severe outcomes, including microcephaly, in our study may be due to the use of a specific ZIKV strain or dose, that rhesus monkeys, in general, are resistant to ZIKV-induced fetal neuropathology, or that there is a difference in ZIKV susceptibility between the rhesus macaques in our study and the single pigtail macaque used in the previous study. Regardless, lack of a severe outcome should not be considered a limitation of our study, since it is also known that only a subset of human maternal infections result in severe fetal outcomes [50], and our current study significantly expands the data available regarding ZIKV infection in nonhuman primates. Modest fetal neurodevelopmental outcomes with the model we have described in this current report may provide an opportunity to further evaluate factors which foster severe fetal developmental impact, such as co-infection or previous exposure to other pathogens, and support the development of strategies to prevent maternal-fetal transmission and reduce fetal virus burden. Further information on the ontogeny of fetal infection and distribution of virus in the fetus during gestation using relevant animal models will be important to establish before consideration of interventional strategies, such as maternal or fetal passive immunization [51] in pregnant women presenting with symptoms of ZIKV infection.

METHODS

Experimental design

Four pregnant rhesus macaques (*Macaca mulatta*) of Indian ancestry were infected subcutaneously with $1x10^4$ PFU ZIKV (Zika virus/H.sapiens-tc/FRA/2013/FrenchPolynesia-01_v1c1) at 31, 38, 104, or 119 days gestation (term 165±10 days). All macaques utilized in the study were free of Macacine herpesvirus 1, Simian Retrovirus Type D (SRV), Simian T-lymphotropic virus Type 1 (STLV), and Simian Immunodeficiency Virus as part of the Specific Pathogen Free (SPF) colony at WNPRC.

Ethics Statement

The rhesus macaques used in this study were cared for by the staff at the Wisconsin National Primate Research Center (WNPRC) according to regulations and guidelines of the University of Wisconsin Institutional Animal Care and Use Committee, which approved this study (protocol g005401) in accordance with recommendations of the Weatherall report and according to the principles described in the National Research Council's Guide for the Care and Use of Laboratory Animals. All animals were housed in enclosures with at least 4.3, 6.0, or 8.0 sq. ft. of floor space, measuring 30, 32, or 36 inches high, and containing a tubular PVC or stainless steel perch. Each individual enclosure was equipped with a horizontal or vertical sliding door, an automatic water lixit, and a stainless steel feed hopper. All animals were fed using a nutritional plan based on recommendations published by the National Research Council. Twice daily macaques were fed a fixed formula, extruded dry diet (2050 Teklad Global 20% Protein Primate Diet) with adequate carbohydrate, energy, fat, fiber (10%), mineral, protein, and vitamin content. Dry diets were supplemented with fruits, vegetables, and other edible objects (e.g., nuts,

cereals, seed mixtures, yogurt, peanut butter, popcorn, marshmallows, etc.) to provide variety to the diet and to inspire species-specific behaviors such as foraging. To further promote psychological well-being, animals were provided with food enrichment, human-to-monkey interaction, structural enrichment, and manipulanda. Environmental enrichment objects were selected to minimize chances of pathogen transmission from one animal to another and from animals to care staff. While on study, all animals were evaluated by trained animal care staff at least twice each day for signs of pain, distress, and illness by observing appetite, stool quality, activity level, physical condition. Animals exhibiting abnormal presentation for any of these clinical parameters were provided appropriate care by attending veterinarians. Prior to all minor/brief experimental procedures, animals were sedated using ketamine anesthesia, which was reversed at the conclusion of a procedure using atipamizole. Animals undergoing surgical delivery of fetuses were pre-medicated with ketamine and general anesthesia was maintained during the course of the procedure with isoflurane gas using an endotracheal tube. Animals were monitored regularly until fully recovered from anesthesia. Delivered fetuses were anesthetized with ketamine, and then euthanized by an intramuscular or intraperitoneal overdose injection of sodium pentobarbital. Adult animals were not euthanized as part of these studies.

Care and use of macaques

Female monkeys were co-housed with compatible males and observed daily for menses and breeding. Pregnancy was detected by ultrasound examination of the uterus at approximately 20-24 days gestation following the predicted day of ovulation. The day of gestation was estimated (+/- 2 days) based on the dams menstrual cycle and previous pregnancy history, observation of copulation, and the greatest length of the fetus at initial ultrasound examination

which was compared to normative growth data in this species [35]. Ultrasound examination of the conceptus was performed subsequent to ZIKV infection as described below. For all procedures (i.e., physical examinations, virus inoculations, ultrasound examinations, blood and swab collection), animals were anesthetized with an intramuscular dose of ketamine (10 mg/kg). Blood samples from the femoral or saphenous vein were obtained using a vacutainer system or needle and syringe. The four pregnant macaques were monitored daily prior to and after infection for any physical signs (e.g., diarrhea, inappetance, inactivity, atypical behaviors).

Inoculations

Zika virus/H.sapiens-tc/FRA/2013/FrenchPolynesia-01_v1c1, originally isolated from a 51-year-old female in France returning from French Polynesia with a single round of amplification on Vero cells, was obtained from Xavier de Lamballerie (European Virus Archive, Marseille France). The inoculating stock was prepared and validated as previously described [28]. A single harvest of virus with a titer of 1.26×10^6 PFU/mL (equivalent to 1.43×10^9 vRNA copies/mL) was used for all 4 challenges. Animals were anesthetized as described above, and 1 mL of inocula was administered subcutaneously over the cranial dorsum. Post-inoculation, animals were closely monitored by veterinary and animal care staff for adverse reactions or any signs of disease.

Immunophenotyping

The number of activated/proliferating peripheral blood lymphocyte subset cells was quantified using a modified version of our protocol detailed step-by-step in OMIP-028 [52] as previously reported [28]. Briefly, 0.1 mL of EDTA-anticoagulated whole blood samples were

incubated for 15 min at room temperature in the presence of a mastermix of antibodies against CD45 (clone D058-1283, Brilliant Violet 786 conjugate, 2.5 µl), CD3 (clone SP34-2 Alexa Fluor 700 conjugate, 5 µl), CD8 (clone SK2, Brilliant Violet 510, 2.5 µl), NKG2A/C (clone Z199, PE-Cy7 conjugate, 5 µl), CD16 (clone 3G8, Pacific Blue conjugate, 5 µl), CD69 (clone TP1.55.3, ECD conjugate, 3 µl), HLA-DR (clone 1D11, Brilliant Violet 650 conjugate, 1 µl), CD4 (clone SK3, Brilliant Violet 711 conjugate, 5 µl), CD28 (clone CD28.2, PE conjugate, 5 µl), and CD95 (clone DX2, PE-Cy5 conjugate, 10 µl) antigens. All antibodies were obtained from BD BioSciences, with the exception of the NKG2A/C-specific antibody, which was purchased from Beckman Coulter, and the CCR7 antibody that was purchased from R&D Systems. The cells were permeabilized using Bulk Permeabilization Reagent (Life Technology), then stained for 15 min with Ki-67 (clone B56, Alexa Fluor 647 conjugate) while the permeabilizer was present. The cells were then washed twice in media and resuspended in 0.125 ml of 2% paraformaldehyde until they were run on a BD LSRII Flow Cytometer. Flow data were analyzed using Flowjo software version 9.9.3.

Plasmablast detection

Peripheral blood mononuclear cells (PBMCs) isolated from four ZIKV-infected pregnant rhesus monkeys at 3, 7, 11, and 14 dpi were stained with the following panel of fluorescently labeled antibodies (Abs) specific for the following surface markers to analyze for plasmablast presence: CD20 FITC (L27), CD80 PE (L307.4), CD123 PE-Cy7(7G3), CD3 APC-Cy7 (SP34-2), IgG BV605 (G18-145) (all from BD Biosciences, San Jose, CA), CD14 AF700 (M5E2), CD11c BV421 (3.9), CD16 BV570 (3G8), CD27 BV650(O323) (all from BioLegend, San Diego, CA), IgD AF647 (polyclonal) (Southern Biotech, Birmingham, AL), and HLA-DR PE-

TxRed (TÜ36) (Invitrogen, Carlsbad, CA). LIVE/DEAD Fixable Aqua Dead Cell Stain Kit (Invitrogen, Carlsbad, CA) was used to discriminate live cells. Cells were analyzed exactly as previously described [28].

Complete blood count (CBC) and serum chemistry panels

CBCs with white blood cell (WBC) differential counts were performed on EDTA-anticoagulated whole blood samples on a Sysmex XS-1000i automated hematology analyzer (Sysmex Corporation, Kobe, Japan). CBCs included the following tests: absolute WBC count, absolute counts and percentages for WBC differentials, red blood cell (RBC) count, hemoglobin and hematocrit, RBC indices (mean corpuscular volume, mean corpuscular hemoglobin, mean corpuscular hemoglobin concentration, and red blood cell distribution width), platelet count, and mean platelet volume. Blood smears were prepared and stained with Wright-Giemsa stain (Wescor Aerospray Hematology Slide Stainer; Wescor Inc, Logan, UT). Manual slide evaluations were performed on samples when laboratory-defined criteria were met (absolute WBC count, WBC differential percentages, hemoglobin, hematocrit, or platelet count outside of reference intervals; automated WBC differential counts unreported by the analyzer; and the presence of analyzer-generated abnormal flags). Manual slide evaluations included WBC differential and platelet counts with evaluation of WBC, RBC, and platelet morphologies.

Chemistry panels composed of 20 tests were performed on serum using a Cobas 6000 analyzer (Roche Diagnostics, Risch-Rotkreuz, Switzerland). Tests in each panel included glucose, blood urea nitrogen, creatinine, creatine kinase, cholesterol, triglycerides, aspartate aminotransferase, alanine aminotransferase, lactic acid dehydrogenase, total bilirubin, gamma-glutamyl transferase, total protein, albumin, alkaline phosphatase, calcium, phosphorous, iron,

sodium, potassium, and chloride. CBC and serum chemistry panel results were recorded in the WNPRC Electronic Health Record (EHR) system with species, age, and sex-specific reference intervals provided within the reports generated through the EHR.

Plaque reduction neutralization test (PRNT90)

Macaque serum samples were screened for ZIKV neutralizing antibodies utilizing a plaque reduction neutralization test (PRNT) on Vero cells (ATCC #CCL-81). Endpoint titrations of reactive sera, utilizing a 90% cutoff (PRNT90) were performed as previously reported [28, 53] against ZIKV strain H.sapiens-tc/FRA/2013/FrenchPolynesia-01_v1c1 [28]. Briefly, ZIKV was mixed with serial 2-fold dilutions of serum for 1 hour at 37°C prior to being added to Vero cells and neutralization curves were generated using GraphPad Prism software. The resulting data were analyzed by non-linear regression to estimate the dilution of serum required to inhibit both 90% and 50% of infection.

Fetal Rhesus Biometric Measurements

Dams were sedated with ketamine hydrochloride (10 mg/kg) for sonographic assessments and amniocentesis. The biparietal diameter (BPD) and head circumference (HC) were measured on an axial image at the level of the hypoechoic thalami, with the echogenic interhemispheric fissure/falx all well visualized [54, 55]. The BPD was measured from the outer margin of the near calvarial echo to the inner margin of the deep calvarial echo. The HC was measured circumferentially at the outer margin of the calvaria [55-57]. The abdominal circumference was measured on an axial plane at the level of the stomach and the bifurcation of the main portal vein into the left and right branches, approximately perpendicular to the spine; the abdominal

circumference was measured around the outside of the margin of the fetal abdomen [55, 58]. The femur length (FL) was measured from the greater trochanter to the lateral condyle along the distal end of the shaft, excluding the femoral head and the distal epiphysis [57]**.** Growth curves were developed [55] for ZIKV-infected monkeys for BPD, HC, and FL. Mean measurements and standard deviations at specified days of gestation in Rhesus macaques were retrieved from Tarantal [35].

Fetal Rhesus Amniocentesis

Under real-time ultrasound guidance, a 22 gauge, 3.5 inch Quincke spinal needle was inserted into the amniotic sac. After 1.5-2 mL of fluid were removed and discarded due to potential maternal contamination, an additional 3-4 mL of amniotic fluid were removed for viral qRT-PCR analysis as described elsewhere [28]. These samples were obtained at the gestational ages specified in Fig. 1A. All fluids were free of any blood contamination.

Magnetic Resonance Imaging

Noninvasive imaging of the fetal brain was performed on isoflurane-anesthetized monkeys on a clinical 3T Magnetic Resonance Imaging (MRI) system (MR750, GE Healthcare, Waukesha, WI). T1 and T2-weighted axial and sagittal images were acquired. T2-weighted axial images were acquired with a single shot fast spin echo (SSFSE) sequence. Scan protocol for Supplementary Fig. S2A: respiratory gated multislice 2D acquisition; TE/TR = 141 / 2526 ms; Slice thickness: 2 mm; acquired spatial resolution = 1.25 mm x 1.25 mm; receiver bandwidth = 651 Hz/pixel. For Supplementary Fig. S2B, T1-weighted axial images were acquired with a multiecho spoiled gradient echo sequence. The scan protocol for respiratory gated 3D acquisition

under isoflurane anesthesia was iterative decomposition with echo asymmetry and least-squares estimation (IDEAL) processing for reconstruction of in-phase images from 8 echoes; 2 shots, 4 echoes each shot; flip angle = 15 deg; TE min = 1.6 ms; TR = 15.4 ms; Slice thickness: 1 mm; acquired spatial resolution = 1.1 mm x 1.1 mm; receiver bandwidth = 488 Hz/pixel. Animals were intubated for anesthesia under ketamine sedation, and imaging sessions lasted for approximately 1 hour.

Viral RNA isolation from urine, amniotic fluid, and oral/vaginal swabs

RNA was isolated from maternal and fetal plasma and PBMC, urine, amniotic fluid, and oral and vaginal swabs using the Viral Total Nucleic Acid Purification Kit (Promega, Madison, WI) on a Maxwell 16 MDx instrument as previously reported [28].

Viral RNA isolation from fetal and maternal tissues

Fetal and maternal tissues were processed with RNAlater (Invitrogen, Carlsbad, CA) according to the manufacturer protocols. Viral RNA was isolated from the tissues using the Maxwell 16 LEV simplyRNA Tissue Kit (Promega, Madison, WI) on a Maxwell 16 MDx instrument (Promega, Madison, WI). A range of 20-40 mg of each tissue was homogenized using homogenization buffer from the Maxwell 16 LEV simplyRNA Tissue Kit, the TissueLyser (Qiagen, Hilden, Germany) and two 5 mm stainless steel beads (Qiagen, Hilden, Germany) in a 2 ml snapcap tube, shaking twice for 3 minutes at 20 Hz each side. The isolation was continued according to the Maxwell 16 LEV simplyRNA Tissue Kit protocol, and samples were eluted into 50 µl RNase free water.

Quantitative reverse transcription PCR (qRT-PCR)

Viral RNA isolated from plasma, urine, oral swabs, amniotic fluid, and maternal or fetal tissues was quantified by qRT-PCR using modified primers and probe adapted from Lanciotti *et al.* [59] as previously described [53]. The SuperScript III Platinum one-step quantitative RT-PCR system was used (Invitrogen, Carlsbad, CA) on the LightCycler 480 instrument (Roche Diagnostics, Indianapolis, IN). Assay probes were used at final concentrations of 600 nM and 100 nM respectively, along with 150 ng random primers (Promega, Madison, WI). Conditions and methods were as previously described [28]. Tissue viral loads were calculated per mg of tissue.

Cesarean Section and Tissue Collection (Necropsy)

At ~155 days gestation, fetal and maternal tissues were surgically removed at laparotomy. These were survival surgeries for the dams. The entire conceptus within the gestational sac (fetus, placenta, fetal membranes, umbilical cord, and amniotic fluid) was collected and submitted for necropsy. The fetus was euthanized with an overdose of sodium pentobarbitol (50 mg/kg). Tissues were carefully dissected using sterile instruments that were changed between each organ and tissue type to minimize possible cross contamination. Each organ/tissue was evaluated grossly *in situ*, removed with sterile instruments, placed in a sterile culture dish, and sectioned for histology, viral burden assay, or banked for future assays. Sampling priority for small or limited fetal tissue volumes (e.g., thyroid gland, eyes) was vRNA followed by histopathology, so not all tissues were available for both analyses. Sampling of all major organ systems and associated biological samples included the CNS (brain, spinal cord, eyes), digestive, urogenital, endocrine, musculoskeletal, cardiovascular, hematopoietic, and

respiratory systems as well as amniotic fluid, gastric fluid, bile, and urine. A comprehensive listing of all specific tissues collected and analyzed is presented in Fig. 6 and Supplementary Fig. S3.

Biopsies of the placental bed (uterine placental attachment site containing deep decidua basalis and myometrium), maternal liver, spleen, and a mesenteric lymph node were collected aseptically during surgery into sterile petri dishes, weighed, and further processed for viral burden and when sufficient sample size was obtained, histology. Maternal decidua was dissected from the maternal surface of the placenta.

Histology

Tissues were fixed in 10% neutral buffered formalin for 14 days and transferred into 70% ethanol until routinely processed and embedded in paraffin. Paraffin sections (5 µm) were stained with hematoxylin and eosin (H&E). Pathologists were blinded to vRNA findings when tissue sections were evaluated microscopically. Lesions in each tissue were described and scored for severity as shown in Fig. 6B, and assigned morphologic diagnoses assigned as listed in Supplementary Data S1. Photomicrographs were obtained using a bright light microscope Olympus BX43 and Olympus BX46 (Olympus Inc., Center Valley, PA) with attached Olympus DP72 digital camera (Olympus Inc.) and Spot Flex 152 64 Mp camera (Spot Imaging), and captured using commercially available image-analysis software (cellSens Dimension^{R}, Olympus Inc. and spot software 5.2).

For immunohistochemistry, tissues were fixed in 4% paraformaldehyde/PBS overnight then paraffin embedded. 5 µm sections were cut and deparaffinized. Antigen retrieval was accomplished by incubation in heated (95°C) 10 mM citrate buffer (pH 6.0) plus 0.05% Tween-

20. The sections were blocked with 5% normal donkey serum for 1 hour at room temp then incubated overnight at 4°C with rabbit anti Zika NS2B 1:100 (GeneTex GTX133308, Irvine, CA) and mouse anti-CD163 1:100 (Novus, NB110-40686, Littleton, CO) or comparable control IgGs (Santa Cruz, Santa Cruz CA). Sections were rinsed with TBS + tween-20 (TBST) 3x and incubated with the appropriate secondary antibodies; donkey anti-rabbit Alexa 647 (1:5000), donkey anti-mouse Alexa 488 (1:2500) for 1 hour at room temperature (Jackson ImmunoResearch Laboratories, West Grove, PA). Sections were washed (3x TBST), exposed to DAPI and mounted with Aqua Poly Seal (Polysciences Inc, Warrington, PA). Sections were evaluated on a Leica SP8 confocal microscope.

Data availability

Primary data that support the findings of this study are available at the Zika Open-Research Portal (https://zika.labkey.com). Zika virus/H.sapiens-tc/FRA/2013/FrenchPolynesia-01_v1c1 sequence data have been deposited in the Sequence Read Archive (SRA) with accession code SRP072852. The authors declare that all other data supporting the findings of this study are available within the article and its supplementary information files.

ACKNOWLEDGEMENTS

We thank the WNPRC Veterinary, Scientific Protocol Implementation, and Pathology Services staff for assistance with animal procedures, including breeding, ultrasound monitoring, and sample collection, and Ms. Rebecca Black for editorial assistance. We thank Adam Ericsen, Jenna Kropp, and Jiro Wada for help in figure design and illustration.

SUPPLEMENTARY DATA

Supplementary Data S1. Morphologic diagnoses from gross and histologic examination of maternal, fetal, and maternal-fetal interface tissues.

Necropsy 598248	● Placenta: minimal to mild multifocal suppurative and necrotizing placentitis. ● Decidua: minimal lymphocytic and neutrophilic deciduitis. ● Amnion: mild diffuse suppurative amnionitis. ● Chorion: Mild diffuse suppurative chorioamnionitits with multifocal mineralization. ● Spleen, fetus: minimal diffuse splenitis. ● Pancreatic lymph node, fetus: moderate diffuse suppurative lymphadenitis. ● Gastric lymph node, fetus: mild diffuse suppurative lymphadenitis. ● Lungs, fetus: mild diffuse suppurative alveolitis (pneumonia) with intra-alveolar squamous cells and occasional macrophages. ● Liver, fetus: mild suppurative and lymphoplasmacytic cholangiohepatitis and serositis with mild multifocal extramedullary hematopoiesis.
Necropsy 357676	● Placenta: moderate multifocal suppurative placentitis with thrombosis and multifocal mineralization. ● Decidua: mild multifocal suppurative deciduitis with

	thrombosis and multifocal mineralization. ● Amnion: Severe diffuse edema with minimal diffuse suppurative amnionitis. ● Chorion: moderate multifocal to diffuse suppurative chorioamnionitis. ● Spleen, maternal: mild suppurative splenitis. ● Axillary lymph node, fetus: minimal suppurative lymphadenitis. ● Inguinal lymph node, fetus: minimal suppurative lymphadenitis. ● Lung, fetus: scattered single intra-alveolar squamous cells and minimal pulmonary edema. ● Pericardium, fetus: mild multifocal nodular lymphoid hyperplasia. ● Liver, fetus: minimal multifocal extramedullary hematopoiesis. ● Buccal mucosa, fetus: mild multifocal ballooning degeneration.
Necropsy 827577	● Placenta: moderate multifocal suppurative placentitis, multifocal mineralization, and perivascular lymphocytic infiltration. ● Decidua: moderate multifocal suppurative deciduitis. ● Amnion: minimal multifocal suppurative amnionitis, multifocal perivascular lymphocytic infiltration. ● Spleen, maternal: mild diffuse suppurative splenitis. ● Eye, fetus: Minimal lymphocytic iritis, minimal lymphocytic conjunctivitis, mild peripheral retinal and optic nerve gliosis. ● Spleen, fetus: Mild suppurative splenitis. ● Lungs, fetus: moderate intra-alveolar squamous cells.

Necropsy 660875	• Placenta: Moderate multifocal necrosuppurative placentitis. • Decidua: mild to moderate diffuse suppurative deciduitis. • Spleen, maternal: moderate diffuse suppurative splenitis with severe multifocal lymphoid hyperplasia with follicular dysplasia. • Liver, maternal: minimal multifocal periportal lymphosuppurative hepatitis. • Lymph node, maternal: moderate diffuse lymphoid hyperplasia. • Umbilical cord, infant: focal fibrin thrombus with intralesional neutrophils. • Eye, fetus: minimal lymphocytic iritis, moderate neutrophilic cyclitis, minimal lymphocytic conjunctivitis, moderate optic nerve gliosis. • Spleen, fetus: mild diffuse suppurative splenitis. • Axillary lymph node, fetus: moderate diffuse suppurative lymphadenitis. • Submandibular lymph node, fetus: moderate diffuse suppurative lymphadenitis. • Inguinal lymph node, fetus: moderate diffuse suppurative lymphadenitis. • Lungs, fetus: Moderate diffuse suppurative alveolitis with intra-alveolar squamous cells. • Liver, fetus: minimal multifocal suppurative periportal and serosal hepatitis.

REFERENCES

1. Hahn MB, Eisen RJ, Eisen L, Boegler KA, Moore CG, McAllister J, et al. Reported Distribution of Aedes (Stegomyia) aegypti and Aedes (Stegomyia) albopictus in the United States, 1995-2016 (Diptera: Culicidae). J Med Entomol. 2016.
2. Musso D, Gubler DJ. Zika Virus. Clin Microbiol Rev. 2016;29(3):487-524.
3. Barzon L, Pacenti M, Franchin E, Lavezzo E, Trevisan M, Sgarabotto D, et al. Infection dynamics in a traveller with persistent shedding of Zika virus RNA in semen for six months after returning from Haiti to Italy, January 2016. Euro Surveill. 2016;21(32).
4. Brooks JT, Friedman A, Kachur RE, LaFlam M, Peters PJ, Jamieson DJ. Update: Interim Guidance for Prevention of Sexual Transmission of Zika Virus - United States, July 2016. MMWR Morb Mortal Wkly Rep. 2016;65(29):745-7.
5. Davidson A, Slavinski S, Komoto K, Rakeman J, Weiss D. Suspected Female-to-Male Sexual Transmission of Zika Virus - New York City, 2016. MMWR Morb Mortal Wkly Rep. 2016;65(28):716-7.
6. Deckard DT, Chung WM, Brooks JT, Smith JC, Woldai S, Hennessey M, et al. Male-to-Male Sexual Transmission of Zika Virus--Texas, January 2016. MMWR Morb Mortal Wkly Rep. 2016;65(14):372-4.
7. Foy BD, Kobylinski KC, Chilson Foy JL, Blitvich BJ, Travassos da Rosa A, Haddow AD, et al. Probable non-vector-borne transmission of Zika virus, Colorado, USA. Emerg Infect Dis. 2011;17(5):880-2.
8. Hills SL, Russell K, Hennessey M, Williams C, Oster AM, Fischer M, et al. Transmission of Zika Virus Through Sexual Contact with Travelers to Areas of Ongoing

Transmission - Continental United States, 2016. MMWR Morb Mortal Wkly Rep. 2016;65(8):215-6.

9. Rowland A, Washington CI, Sheffield JS, Pardo-Villamizar CA, Segars JH. Zika virus infection in semen: a call to action and research. J Assist Reprod Genet. 2016;33(4):435-7.

10. Cauchemez S, Besnard M, Bompard P, Dub T, Guillemette-Artur P, Eyrolle-Guignot D, et al. Association between Zika virus and microcephaly in French Polynesia, 2013-15: a retrospective study. Lancet. 2016;387(10033):2125-32.

11. Schuler-Faccini L, Ribeiro EM, Feitosa IM, Horovitz DD, Cavalcanti DP, Pessoa A, et al. Possible Association Between Zika Virus Infection and Microcephaly - Brazil, 2015. MMWR Morb Mortal Wkly Rep. 2016;65(3):59-62.

12. Brasil P, Pereira JP, Jr., Moreira ME, Ribeiro Nogueira RM, Damasceno L, Wakimoto M, et al. Zika Virus Infection in Pregnant Women in Rio de Janeiro. N Engl J Med. 2016;375(24):2321-34.

13. Martines RB, Bhatnagar J, de Oliveira Ramos AM, Davi HP, Iglezias SD, Kanamura CT, et al. Pathology of congenital Zika syndrome in Brazil: a case series. Lancet. 2016;388(10047):898-904.

14. Noronha L, Zanluca C, Azevedo ML, Luz KG, Santos CN. Zika virus damages the human placental barrier and presents marked fetal neurotropism. Mem Inst Oswaldo Cruz. 2016;111(5):287-93.

15. Oliveira Melo AS, Malinger G, Ximenes R, Szejnfeld PO, Alves Sampaio S, Bispo de Filippis AM. Zika virus intrauterine infection causes fetal brain abnormality and microcephaly: tip of the iceberg? Ultrasound Obstet Gynecol. 2016;47(1):6-7.

16. Soares de Oliveira-Szejnfeld P, Levine D, Melo AS, Amorim MM, Batista AG, Chimelli L, et al. Congenital Brain Abnormalities and Zika Virus: What the Radiologist Can Expect to See Prenatally and Postnatally. Radiology. 2016;281(1):203-18.

17. de Paula Freitas B, de Oliveira Dias JR, Prazeres J, Sacramento GA, Ko AI, Maia M, et al. Ocular Findings in Infants With Microcephaly Associated With Presumed Zika Virus Congenital Infection in Salvador, Brazil. JAMA Ophthalmol. 2016.

18. Moore CA, Staples JE, Dobyns WB, Pessoa A, Ventura CV, Fonseca EB, et al. Characterizing the Pattern of Anomalies in Congenital Zika Syndrome for Pediatric Clinicians. JAMA Pediatr. 2016.

19. van der Linden V, Filho EL, Lins OG, van der Linden A, Aragao Mde F, Brainer-Lima AM, et al. Congenital Zika syndrome with arthrogryposis: retrospective case series study. BMJ. 2016;354:i3899.

20. Leal MC, Muniz LF, Ferreira TS, Santos CM, Almeida LC, Van Der Linden V, et al. Hearing Loss in Infants with Microcephaly and Evidence of Congenital Zika Virus Infection - Brazil, November 2015-May 2016. MMWR Morb Mortal Wkly Rep. 2016;65(34):917-9.

21. Costello A, Dua T, Duran P, Gulmezoglu M, Oladapo OT, Perea W, et al. Defining the syndrome associated with congenital Zika virus infection. Bull World Health Organ. 2016;94(6):406-A.

22. Franca GV, Schuler-Faccini L, Oliveira WK, Henriques CM, Carmo EH, Pedi VD, et al. Congenital Zika virus syndrome in Brazil: a case series of the first 1501 livebirths with complete investigation. Lancet. 2016;388(10047):891-7.

23. Miranda-Filho Dde B, Martelli CM, Ximenes RA, Araujo TV, Rocha MA, Ramos RC, et al. Initial Description of the Presumed Congenital Zika Syndrome. Am J Public Health. 2016;106(4):598-600.

24. Meaney-Delman D, Oduyebo T, Polen KN, White JL, Bingham AM, Slavinski SA, et al. Prolonged Detection of Zika Virus RNA in Pregnant Women. Obstet Gynecol. 2016;128(4):724-30.

25. Driggers RW, Ho CY, Korhonen EM, Kuivanen S, Jaaskelainen AJ, Smura T, et al. Zika Virus Infection with Prolonged Maternal Viremia and Fetal Brain Abnormalities. N Engl J Med. 2016.

26. van der Eijk AA, van Genderen PJ, Verdijk RM, Reusken CB, Mogling R, van Kampen JJ, et al. Miscarriage Associated with Zika Virus Infection. N Engl J Med. 2016;375(10):1002-4.

27. Abbink P, Larocca RA, De La Barrera RA, Bricault CA, Moseley ET, Boyd M, et al. Protective efficacy of multiple vaccine platforms against Zika virus challenge in rhesus monkeys. Science. 2016;353(6304):1129-32.

28. Dudley DM, Aliota MT, Mohr EL, Weiler AM, Lehrer-Brey G, Weisgrau KL, et al. A rhesus macaque model of Asian-lineage Zika virus infection. Nat Commun. 2016;7:12204.

29. Osuna CE, Lim SY, Deleage C, Griffin BD, Stein D, Schroeder LT, et al. Zika viral dynamics and shedding in rhesus and cynomolgus macaques. Nature medicine. 2016;22(12):1448-55.

30. Blankenship TN, Enders AC, King BF. Trophoblastic invasion and the development of uteroplacental arteries in the macaque: immunohistochemical localization of cytokeratins, desmin, type IV collagen, laminin, and fibronectin. Cell Tissue Res. 1993;272(2):227-36.

31. Bondarenko GI, Burleigh DW, Durning M, Breburda EE, Grendell RL, Golos TG. Passive immunization against the MHC class I molecule Mamu-AG disrupts rhesus placental development and endometrial responses. J Immunol. 2007;179(12):8042-50.

32. Enders AC. Implantation in the macaque: expansion of the implantation site during the first week of implantation. Placenta. 2007;28(8-9):794-802.

33. Adams Waldorf KM, Rubens CE, Gravett MG. Use of nonhuman primate models to investigate mechanisms of infection-associated preterm birth. BJOG. 2011;118(2):136-44.

34. Adams Waldorf KM, Stencel-Baerenwald JE, Kapur RP, Studholme C, Boldenow E, Vornhagen J, et al. Fetal brain lesions after subcutaneous inoculation of Zika virus in a pregnant nonhuman primate. Nature medicine. 2016;22(11):1256-9.

35. Tarantal AF. Ultrasound Imaging in Rhesus (Macaca mulatta) and Long-tailes (Macaca fascicularis) Macaques: Reproductuve and Research Applications. In: Wolfe-Coote S, editor. The Laboratory Primate. London: Elsevier; 2005. p. 317-52.

36. Tarantal AF, Hendrickx AG. Prenatal Growth in the Cynomolgus and Rhesus Macaque (Macaca fascicularis and Macaca mulatta): A Comparison by Ultrasonography. American journal of primatology. 1988;15:309-23.

37. Mlakar J, Korva M, Tul N, Popovic M, Poljsak-Prijatelj M, Mraz J, et al. Zika Virus Associated with Microcephaly. N Engl J Med. 2016;374(10):951-8.

38. van der Linden V, Pessoa A, Dobyns W, Barkovich AJ, Junior HV, Filho EL, et al. Description of 13 Infants Born During October 2015-January 2016 With Congenital Zika Virus Infection Without Microcephaly at Birth - Brazil. MMWR Morb Mortal Wkly Rep. 2016;65(47):1343-8.

39. Cugola FR, Fernandes IR, Russo FB, Freitas BC, Dias JL, Guimarães KP, et al. The Brazilian Zika virus strain causes birth defects in experimental models. Nature. 2016;534(7606):267-71.

40. Miner JJ, Cao B, Govero J, Smith AM, Fernandez E, Cabrera OH, et al. Zika Virus infection during pregnancy in mice causes placental damage and fetal demise. Cell. 2016;165(5):1081-91.

41. Yockey LJ, Varela L, Rakib T, Khoury-Hanold W, Fink SL, Stutz B, et al. Vaginal exposure to Zika virus during pregnancy leads to fetal brain infection. Cell. 2016;166(5):1247-56.

42. Vermillion MS, Lei J, Shabi Y, Baxter VK, Crilly NP, McLane M, et al. Intrauterine Zika virus infection of pregnant immunocompetent mice models transplacental transmission and adverse perinatal outcomes. Nat Commun. 2017;8:14575.

43. Grant A, Ponia SS, Tripathi S, Balasubramaniam V, Miorin L, Sourisseau M, et al. Zika virus targets human STAT2 to inhibit type I Interferon signaling. Cell Host Microbe. 2016;19(6):882-90.

44. Tarantal AF, Salamat MS, Britt WJ, Luciw PA, Hendrickx AG, and Barry PA. Neuropathogenesis induced by rhesus cytomegalovirus in fetal rhesus monkeys (Macaca mulatta). J Infect Dis. 1998;177(2):446-50.

45. Bialas KM, Tanaka T, Tran D, Varner V, Cisneros De La Rosa E, Chiuppesi F, et al. Maternal CD4+ T cells protect against severe congenital cytomegalovirus disease in a novel nonhuman primate model of placental cytomegalovirus transmission. Proc Natl Acad Sci U S A. 2015;112(44):13645-50.

46. Schoondermark-van de Ven EM, Melchers WJ, Galama JM, Meuwissen JH, and Eskes TK. Prenatal diagnosis and treatment of congenital Toxoplasma gondii infections: an experimental study in rhesus monkeys. Eur J Obstet Gynecol Reprod Biol. 1997;77(2):183-8.

47. Smith MA, Takeuchi K, Anderson G, Ware GO, McClure HM, Raybourne RB, et al. Dose-response model for Listeria monocytogenes-induced stillbirths in nonhuman primates. Infect Immun. 2008;76(2):726-31.

48. Wolfe B, Wiepz GJ, Schotzko M, Bondarenko GI, Durning M, Simmons HA, et al. Acute fetal demise with first trimester maternal infection resulting from Listeria monocytogenes in a nonhuman primate model. MBio. 2017;8(1).

49. Adams Waldorf KM, Rubens CE, and Gravett MG. Use of nonhuman primate models to investigate mechanisms of infection-associated preterm birth. BJOG. 2011;118(2):136-44.

50. Reynolds MR, Jones AM, Petersen EE, Lee EH, Rice ME, Bingham A, et al. Vital Signs: Update on Zika virus-associated birth defects and evaluation of all U.S. infants with congenital Zika virus exposure - U.S. Zika Pregnancy Registry, 2016. MMWR Morb Mortal Wkly Rep. 2017;66(13)366-73.

51. Juckstock J, Rothenburger M, Friese K, Traunmuller F. Passive Immunization against Congenital Cytomegalovirus Infection: Current State of Knowledge. Pharmacology. 2015;95(5-6):209-17.

52. Pomplun N, Weisgrau KL, Evans DT, Rakasz EG. OMIP-028: Activation panel for Rhesus macaque NK cell subsets. Cytometry Part A. 2015;87(10):890-3.

53. Aliota MT, Dudley DM, Newman CM, Mohr EL, Gellerup DD, Breitbach ME, et al. Heterologous Protection against Asian Zika Virus Challenge in Rhesus Macaques. PLoS Negl Trop Dis. 2016;10(12):e0005168.

54. Shepard M, Filly RA. A standardized plane for biparietal diameter measurement. J Ultrasound Med. 1982;1(4):145-50.

55. Tarantal AF, Hendrickx AG. Use of ultrasound for early pregnancy detection in the rhesus and cynomolgus macaque (Macaca mulatta and Macaca fascicularis). J Med Primatol. 1988;17(2):105-12.

56. Altman DG, Chitty LS. New charts for ultrasound dating of pregnancy. Ultrasound Obstet Gynecol. 1997;10(3):174-91.

57. Ville Y, Nyberg DA. Growth, Doppler, and Fetal Assessment. In: Nyberg DA, McGahan JP, Pretorius DH, Pilu G, editors. Diagnostic Imaging of Fetal Anomalies. Philadelphia, PA: Lippincott Williams & Wilkins; 2003. p. 32-4.

58. Deter RL, Harrist RB, Hadlock FP, Carpenter RJ. The use of ultrasound in the assessment of normal fetal growth: a review. J Clin Ultrasound. 1981;9(9):481-93.

59. Lanciotti RS, Kosoy OL, Laven JJ, Velez JO, Lambert AJ, Johnson AJ, et al. Genetic and serologic properties of Zika virus associated with an epidemic, Yap State, Micronesia, 2007. Emerg Infect Dis. 2008;14(8):1232-9.

Chapter 3:

Impact of Ferumoxytol Magnetic Resonance Imaging on the Rhesus Macaque Maternal-Fetal Interface

Publication: Sydney M. Nguyen, Gregory J. Wiepz, Michele Schotzko, Heather A. Simmons, Andres Mejia, Kai D. Ludwig, Ante Zhu, Kevin Brunner, Diego Hernando, Scott B. Reeder, Oliver Wieben, Kevin Johnson, Dinesh Shah, Thaddeus G. Golos. 2020. Impact of Ferumoxytol Magnetic Resonance Imaging on the Rhesus Macaque Maternal-Fetal Interface. BOR. doi: 10.1093/biolre/ioz181.

ABSTRACT

Ferumoxytol is a superparamagnetic iron oxide nanoparticle (SPION) used off-label as an intravascular magnetic resonance imaging (MRI) contrast agent. Additionally, ferumoxytol-uptake by macrophages facilitates detection of inflammatory sites by MRI through ferumoxytol-induced image contrast changes. Therefore, ferumoxytol-enhanced MRI holds great potential for assessing vascular function and inflammatory response, critical to determine placental health in pregnancy. This study sought to assess the fetoplacental unit and selected maternal tissues, pregnancy outcomes, and fetal well-being after ferumoxytol administration. In initial developmental studies, seven pregnant rhesus macaques were imaged with or without ferumoxytol administration. Pregnancies went to term with vaginal delivery and infants showed normal growth rates compared to control animals born the same year that did not undergo MRI. To determine the impact of ferumoxytol on the maternal-fetal interface, fetal well-being, and pregnancy outcome, four pregnant rhesus macaques at ~100 gestational day (GD) underwent

MRI before and after ferumoxytol administration. Collection of the fetoplacental unit and selected maternal tissues was performed 2-3 days following ferumoxytol administration. A control group that did not receive ferumoxytol or MRI was used for comparison. Iron levels in fetal and maternal-fetal interface tissues did not differ between groups, and there was no significant difference in tissue histopathology with or without exposure to ferumoxytol, and no effect on placental hormone secretion. Together, these results suggest that the use of ferumoxytol and MRI in pregnant rhesus macaques does not negatively impact the maternal-fetal interface and can be a valuable experimental tool in research with this important animal model.

INTRODUCTION

In the hemochorial human and nonhuman primate placenta, maternal intervillous blood bathes the placental villi, allowing oxygen and nutrient transfer to the fetal blood circulating within the capillaries of the villous stroma. Pregnancy complications may stem from maladaptation of maternal vessels causing insufficient placental perfusion, leading to macrophage recruitment, cytokine release, and hypoxia at the maternal-fetal interface (MFI). Compromised intervillous flow is associated with adverse pregnancy outcomes [1-4]: insufficient placental perfusion could result in fetal growth restriction, preeclampsia, and pregnancy loss. The ability to identify abnormal uteroplacental vascular adaptation, compromised perfusion, and attendant inflammation could be valuable in identifying at-risk pregnancies before clinical manifestations.

Currently, ultrasound is the most commonly used method to assess fetal growth. It is also used to detect umbilical and uteroplacental blood flow abnormalities, but only indirectly through velocity waveform analysis. Further, ultrasound lacks the ability to detect immune cell homing to

the MFI that may precede adverse pregnancy outcomes. Magnetic resonance imaging (MRI) can provide high-resolution anatomic and functional information including blood velocities and flow, perfusion, and oxygenation to characterize placental implantation site, visualize maternal pelvic structures, and diagnose abnormally aggressive trophoblast invasion or placental abruption [5]. In many clinical applications, gadolinium-based contrast agents (GBCAs) are used to quantify tissue perfusion and perform high-resolution angiography [6]. In the non-human primate, gadolinium MRI has been used to investigate spiral artery and perfusion domain (cotyledon) location, and quantify placental perfusion [7,8], the latter of which has also been achieved in humans [9]. However, GBCAs have been shown to cross the placenta into the fetus with uncertainty in the long-term consequences of in utero GBCA exposure [10]. Although there is no specific evidence that it causes teratogenic or chromosomal damage [11-13], the risk to the fetus of gadolinium-based MR contrast agent administration remains unknown and should not be routinely provided to pregnant patients [14].

In this study, we explored an alternative approach for quantitative tissue perfusion and MR angiography in pregnancy, using the SPION ferumoxytol as a contrast agent. Ferumoxytol is approved by the FDA for the treatment of anemia in adults with renal insufficiency and for iron deficiency anemias refractory to oral iron therapy [15] It is considered to be safe and effective for treatment of iron deficiency anemia refractory to oral iron therapy in pregnant women [16]. Ferumoxytol has also emerged as an off-label MR contrast agent at a much lower dose than is used therapeutically for anemia. Ferumoxytol has favorable MR properties [17,18] that can yield high-detail angiography and functional information about the MFI non-invasively, including quantitative perfusion maps of maternal blood that allow for analysis of individual cotyledons in the placenta [19], as seen in imaging with gadolinium [7]. As such, it has high potential to

identify local and global perfusion abnormalities that might be indicative of placenta pathologies. Ferumoxytol also has the potential to spatially localize inflammatory events, as the nanoparticles are taken up by activated cells of the mononuclear phagocyte system at sites of tissue inflammation, which can then be imaged after ferumoxytol in the blood space has cleared [17, 20-24]. The MRI transverse relaxation rate R2* has a relationship with the concentration of iron in tissue. Therefore, R2* mapping may enable localization of iron-laden macrophages, as well as quantification of their density. Ferumoxytol's safety profile and properties for MR imaging make it a promising contrast agent to address the unmet need for non-invasive diagnosis of placental health with potential for clinical routine use. Importantly, demonstrating its use for placental imaging is a necessary step in this application. Therefore, the purpose of this work was to assess the feasibility of ferumoxytol imaging and the impact of administration on the MFI, fetal well-being, and pregnancy outcomes in a non-human primate model. The rhesus macaque provides an accurate experimental model of the human MFI and immune system, having hemochorial placentation, endovascular trophoblast invasion with attendant spiral artery remodeling, and chorionic villous placental architecture.

METHODS

Care and Use of Macaques

Female rhesus macaques in the Wisconsin National Primate Center (WNPRC) breeding colony were housed with compatible males and monitored for breeding and menses. Pregnancies were confirmed and dated (+/- 2 days) based on menstrual cycle, observation of copulation, and ultrasound measurements of gestational sac and fetuses. Blood samples were collected using a needle and syringe or vacutainer system from the femoral or saphenous vein. All infants born

from this study (i.e., were not taken by fetectomy) joined the WNPRC colony. All macaques were cared for by WNPRC staff in accordance with the regulations and guidelines outlined in the Animal Welfare Act and the Guide for the Care and Use of Laboratory Animals. All animals including infants born from pregnancies that received MRI are systematically monitored twice daily by WNPRC staff and veterinarians, and additionally as needed. All irregular observations are immediately entered into the colony electronic health records. Observations may include the presence of blood, trauma, irregular feces, variation in eating patterns, lethargy, vomit, abnormal behavior including self-injury, evidence of breeding behavior, and infant nursing. This study was approved by the University of Wisconsin-Madison Graduate School Institutional Animal Care and Use Committee (IACUC). 12 pregnant macaques in the WNPRC breeding colony were used for peripheral blood mononuclear cell (PBMC) experiments, placentas from six macaques from unrelated projects were used for placenta explant experiments, four pregnant macaques were imaged by MRI without ferumoxytol, and seven pregnant macaques were imaged by MRI with ferumoxytol, four of which ended in fetectomy. An additional four pregnant macaques went to fetectomy without imaging.

Immune Cell Isolation and Incubation with Ferumoxytol

Monocytes and macrophages for in vitro ferumoxytol-uptake studies were isolated from whole blood drawn from 12 pregnant rhesus macaques, at approximately 100 gestational day (GD) (term=165GD), as previously reported [25]. Neutrophils were isolated as previously published [26]. All three cell types were incubated in ferumoxytol (Feraheme, AMAG Pharmaceuticals, Waltham, MA) at 0, 50, 100 or 200 μg/ml for one hour. Additionally, there were incubations of 0 μg/ml or 200 μg/ml with activating agents (50 ng/ml phorbol-12-

myristate-13-acetate (PMA; Sigma-Aldrich, St. Louis MO)) for all cell types, 750 ng/ml ionomycin (Sigma-Aldrich, St. Louis MO) for monocytes only). Following incubation, cells were washed and fixed with 2% paraformaldehyde (PFA) for visualization of iron content by Prussian Blue staining [27-29]. Cells were imaged using a Nikon Eclipse TE300 microscope with NIS-Elements image capture.

Placental Explant Incubations in Ferumoxytol

Prior to imaging experiments, placental explants were prepared from tissues obtained from untreated animals undergoing fetectomy or caesarean section in unrelated studies, during first trimester of pregnancy (n=2) or at term (n=4). Explants were incubated in ferumoxytol at 0, 100, or 200 μg/ml, diluted in DMEM/F12 with 10% fetal calf serum, for two, four, and 24 hours at 37°C in room air/5% CO2. Explants were fixed in 2% PFA overnight and embedded in paraffin blocks. Tissues were imaged using a Nikon Eclipse TE300 microscope with NIS-Elements image capture.

Prussian Blue Staining

To visualize cellular iron content, isolated, fixed immune cells grown on coverslips or deparaffinized rehydrated tissue sections were incubated in Prussian blue solution [27-29] for 20 minutes, washed with deionized water, and mounted with Aquapolymount (Polysciences, Warrington PA).

MRI Impact on Pregnancy Outcome and Postnatal Growth

There were two imaging phases in this study. In the first phase (Fig. 1 A), seven pregnant macaques were imaged, three with ferumoxytol and four without, to establish standard methods for anesthesia and imaging, and to pilot scan settings. These pregnancies went to term after imaging for spontaneous delivery. Animals that did not receive ferumoxytol had a single imaging session and were completed first to determine feasibility and ascertain appropriate imaging sequences prior to the addition of contrast agent. Animals that received ferumoxytol also had four non-ferumoxytol follow-up imaging sessions at approximately one day, one week, two weeks, and three weeks post-ferumoxytol. Infants joined the WNPRC colony and weights of infants exposed to MRI with or without ferumoxytol in-utero were compared to 116 untreated WNPRC 2016 colony infants through their first year of life. Mean and standard deviation weights for untreated colony infants were calculated at different ages, similar to the approach previously published [30]. These experiments were completed before moving to the second phase of the study.

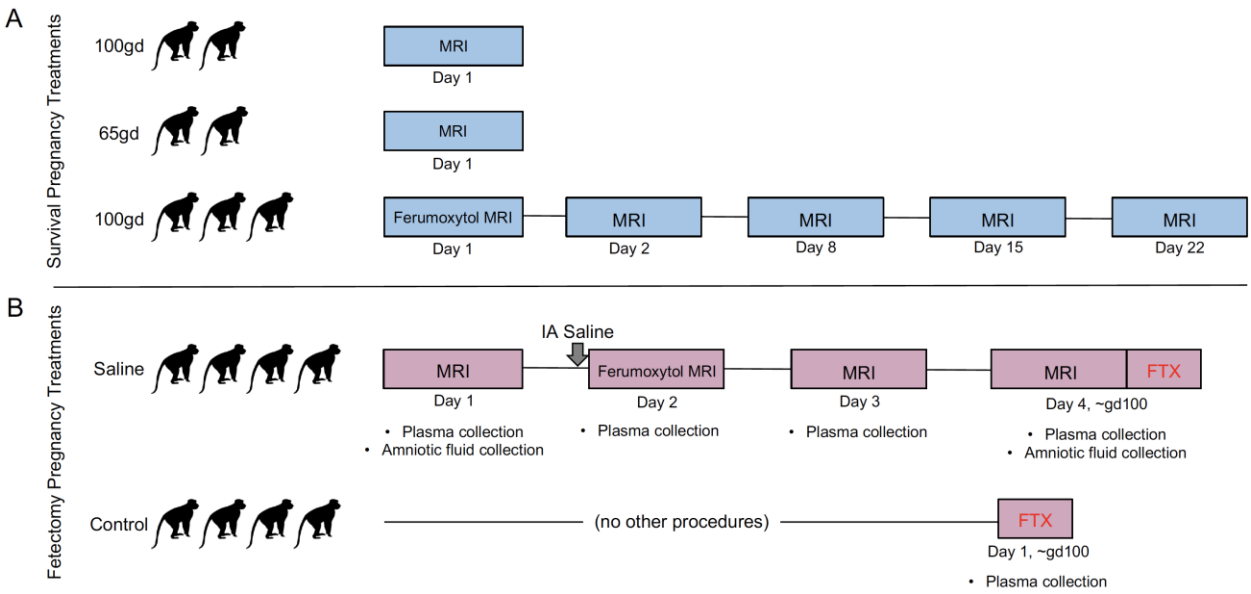

Figure 1. Experimental Design. Monkey outlines represent a single animal that received each treatment, represented on their respective timeline. (A) Blue timelines outline experimental design for animals where pregnancy proceeded to term and the infants were born by spontaneous vaginal delivery. (B) Pink timelines outline the series of procedures that animals received whose pregnancies were terminated by fetectomy. IA=intra-amniotic, FTX=fetectomy.

Use of IL-1β to Induce MFI Inflammation

In the second phase (Fig. 1 B), we used a paradigm of ferumoxytol MRI following intra-amniotic injection of 10mg human recombinant IL-1β (PeproTech, Rocky Hill, NJ) in 0.5ml sterile saline (n=4). This paradigm has been reported previously to increase decidual macrophage numbers and model chorioamnionitis and preterm labor [31,32] or sterile saline (n=4), and we used it to test the efficacy of ferumoxytol detection of mononuclear phagocytes and inflammation [17,20-24] at the MFI. At ~100GD both saline and IL-1β animals received a baseline MRI without ferumoxytol on day 1, MRI with ferumoxytol on day 2, and follow-up non-ferumoxytol MRIs on days 3 and 4. Untreated controls (n=4) did not receive intra-amniotic

injections, ferumoxytol, or MRI. While the resulting R2* maps of the MFI from IL-1β-exposed animals did not differ from those of animals receiving intra-amniotic saline (Zhu et al, under review), comparison of saline-injected and untreated animals allows determination of any impact of ferumoxytol MRI at the MFI or on the fetus. The results of the IL-1β-exposed animals will not be discussed in this report.

Intra-amniotic Injection

Procedures were performed under transabdominal ultrasound guidance on the lateral aspect of the abdomen. A syringe filled with sterile saline was attached to a biopsy needle and inserted through an aseptically prepared site of the abdominal wall until the tip reached the wall of the uterus, avoiding the bowel and bladder (n=4, Fig. 1 B). The needle was advanced into the amniotic cavity and a small amount of amniotic fluid was drawn to confirm needle placement. The contents of the syringe were then slowly injected into the amniotic cavity, and the needle was withdrawn. Following withdrawal of the needle, the insertion site in the uterus was observed by ultrasound to confirm lack of bleeding.

Magnetic Resonance Imaging

A total of 11 monkeys were imaged for the current study, seven with ferumoxytol. Experiments took place between January 2016 and April 2018. All animals that underwent an MRI exam, regardless of whether they also received ferumoxytol, were sedated by injection of up to 10 mg/kg ketamine, intubated, and anesthesia was maintained by inhalation of oxygen and 1.5% isoflurane. A pulse oximeter probe was placed and vital signs were monitored every 15 minutes. Animals were imaged in the right-lateral position and a respiratory bellow was placed

around the animal's belly during imaging to enable respiratory-compensated imaging that minimizes motion-related artifacts. Animals that received ferumoxytol had an intravenous catheter placed for injection during imaging.

For scans with ferumoxytol, dynamic contrast enhanced (DCE) images were acquired on a clinical 3.0T MRI system (Discovery MR750, GE Healthcare, Waukesha, WI) utilizing a 32-channel torso radiofrequency coil (Neocoil, Pewaukee, WI). Time resolved T1-weighted DCE images with 5 second temporal resolution were obtained throughout the ferumoxytol administration [33]. Scanner time for animals that did not undergo DCE scanning, including animal set-up in the magnet and all time between scans, ranged from 1.5 to 2.5 hours. Animals that underwent DCE scanning had times ranging from 2 to 4.5 hours to do pre and post ferumoxytol imaging and calibrations required for DCE. Ferumoxytol diluted 5:1 with normal saline was administered at 4 mg/kg body weight over a 20 second interval using a power injector, followed by a 20 ml saline flush at the same rate. A baseline R2* MRI scan (an MRI relaxation parameter highly correlated and sensitive to detect iron concentration) was performed before ferumoxytol administration. R2* measurements were estimated in the maternal, MFI, and fetal tissues by region-of-interest analysis directly from the MRI images. Follow-up R2* MRI scans were performed on subsequent days after contrast injection to determine the persistence of ferumoxytol in various tissues. MRI acquisition parameter details can be found elsewhere [33,34].

Assessment of Maternal Clinical Outcomes with Ferumoxytol Administration

Additional to the seven animals in this study that received MRI with ferumoxytol, one time each, there are several studies not discussed here being completed that also utilize

ferumoxytol MRI. Within these studies there are 28 animals that have received MRI with ferumoxytol up to three times, at the same dose discussed here per imaging session. The seven animals in our current study and these additional 28 animals are considered together to estimate the frequency of potential acute allergic reaction to ferumoxytol. No other information for these additional 28 animals will be considered in this report.

Fetectomy

At ~100GD the fetoplacental unit was collected via hysterotomy (n=8, Fig. 1 B). Maternal biopsies were collected aseptically during surgery and the dam recovered. The fetus was euthanized by intravenous or intracardiac injection of 50 mg/kg sodium pentobarbital. Fetal and MFI tissues were dissected for histology, iron content mass spectrometry, and protein assay.

Tissue Homogenates

Tissues collected at fetectomy (0.1-0.7g) (Supplemental Data 1) were homogenized in a Bullet Blender (Next Advance, Troy NY) at full power for 10 minutes with non-metal blending beads and 500 µL PBS. Tissue homogenate was stored at -80°C until use. A 96-well format micro BCA protein assay (Thermo Scientific, 23235) was used to determine protein concentrations in homogenates assayed for iron content according to the manufacturer's instructions.

Iron content determinations

Tissue homogenates were assayed for iron concentrations at the Wisconsin State Laboratory of Hygiene Trace Element Research Group in selected maternal, fetal, and MFI

tissues via inductively coupled plasma - optical emission spectrometry [35-38]. The limit of detection is 1μg/g tissue.

Steroid Hormone Extraction and LC/MS/MS Analysis

Maternal plasma samples (450 μl) collected for multi-steroid analysis from animals that had tissues collected at fetectomy (Fig. 1 B) were extracted and assayed as previously reported [39,40]. The limit of detection is 30pg/ml for progesterone; 6pg/ml for estrone and estradiol.

Histology

Tissues collected for histology were fixed in 4% PFA overnight, 70% ethanol overnight, and routinely processed and embedded in paraffin. 5μm sections were stained with H&E and assessed by veterinary pathologists blinded to treatment groups. Tissues were evaluated for the presence or absence of physiologically significant pathologic changes, normal anatomic variations, and inflammation. Morphologic diagnoses (Supplemental Data 2) summarize these histologic findings. Organs not given a morphologic diagnosis are considered to have no significant pathologic or inflammatory changes and were scored as a 0. Severity (none=0, minimal=1, mild=2, moderate=3, severe=4) was determined by the extent and distribution of inflammation, vascular change (infarction, thrombosis, pregnancy associated vascular remodeling and/or the lack thereof), and non-vascular necrosis across the tissue section or organ (multiple slides were necessary to evaluate the placenta). Scores were averaged and compared between treatment groups as previously reported [41]. Some MFI tissue sections were stained with Prussian Blue for iron localization.

Statistics

Iron concentrations in tissue homogenates were compared between treatment groups by 2-way ANOVA and Sidak's multiple comparison test. Differences in pathology and changes in R2* values were assessed by 2-way ANOVA. Hormone level changes were assessed by 1-way ANOVA.

RESULTS

PBMC Incubations

To determine whether rhesus macaque cells take up ferumoxytol as reported with human cells [17,20-24], prior to initiating the imaging phases of this study, rhesus monocytes, macrophages, and neutrophils were incubated in 100 µg/ml ferumoxytol (Supplemental Fig. 1), the approximate concentration of ferumoxytol in the blood with administration for MRI, and iron was visualized by Prussian blue staining. Staining was seen in differentiated macrophages but not monocytes or neutrophils. Activation with PMA and ionomycin did not affect iron staining. No staining was seen without ferumoxytol incubation.

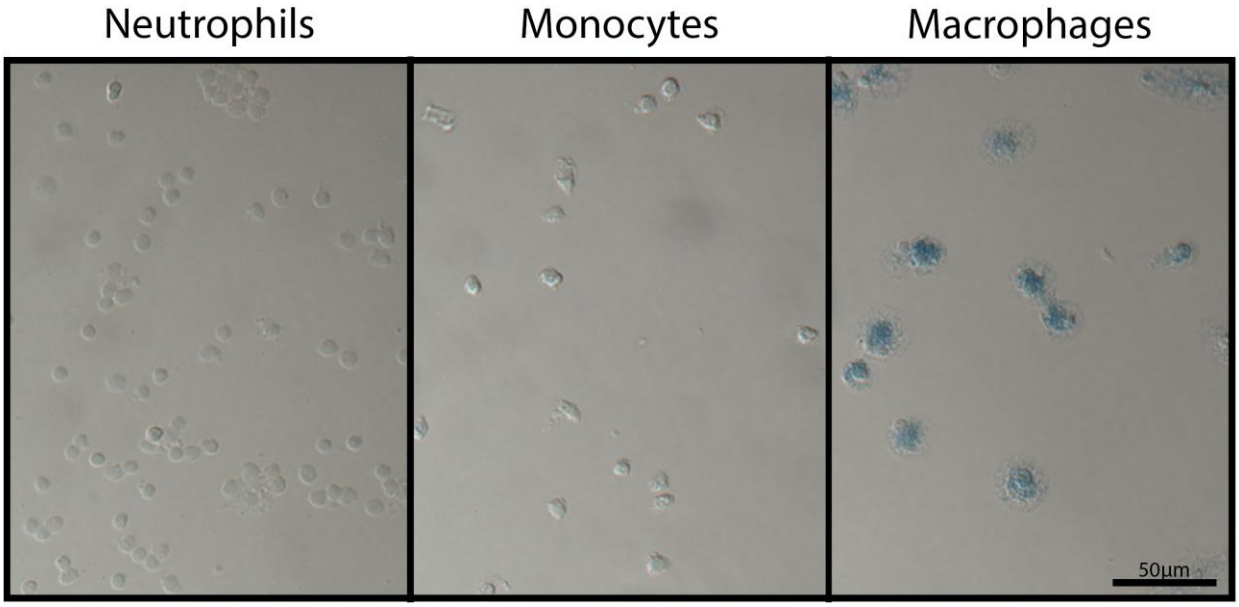

Supplemental Figure 1. Localization of iron in rhesus immune cells incubated with ferumoxytol. Peripheral blood neutrophils (left), monocytes (center), and *in vitro*-differentiated macrophages (right) from rhesus macaque whole blood were incubated in 100 µg/ml ferumoxytol for one hour and stained with Prussian Blue. Photomicrographs are of cytospins of neutrophils, or monocytes or macrophages grown on coverslips in culture.

Placental Explants Incubations

To determine whether placental ferumoxytol uptake by placental tissue may confound use for inflammation mapping in vivo, prior to initiating the imaging phases of this study, rhesus placental explants were incubated with ferumoxytol and stained with Prussian Blue. Modest background Prussian Blue iron staining in tissue was observed independent of ferumoxytol incubation, likely indicating endogenous iron content (Supplemental Fig. 2). Minimal increase in iron staining was observed after two hours of ferumoxytol-incubation. An increase in iron staining appeared after 24 hours incubation, specifically in the villous endothelium of the placental tissue. Not substantial staining of the syncytiotrophoblasts was observed, the primary

interface exposed to ferumoxytol in maternal blood in vivo. Low levels of endogenous iron and modest increases in ferumoxytol uptake in control placental explants ex vivo after incubations suggests that in vivo inflammation detection by ferumoxytol-enhanced MRI would be feasible and not confounded by background placental iron content/uptake.

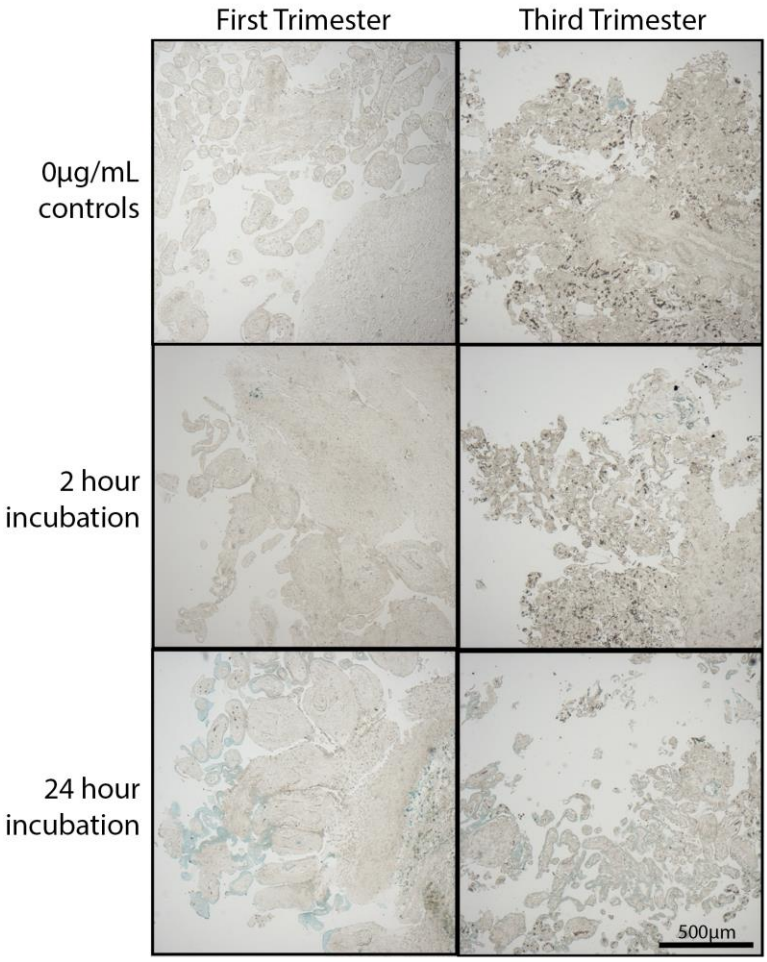

Supplemental Figure 2. Histological analysis of rhesus placental explants. Placental explants from tissue from first (left column) and third (right column) trimester pregnancies were incubated in ferumoxytol for two and 24 hours (200 µg/ml ferumoxytol for first trimester, 100 µg/ml ferumoxytol for third trimester). Original experiments were at the 200 µg/ml concentration but changed to 100 µg/ml as this concentration better reflects the concentration of

ferumoxytol in the blood when imaging. Tissue explants were embedded in paraffin and sections were cut and stained with Prussian Blue to localize iron. The top row shows control tissue that was not incubated in ferumoxytol. The middle row shows the two hour incubation. The bottom row shows the 24 hour incubation.

Maternal Clinical Outcomes with Ferumoxytol Administration

In addition to the seven animals in this study that received ferumoxytol for MRI (Fig. 1), 28 pregnant rhesus monkeys from other ongoing studies (unpublished) had up to three ferumoxytol imaging sessions. In 35 total experimental subjects who had ferumoxytol imaging sessions, two animals required moderate medical attention following ferumoxytol administration. Both animals had periocular edema following IV bolus administration of ferumoxytol that was treated with 10 mg diphenhydramine hydrochloride. One animal had a short period of increased heart rate and SPO2 levels. This animal had previous ocular swelling not associated with ferumoxytol, so it is unclear whether this event was due to ferumoxytol or other drugs used to anesthetize the animal. These mild allergic reactions responded to diphenhydramine and the animals recovered without further medical intervention.

Pregnancy Outcomes

Seven pregnant rhesus macaques (Fig. 1 A) who underwent MRI gave birth via vaginal delivery at term, and the infants joined the WNPRC colony. Results of these imaging studies are described in separate reports [33,42]. Pregnancy outcomes were generally unremarkable, with one retained placenta (which occurs in ~2.6% of WNPRC pregnancies). None of the seven dams had immediate or long-term reactions to the ferumoxytol treatment.

Infant growth data from these pregnancies are plotted along with their birth year cohort weights (Fig. 2). The weights of the MRI offspring generally stayed within one standard deviation of the average infant weights. Infants followed normal physiological and sociobehavioral patterns seen in other colony infants as assessed by daily veterinary observations.

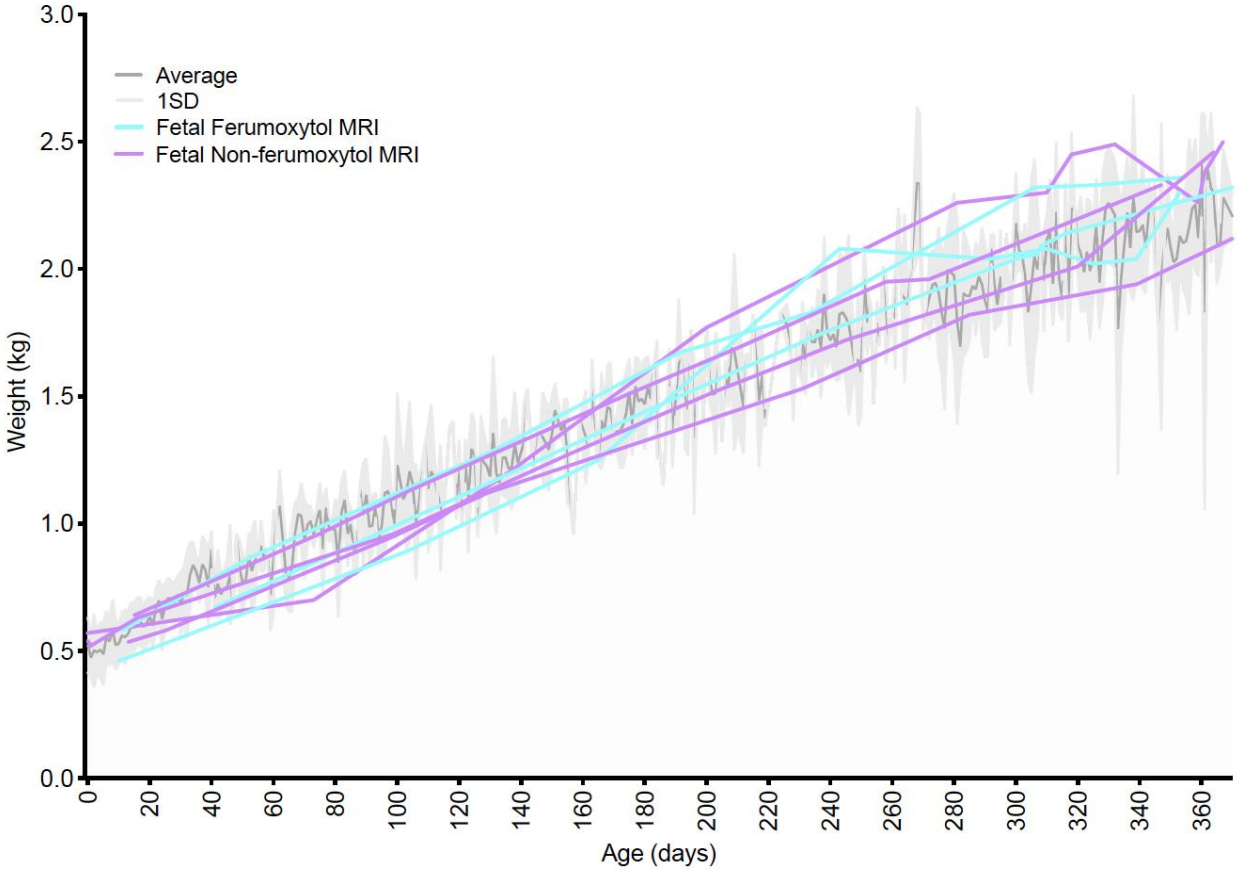

Figure 2. Infant growth rates with maternal ferumoxytol treatment compared to animal colony controls. The dark grey line represents the mean weight (kg) for 116 infants born at the WNPRC in 2016, weighed at the age in days listed on the x-axis. The light grey shaded region represents one standard deviation from the mean. Purple lines represent one animal each that was imaged by MRI without ferumoxytol. Aqua lines represent one animal each that was imaged

with ferumoxytol, plus four additional scans without additional ferumoxytol administration. The irregular mean and standard deviation lines reflect the fact that not all colony animals were weighted on any given day so the data represent a different population of animals at any specific time point.

Ferumoxytol Detection by MRI Following Administration

Three of the seven pregnant rhesus macaques that carried infants to term (Fig. 1 A) had been imaged with ferumoxytol at ~100GD. Imaging occurred immediately before (to establish a baseline R2* values in maternal, MFI, and fetal tissue) and 15 minutes after administration of ferumoxytol, followed by four follow-up MRI scans at approximately one day, one week, two weeks and three weeks following ferumoxytol administration. In all three animals, an increase in R2* values in both the primary and secondary placental disks is seen immediately following ferumoxytol injection (Fig. 3). The R2* values in fetal lung remained close to baseline though all scans while fetal liver R2* values increased slightly in two of the three animals. This may reflect an increase in physiological iron transport to the fetus over time in normal pregnancy, unrelated to ferumoxytol. The R2* values in the placenta, which increased dramatically following ferumoxytol administration, returned to approximate baseline levels within one day post-ferumoxytol, supporting a rapid clearance of ferumoxytol from the blood. Ferumoxytol accumulation in the placenta or transfer to the fetus was not detectable by R2* (Zhu et al, under review).

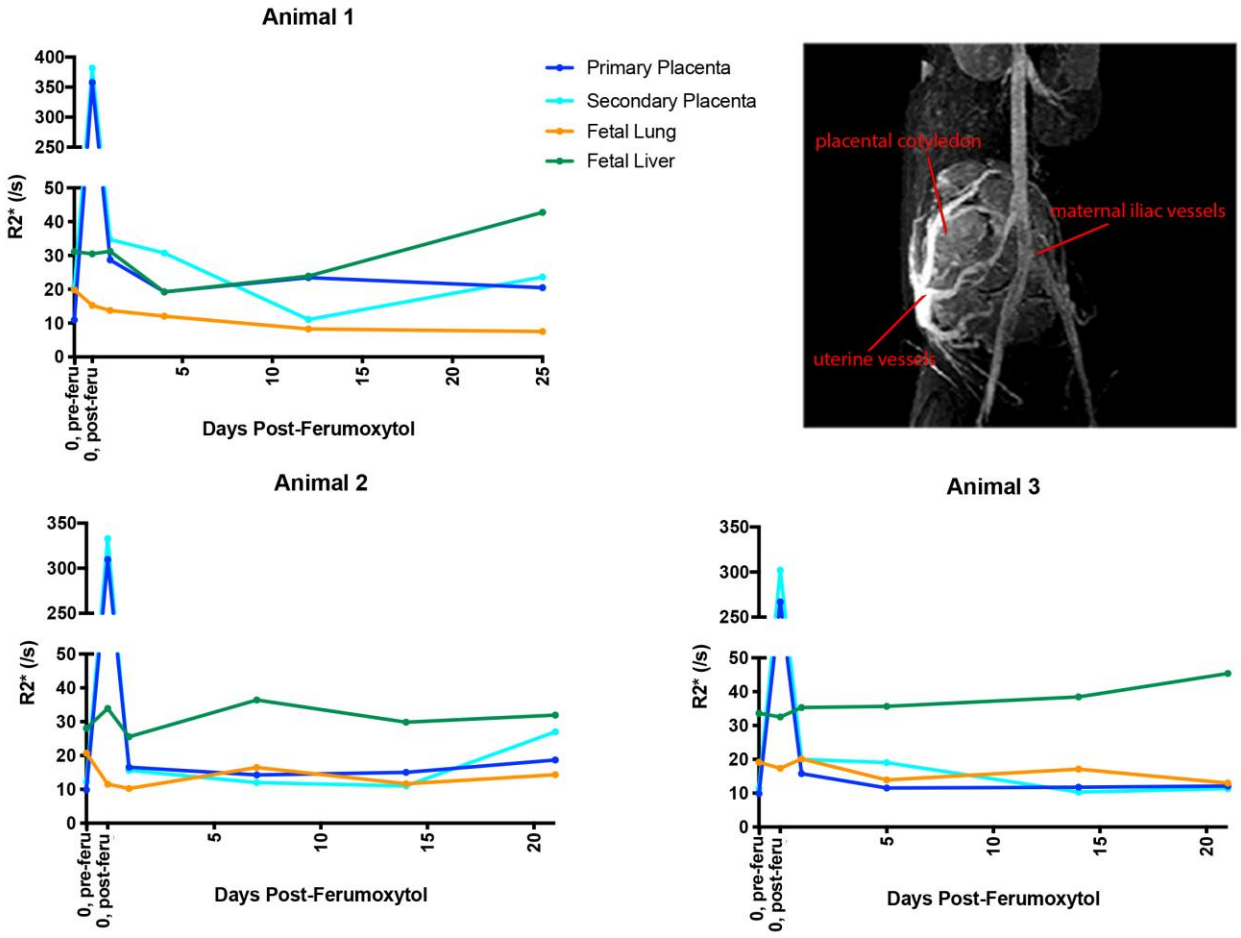

Figure 3. R2* values following ferumoxytol injection. R2* values were monitored in three pregnant rhesus macaques immediately following and one day, one week, two weeks, and three weeks ferumoxytol injection. The image on the top right is a representative Dynamic Contrast Enhanced (DCE) image of maternal and uterine ferumoxytol detection, including placental intervillous flow, illustrating the imaging data used to determine R2* values. The first point represents pre-injection ("0, pre-feru") and the second point represents the same day post-injection ("0, post-feru"). Primary placental disc values are in dark blue, secondary placenta in aqua, fetal lung in orange, and fetal liver in green.

Iron Content in Tissues

Maternal, MFI, and fetal tissues from eight pregnancies (Fig. 1B) were surgically collected at ~100GD following MRI and iron concentrations were determined in these tissues (Fig. 4). When ferumoxytol-exposed and untreated control groups were compared, only maternal liver showed a significant increase in iron concentration with maternal ferumoxytol administration over control (p<0.0001). There are no significant differences in fetal tissue iron levels in ferumoxytol vs. non-ferumoxytol-exposed animals.

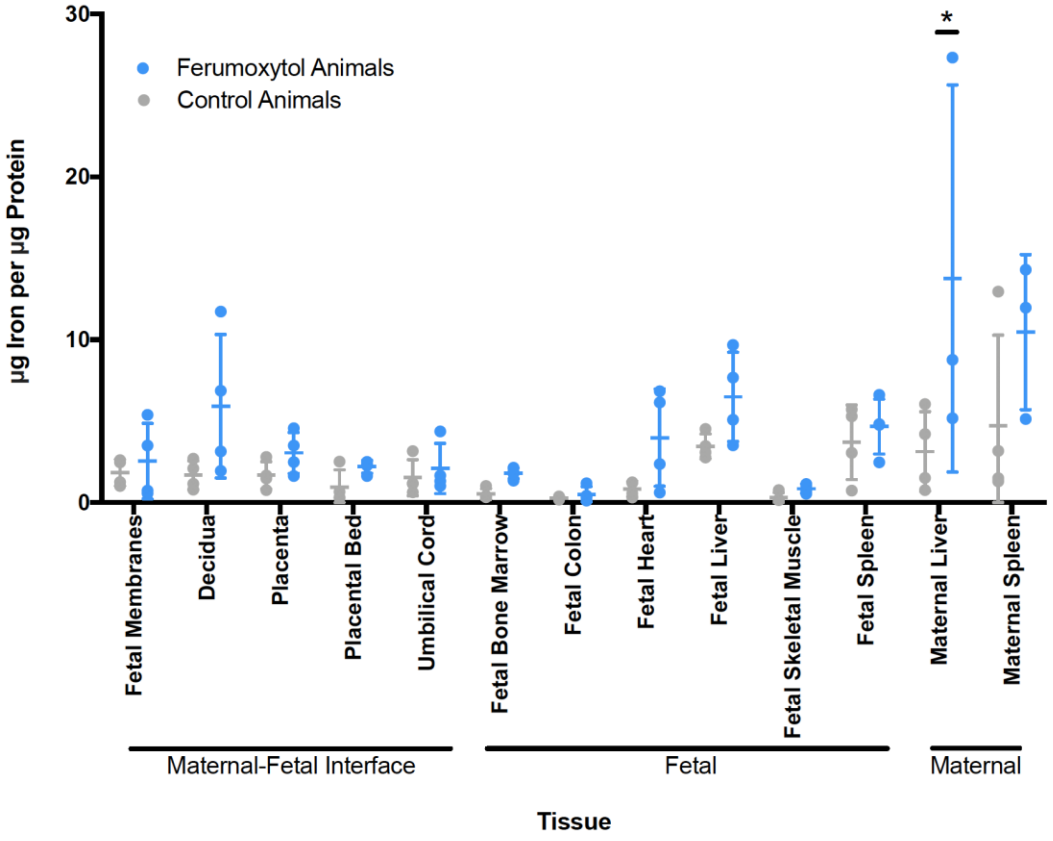

Figure 4. Iron content of maternal and fetal tissues. Iron content of selected tissues was determined by mass spectrometry. Non-imaged animals are represented by grey circles (n=4). Animals that received ferumoxytol imaging with intra-amniotic saline are in blue (n=4, except

for maternal liver and maternal spleen where n=3). Mean and standard error are denoted by horizontal lines for each tissue.

Prussian Blue Staining of MFI Tissues

Prussian Blue staining varied animal-to-animal in the placenta, decidua, and fetal membranes from animals that underwent fetectomy. Tissues from ferumoxytol-receiving animals, overall, did not have noticeably different staining compared to non-ferumoxytol-receiving animals. Interestingly, the animal with the most consistent staining had not received ferumoxytol (Supplemental Fig. 3), likely reflecting normal physiological iron.

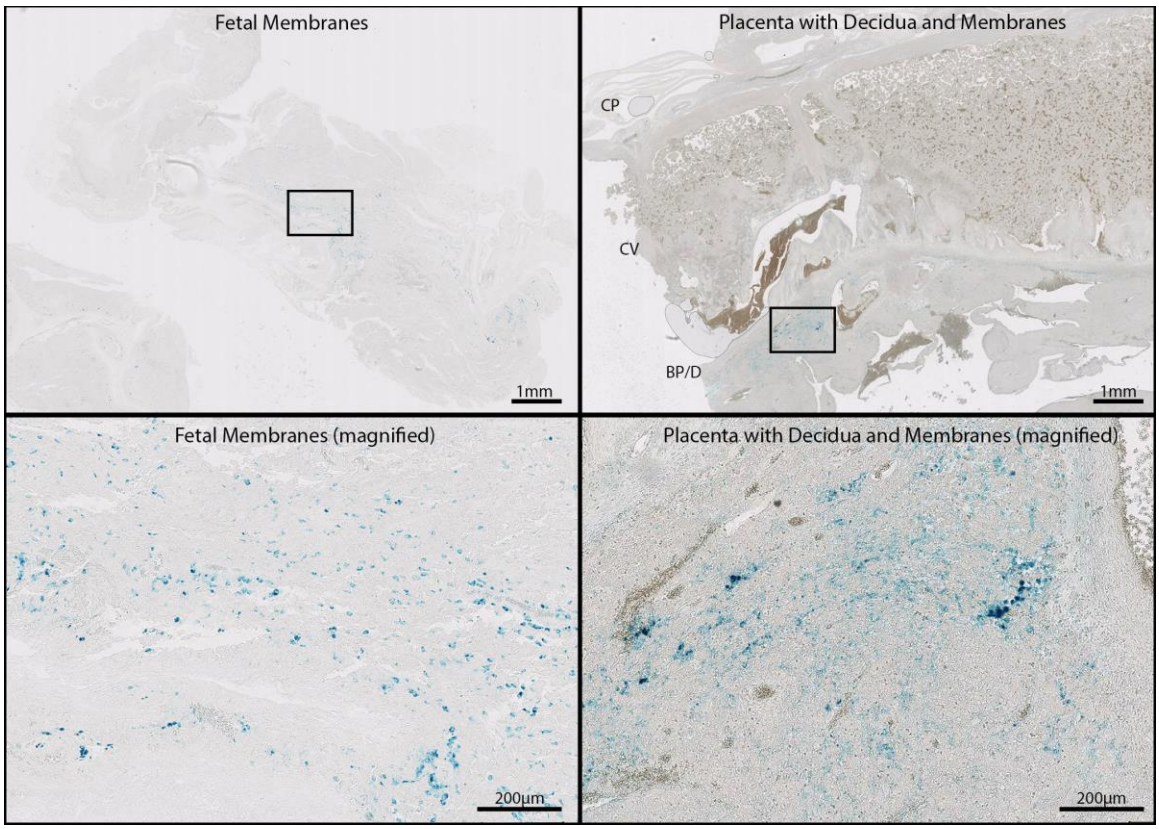

Supplemental Figure 3. Histochemical analysis of iron at the MFI. The left image presents a representative chorioamniotic membrane sample stained with Prussian Blue, the right image

presents a full-thickness placental section (with decidua and membranes attached) similarly stained. Both samples were collected from a non-MRI, non-ferumoxytol control animal. The lower panels present a higher magnification view of the regions depicted by rectangles in the upper panels. These images are from an animal that did not receive ferumoxytol, the degree of Prussian Blue staining was not seen to increase in animals that received ferumoxytol (not shown).

Ferumoxytol Effects on Plasma Progesterone, Estrone, and Estradiol

For each imaging day in animals that underwent fetectomy (Fig. 1 B), maternal plasma samples were assessed by mass spectrometry for progesterone, estrone, and estradiol levels [39,40] to assess the impact of MRI imaging and ferumoxytol administration on placental endocrine function. Non-imaged controls (Fig. 1 B) received a one-time plasma-collection at time of fetectomy. There was no statistically significant change in placental hormone levels following administration of ferumoxytol and hormone levels generally stayed within the range of levels seen in non-imaged controls (Fig. 5).

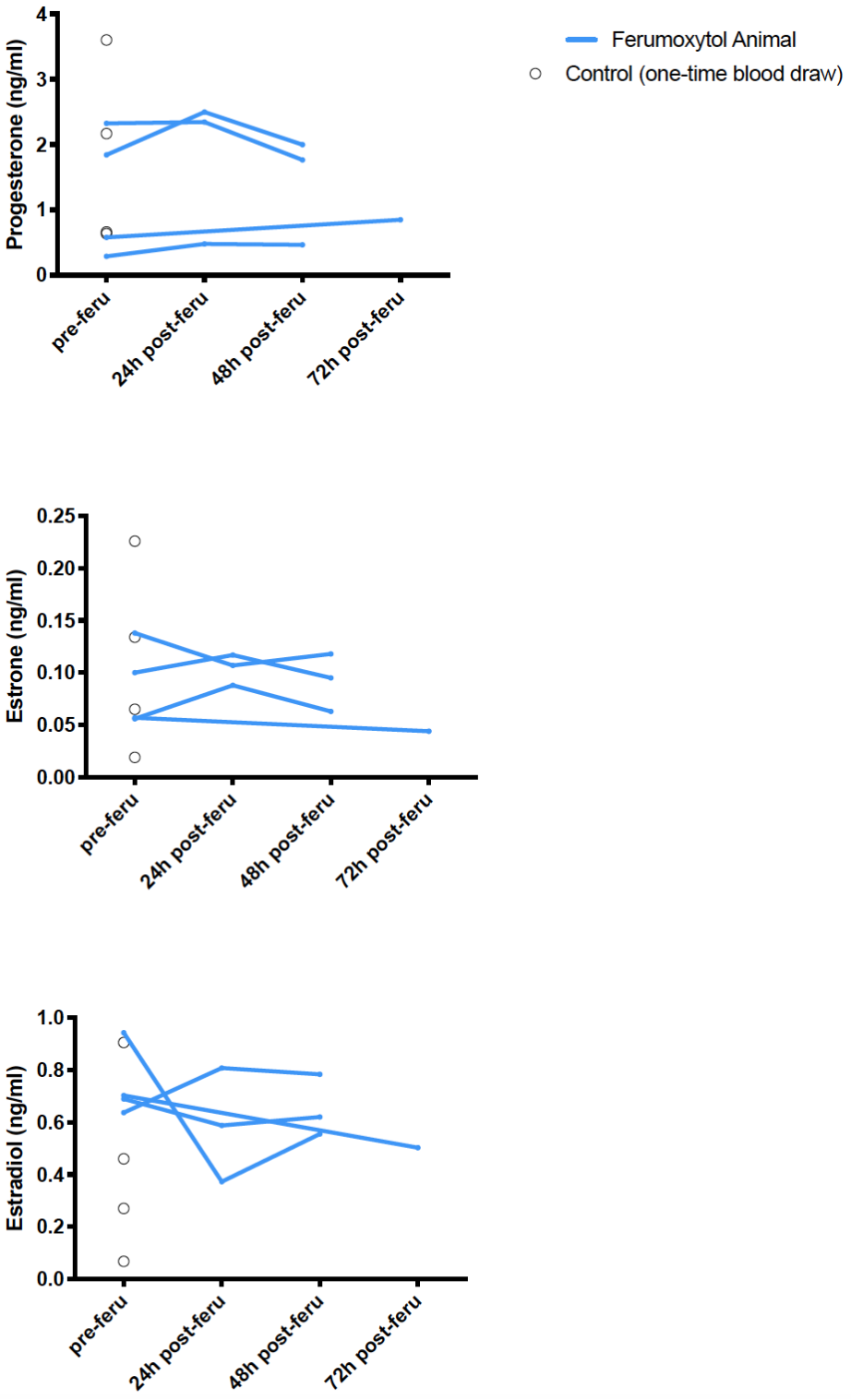

Figure 5. Plasma hormone levels in MRI animals assessed by mass spectrometry. Blue lines represent progesterone, estrogen, and estradiol levels in ferumoxytol-infused animals before

injection, 24h following injection, and 48h or 72h following injection. Black circles represent single blood draw readings from non-ferumoxytol control animals, indicating the expected range of peripheral blood steroid hormone levels in pregnant macaques.

Ferumoxytol Effects on Histopathology

Of 37 maternal and fetal tissues collected at fetectomy (Supplemental Data 1), the placenta, decidua, amniotic membranes, placental bed, maternal spleen, and maternal liver had notable histopathology. Animals that did and did not receive ferumoxytol MRI had no statistically significant differences in individual tissue histopathology scores (Fig. 6). Morphologic Diagnoses are provided in Supplemental Data 2.

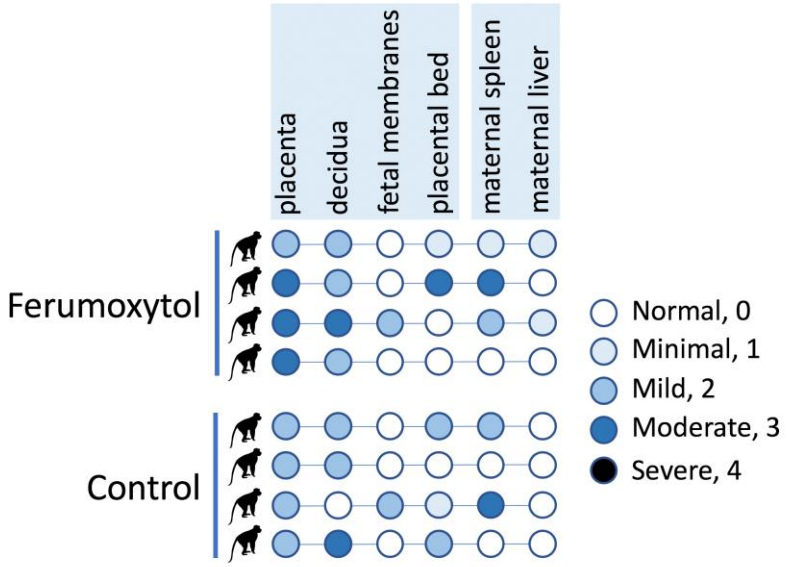

Average Pathology Scores with Standard Error

	Placenta	Decidua	Fetal Membranes	Placental Bed	Maternal Spleen	Maternal Liver
Ferumoxytol	2.75±0.25	2.25±0.25	0.5±0.5	1±0.71	1.5±0.65	0.5±0.29
Control	2±0	1.75±0.63	0.5±0.5	1.25±0.48	1.25±0.75	0±0

Figure 6. Chart summarizing histopathology scores of all tissues that showed pathology. For each animal, the circle representing each tissue is colored to denote severity of pathology.

The top four rows represent the ferumoxytol-receiving intra-amniotic saline animals and the bottom four rows are for non-ferumoxytol non-MRI controls. Numbers were assigned to each severity rating and used to analyze pathologies (normal=0, minimal=1, mild=2, moderate=3, severe=4). The chart below presents the average pathology scores for each tissue per treatment, used to assess statistical significance.

DISCUSSION

In this study, we examined the impact of MRI with and without ferumoxytol on the fetoplacental and maternal tissues, pregnancy outcomes, and fetal well-being in the pregnant rhesus macaque. Offspring from imaged pregnancies with or without ferumoxytol had uneventful labor and normal growth in comparison with contemporary pregnancies from the WNPRC breeding colony. No significant impact of MRI with ferumoxytol on iron content or histopathology of fetal and MFI tissues (decidua, placenta, fetal membranes) was observed. Placental function as indicated by peripheral blood steroid hormone levels was unaffected by MRI with ferumoxytol. The lack of significant adverse outcomes in the rhesus subjects also suggests the utility of ferumoxytol as a non-gadolinium contrast agent for MRI in pregnancy studies.

In vitro culture experiments demonstrated that ferumoxytol was taken up by macrophages differentiated from peripheral blood monocytes, but not by undifferentiated monocytes or granulocytes. This indicates that ferumoxytol is a feasible reagent to detect the accumulation of phagocytic macrophages at sites of inflammation. Tissue macrophages take up ferumoxytol and clear these iron nanoparticles more slowly than those in the blood, therefore, sites of inflammation can be located by performing delayed imaging following ferumoxytol

administration. This paradigm may help identify inflammation at the MFI, which could predict an insult to the pregnancy.

Concerns about ferumoxytol uptake by the placenta and the potential for transport of elevated levels of iron to the fetus, putting the fetus at risk for hemochromatosis or pulmonary hemosiderosis since these disorders result in fetal growth restriction, hepatic failure, alveolar hemorrhage, and stillbirth [43-45] were addressed. Placental villous explants were incubated *in vitro* with physiologically relevant concentrations of ferumoxytol, and staining of explant tissue sections for iron content with Prussian Blue did not demonstrate any significant uptake of SPION by placental tissues in a physiologically meaningful pattern (i.e., syncytiotrophoblast uptake) that would be anticipated with exposure of the placenta to ferumoxytol in the maternal blood in the intervillous space.

The fetus acquires iron during pregnancy through transferrin receptor acquisition of ferritin and transit across the placental syncytiotrophoblast and cytotrophoblast to the fetal vasculature within villous stroma [46]. Placental tissues collected from MRI experiments and stained with Prussian Blue for iron content did not reveal discernible differences between tissues from control and ferumoxytol-treated pregnancies. Additionally, decidual tissues and fetal membranes did not demonstrate any consistent differences between experimental groups. There were focally distributed areas of iron detected by Prussian Blue staining, however interestingly, the tissues with the clearest demonstration of iron content were the decidua and fetal membranes rather than the placental villi. It is important to note that the animal in which iron was most readily demonstrated in these tissues did *not* receive ferumoxytol and thus SPION-delivered iron was not the source of Prussian Blue staining. These data suggest that although the placenta directly transports iron to the fetus via a biologically conserved ferritin/ferritin receptor-mediated

pathway, this active pathway does not participate in the uptake of ferumoxytol by the syncytiotrophoblasts. We hypothesize that cellular iron sequestration, as indicated by Prussian Blue staining, may be largely attributable to macrophage uptake of erythrocytes as a routine surveillance function at the MFI.

Consistent with a lack of increase in iron content of MFI tissues by histochemical methods, there was no significant increase in iron concentration in MFI tissues by mass spectrometry. Likewise, fetal tissues that would be anticipated to accumulate iron did not show a statistically significant increase. While there does appear to be a trend for slightly higher, though not statistically significant, iron content in fetal tissues, further studies will be needed to determine if this is a consistent result. There was a statistically significant increase in maternal liver iron content, which was expected since the liver is a main clearance organ for ferumoxytol, with resident hepatic macrophages (Kupffer cells) taking up ferumoxytol particles in studies in rabbit [47] and human subjects [48,49].

Histopathology was evaluated in selected maternal tissues, the MFI, and in fetal tissues. There was no detectable histopathology in any fetal tissues. While histopathology was noted in tissues at the MFI, there were not significant differences between ferumoxytol-receiving and control animals. Some histopathological features were noted among placentas even in untreated "normal" pregnancies. Functional assessment of the placenta by monitoring of placental hormone secretion (progesterone, estradiol, estrone) likewise revealed no significant difference between animals receiving ferumoxytol MRI imaging, and untreated animals.

The use of an animal model to evaluate MRI methodologies has significant advantages. The pregnant dam is anesthetized for the imaging procedure in the nonhuman primate model, and the inhaled anesthetic is transferred to the fetus, which is also anesthetized. Therefore, the

fetal motion is minimized in MRI of the animals, leading to reliable MRI results. However, anesthesia is not the standard of care for MRI evaluation of pregnant humans and the potential fetal motion in MRI of pregnant human subjects will need to be addressed. A motion-robust R2* mapping technique has been proposed by our group and showed to effectively diminish motion effects in human scans [34]. Upon successful validation, the motion-robust MRI technique may enable detection of macrophage homing in pregnant women. It should also be noted that ferumoxytol was injected as a diluted bolus in our current macaque study, while it is administered as a slow infusion in humans to reduce the risk of anaphylactic reactions.

In summary, we conclude that ferumoxytol administration for imaging in this rhesus pregnancy model is feasible. Ferumoxytol effects on the fetus were minimal in this study with evidence that the SPION may not cross the placenta. Future studies will explore the use of ferumoxytol to detect placental inflammation and the diagnostic value of DCE MRI in the presence of placental dysfunction. The rhesus macaque will be an important platform for initial development of novel imaging approaches in an experimentally tractable model.

ACKNOWLEDGEMENTS

The authors wish to thank GE Healthcare who provides research support to the University of Wisconsin-Madison and AMAG Pharmaceuticals for providing Ferumoxytol for this study. Dr. Reeder is a Romnes Faculty Fellow, and has received an award provided by the University of Wisconsin-Madison Office of the Vice Chancellor for Research and Graduate Education with funding from the Wisconsin Alumni Research Foundation.

SUPPLEMENTARY DATA

Supplemental Data 1: Tissues Collected at Fetectomy.

Maternal Biopsies	Spleen, Liver, Mesenteric Lymph Node
Maternal-Fetal Interface	Placenta, Decidua, Placental Bed, Umbilical Cord, Chorioamniotic Membranes, Amniotic Fluid
Fetal Central Nervous System	Cerebrospinal Fluid, Frontal Cortex, Mid Cortex, Occipital Lobe, Cerebellum, Brain Stem, Cervical Spinal Cord
Fetal Ocular	Eye
Fetal Cardiopulmonary	Lung, Heart
Fetal Reproductive	Uterus or Prostate/Seminal Vesicles, Ovary or Testis
Fetal Musculoskeletal	Bone Marrow, Skeletal Muscle
Fetal Immune	Spleen, Thymus, Mesenteric Lymph Node, Tracheobronchial Lymph Node
Fetal Gastrointestinal	Liver, Duodenum/Jejunum, Ileum, Cecum, Colon
Fetal Urinary	Kidney
Fetal Endocrine	Adrenal, Pancreas, Pituitary

Supplemental Data 2: Pathology Reports.

	Morphologic Diagnoses
Ferumoxytol 1	● Placenta: mild multifocal basal plate thrombosis with mild acute multifocal villitis and intervillositis with increased intervillous fibrin, syncytial knots, moderate multifocal subchorionic fibrin and minimal segmental neutrophilic subchorionitis ● Decidua: mild multifocal to diffuse acute (neutrophilic) deciduitis with minimal multifocal necrosis and hemosiderophages ● Placental Bed: minimal multifocal lymphocytic endometritis ● Spleen, maternal: minimal diffuse neutrophilic splenitis ● Liver, maternal: minimal multifocal centrilobular lymphocytic hepatitis
Ferumoxytol 2	● Placenta: moderate multifocal basal plate thrombosis with minimal to mild multifocal neutrophilic intervillositis and villositis, with increased intervillous fibrin and syncytial knots and mild multifocal segmental subchorionic fibrin ● Decidua: mild multifocal lymphocytic deciduitis with mild diffuse hemosiderophage accumulation

	• Placental Bed: moderate diffuse necrosuppurative superficial endometritis and mild multifocal lymphocytic perivascular myometritis • Spleen, maternal: moderate multifocal lymphoid hyperplasia
Ferumoxytol 3	• Placenta: moderate multifocal basal plate thrombosis, mild multifocal subchorionic fibrin, minimal multifocal acute subchorionitis, rare avascular villi, mild multifocal neutrophilic villitis and intervillositis • Decidua: moderate chronic lymphoplasmacytic deciduitis • Fetal membranes, decidua: mild multifocal chronic lymphoplasmacytic deciduitis with occasional neutrophils • Spleen maternal: mild diffuse neutrophilic splenitis • Liver, maternal: minimal periportal lymphoplasmacytic hepatitis with rare neutrophils
Ferumoxytol 4	• Placenta: moderate multifocal decidual arteriopathy with multifocal vascular fibrinoid necrosis and intraluminal thrombi with perivascular edema • Decidua: mild multifocal perivascular and interstitial lymphoplasmacytic deciduitis

Non-ferumoxytol Control 1	• Placenta: mild random multifocal villous avascularization, minimal multifocal mineralization, three small transmural infarctions • Decidua: mild multifocal lymphocytic deciduitis with rare neutrophils and focal occlusive fibrin thrombi • Placental Bed: mild multifocal lymphocytic endometritis • Spleen, maternal: mild diffuse neutrophilic splenitis
Non-ferumoxytol Control 2	• Placenta: mild retroplacental hemorrhage, mild multifocal basal plate infarction and vascular thrombosis with minimal multifocal mineralization and moderate basal plate hemorrhage • Decidua: mild multifocal chronic lymphoplasmacytic deciduitis
Non-ferumoxytol Control 3	• Placenta: mild multifocal remote (chronic) thrombosis and infarction with minimal acute (neutrophilic) inflammation and moderate multifocal mineralization • Fetal membranes: mild diffuse chorioamniotic hemosiderosis • Placental Bed: minimal neutrophilic vasculitis • Spleen, maternal: moderate multifocal lymphoid hyperplasia and mild diffuse neutrophilic splenitis

Non-ferumoxytol Control 4	● Placenta: mild neutrophilic intervillositis and villitis with syncytial knot formation; mild multifocal basal plate necrosis, hemorrhage, and mineralization; mild multifocal chorionic necrosis with acute inflammation ● Decidua: moderate chronic lymphoplasmacytic deciduitis with marked organized hemorrhage ● Placental Bed: mild multifocal vasculitis and perivasculitis

REFERENCES

1. Alexander BT. Placental insufficiency leads to development of hypertension in growth-restricted offspring. Hypertension 2003; 41:457-462.
2. Brosens I, Pijnenborg R, Vercruysse L, Romero R. The "Great Obstetrical Syndromes" are associated with disorders of deep placentation. Am J Obstet Gynecol 2011; 204:193-201.
3. Krishna U, Bhalerao S. Placental insufficiency and fetal growth restriction. J Obstet Gynaecol India 2011; 61:505-511.
4. Roberts DJ, Post MD. The placenta in pre-eclampsia and intrauterine growth restriction. J Clin Pathol 2008; 61:1254-1260.
5. Chalouhi GE, Deloison B, Siauve N, Aimot S, Balvay D, Cuenod CA, Ville Y, Clément O, Salomon LJ. Dynamic contrast-enhanced magnetic resonance imaging: definitive imaging of placental function? Semin Fetal Neonatal Med 2011; 16:22-28.
6. Lohrke J, Frenzel T, Endrikat J, Alves FC, Grist TM, Law M, Lee JM, Leiner T, Li KC,

Nikolaou K, Prince MR, Schild HH, et al. 25 Years of Contrast-Enhanced MRI: Developments, Current Challenges and Future Perspectives. Adv Ther 2016; 33:1-28.

7. Frias AE, Schabel MC, Roberts VH, Tudorica A, Grigsby PL, Oh KY, Kroenke CD. Using dynamic contrast-enhanced MRI to quantitatively characterize maternal vascular organization in the primate placenta. Magn Reson Med 2015; 73:1570-1578.
8. Schabel MC, Roberts VHJ, Lo JO, Platt S, Grant KA, Frias AE, Kroenke CD. Functional imaging of the nonhuman primate Placenta with endogenous blood oxygen level-dependent contrast. Magn Reson Med 2016; 76:1551-1562.
9. Siauve N, Chalouhi GE, Deloison B, Alison M, Clement O, Ville Y, Salomon LJ. Functional imaging of the human placenta with magnetic resonance. Am J Obstet Gynecol 2015; 213:S103-114.
10. Ray JG, Vermeulen MJ, Bharatha A, Montanera WJ, Park AL. Association Between MRI Exposure During Pregnancy and Fetal and Childhood Outcomes. JAMA 2016; 316:952-961.
11. Rogosnitzky M, Branch S. Gadolinium-based contrast agent toxicity: a review of known and proposed mechanisms. Biometals 2016; 29:365-376.
12. Oh KY, Roberts VH, Schabel MC, Grove KL, Woods M, Frias AE. Gadolinium Chelate Contrast Material in Pregnancy: Fetal Biodistribution in the Nonhuman Primate. Radiology 2015; 276:110-118.
13. Prola-Netto J, Woods M, Roberts VHJ, Sullivan EL, Miller CA, Frias AE, Oh KY. Gadolinium Chelate Safety in Pregnancy: Barely Detectable Gadolinium Levels in the Juvenile Nonhuman Primate after in Utero Exposure. Radiology 2018; 286:122-128.
14. Kanal E, Barkovich AJ, Bell C, Borgstede JP, Bradley WG, Froelich JW, Gimbel JR,

Gosbee JW, Kuhni-Kaminski E, Larson PA, Lester JW, Nyenhuis J, et al. ACR guidance document on MR safe practices: 2013. J Magn Reson Imaging 2013; 37:501-530.

15. AMAG Pharma. Feraheme: Highlights of Prescribing Information [Internet]. 2018. https://www.accessdata.fda.gov/drugsatfda_docs/label/2009/022180lbl.pdf. Accessed 2 August 2020.

16. Auerbach M, Landy HJ. Anemia in pregnancy [Internet]. UpToDate 2019. https://www.uptodate.com/contents/anemia-in-pregnancy?topicRef=7148&source=see_link. Accessed 2 August 2020.

17. Bashir MR, Bhatti L, Marin D, Nelson RC. Emerging applications for ferumoxytol as a contrast agent in MRI. J Magn Reson Imaging 2015; 41:884-898.

18. Knobloch G, Colgan T, Wiens CN, Wang X, Schubert T, Hernando D, Sharma SD, Reeder SB. Relaxivity of Ferumoxytol at 1.5 T and 3.0 T. Invest Radiol 2018; 53:257-263.

19. Ludwig KD, Fain SB, Adamson EB, Nguyen S, Golos TG, Reeder SB, Bird IM, Wieben O, Shah DM, Johnson KM. Quantitative ferumoxytol DCE MRI of the primate placental perfusion domains. Proceedings from the 26th Annual Meeting of ISMRM. Paris, France. June 2018.

20. Toth GB, Varallyay CG, Horvath A, Bashir MR, Choyke PL, Daldrup-Link HE, Dosa E, Finn JP, Gahramanov S, Harisinghani M, Macdougall I, Neuwelt A, et al. Current and potential imaging applications of ferumoxytol for magnetic resonance imaging. Kidney Int 2017; 92:47-66.

21. Hasan DM, Amans M, Tihan T, Hess C, Guo Y, Cha S, Su H, Martin AJ, Lawton MT, Neuwelt EA, Saloner DA, Young WL. Ferumoxytol-enhanced MRI to Image

Inflammation within Human Brain Arteriovenous Malformations: A Pilot Investigation. Transl Stroke Res 2012; 3:166-173.

22. Iv M, Samghabadi P, Holdsworth S, Gentles A, Rezaii P, Harsh G, Li G, Thomas R, Moseley M, Daldrup-Link HE, Vogel H, Wintermark M, et al. Quantification of Macrophages in High-Grade Gliomas by Using Ferumoxytol-enhanced MRI: A Pilot Study. Radiology 2018:181204.

23. Neuwelt A, Sidhu N, Hu CA, Mlady G, Eberhardt SC, Sillerud LO. Iron-based superparamagnetic nanoparticle contrast agents for MRI of infection and inflammation. AJR Am J Roentgenol 2015; 204:W302-313.

24. Gaglia JL, Harisinghani M, Aganj I, Wojtkiewicz GR, Hedgire S, Benoist C, Mathis D, Weissleder R. Noninvasive mapping of pancreatic inflammation in recent-onset type-1 diabetes patients. Proc Natl Acad Sci U S A 2015; 112:2139-2144.

25. Rozner AE, Dambaeva SV, Drenzek JG, Durning M, Golos TG. Generation of macrophages from peripheral blood monocytes in the rhesus monkey. J Immunol Methods 2009; 351:36-40.

26. Roberts RL, Gallin JI. Rapid method for isolation of normal human peripheral blood eosinophils on discontinuous Percoll gradients and comparison with neutrophils. Blood 1985; 65:433-440.

27. Sheehan D, Hrapchak B. Theory and practice of Histotechnology, 2nd Ed, 1980, pp217-218, Battelle Press, Ohio.

28. Luna L. Manual of Histologic Staining Methods of the AFIP, 3rd Ed, 1968, pp 183, McGraw-Hill, NY.

29. Crookham J, Dapson R. Hazardous Chemicals in the Histopathology Laboratory, 2nd

ED, 1991, Anatech.

30. Tarantal AF. Ultrasound Imaging in Rhesus (Macaca mulatta) and Long-tailed (Macaca fascicularis) Macaques: Reproductive and Research Applications. In: Wolfe-Coote S, editor. The Laboratory Primate. London: Elsevier; 2005. p. 317–52.

31. Presicce P, Senthamaraikannan P, Alvarez M, Rueda CM, Cappelletti M, Miller LA, Jobe AH, Chougnet CA, Kallapur SG. Neutrophil recruitment and activation in decidua with intra-amniotic IL-1beta in the preterm rhesus macaque. Biol Reprod 2015; 92:56.

32. Kallapur SG, Presicce P, Senthamaraikannan P, Alvarez M, Tarantal AF, Miller LM, Jobe AH, Chougnet CA. Intra-amniotic IL-1β induces fetal inflammation in rhesus monkeys and alters the regulatory T cell/IL-17 balance. J Immunol 2013; 191:1102-1109.

33. Ludwig KD, Fain SB, Nguyen SM, Golos TG, Reeder SB, Bird IM, Shah DM, Wieben OE, Johnson KM. Perfusion of the placenta assessed using arterial spin labeling and ferumoxytol dynamic contrast enhanced magnetic resonance imaging in the rhesus macaque. Magn Reson Med 2018.

34. Zhu A, Reeder SB, Johnson KM, Nguyen SM, Golos TG, Shimakawa A, Muehler MR, Francois CJ, Bird IM, Fain SB, Shah DM, Wieben O, Hernando D. Evaluation of a motion-robust 2D chemical shift-encoded technique for R2* and field map quantification in ferumoxytol-enhanced MRI of the placenta in pregnant rhesus macaques. J Magn Reson Imaging 2019. doi: 10.1002/mrm.27876

35. Krynitsky AJ. Preparation of Biological Tissue for the Determination of Arsenic and Selenium by Graphite Furnace Atomic Absorption Spectrometry. Anal. Chem., Vol. 59, pp 1884-1886. (1987).

36. Giesy JP, Wagner JG. Frequency Distributions of Trace Metal Concentrations in Five

Freshwater Fishes. Trans. Am. Fis. Soc., Vol. 106, No. 4, pp 393-403. (1977),

37. Test Methods for Evaluating Solid Waste Physical/Chemical Methods. Third edition, SW-846, USEPA. November 1986, including July 1992, August 1993, September 1994, and January 1995 updates. Method 6010B.

38. Methods for the Determination of Metals in Environmental Samples. USEPA, 200.7, 1994.

39. Kenealy BP, Kapoor A, Guerriero KA, Keen KL, Garcia JP, Kurian JR, Ziegler TE, Terasawa E. Neuroestradiol in the hypothalamus contributes to the regulation of gonadotropin releasing hormone release. J Neurosci 2013; 33:19051-19059.

40. Kenealy BP, Keen KL, Kapoor A, Terasawa E. Neuroestradiol in the Stalk Median Eminence of Female Rhesus Macaques Decreases in Association With Puberty Onset. Endocrinology 2016; 157:70-76.

41. Nguyen SM, Antony KM, Dudley DM, Kohn S, Simmons HA, Wolfe B, Salamat MS, Teixeira LBC, Wiepz GJ, Thoong TH, Aliota MT, Weiler AM, et al. Highly efficient maternal-fetal Zika virus transmission in pregnant rhesus macaques. PLoS Pathog 2017; 13:e1006378.

42. Macdonald JA, Corrado PA, Nguyen SM, Johnson KM, Francois CJ, Magness RR, Shah DM, Golos TG, Wieben O. Uteroplacental and Fetal 4D Flow MRI in the Pregnant Rhesus Macaque. J Magn Reson Imaging 2018.

43. Kelly AL, Lunt PW, Rodrigues F, Berry PJ, Flynn DM, McKiernan PJ, Kelly DA, Mieli-Vergani G, Cox TM. Classification and genetic features of neonatal haemochromatosis: a study of 27 affected pedigrees and molecular analysis of genes implicated in iron metabolism. J Med Genet 2001; 38:599-610.

44. Fellman V, Rapola J, Pihko H, Varilo T, Raivio KO. Iron-overload disease in infants involving fetal growth retardation, lactic acidosis, liver haemosiderosis, and aminoaciduria. Lancet 1998; 351:490-493.

45. Limme B, Nicolescu R, Misson JP. Neonatal pulmonary hemosiderosis. Case Rep Pediatr 2014; 2014:463973.

46. Fuchs R, Ellinger I. Endocytic and transcytotic processes in villous syncytiotrophoblast: role in nutrient transport to the human fetus. Traffic 2004; 5:725-738.

47. Yancy AD, Olzinski AR, Hu TC, Lenhard SC, Aravindhan K, Gruver SM, Jacobs PM, Willette RN, Jucker BM. Differential uptake of ferumoxtran-10 and ferumoxytol, ultrasmall superparamagnetic iron oxide contrast agents in rabbit: critical determinants of atherosclerotic plaque labeling. J Magn Reson Imaging 2005; 21:432-442.

48. Lim JH, Choi D, Cho SK, Kim SH, Lee WJ, Lim HK, Park CK, Paik SW, Kim YI. Conspicuity of hepatocellular nodular lesions in cirrhotic livers at ferumoxides-enhanced MR imaging: importance of Kupffer cell number. Radiology 2001; 220:669-676.

49. Ramanathan RK, Korn RL, Raghunand N, Sachdev JC, Newbold RG, Jameson G, Fetterly GJ, Prey J, Klinz SG, Kim J, Cain J, Hendriks BS, et al. Correlation between Ferumoxytol Uptake in Tumor Lesions by MRI and Response to Nanoliposomal Irinotecan in Patients with Advanced Solid Tumors: A Pilot Study. Clin Cancer Res 2017; 23:3638-3648.

Chapter 4:

A Placental Dissection Guide: 3D Printed Magnetic Resonance Imaging Data of Placental Blood Space in a Rhesus Macaque

Sydney M. Nguyen, Daniel Seiter, Kai D. Ludwig, Jason A. Bleedorn, Megan E. Murphy, Michele L. Schotzko, Dinesh M. Shah, Oliver E. Wieben, Thaddeus G. Golos.

ABSTRACT

Histological analysis of the placenta plays an important role in the study of adverse pregnancy outcomes. Placental lesions arising from infarctions, infection, and other insults are often focal and challenging to discern upon gross inspection of the delivered organ. Tissue sampling with preordained biopsy methodologies are prone to miss focal lesions. In addition, molecular analysis of samples requires maximal preservation of tissue integrity, often logistically prohibiting a histological examination of the entire placenta. This report introduces a novel approach using a 3D printed model based on functional information obtained from dynamic contrast-enhanced magnetic resonance imaging data as a dissection guide. Feasibility is demonstrated in a rhesus macaque model.

INTRODUCTION

The rhesus macaque placenta has many similarities to that of humans, making it an excellent model for the study of pregnancy for application in human healthcare [1]. Like humans, the macaque has hemochorial placentation in which trophoblasts invade the maternal decidua and have direct contact with maternal blood. The internal structure of the organ is villous, where

fetal villi are bathed in maternal blood and serve as the site of oxygen, nutrient, and waste exchange. The placentas are discoid, though macaques most often have two disks, with the umbilical cord connecting the primary disk to the fetus, and peripheral inter-placental vessels connecting the primary and secondary disks. Human gestation is approximately 280 days while rhesus macaques gestate on average 165 days [2].

In placental bacterial and viral infection, colonization and resulting histopathology findings are often focal [3-6]. This raises a major obstacle when studying infection in this organ. The placenta at term is a large organ (~120 grams in the rhesus) [7] and comprehensive histological evaluation is challenging. Generally, tissue from a preordained set of regions are collected as representative samples of the whole organ. However, the focal nature of placental infection (or other lesions of interest) means that the desired tissue may not be included in the biopsy samples. In these cases, it remains ambiguous whether the organ was infection-free or if the infected regions were simply missed by biopsy. Research in placental biology would benefit immensely from a method that prospectively informs researchers of the condition of a specific region of interest while the organ is in situ, enabling targeted biopsies for areas that may not be grossly visible.

This report describes the use of a non-invasive medical imaging technique using magnetic resonance imaging (MRI) with a contrast agent, ferumoxytol, in combination with a 3D printing methodology to enhance understanding of placental function and develop a tissue dissection guide model. Ferumoxytol is a superparamagnetic iron oxide nanoparticle approved for intravenous treatment of anemia but can also be used a contrast agent for MRI [8]. It has been successfully applied to placental MRI [9-10]. Dynamic contrast enhanced (DCE) imaging with ferumoxytol permits tracking of the contrast distribution so that blood flow into the placental

intervillous space can be quantitatively assessed. Further processing enables the identification of perfusion domains, which can be related to the placental functional domains, or cotyledons and their perfusion [9]. This anatomic and functional information can be used to plan the dissection such that normal and abnormally functioning tissue are represented, potentially reducing the number of biopsies. In addition, 3D printed models of the MRI data can improve the dissection process. The biopsy location can be matched to areas of specific interest as identified in the 3D model of placenta functional data, based on placental shape and location of morphological landmarks. With such guidance, the dissection can be conducted more quickly, ensuring optimal condition of collected samples. Furthermore, because these biopsies are matched to the MRI data at the time of dissection, histological assessment could be related to blood flow and other functional aspects measured by MRI to develop a deeper understanding of the effects of infection, or non-infection-related pathology, in the placental tissue. For these reasons, we developed a workflow based on DCE MRI and 3D printing for the proper identification of functional perfusion domains in the placenta and the creation of physical, color-coded 3D models to guide placental dissection.

METHODS

Care and Use of Macaques

Female rhesus macaques in the Wisconsin National Primate Center (WNPRC) breeding colony were housed with compatible males and monitored for breeding and menses. Pregnancies were confirmed and dated (+/- 2 days) based on menstrual cycle, observation of copulation, and ultrasound measurements of gestational sac and fetuses. All macaques were cared for by WNPRC staff in accordance with the regulations and guidelines outlined in the Animal Welfare

Act and the Guide for the Care and Use of Laboratory Animals. This study was approved by the University of Wisconsin-Madison College of Letters and Sciences and Vice Chancellor Office for Research and Graduate Education Institutional Animal Care and Use Committee. A pregnant rhesus macaque was imaged at gestational day 145 for the development of the 3D printed dissection guide.

Preparing the Macaque for Imaging

The subject was food deprived 4-20 hours prior to sedation for the MRI procedure. Sedation was completed by injection of up to 10 mg/kg ketamine, followed by intubation and maintenance anesthesia by inhalation of a mixture of oxygen and 1.5% isoflurane. A pulse oximeter probe was used to monitor blood oxygen and vital signs were monitored every 15 minutes. Imaging was conducted in the right-lateral position and a respiratory bellows was used to compensate for respiratory motion. An intravenous catheter was used for delivery of ferumoxytol during imaging.

Magnetic Resonance Imaging with Ferumoxytol

MR images were acquired on a clinical 3.0T MRI system (Discovery MR750, GE Healthcare, Waukesha, WI) utilizing a 32-channel torso coil (Neocoil, Pewaukee, WI). Time resolved T1-weighted DCE images with five second temporal resolution were obtained throughout the ferumoxytol administration [9]. Ferumoxytol (AMAG Pharmaceuticals, Waltham, MA) diluted 5:1 with saline was administered at 4 mg/kg body weight over a 20 second interval using a power injector, followed by a 20 ml saline flush at the same rate. MRI

acquisition parameter details can be found elsewhere [9,11]. The workflow to generate 3D printed models from MRI data is described below and represented on Fig. 1.

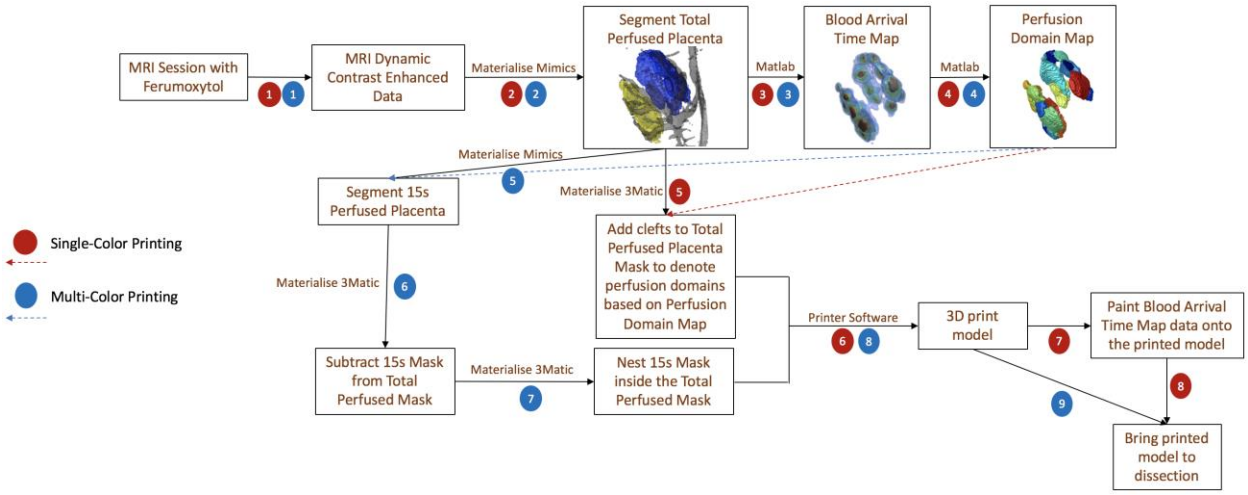

Figure 1. Workflow for MRI data processing and 3D printing. Step order is denoted by numbers in red circles for the single-color printing method and by numbers in blue circles for the multi-color printing method.

Processing of MRI Data

Placental volume segmentation was conducted based on a 3D volume representing a time after contrast had arrived in the whole placenta, about 90 seconds after the start of contrast injection. A multi-slice editing tool (Mimics v20, Materialise, Belgium) was used to segment the outer boundaries of the placenta identified by high signal from ferumoxytol uptake within the organ. In addition, contrast arrival maps were generated by automated processing of the dynamic DCE images using Matlab (Mathworks, Natic, MA) [9] as shown in Fig. 2. The DCE data was further processed to identify individual perfusion domains based on the contrast dispersion pattern in the placenta [12]. Individual perfusion domains can be analyzed for shape and volume

as shown in the color-coded maps in Fig. 2. The segmented placental volume map was used to create a 3D volume mesh of the placental disks and imported into a mesh-handling software (Mimics v12, Materialise). Using the 3D editor, clefts were manually created on the fetal side of the 3D virtual model to mark boundaries between the cotyledons according to the perfusion domain map.

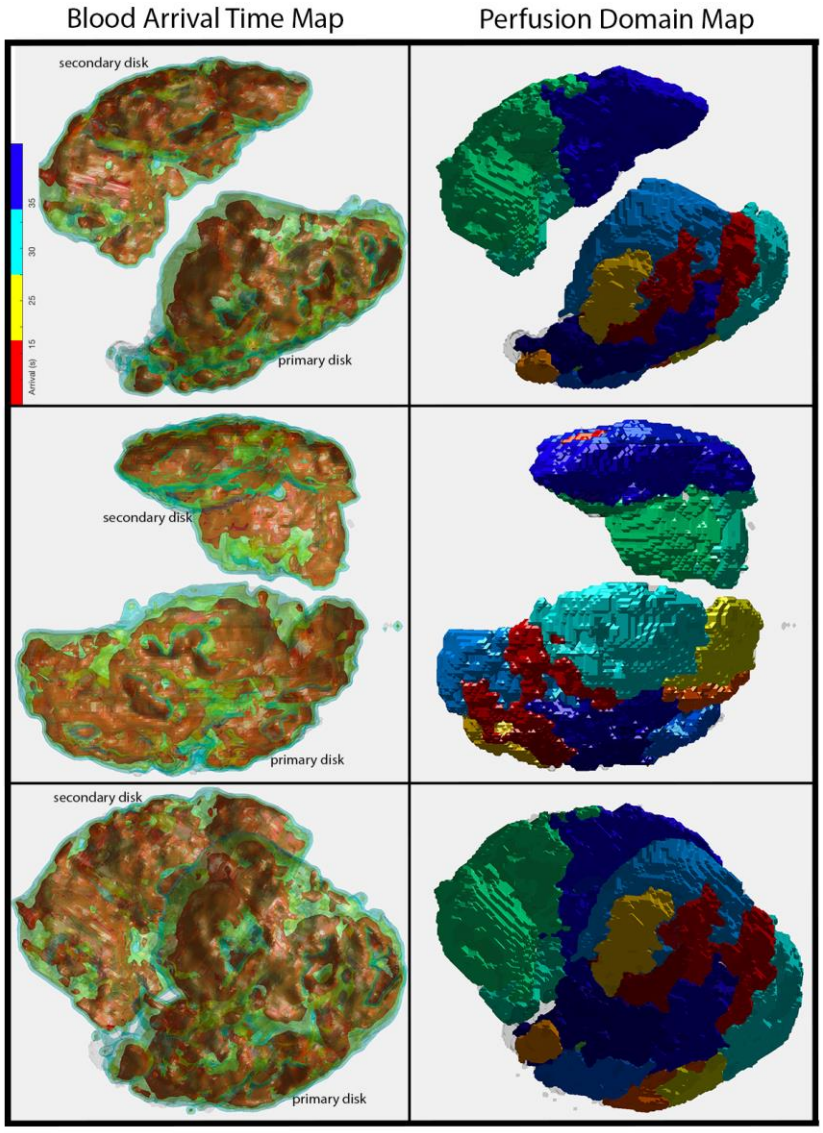

Figure 2. Placental MRI data models. The left column displays three views of the blood arrival time map for the two placental disks of a single rhesus macaque. This map shows regions of

early ferumoxytol-infused-blood arrival in red, later arrival in green, and the latest arrival in blue. Primary and secondary placental disks are labeled. The right column displays computer generated perfusion domain maps in the same orientation as the matched blood arrival time map to its left. This map shows each perfusion domain in a different color.

3D Printing Method for Single-Color Printer

A stereolithographic (SLA) 3D printer (Form2, Form Labs, Somerville, MA) with Clear resin (Form Labs) was used to generate physical 3D models of the primary and secondary placenta. The model was orientated with support on the maternal side of the model, which kept the perfusion domain mapping on the fetal side of the model easily identifiable, and printed with a resolution of 100 microns. The placental 3D print was processed routinely by washing (15 minutes, Isopropyl 99%, Form Rinse) and curing (15 minutes, Form Cure). Needle-nose pliers were used to remove the support matrix from the models and sandpaper was used to smooth the model where the support matrix had been attached. A dry bristle brush was used to remove powder from sanding.

Black paint was applied manually to highlight the clefts on the fetal side of the model to clearly mark the boundaries between the perfusion domains. The perfusion domain map was aligned with the maternal side of the model and red and blue paint was applied manually to mark regions of early blood arrival. Red denoted earliest contrast arrival (0-15 seconds), blue denotes regions of later contrast arrival nested in red zones, and unpainted denotes last contrast arrival, outside of the early arrival red zones. Due to the translucent resin used, the painted regions representing the arrival times could be seen from the fetal side of the model without distracting from the perfusion domain delineations (Fig. 3).

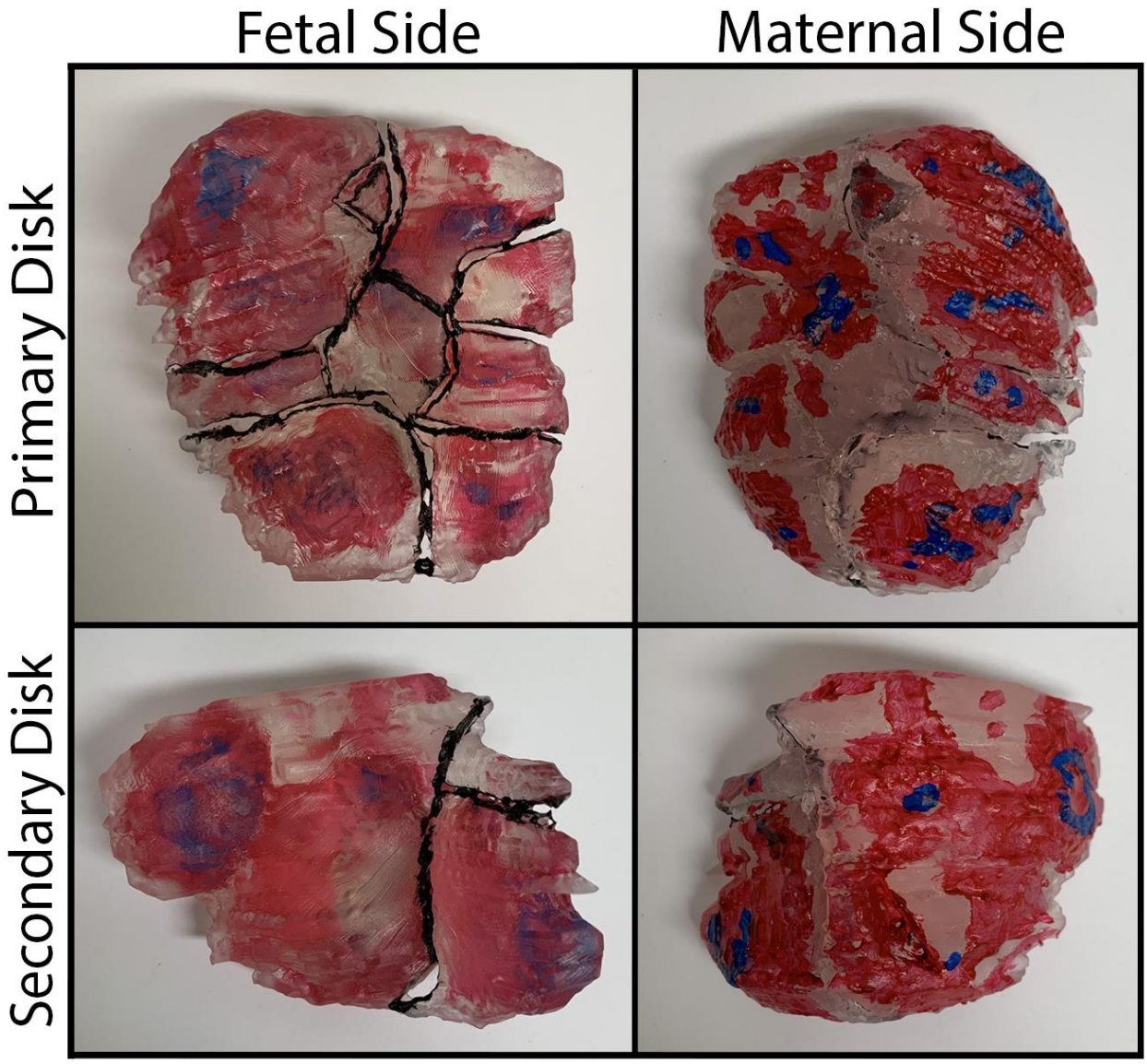

Figure 3. Single-color 3D-printed placenta models using SLA resin. Single-color 3D-printed placenta models based on the MRI data in Figure 2. The left column displays the fetal (chorionic plate) side of the primary disk (top) and secondary disk (bottom). The right column displays the maternal (placental attachment) side of the respective disks. Black paint was used to show delineation between cotyledons based on the computer-generated perfusion domain map. Red

paint was used to show early blood arrival regions based on the blood arrival time map. Blue denotes regions of later arrival time nested within red regions.

Modeling Method for Multi-Color Printers

Painting the translucent single-color model introduces human interpretation to the location of blood arrival patterns. Development of a multi-color model that defines the location of blood arrival based on the MRI data provides more precise information. To develop such a model, a second set of masks was created at the time point where the placenta volume is approximately 50% perfused (~15 seconds after bolus arrival in the placenta). Thereby, an early-arrival perfusion map was created in addition to the perfusion map that represents contrast distribution in the whole placenta. The regions of the placenta with non-detectable perfusion were removed when creating the fully perfused placenta map, which better reflected the shape of the perfusion domains and negated the need for the addition of clefts. The early-arrival mask area was subtracted from the fully perfused map using 3D mesh software (3-Matic v13, Materialise) and were processed by smoothing (0.3 smoothing factor, 10 iterations). This resulted in a single 3D model in which the early arrival regions were visible within the larger placental model (Fig. 4). This file was exported as a merged STL file and printing using a polyjet Connex 500 3D printer (Stratasys, Eden Prairie, MN) (Fig. 5) in VeroBlack (Stratasys) (early blood arrival) and VeroClear (Stratasys) (fully perfused placenta).

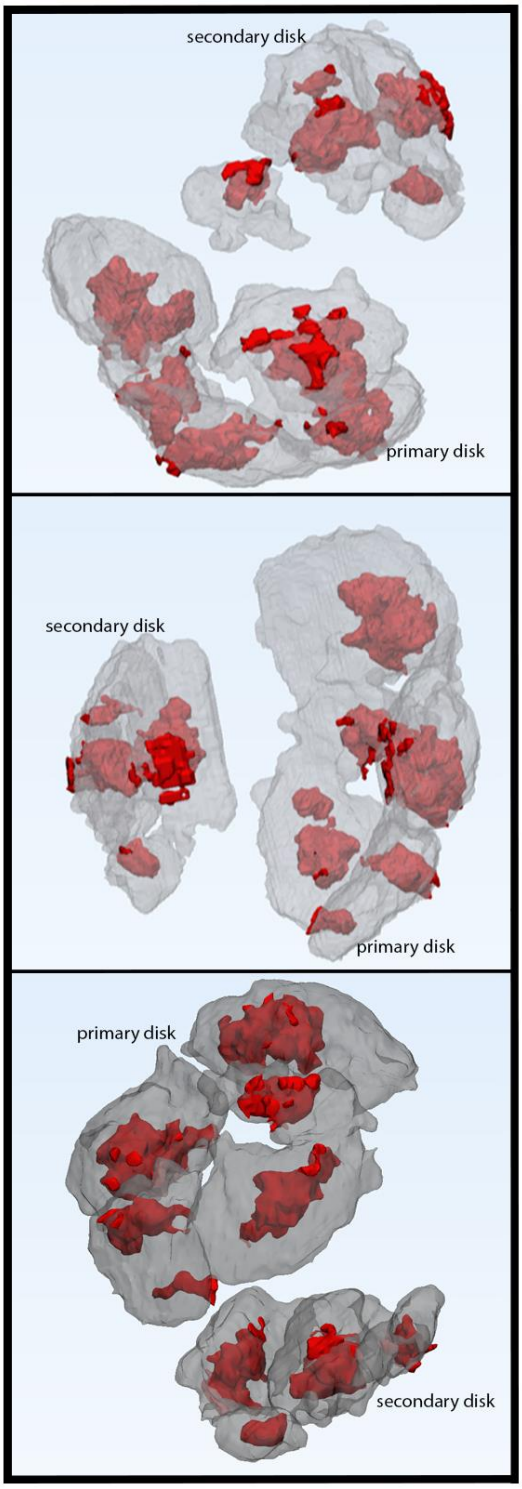

Figure 4. Virtual Multi-color 3D placenta models. Multi-color 3D placenta models based on the MRI data in figure 2. Primary and secondary placental disks are labeled. Early ferumoxytol-infused blood arrival is shown in red and later blood arrival is translucent grey.

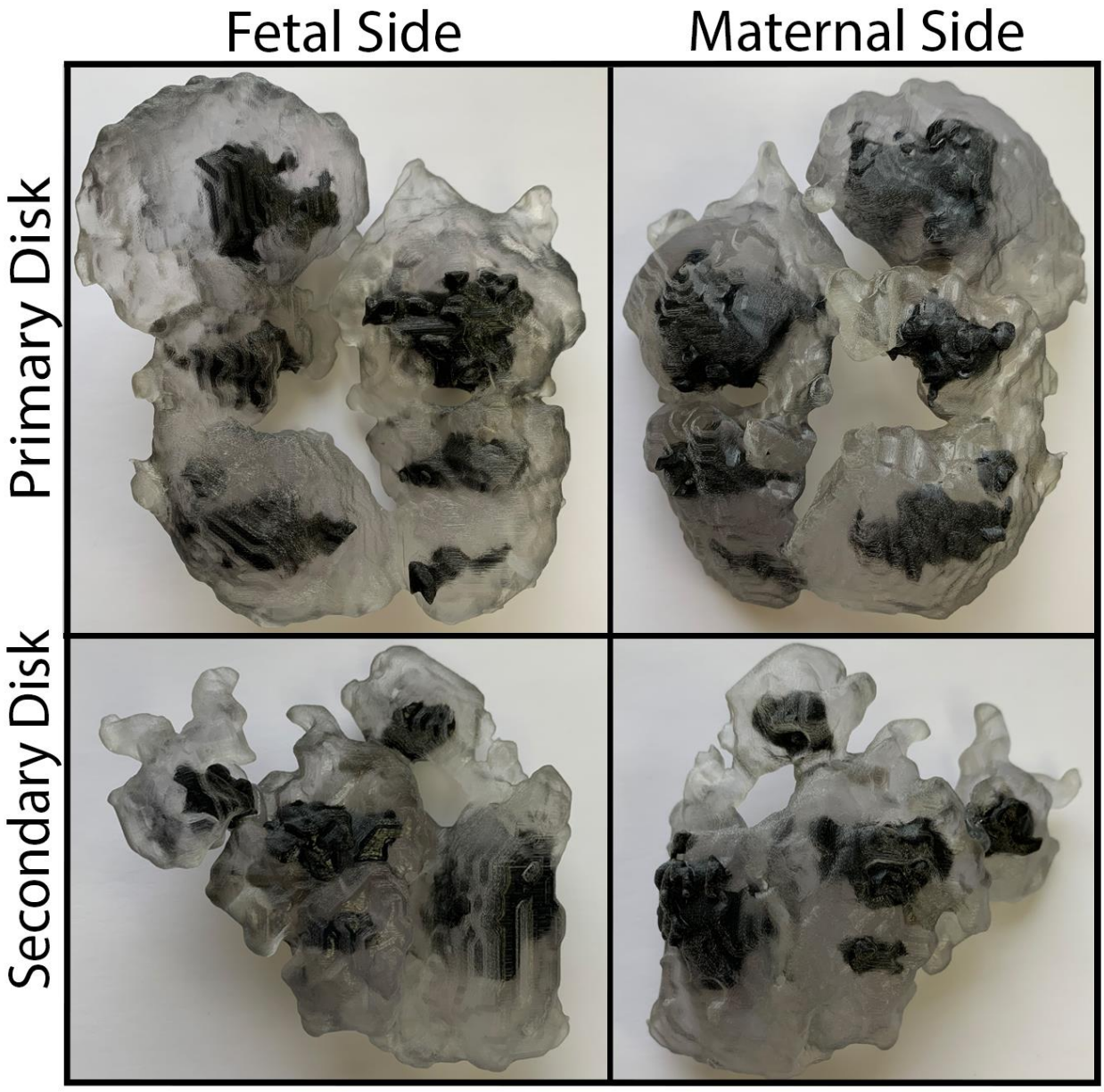

Figure 5. Multi-color 3D-printed placenta models using VeroBlack and VeroClear. Multi-color 3D-printed placenta models based on the models in Figure 4. The left column displays the fetal (chorionic plate) side of the primary disk (top) and secondary disk (bottom). The right column displays the maternal (placental attachment) side of the respective disks. Black denotes region of earlier arrival time within the full translucent model.

Placental Collection at Caesarian Section

At gestational day 155 (term=~165), the macaque was sedated by injection of up to 10 mg/kg ketamine, intubated, and anesthesia was maintained by inhalation of oxygen and 1.5% isoflurane. The fetoplacental unit was collected via hysterotomy in an aseptic environment and the dam was recovered. Following delivery of the fetus, the placenta was collected for processing.

Placental Biopsy Method

The placenta was photographed (chorionic plate and basal plate) using an Apple iPad (version 9.3.5, model MC954LL/A), then laid next to the single-color 3D printed model, fetal-side up, in the same orientation (Fig. 6). The photograph of the placenta on the iPad was annotated electronically with the free app You Doodle to identify the cotyledons, which were labeled Primary A-G and Secondary A-E. A scalpel was used to dissect apart the cotyledons and each were placed in separate petri dishes to match the photograph. Full-thickness sections (from chorionic plate to decidua) of each cotyledon were collected using single-use straight-razors and laid in a labelled cassette so that later sectioning of this tissue for histopathological assessment would show chorionic plate, placenta, and decidua (e.g., Fig. 7).

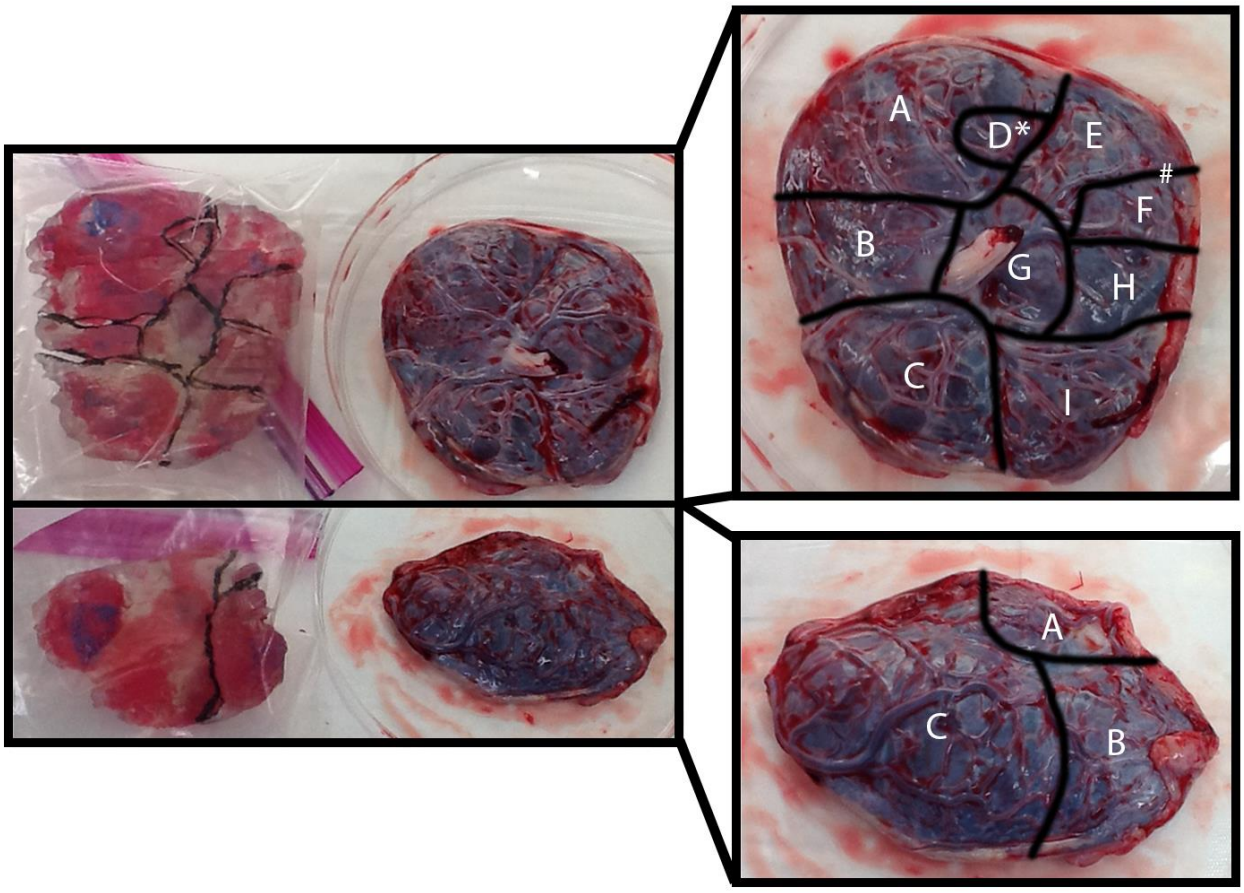

Figure 6. Matched single-color 3D model to tissue at dissection. The top left image shows the final single-color 3D printed model of the primary placental disk (right) oriented to the placental tissue (left). The bottom left image shows the same, for the secondary placental disk. The right images show the dissection plan for each respective placental disk, based on the 3D printed model. Black lines show delineation between cotyledons. White letters establish a location map for each tissue piece collected for analysis. The white asterisk (*) denotes a small cotyledon that was not identifiable by gross examination of the tissue alone and would have not been dissected had it not been identified by MRI. The white number symbol (#) denotes a delineation between two cotyledons that was unclear at gross examination and made clearer through MRI analysis.

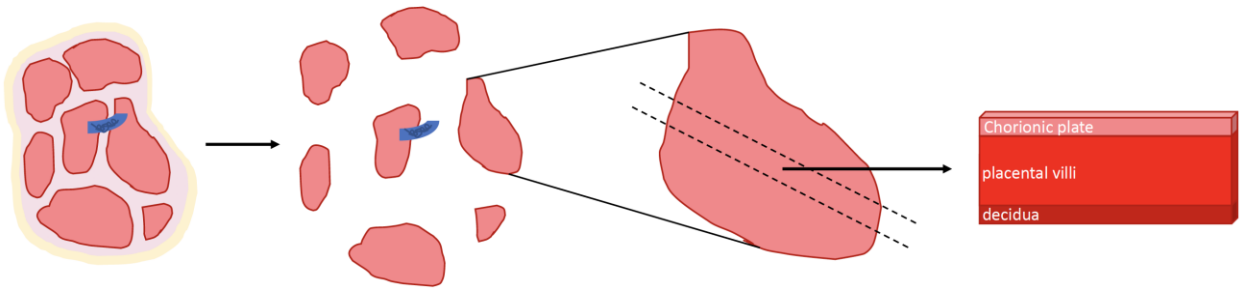

Figure 7. Dissection method diagram. Diagram of the placental dissection method for sampling of all cotyledons. Dissection involves separating the cotyledons and collecting a full-thickness section through each. The diagram represents the fetal side of the placenta, with each cotyledon outlined in red and the umbilical cord represented in blue.

RESULTS AND DISCUSSION

Bringing the 3D printed model to the placental dissection was an effective and efficient method for matching the placental tissue to its functional information identified by MRI. As the MRI was completed only 10 days prior to dissection, the size and shape of the placenta model was faithful to the tissue. Using the overall placental shape and the location of the largest cotyledon, which is easiest to discern in the fresh tissue (small cotyledons may be difficult to discern grossly), the 3D model was quickly oriented to match the placental tissue, in less time than it takes to identify each cotyledon in fresh placental tissue without the 3D printed guide.

The location of the umbilical cord on the tissue was matched to a region of undetectable perfusion on the 3D printed model. It is noted that the contrast agent, ferumoxytol, is injected into the maternal blood pool and does not cross into the fetal blood pool [10]. It is possible that the increased density of fetal vessels in this region displaces maternal blood in the organ, forming a gap in the MRI maternal blood flow data. This gap was useful in further confirming correct orientation of the placental tissue to the 3D model, as the umbilical cord was not located

in the exact center of the placenta, though this benefit only exists for the primary disk in macaque research. Furthermore, the 3D model based on computer-identified perfusion domains allowed the identification of a small cotyledon that would have otherwise been missed and clarified delineation between two cotyledons that would have been uncertain without matching to the 3D model (Fig. 6).

This method was developed using a normal, uninfected pregnancy in the rhesus macaque as a proof-of-concept. The placental tissue exhibited no gross pathology at dissection. As described earlier, placental infection is often focal [3-6] and has the potential to affect function, which could be identified by MRI [6,13-15]. It remains unexplored how these differences in MRI data will translate into a dissection aid. With the addition of placental pathology, maternal blood perfusion patterns may deviate, which can translate into a perfusion domain map that does not exactly match the cotyledons on the organ. Further research is needed to determine if the resulting 3D model is still effective in identifying small cotyledons or those with unclear delineation from neighbors. Regardless, regions of normal and abnormal tissue function can be identified by orienting the placenta based on organ shape, to a model derived from MRI data that conveys blood arrival time. The benefit of this dissection method is evident in research but can also be applicable clinically, as an education tool for identifying abnormal pregnancies. Models of healthy and unhealthy placentas could aid students in understanding the impact of particular infections or lesions on the placenta and, thus, the infant. A tactile model could also improve doctor-patient communication in explaining abnormalities in the pregnancy to the patient, aiding understanding so that the patient is fully informed of their condition and possible interventions, similarly to the use of such models in congenital heart disease [16]. The value of 3D modeled imaging data is evident in medicine, providing clarity in research and clinical environments.

ACKNOLEDGEMENTS

We thank Midwest Prototyping for 3D printing support, AMAG Pharmaceuticals for providing the ferumoxytol used, and Lindsey Block for thoughtful editing of the manuscript. This work was supported by the National Institutes of Health Grants U01-HD087216 (to OW and DMS), Endocrinology-Reproductive Physiology Training Grant T32 HD041921 (to SMN), and P51 OD011106 (to the WNPRC). We also are grateful to the WNPRC Veterinary, Scientific Protocol Implementation, and Animal Services staff for assistance with animal procedures, including breeding, ultrasound monitoring, surgery and sample collection. The content is solely the responsibility of the authors and does not represent the official views of the NIH.

REFERENCES

1. de Rijk, E.P.C.T and E. Van Esch. 2008. The Macaque Placenta—A Mini-Review, p. 108S-118S. SAGE Journals, Toxicologic Pathology.
2. Joffe, T.H., A.F. Tarantal, K. Rice, M. Leland, A.K. Oerke, C. Rodeck, M. Geary, P. Hindmarsh, et al. 2005. Fetal and infant head circumference sexual dimorphism in primates. Am J Phys Anthropol *126*:97-110.
3. Vázquez-Boland, J.A., E. Krypotou, and M. Scortti. 2017. Placental Infection. mBio *8*.
4. Tabata, T., M. Petitt, J. Fang-Hoover, M. Zydek, and L. Pereira. 2016. Persistent Cytomegalovirus Infection in Amniotic Membranes of the Human Placenta. Am J Pathol *186*:2970-2986.
5. McDonagh, S., E. Maidji, W. Ma, H.T. Chang, S. Fisher, and L. Pereira. 2004. Viral and bacterial pathogens at the maternal-fetal interface. J Infect Dis *190*:826-834.
6. Hirsch, A.J., V.H.J. Roberts, P.L. Grigsby, N. Haese, M.C. Schabel, X. Wang, J.O. Lo, Z.

Liu, et al. 2018. Zika virus infection in pregnant rhesus macaques causes placental dysfunction and immunopathology. Nat Commun *9*:263.

7. Van Wagenen and H.R. Catchpole. 1965. GROWTH OF THE FETUS AND PLACENTA OF THE MONKEY (MACACA MULATTA). Am J Phys Anthropol *23*:22-33.
8. Vasanawala, S.S., K.L. Nguyen, M.D. Hope, M.D. Bridges, T.A. Hope, S.B. Reeder, and M.R. Bashir. 2016. Safety and technique of ferumoxytol administration for MRI. Magn Reson Med *75*:2107-2111.
9. Ludwig, K.D., S.B. Fain, S.M. Nguyen, T.G. Golos, S.B. Reeder, I.M. Bird, D.M. Shah, O.E. Wieben, and K.M. Johnson. 2019. Perfusion of the placenta assessed using arterial spin labeling and ferumoxytol dynamic contrast enhanced magnetic resonance imaging in the rhesus macaque. Magn Reson Med *81*:1964-1978.
10. Nguyen, S.M., G.J. Wiepz, M. Schotzko, H.A. Simmons, A. Mejia, K.D. Ludwig, A. Zhu, K. Brunner, et al. 2019. Impact of Ferumoxytol Magnetic Resonance Imaging on the Rhesus Macaque Maternal-Fetal Interface. Biol Reprod.
11. Zhu, A., S.B. Reeder, K.M. Johnson, S.M. Nguyen, T.G. Golos, A. Shimakawa, M.R. Muehler, C.J. Francois, et al. 2020. Evaluation of a motion-robust 2D chemical shift-encoded technique for R2* and field map quantification in ferumoxytol-enhanced MRI of the placenta in pregnant rhesus macaques. J Magn Reson Imaging *51*:580-592.
12. Frias, A.E., M.C. Schabel, V.H. Roberts, A. Tudorica, P.L. Grigsby, K.Y. Oh, and C.D. Kroenke. 2015. Using dynamic contrast-enhanced MRI to quantitatively characterize maternal vascular organization in the primate placenta. Magn Reson Med *73*:1570-1578.
13. Roberts, V.H., J.E. Gaffney, K.S. Lewandowski, M.C. Schabel, T.K. Morgan, and A.E.

Frias. 2019. A standardized method for collection of human placenta samples in the age of functional magnetic resonance imaging. Biotechniques *67*:45-49.

14. Lo, J.O., V.H.J. Roberts, M.C. Schabel, X. Wang, T.K. Morgan, Z. Liu, C. Studholme, C.D. Kroenke, and A.E. Frias. 2018. Novel Detection of Placental Insufficiency by Magnetic Resonance Imaging in the Nonhuman Primate. Reprod Sci *25*:64-73.
15. Schabel, M.C., V.H.J. Roberts, J.O. Lo, S. Platt, K.A. Grant, A.E. Frias, and C.D. Kroenke. 2016. Functional imaging of the nonhuman primate Placenta with endogenous blood oxygen level-dependent contrast. Magn Reson Med *76*:1551-1562.
16. Sun, Z., I. Lau, Y.H. Wong, and C.H. Yeong. 2019. Personalized Three-Dimensional Printed Models in Congenital Heart Disease. J Clin Med *8*.

Chapter 5:

Association of Quantitative Ferumoxytol Dynamic Contrast Enhanced Magnetic Resonance Imaging with Placental Pathology in the Rhesus Macaque Placenta

Sydney Nguyen, Daniel Seiter, Terry Morgan, Lu Mao, Michelle Schotzko, Megan Murphy, Kai Ludwig, Ruiming Chen, Archana Dhyani, Ante Zhu, Kevin Brunner, Dinesh Shah, Kevin Johnson, Thaddeus Golos, Oliver Wieben.

ABSTRACT

Ferumoxytol, a super-paramagnetic iron oxide nanoparticle (SPION) used in the treatment of anemia in adults with renal insufficiency, has recently seen success as an off-label dynamic contrast enhanced (DCE) magnetic resonance imaging (MRI) contrast agent and is considered safe by obstetricians to treat iron deficiency anemia in pregnant women. Utilizing ferumoxytol, DCE MRI can be used during pregnancy to quantify maternal blood flow and volume in placental cotyledons to assess placental health. In this study, 14 pregnant rhesus macaques, 11 of which received subcutaneous or intra-amniotic Zika virus (ZIKV) inoculation around gd (gestational day) 45-55 underwent DCE MRI with ferumoxytol up to three times: ~gd65, gd100, and gd145 (gd165=term). The purpose of this work was to explore the relationship between placental pathology and MRI derived functional information for the non-invasive identification of placental pathology, while also describing potential limitations of MRI in this identification. Virtual models of cotyledon flow at gd145 were

matched to term placental tissue and cotyledon-specific histopathological assessments were made to relate tissue pathology to flow and volume values. Analysis of these data suggests that while MRI was not able to detect significant change in flow in pathological versus non-pathological individual cotyledons with a single placenta, placentas with higher levels of overall pathology and placentas with a higher number of infarctions had lower average cotyledon volume and flow than was seen in less-pathological placentas. Further assessment of MRI-derived placental functional data through gestation suggested that average cotyledon volume was lower through gestation in more pathological placentas, but the trend in flow and volume change over gestation was not different than that of non-pathological placentas. Research utilizing other infection models would be useful in further investigation of the value if MRI in the assessment of placental health.

INTRODUCTION

Appropriate placental development is crucial for a healthy pregnancy. If the placenta cannot provide sufficient oxygen or nutrients to the developing fetus, the pregnancy may result in fetal growth restriction, preterm birth, or miscarriage [1-4]. One cause of placental insufficiency is low flow of maternal blood to the placental chorionic villi [5]. Disease or placental insult during pregnancy can result in maldevelopment of these crucial sites of oxygen and nutrient transfer, preventing exchange [5,6]. The effects of disease and maldevelopment are manifested as placental pathology, which can be studied in the tissue following delivery. An area of great basic and clinical research interest is whether placental pathology can be detected using imaging during gestation. Identification of placental

pathology and dysfunction early in pregnancy could be a valuable tool for assessing maternal and fetal risk.

Ultrasound is commonly used to evaluate pregnancy health, but does not provide adequate resolution for the identification of most placental pathology. [7-10] Placental pathology is often focal rather than homogeneous throughout the tissue [11-14], further hampering identification of pathology through the narrow 2D ultrasound view. Recent work indicates that dynamic contrast enhanced (DCE) magnetic resonance imaging (MRI) is a powerful tool for interrogating placenta health [15]. DCE MRI uses an injected contrast agent to obtain functional images with high resolution. As contrast agent enters the region of interest, perfusion can be imaged and quantified. Determining relative perfusion can offer insight into the regional physiological environment. For example, DCE MRI can be used to characterize the severity of certain cancers by capturing irregularities in local blood supply: the ability to quantify functional information has made DCE MRI the gold standard for assessing cancer and other pathologies in the breast, brain, and spine. [16-18] Traditionally, gadolinium-based (Gd) contrast agents have been used for DCE MRI, and success has been seen in previous placenta studies [19-21]. However, it has been shown that gadolinium crosses the placenta into the fetus [22], and there is uncertainty about the long-term consequences of Gd exposure in utero [23-26].

The current study has used ferumoxytol, an alternative contrast agent. Ferumoxytol is a super-paramagnetic iron oxide nanoparticle (SPION) used in the treatment of anemia in adults with renal insufficiency [27]. Ferumoxytol has recently seen success as an off-label DCE MRI contrast agent [28,29]. It is also considered safe by obstetricians to treat iron deficiency anemia in pregnant women [30]. Previous studies have shown the feasibility of

ferumoxytol imaging in the rhesus macaque model [31-34], and illustrate its ability to quantify perfusion of placental functional groups, called cotyledons [35]. We hypothesize that functional information from ferumoxytol DCE MRI scans can be analyzed and correlated with observed histopathology in individual cotyledons.

The rhesus macaque placenta has many structural and functional similarities to that of humans, including a villous structure segmented into functional units called cotyledons. Cotyledons are where maternal blood enters the intervillous space and bathes the fetal villi, allowing oxygen, nutrient, and waste exchange [36,37]. Macaque gestation is approximately 165 days [38] while human gestation averages 280 days, however placental function and fetal development through gestation is well-aligned. These similarities make the rhesus macaque pregnancy model an excellent option for study of potential applications in human healthcare.

This report explores the relationship between placental pathology at term and placental and cotyledon perfusion determined by MRI. Pathology was assessed in individual cotyledons of 14 rhesus macaque placentas and matched to flow and volume measures as assessed by DCE MRI in early, mid, and late gestation. Review of this information was extended from individual cotyledons to assessment across entire placentas, and across gestation, with the goal of identifying ways in which MRI might be utilized as a non-invasive predictor of placental pathology. We hypothesized that cotyledons containing pathology will have altered perfusion compared to non-pathological cotyledons, which can be detected by DCE MRI with ferumoxytol through blood flow and volume values. As a model of infection to induce pathology in a subset of these animals, we utilized ZIKV: Puerto Rican strain virus/H.sapiens-tc/PUR/2015/PRVABC59_v3c2. This isolate has been shown to cause a

variety of severe placental pathologies [39-41] appropriate for studying the effects of pathology on placental cotyledon volume and maternal blood flow.

METHODS

Care and Use of Macaques

Wisconsin National Primate Research Center (WNPRC) female rhesus macaques were housed with compatible males and monitored for breeding and menses, to identify pregnancy. Date of conception was determined (+/- 2 days) based on observation of copulation, menstrual cycle, and ultrasound measurements of fetus and gestational sac. Macaques were cared for by WNPRC staff as outlined in the Animal Welfare Act and the Guide for the Care and Use of Laboratory Animals. This study was approved by the University of Wisconsin-Madison College of Letters and Sciences and Vice Chancellor Office for Research and Graduate Education Institutional Animal Care and Use Committee. 14 pregnant macaques were utilized in this study.

ZIKV Infection Models

Animals were part of three different animal study protocols, all of which included our imaging procedure. Animals on all protocols received Puerto Rican Zika (PV ZIKV) virus/H.sapiens-tc/PUR/2015/PRVABC59_v3c2, but differed in injection method. A total of 14 animals were imaged for this study. 1 animal received 10^4 PV ZIKV by subcutaneous injection at ~gd45. 6 animals received 1x10^4 PV ZIKV (n=2), 1x10^6 PV ZIKV (n=1), or a saline injection (n=3) into the amniotic sac at ~gd55. 7 animals received 10^4 PV ZIKV by subcutaneous injection at ~gd45, followed by intravenous infusions over 2-3 minutes of

50mg/kg ZIKV-specific human immunoglobulin (n=4) or nonspecific human immunoglobulin (n=3) at 1 and 5 days post-infection. Fetuses from these pregnancies were studied as stated on the study protocol to which they were assigned; those findings will not be reported here.

Magnetic Resonance Imaging

All animals were imaged up to three times, at ~gd65, ~gd100, and ~gd145 (term=165gd), with 10 of the 14 receiving all three scans, and 13 of the 14 receiving the gd145 scan which enabled the matching of MRI data to placental tissue pathology (Table 1). Subjects were food deprived 4-20 hours prior to sedation for the imaging procedures. Sedation was completed by injection of up to 10 mg/kg ketamine, followed by intubation and maintenance anesthesia by inhalation of a mixture of oxygen and 1.5% isoflurane. A pulse oximeter probe was used to monitor blood oxygen. Imaging was conducted in the right-lateral recumbent position and a respiratory bellows was used to compensate for respiratory motion. An intravenous catheter was used for delivery of ferumoxytol (AMAG Pharmaceuticals) during imaging.

	Received gd65 MRI	Received gd100 MRI	Received gd145 MRI	Inclusion for Assessment: Cotyledon Flow/Volume in the Presence or Absence of Cotyledon-Specific Pathology (Fig 4, 5)	Inclusion for Assessment: Perfusion Domain Flow/Volume in Pathological and Non-Pathological Placentas, by Specific Pathology (Fig 6, 7)	Inclusion for Assessment: Perfusion Domain Flow and Volume in Pathological and Non-Pathological Placentas in Early, Mid, and Late Pregnancy (Fig 8, 9)	Inclusion for Assessment: Trajectory of Perfusion Domain Flow/Volume in Pathological and Non-Pathological Placentas (Fig 10, 11)
Animal 1	✓	✓	✓	✓	✓	✓	✓
Animal 2	✓	✓	✓	✓	✓	✓	✓
Animal 3	✗	✗	✓	✓	✓	✗	✗
Animal 4	✓	✓	✓	✓	✓	✓	✓
Animal 5	✓	✓	✓	✓	✓	✓	✓
Animal 6	✓	✓	✓	✓	✓	✓	✓
Animal 7	✗	✗	✓	✓	✓	✗	✗
Animal 8	✓	✓	✓	✓	✓	✓	✓
Animal 9	✓	✓	✓	✓	✓	✓	✓
Animal 10	✗	✓	✓	✓	✓	✗	✗
Animal 11	✓	✓	✓	✓	✓	✓	✓
Animal 12	✓	✓	✓	✓	✓	✓	✓
Animal 13	✓	✓	✓	✓	✓	✓	✓
Animal 14	✓	✓	✗	✗	✓	✗	✗

Table 1. List of MRI Scans and Analysis Per Animal. Listing of MRI scans completed for all animals, as well as a visual representation of which animal data was used for each analysis, depending on the scans received.

MR images were acquired on a clinical 3.0T MRI system (Discovery MR750, GE Healthcare, Waukesha, WI) using a 32-channel torso coil (Neocoil, Pewaukee, WI). 4D DCE data sets were acquired during ferumoxytol infusion using a dynamic, respiratory-gated T_1 weighted spoiled gradient echo product sequence (DISCO, TR=4.8ms, TE=1.82ms, 2.4ms, spatial res.=0.86×0.86×1.00 mm^3, temporal resolution=5.48s, tip=12^o). [33,35]. The

ferumoxytol was diluted 5:1 with saline and administered at 4 mg/kg body weight over a 20 second interval using a power injector, followed by a 20 ml saline flush at the same rate.

Calculation of Perfusion Domain Maps from MRI Data

The placenta was segmented using DCE images averaged over time in order to visualize the full extent of contrast enhancement in the tissue (Figure 1A). Segmentation was performed in Mimics (Materialise NV, Leuven, Belgium). The DCE data was processed using a watershed algorithm similar to Frias [19] and Ludwig [35]. Contrast arrival time for each pixel was calculated by thresholding the pixel's signal intensity using a multiple of the standard deviation of initial time points considered to be background noise without enhancement. Intersection of threshold and average enhancement curve at approximately 50% enhancement reliably produced the best results by rejecting noisy non-placenta pixels but accepting inflow areas with proper sigmoid enhancement (Figure 1B). The resulting arrival time map is shown in Figure 1D. Finally, a watershed algorithm was applied in order to automatically segment perfusion domains (Figure 1D). The total number of perfusion domains, reflective of individual tissue cotyledons, perfusion domain sizes (mL), and perfusion domain blood flow (mL/min) were calculated for each placenta. Segmented perfusion domains with a volume <0.5 cm^3 were discarded after comparing calculated results with dissected placentas.

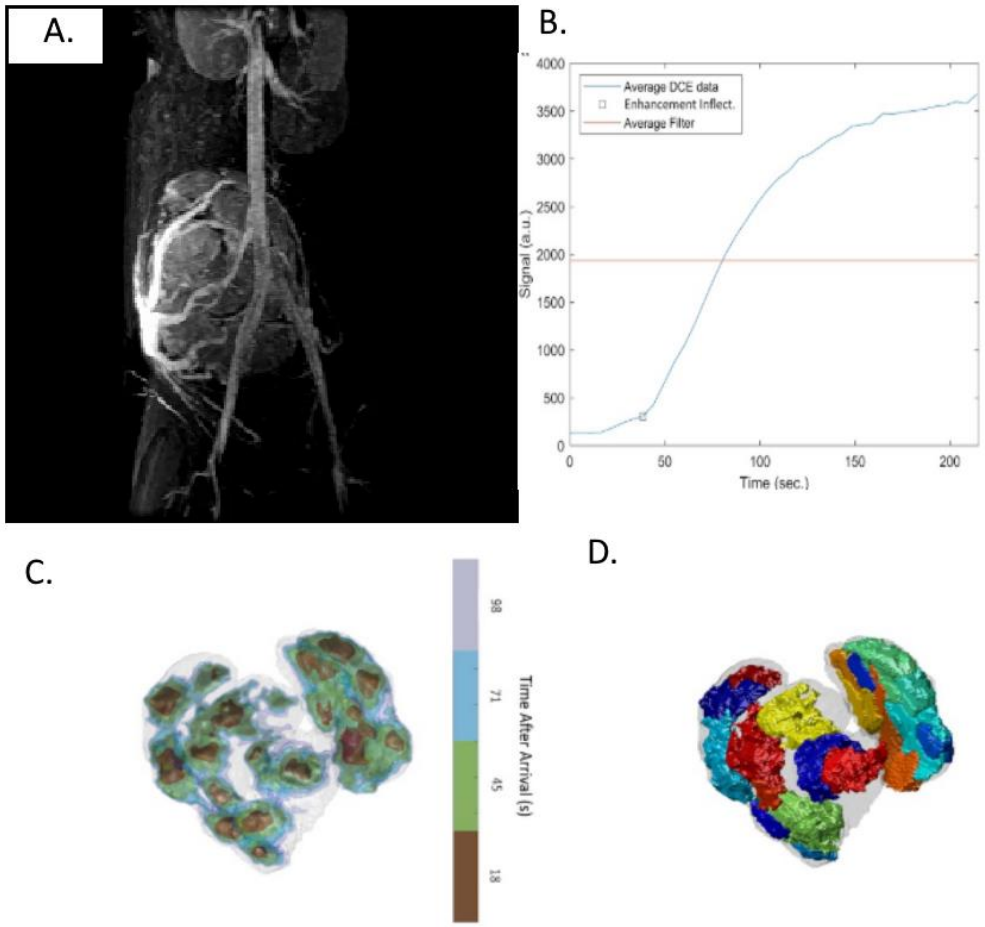

Figure 1. Image Processing Workflow. (A) An example DCE MRI image of the uteroplacental region of a pregnant rhesus macaque, shown as a maximum intensity projection (MIP) at full perfusion (B). Enhancement by ferumoxytol signal begins at the inflection point, indicated by a square on the curve. Time frames before the inflection time are designated background, and the standard deviation of the average background signal is calculated. This threshold ($22 \times \sigma_{bkgd}$) is optimal for formation of the arrival time map (C), plotted with isovalues at 18, 45, 71, and 98 seconds (after inflection) to visualize the inflow and spreading of blood into the placenta. The perfusion domain map (D) shows the resulting segmentation of functional groups based on MRI signal, with a perfusion domain lower volume threshold of 0.5 cm^3.

Infant Delivery and Placental Dissection

The macaques were sedated by injection of up to 10 mg/kg ketamine at gestational day 155 (term=~165). The animals were intubated, and anesthesia was maintained by inhalation of oxygen and 1.5% isoflurane. The fetoplacental unit of each animal was collected via hysterotomy in an aseptic environment, and the placenta was collected for tissue sampling. The dams were recovered.

The placenta was photographed, then dissected. Using an Apple iPad (version 9.3.5, model MC954LL/A) with the free app You Doodle, the photograph of the placenta was annotated electronically to identify and differentiate the placental cotyledons, as determined visually on the organ. The cotyledons were then dissected apart from one another and full-thickness sections (from chorionic plate to decidua) of each were collected with single-use straight-razors. These sections were laid in tissue cassettes labeled to match the tissue biopsy to its location on the annotated photograph. Cassettes with tissue were fixed in 4% PFA for 24 hours before being placed in 70% EtOH until tissue embedding in paraffin blocks. The paraffin embedded tissues were sectioned at 5μm by microtome, then stained with H&E.

Histopathological Analysis and Scoring of Term Tissue

Placental tissue was assessed by a histopathologist (TKM) blinded to treatment and imaging data. H&E-stained cotyledon sections from all placentas in this study were evaluated for presence of chorionic histiocytic intervillositis (CHIV), placental infarctions (PI), and maternal decidual vasculitis (MDV) according to published criteria [42] (example images of pathology in Figure 2). The presence or absence of CHIV, PI, MDV, CHIV and PI, CHIV and MDV, and PI and MDV in each cotyledon was recorded for the purpose of creating

pathological rankings between the assessed placentas (Supplemental Table 1). Only one cotyledon showed evidence of CHIV and PI and MDV, so this combination was not included in assessment. Rather than comparing MRI data to pathology type, results were binned by an average total pathology score. The score was calculated by adding the total number of pathologies in all of the placental cotyledons and dividing by the number of cotyledons (Supplemental Table 1). This number, while not a standard pathological rating, provided a ranking of the relative degree of pathology between the placentas being studied here. For comparisons shown here, placentas with an average total pathology score above 0.5 were determined to be pathological, and placentas with a score of less than 0.5 were determined to be non-pathological. Three cotyledons from one animal (Animal 5 on Supplemental Table 1) were lost during processing -- data on this tissue is not reported.

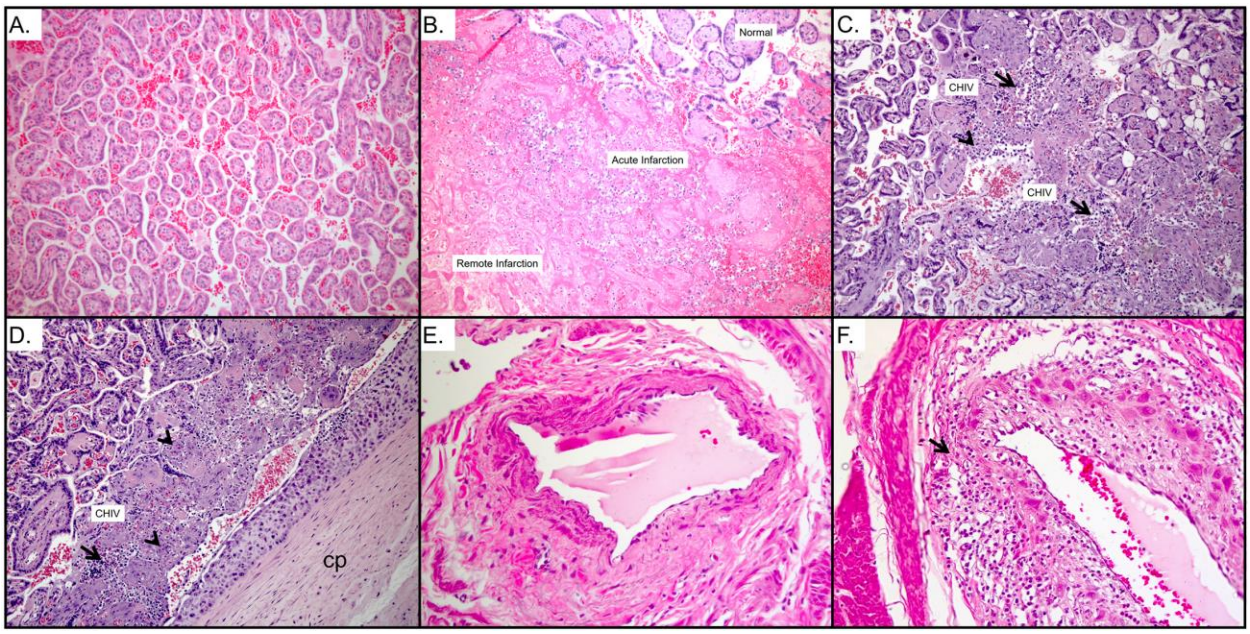

Figure 2. Chronic Histiocytic Intervillositis (CHIV), Infarctions, and Leukocytoclastic Vasculitis at the Uteroplacental Interface. A) Normal chorionic villi near term compared

with cases infected with ZIKV that had more areas of remote infarction (B) and patchy areas of CHIV involving floating villi (C) and beneath the sub-chorionic plate (D) that is unusual for TORCH infections. Compared with normal maternal arteries (E), ZIKV infected cases occasionally had leukocytoclastic vasculitis (F) composed of a mixture of lymphocytes, neutrophils, plasma cells, and a few eosinophils.

Matching Term Tissue and MRI Data

The annotated photos of the placentas were compared to the MRI perfusion domain map developed for the same placenta at the GD145 scan. A single animal that did not receive the gd145 scan was not included in this assessment. Cotyledons, as dissected, were matched to perfusion domains guided by overall shape of the organ and location of particularly large and small functional groups (Figure 3). When perfusion domains correlated to multiple cotyledons, total perfusion and volume was distributed between the cotyledons based on their approximate dissected area relative to one another. When multiple perfusion domains were correlated to one cotyledon, total perfusion and volume values of the perfusion domains were pooled. Once all perfusion domain data was matched to cotyledons, volume and flow data were associated with the appropriate cotyledon pathological scoring as assessed by the pathologist (Supplemental Table 1).

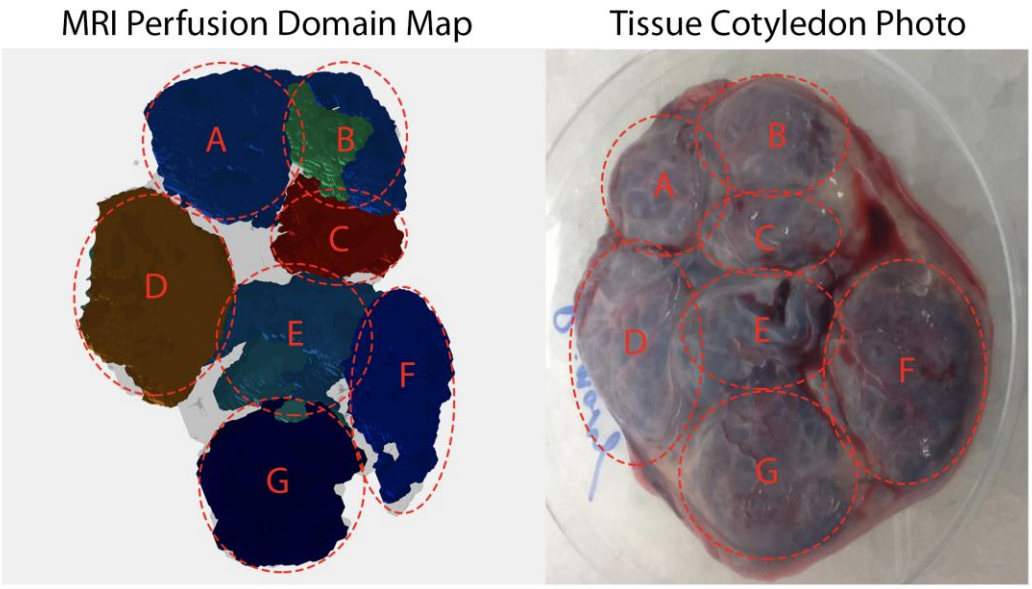

Figure 3. Example of a Perfusion Domain Map Matched to Placental Tissue. The perfusion domain map at gd145 (left) and the photo of the term placenta (right) of a particular animal, are presented in the same orientation. Perfusion domains in the left image are circled in red and labeled with red letters, to match the cotyledons circled and labeled in red in the right image.

Measurement of Volume and Flow Across Gestation

Perfusion domain flow and volume measurements were collated from the gd65, gd100, and gd145 MRI scans for each animal. These measurements were averaged for each animal, at each timepoint (Supplemental Table 2). These resulting averages served as representative measurements of placental function and structure, and were used to compare flow and volume in animals relative to level of pathology, based on the average total pathology score seen in the placenta at term. The regression of average perfusion domain flow and volume

through gestation per animal was also calculated to compare trends in placental function over time between animals with pathological placentas at term (Supplemental Table 3).

Statistical Analysis: Term Individual Cotyledon Flow and Volume by Individual Pathologies

Placental cotyledon pathology data was matched to MRI perfusion domain volume and flow data. Only animals that received the gd145 MRI scan were included in this analysis (n=13). For each animal, the flow and volume values for cotyledons with a particular pathology were compared to cotyledons in the same animal without that particular pathology. Comparison between the pathological and non-pathological cotyledons was completed by two-way ANOVA, adjusted for each animal. This process was repeated for each pathology and combination of pathologies measured. Comparisons were restricted to animals that had both pathological and non-pathological cotyledons.

Statistical Analysis: Term Average Cotyledon Flow and Volume by Total Relative Pathology and Individual Pathologies

Average flow and volume values per placenta were calculated for each animal. Only animals that received the gd145 MRI scan were included in this analysis (n=13). Based on the overall average pathology score, animals were binned into two groups. A term total average pathology score of >0.5 denoted pathological placentas (n=5) and a total average pathology score of <0.5 denoted non-pathological placentas (n=9). Average flow and volume values for pathological placentas were compared by the Wilcoxon rank sum test. Additionally, these averaged flow and volume values were applied to individual pathologies

to compare values of animals with and without the presence of specific pathologies or combinations of specific pathologies, also by Wilcoxon rank sum test. The cutoff for pathological placentas in the analysis of individual pathology features was based on the median individual pathology score value (CHIV >0.067, PI >0.2, MDV >0, CHIV and PI >0.062, CHIV and MDV >0, PI and MDV >0). Median was used for application of the Wilcoxon rank sum test, as the data was not normally distributed.

Statistical Analysis: 65gd, 100gd, 145gd Average Perfusion Domain Flow and Volume by Total Relative Pathology and PI

Average perfusion domain flow and volume at gd65, gd100, and gd145 was calculated for each animal in this study (n=14). Some animals did not receive all three scans, so that missing data was not included in analysis. Comparisons were made binning animals by total pathology score and by PI, as these pathology measures showed evidence of significance in previous assessments. The average flow and volume values for animals with a term total pathology score of >0.5 (pathological, n=5) were compared to flow and volume values for animals with a total average pathology score of <0.5 (non-pathological, n=9), at each time point individually, by Wilcoxon rank sum test. PI pathological assignment was binned at <0.2, based on the median value, and assessment was completed by Wilcoxon rank sum test.

Statistical Analysis: Trends Over Gestation in Average Perfusion Domain Flow and Volume

Gd65, gd100, and gd145 average perfusion domain flow and volume were plotted individually for each animal. Only animals which underwent all three scan dates were

included in this analysis (n=10). Linear regression was completed to determine the slopes of the flow and volume over time. Slopes for animals with a term total average pathology score of >0.5 (pathological, n=4) were compared to slopes for animals with a total average pathology score of <0.5 (non-pathological, n=6) by Wilcoxon rank sum test.

RESULTS

Term Individual Cotyledon Flow and Volume by Individual Pathologies

To determine if the presence at term of particular placental pathologies is associated with altered flow or volume measured by MRI, animals underwent imaging at gd145 and careful matching of flow and volume MRI data to placental tissue at term. Following individual paired analysis of cotyledon flow values to cotyledon tissue pathology, p-values were found to be insignificant for all comparisons (CHIV p=0.724, PI p=0.494, MDV p=0.823, CHIV and PI p=0.799, PI and MDV p=0.755) (Figure 4). Paired analysis of cotyledon volume data to cotyledon tissue pathology also yielded non-significant p-values (CHIV p=0.141, PI p=0.33, MDV p=0.568, CHIV and PI p=0.553, PI and MDV p=0.373) (Figure 5). The comparison of CHIV and MDV contained only one animal with one pathological cotyledon, and therefore analysis could not be completed for flow or volume. The absence of significant differences in analysis of specific pathology in cotyledons suggests that changes in cotyledon-specific blood flow due to the development of tissue pathology may not be sufficient to be reliably identified non-invasively by MRI.

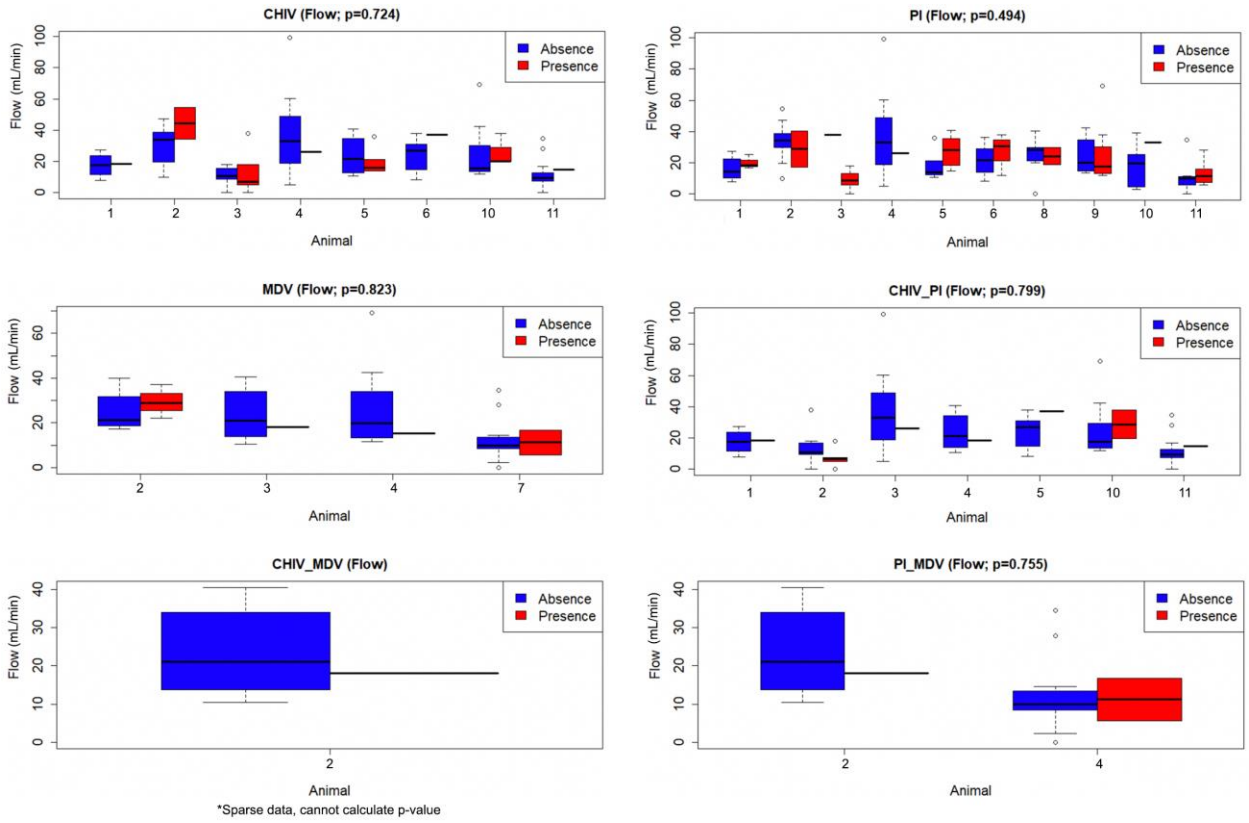

Figure 4. Cotyledon Flow (mL/min) in the Presence or Absence of Cotyledon-Specific Pathology. Cotyledon-specific flow measured in individual cotyledons at gd145, in specific animals numbered 1-11. Flow values are compared in cotyledons that do (red) or do not (blue) have particular pathology: CHIV, PI, MDV, CHIV and PI, CHIV and MDV, and PI and MDV. The associated p-value is an assessment of the relation between flow values in cotyledons with or without a particular pathology, across all animals. Animals without a particular pathology in at least one cotyledon were not included in analysis.

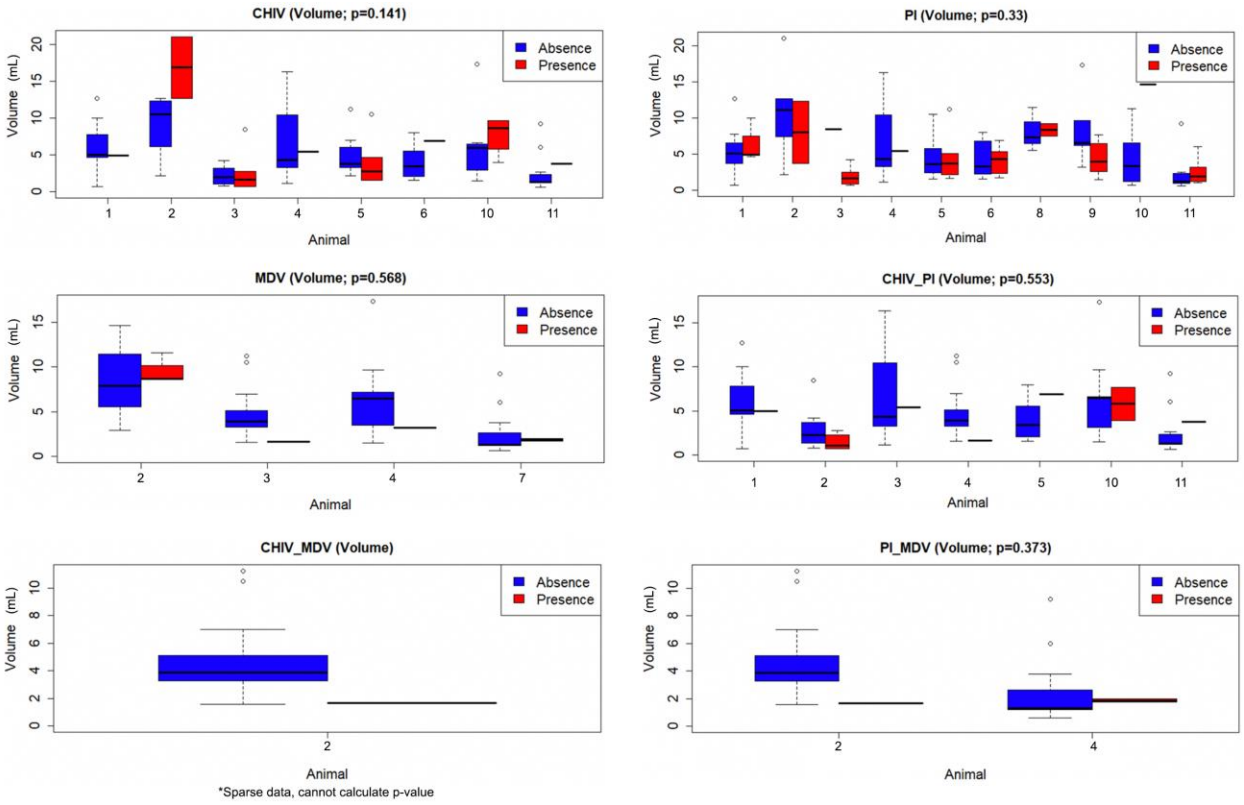

Figure 5. Cotyledon Volume (mL) in the Presence or Absence of Cotyledon-Specific Pathology. Cotyledon-specific volume measured in individual cotyledons at gd145, in specific animals numbered 1-11. Volume values are compared in cotyledons that do (red) or do not (blue) have particular pathology: CHIV, PI, MDV, CHIV and PI, CHIV and MDV, and PI and MDV. The associated p-value is an assessment of the relation between volume values in cotyledons with or without a particular pathology, across all animals. Animals without a particular pathology in at least one cotyledon were not included in analysis.

Term Average Cotyledon Flow and Volume by Total Relative Pathology and Individual Pathologies

Following assessment of specific cotyledons and their relationship with flow and volume in the presence of pathology, the flow and volume values from the gd145 scans were

averaged per placenta and analysis took place to determine if more pathological placentas would have altered flow and volume compared to non-pathological placentas. When average flow values were compared for pathological and non-pathological placentas for particular pathologies (Figure 6), a significant difference was seen when sorted by PI ($p=0.022$) and the comparison approached significance when sorted by total pathology score ($p=0.093$). All other comparisons were non-significant (CVIV $p=0.731$, MDV $p=0.604$, CHIV and PI $p=0.445$, CHIV and MDV $p=0.769$, PI and MDV $p=0.231$). When average volume values were compared by pathology (Figure 7), significant differences were seen in placentas sorted by PI ($p=0.008$) and total pathology score ($p=0.011$). All other comparisons were non-significant (CHIV $p=0.945$, MDV $p=0.825$, CHIV and PI $p=0.138$, CHIV and MDV $p=6.15$, PI and MDV $p=0.154$). These results suggest that the presence of PI, or the general presence of pathology, may alter both overall flow and volume in the placenta in a detectable way, which can be identified by MRI near term.

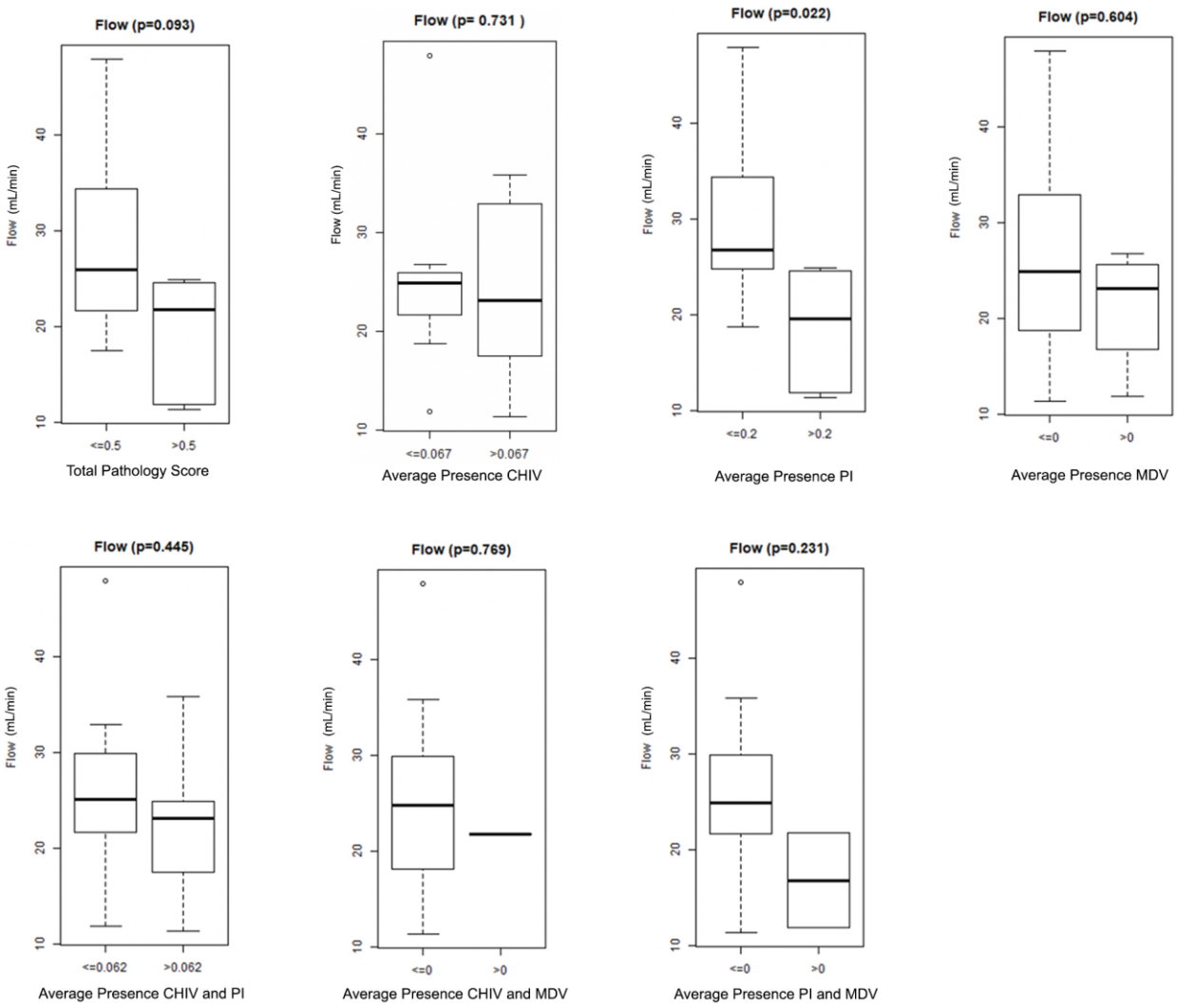

Figure 6. Perfusion Domain Flow (mL/min) in Pathological and Non-Pathological Placentas, by Specific Pathology. Perfusion domain flow values at gd145 were averaged per animal and compared between animals with a particular pathology, versus those without. Analysis was completed for each pathology separately: Total pathology score, CHIV, PI, MDV, CHIV and PI, CHIV and MDV, and PI and MDV. Total pathology score is denoted as pathological when above 0.5. All other pathologies have cutoffs based on median flow value. P-values are specific to the pathology listed.

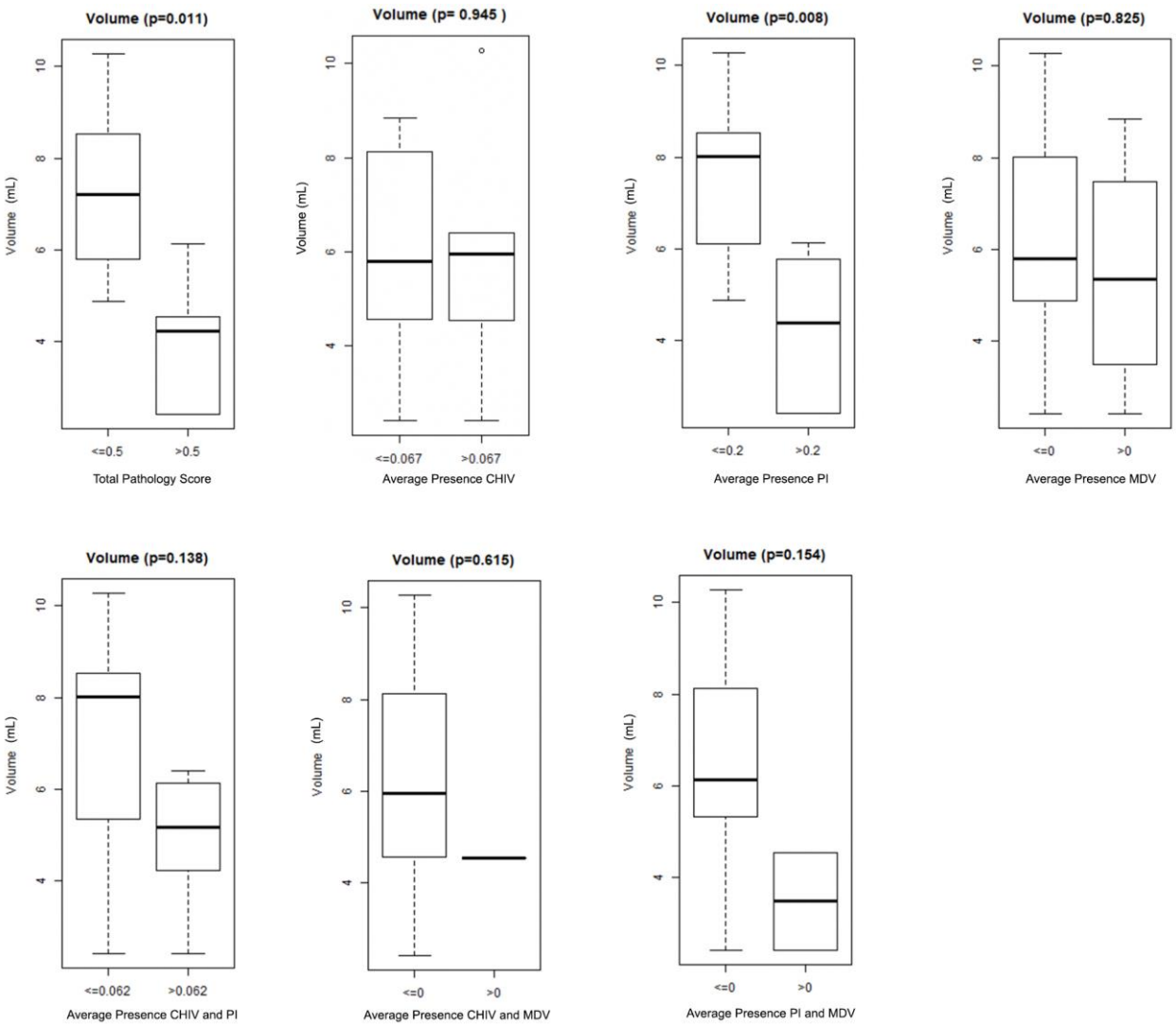

Figure 7. Perfusion Domain Volume (mL) in Pathological and Non-Pathological Placentas, by Specific Pathology. Perfusion domain volume values at gd145 were averaged per animal and compared between animals with a particular pathology, versus those without. Analysis was completed for each pathology separately: Total pathology score, CHIV, PI, MDV, CHIV and PI, CHIV and MDV, and PI and MDV. Total pathology score is denoted as pathological when above 0.5. All other pathologies have cutoffs based on median volume value. P-values are specific to the pathology listed.

gd65, gd100, gd145 Average Perfusion Domain Flow and Volume by Total Relative Pathology and PI

Perfusion domain flow and volume was assessed over gestation at gd65, gd100, and gd145. To determine if animals that have placentas with higher levels of pathology at term had altered intervillous flow through gestation, or if a timepoint of altered flow could be identified, flow and volume values were averaged per placenta at each scan time point and pathological placenta values were compared to those of non-pathological placentas. Total pathology score and PI were individually used to bin placentas for assessment, as these two pathology scores had resulted in significant differences when measuring placental function in averaged term placental function. When pathology was binned by total pathology score (Figure 8), average flow was not seen to be statistically significant at any time point (gd65 p=0.109, gd100 p=0.109, gd145 p=0.354). However, average volume was seen to be significantly different at gd65 (p=0.042) and approached significance at gd100 (p=0.073) and gd145 (p=0.093). When pathology was binned by PI (Figure 9), both flow (p=0.03) and volume (p=0.048) are significantly different at the gd100 scan date, but are non-significant at gd65 and gd145 (gd65 flow p=0.247, gd65 volume p=0.177, gd145 flow p=0.138, gd145 volume p=0.181). Measures of both flow and volume through gestation by MRI may help identify pathological placentas if severe infection had been encountered early in pregnancy, though likely cannot be correlated with a specific type of pathology and rather would alert of general placental dysfunction.

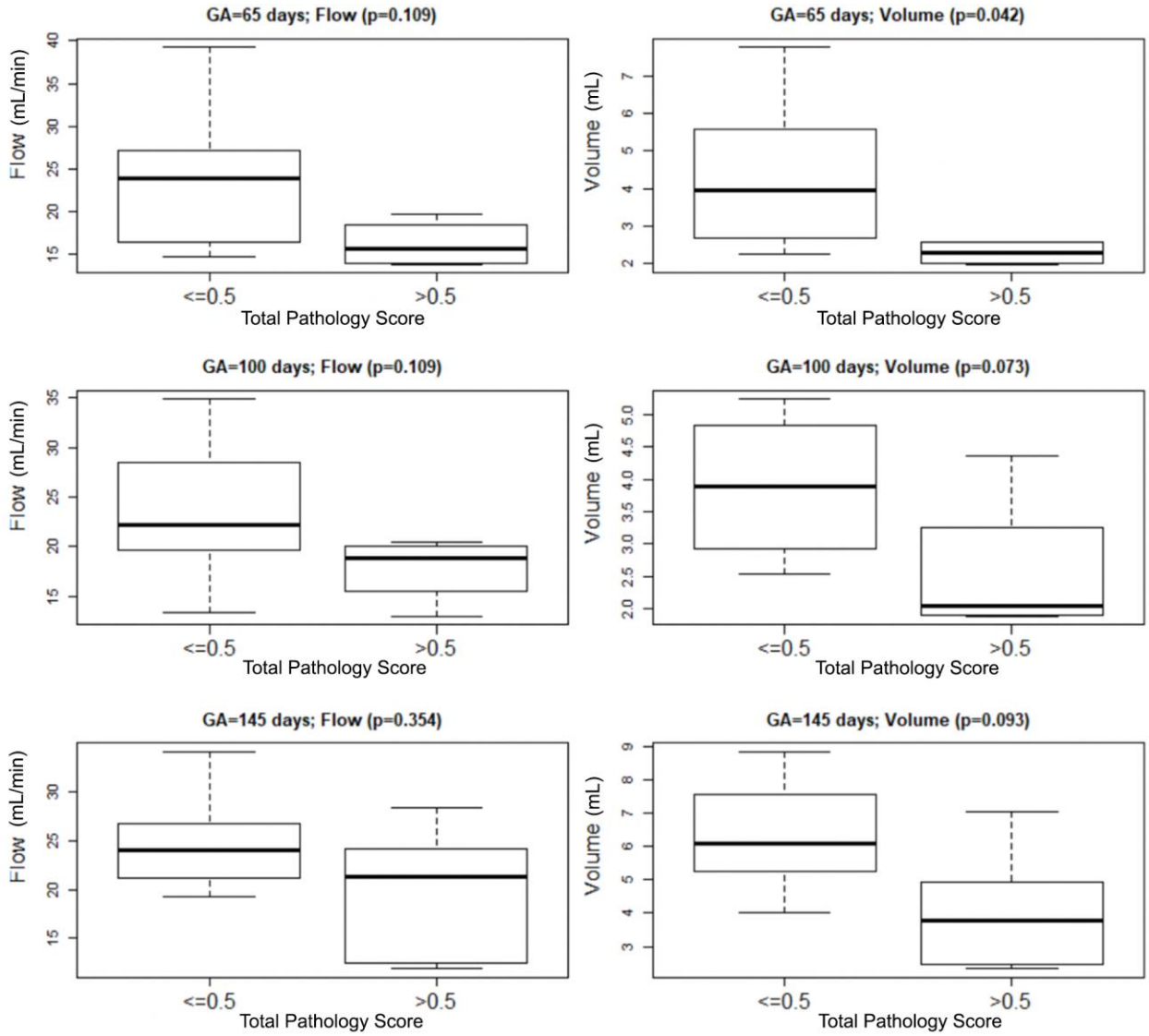

Figure 8. Perfusion Domain Flow (mL/min) and Volume (mL) in Pathological and Non Pathological Placentas by Total Pathology Score, in Early, Mid, and Late Pregnancy. Perfusion domain flow values (left) and volume values (right) were averaged for each animal at the gd65 (top row), gd100 (middle row) and gd145 (bottom row) scan dates. Comparisons were made between the average flow and volume values of animals with pathological placentas according to the total pathology score (>5 is pathological, <=5 is non-pathological) and those with non-pathological placentas. P-values are recorded for each gestational age (GA) at which the animals were imaged.

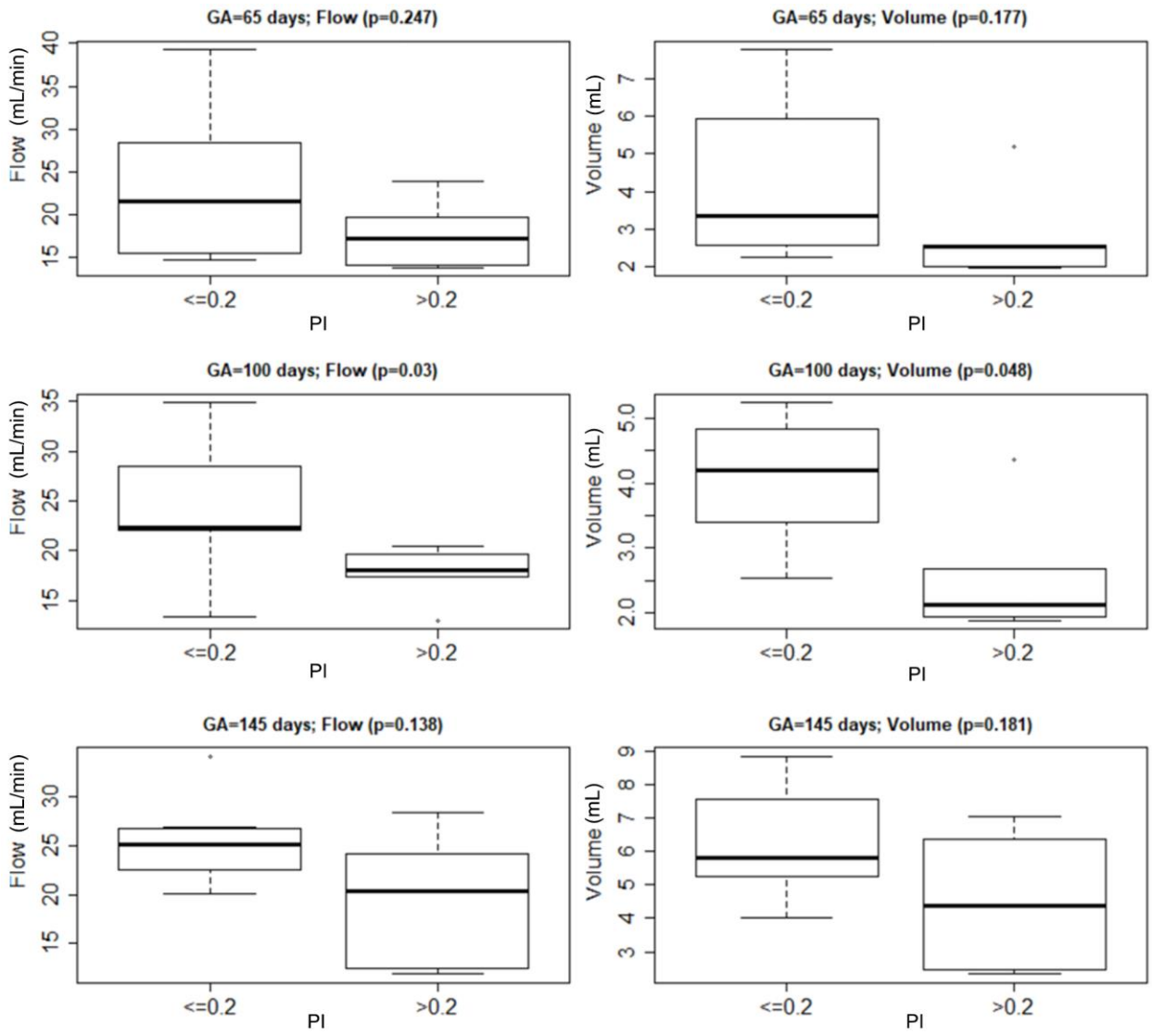

Figure 9. Perfusion Domain Flow (mL/min) and Volume (mL) in Pathological and Non-Pathological Placentas by PI, in Early, Mid, and Late Pregnancy. Perfusion domain flow values (left) and volume values (right) were averaged for each animal at the gd65 (top row), gd100 (middle row) and gd145 (bottom row) scan dates. Comparisons were made between the average flow and volume values of animals with pathological placentas according to the PI score (>0.2 is pathological, <=0.2 is non-pathological) and those with non-pathological placentas. P-values are recorded for each gestational age (GA) at which the animals were imaged.

Trends Over Gestation in Average Perfusion Domain Flow and Volume

To determine if there is a relation between pathology at term and the trajectory of increased flow and volume over gestation, the slopes of these measures in pathological placentas was compared to those in non-pathological placentas. Pathology was binned by total pathology score (Figure 10) or by PI (Figure 11), as these pathologies showed significant differences in average measures of placental volume and flow at term. When placentas were binned for pathology based on total pathology score, neither flow ($p=0.7619$) nor volume ($p>0.9999$) showed significance. The same was found for flow ($p>0.9999$) and volume ($p>0.9999$) when pathology was binned by PI. This suggests that, in the case of our infection model, the trajectory of increases in these parameters over gestation could not be used to predict a pathological placenta, as pathological and non-pathological placentas maintain similar trajectories.

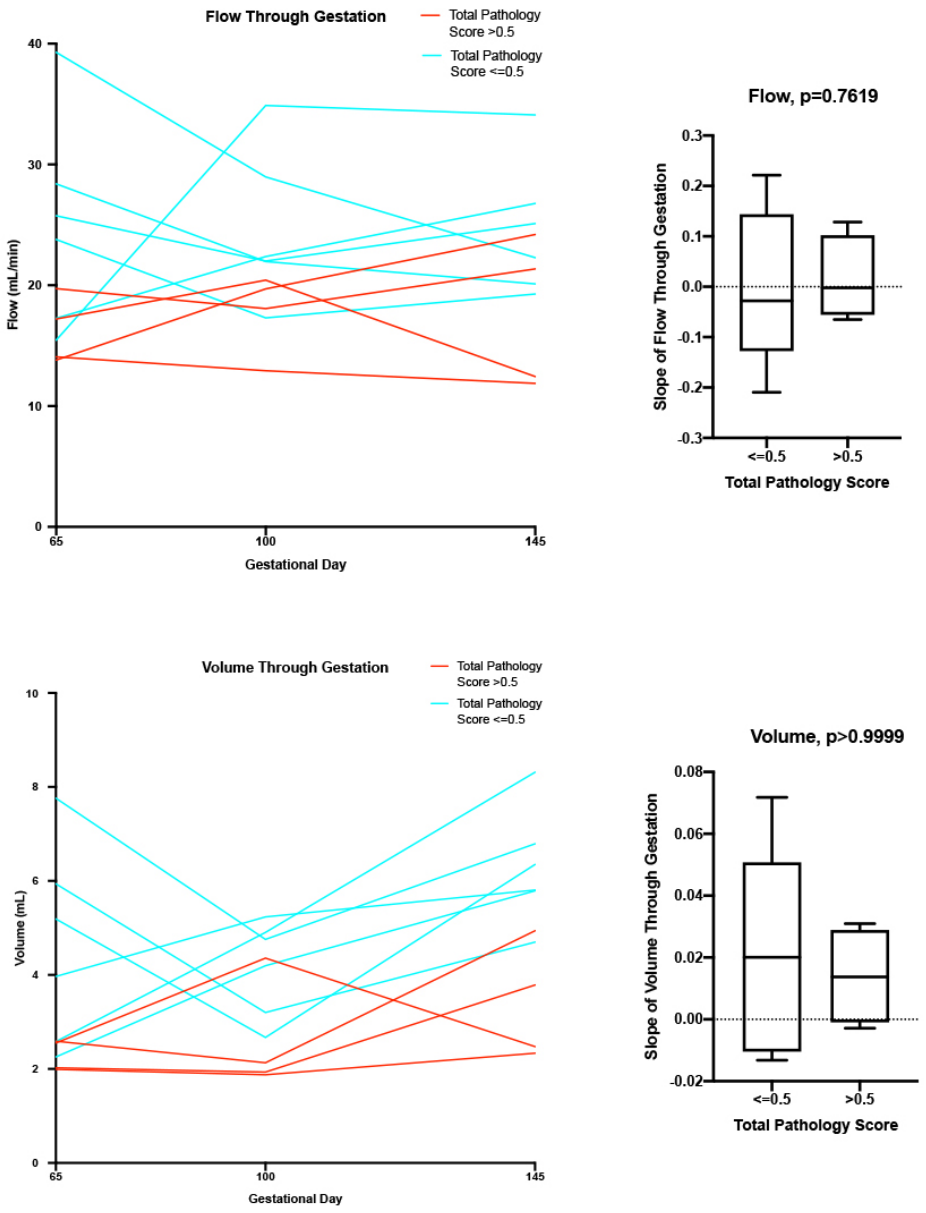

Figure 10. Trajectory of Perfusion Domain Flow and Volume in Pathological and Non-Pathological Placentas by Total Pathology Score. Perfusion domain flow (top row) and volume (bottom row) values were averaged for each animal at the three timepoints at which they were imaged: gd65, gd100, gd145. The averages are plotted (left) as a trajectory of placental function, where red lines represent animals that had a total pathology score above 0.5 (denoted as pathological) and blue lines represent animals with scores denoting non-

pathological placentas. The slopes were plotted (right) to assess potential differences. P-values are listed for assessment of slopes.

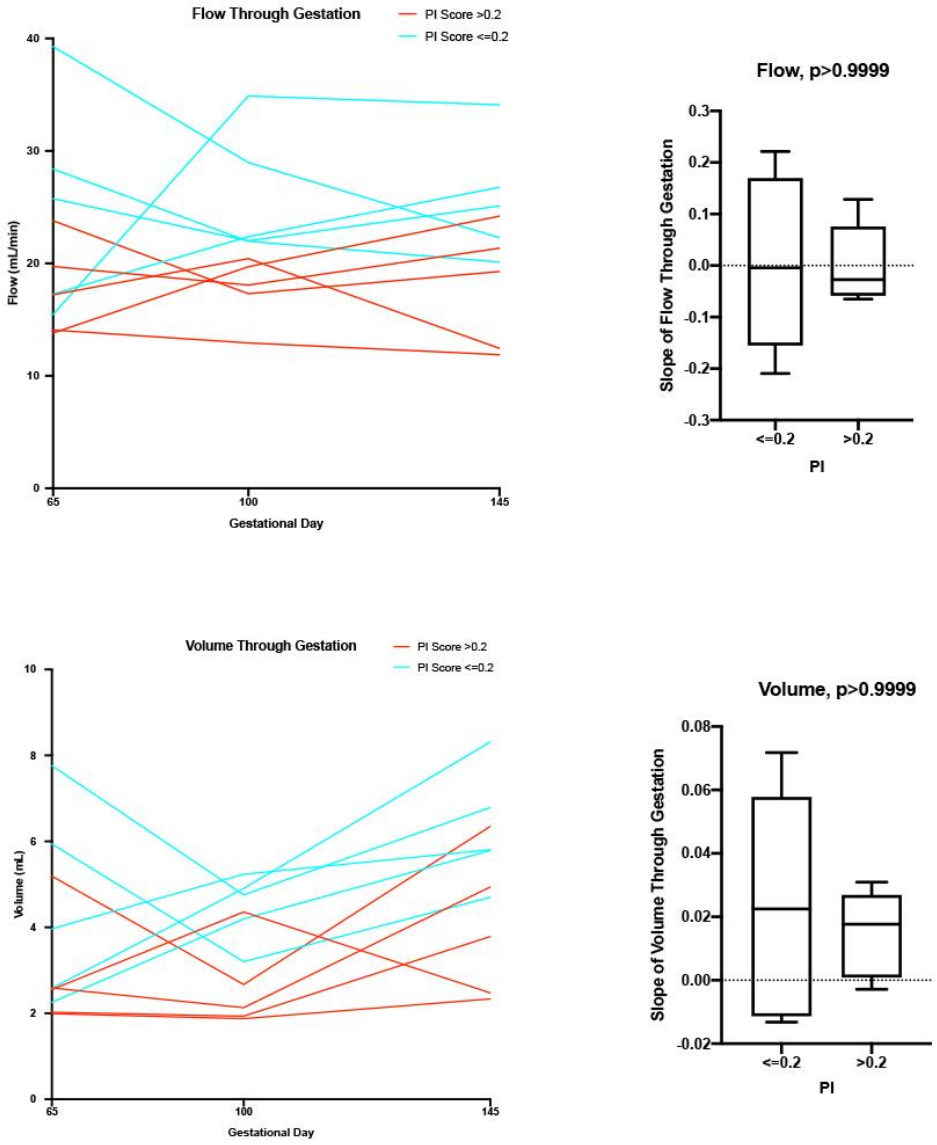

Figure 11. Trajectory of Perfusion Domain Flow and Volume in Pathological and Non-Pathological Placentas by PI. Perfusion domain flow (top row) and volume (bottom row) values were averaged for each animal at the three timepoints at which they were imaged: gd65, gd100, gd145. The averages are plotted (left) as a trajectory of placental function,

where red lines represent animals that had a PI pathology score above 0.2 (denoted as pathological, based on median score) and blue lines represent animals with scores denoting non-pathological placentas. The slopes were plotted (right) to assess potential differences. P-values are listed for assessment of slopes.

DISCUSSION

In analysis of the relationship between placental pathology at term within individual cotyledons and their flow and volume values as measured by MRI, no significant difference was seen between the flow and volume values of pathological and non-pathological cotyledons. This analysis was completed by independently comparing the presence of the three most-prevalent pathologies seen in the placentas of our ZIKV -infected macaques: CHIV, PI, and MDV, as well as each combination of these three pathologies. These results help to define the sensitivity of the MRI to detect changes in functional values in relation to pathology. It is seen that the presence of a particular pathology does not alter individual cotyledon flow or volume to a degree that can be detected by MRI when compared to non-pathological cotyledons within the same placenta.

However, when average cotyledon flow and volume was determined per placenta and compared to the average presence of these pathologies in the entire organ, as well as a total pathology score used to rank the placentas studied by relative degree of pathology, significant differences were seen in pathological versus non-pathological animals based on binning for PI alone, and for the total pathology score. Significance included both flow and volume for PI, and volume for total pathology score with borderline significance for flow. These findings suggest that DCE MRI is sensitive enough to detect functional changes in the

placenta that occur in the presence of ZIKV-induced pathology, but only when assessed on a whole-organ basis.

When average flow and volume was assessed at the three MRI scan timepoints -- gd65, gd100, and gd145 -- it was found that binning by total pathology score resulted in a significant difference in volume at gd65, with borderline significance at gd100 and gd145. The significant difference in volume at gd65 suggests that changes occurred in the placenta early in gestation that altered the way perfusion domains form, and this change persisted through gestation to term, reflective of the borderline significant scores at gd100 and gd145. While flow is not statistically significantly different in pathological placentas when binning by total pathology, it is consistently lower than is seen in non-pathological placentas, perhaps as a result of the same changes in the placenta affecting perfusion domain volume. These changes are likely in relation to the infection model used, where animals received virus around gd45 or gd55. We hypothesize that the infection acted on the placenta early, and our data shows that the effect on the placenta persists and manifests as pathology that can be seen at term. Interestingly, binning placentas by PI shows there is only a significant difference in flow and volume at gd100, suggesting that while the presence of PI may impact these placental functional readings, other factors are also likely to play a role. This also may be reflective of placental compensation or repair through gestation, as the organ is highly plastic. When the trajectories of flow and volume over time were assessed, no significant differences were seen, supporting that an early change in placental development may have initially stunted function, but placental development proceeded at an approximately normal rate following the initial insult. The assessment of flow and volume trajectory may not provide information that can assist in the identification of pathological placentas by MRI, but

identification of lower than average flow or volume at a particular point in gestation may signify an infectious or other pathological event.

This study serves to begin investigation into the limitations of the use of DCE MRI in the identification of placental pathology. While it was predicted that cotyledon-specific pathology would be identifiable through analysis of functional placenta information via MRI, this was not the case. However, this does not necessarily mean that MRI is not appropriate for the assessment of placental health and potential identification of pathological placentas. There are several possible explanations for the lack of significance in flow and volume values in pathological and non-pathological placentas. The pathology seen here may not have been severe enough to induce such a change. If pathology occurs that is not accompanied by fibrinoid deposition, for example, the intervillous space in the placenta may not be affected. Nonetheless, this study provides evidence that pathology may be linked to detectable average cotyledon flow and volume over entire placentas, though to be useful clinically, there must be data available on normal average cotyledon flow and volume through gestation, which would be difficult to achieve due to prevalence of factors that may affect placental function or development, such as diabetes or obesity, or even fetal sex [43,44].

Our experiments were limited, in that they utilized a single infection model in early gestation. Without imaging data from animals that received infection and resulting pathology later in gestation, it is unknown if later infection will manifest in ways detectable by MRI. With additional work examining varied infection timepoints or viral doses, or with a different infection model or ZIKV isolate, it can be determined if DCE MRI can detect variation in volume or flow at later infection onset, or in the presence of a different type of pathology that is not studied here. The potential for identification of infection onset through monitoring

cotyledon flow and volume could be utilized in research models to better understand the effects of a particular virus on pregnancy.

In summary, our study provides evidence that infection early in gestation can alter average flow and volume in placental cotyledons, which is linked to the presence of some pathologies observed in placentas at term. Unfortunately, the variation in flow of pathological and non-pathological cotyledons within the same placenta could not be identified by MRI in our analysis. Total pathology in the placenta at term in our animals correlated with altered volume through gestation, but the trajectory of change in volume over gestation was not different from growth seen in non-pathological placentas. Future research should be completed utilizing different infection models and later infection time points to further explore the value of MRI in placental research and potential applications for clinical use.

ACKNOWLDGEMENTS

We thank AMAG Pharmaceuticals for providing Ferumoxytol used in our imaging procedures, and the Wisconsin National Primate Research Center (WNPRC) Veterinary, Scientific Protocol Implementation, and Animal Services staff for providing animal care, and assisting in procedures including breeding, pregnancy monitoring, and sample collection. This work was supported by the National Institutes of Health Grants U01-HD087216 (to OW and DMS), R21 AI129308 to TGG, R01Al116382-01S2 to DHO, Endocrinology-Reproductive Physiology Training Grant T32 HD041921 (to SMN), and P51 OD011106 (to the WNPRC). The content of this manuscript is solely the responsibility of the authors and does not represent the official views of the NIH.

SUPPLEMENTARY DATA

Supplemental Table 1. Term Placental Pathology Scoring Matched to Cotyledon Flow and Volume.

Animal Number	Cotyledon flow by MRI (mL/min)	Cotyledon volume by MRI (mL)	Presence of CHIV per cotyledon (1= presence, 0= absence)	Average presence of CHIV per cotyledon (# cotyledon with CHIV/ total # cotyledon)	Presence of PI per cotyledon (1= presence, 0= absence)	Average presence of PI per cotyledon (# cotyledon with PI/total # cotyledon)	Presence of MDV per cotyledon (1= presence, 0= absence)	Average presencce of MDV per cotyledon (# cotyledon with MDV/ total # cotyledon)	Presence of CHIV **AND** PI per cotyledon (1= presence, 0= absence)	Average presence of CHIV **AND** PI per cotyledon (# cotyledon with CHIV AND PI/total # cotyledon)	Presence of CHIV **AND** MDV per cotyledon (1= presence, 0= absence)	Average presence of CHIV **AND** MDV per cotyledon (# cotyledon with CHIV AND MDV/ total # cotyledon)	Presence of PI **AND** MDV per cotyledon (1= presence, 0= absence)	Average presence of PI **AND** MDV per cotyledon (# cotyledon with PI AND MDV/ total # cotyledon)	Total Pathology per cotyledon (presence of CHIV+ presence of PI+ presence of MDV) (1= presence, 0= absence for each; range 0-3)	Average Total Pathology Score ([# cotyledon with CHIV+ # cotyledon with PI+ # cotyledon with MDV] /total # cotyledon)
Animal 1	7.210197	2.267215	1	0.5	1	0.916667	0	0	1	0.416667	0	0	0	0	2	1.417
Animal 1	17.80978	3.170128	0	0.5	1	0.916667	0	0	0	0.416667	0	0	0	0	1	1.417
Animal 1	37.82245	8.429391	1	0.5	0	0.916667	0	0	0	0.416667	0	0	0	0	1	1.417
Animal 1	15.33293	1.604932	0	0.5	1	0.916667	0	0	0	0.416667	0	0	0	0	1	1.417
Animal 1	8.499413	4.210648	0	0.5	1	0.916667	0	0	0	0.416667	0	0	0	0	1	1.417
Animal 1	17.80776	2.800721	1	0.5	1	0.916667	0	0	1	0.416667	0	0	0	0	2	1.417
Animal 1	10.28632	2.277518	0	0.5	1	0.916667	0	0	0	0.416667	0	0	0	0	1	1.417
Animal 1	0	0.687303	1	0.5	1	0.916667	0	0	1	0.416667	0	0	0	0	2	1.417

Animal 1	4.933158	0.687303	1	0.5	1	0.916667	0	0	1	0.416667	0	0	0	0	2	1.417
Animal 1	10.67218	0.75721	0	0.5	1	0.916667	0	0	0	0.416667	0	0	0	0	1	1.417
Animal 1	0	1.030954	0	0.5	1	0.916667	0	0	0	0.416667	0	0	0	0	1	1.417
Animal 1	6.464013	1.030954	1	0.5	1	0.916667	0	0	1	0.416667	0	0	0	0	2	1.417
Animal 2	13.78267	1.575498	1	0.428571	0	0.428571	0	0.071429	0	0.071429	0	0.071429	0	0.071429	1	0.93
Animal 2	20.985	3.881714	1	0.428571	0	0.428571	0	0.071429	0	0.071429	0	0.071429	0	0.071429	1	0.93
Animal 2	40.49098	4.206233	0	0.428571	1	0.428571	0	0.071429	0	0.071429	0	0.071429	0	0.071429	1	0.93
Animal 2	22.11753	11.24998	0	0.428571	1	0.428571	0	0.071429	0	0.071429	0	0.071429	0	0.071429	1	0.93
Animal 2	13.78267	1.575498	1	0.428571	0	0.428571	0	0.071429	0	0.071429	0	0.071429	0	0.071429	1	0.93
Animal 2	18.1181	1.660859	1	0.428571	1	0.428571	1	0.071429	1	0.071429	1	0.071429	1	0.071429	3	0.93
Animal 2	33.99258	3.259168	0	0.428571	1	0.428571	0	0.071429	0	0.071429	0	0.071429	0	0.071429	1	0.93
Animal 2	35.62768	10.51705	1	0.428571	0	0.428571	0	0.071429	0	0.071429	0	0.071429	0	0.071429	1	0.93
Animal 2	10.72221	3.314358	0	0.428571	0	0.428571	0	0.071429	0	0.071429	0	0.071429	0	0.071429	0	0.93
Animal 2	35.20878	5.12975	0	0.428571	1	0.428571	0	0.071429	0	0.071429	0	0.071429	0	0.071429	1	0.93
Animal 2	14.64981	2.18627	0	0.428571	1	0.428571	0	0.071429	0	0.071429	0	0.071429	0	0.071429	1	0.93
Animal 2	10.36689	3.435615	0	0.428571	0	0.428571	0	0.071429	0	0.071429	0	0.071429	0	0.071429	0	0.93
Animal 2	13.9897	4.622161	1	0.428571	0	0.428571	0	0.071429	0	0.071429	0	0.071429	0	0.071429	1	0.93
Animal 2	21.19652	7.003275	0	0.428571	0	0.428571	0	0.071429	0	0.071429	0	0.071429	0	0.071429	0	0.93
Animal 3	13.04686	2.621169	0	0.235294	1	0.529412	0	0.058824	0	0.117647	0	0	0	0	1	0.824

Animal 3	19.57029	3.931753	1	0.235294	1	0.529412	0	0.058824	1	0.117647	0	0	0	0	2	0.824
Animal 3	13.3904	6.468576	0	0.235294	0	0.529412	0	0.058824	0	0.117647	0	0	0	0	0	0.824
Animal 3	28.5054	5.980415	0	0.235294	0	0.529412	0	0.058824	0	0.117647	0	0	0	0	0	0.824
Animal 3	15.40408	3.232085	0	0.235294	0	0.529412	1	0.058824	0	0.117647	0	0	0	0	1	0.824
Animal 3	13.47058	6.50731	0	0.235294	0	0.529412	0	0.058824	0	0.117647	0	0	0	0	0	0.824
Animal 3	37.73076	7.672181	1	0.235294	1	0.529412	0	0.058824	1	0.117647	0	0	0	0	2	0.824
Animal 3	13.3904	6.468576	0	0.235294	1	0.529412	0	0.058824	0	0.117647	0	0	0	0	1	0.824
Animal 3	19.96533	9.644763	1	0.235294	0	0.529412	0	0.058824	0	0.117647	0	0	0	0	1	0.824
Animal 3	19.96533	9.644763	1	0.235294	0	0.529412	0	0.058824	0	0.117647	0	0	0	0	1	0.824
Animal 3	42.43996	17.36727	0	0.235294	0	0.529412	0	0.058824	0	0.117647	0	0	0	0	0	0.824
Animal 3	30.05176	5.059106	0	0.235294	1	0.529412	0	0.058824	0	0.117647	0	0	0	0	1	0.824
Animal 3	12.20928	1.459966	0	0.235294	1	0.529412	0	0.058824	0	0.117647	0	0	0	0	1	0.824
Animal 3	11.61878	1.967716	0	0.235294	1	0.529412	0	0.058824	0	0.117647	0	0	0	0	1	0.824
Animal 3	17.51117	2.969898	0	0.235294	1	0.529412	0	0.058824	0	0.117647	0	0	0	0	1	0.824
Animal 3	69.1705	6.49994	0	0.235294	1	0.529412	0	0.058824	0	0.117647	0	0	0	0	1	0.824
Animal 3	40.79566	6.650131	0	0.235294	0	0.529412	0	0.058824	0	0.117647	0	0	0	0	0	0.824
Animal 4	11.53183	1.17592	0	0.0625	0	0.5	0	0.125	0	0.0625	0	0	0	0.125	0	0.69
Animal 4	6.28468	0.994896	0	0.0625	1	0.5	0	0.125	0	0.0625	0	0	0	0.125	1	0.69
Animal 4	16.80783	1.988321	0	0.0625	1	0.5	1	0.125	0	0.0625	0	0	1	0.125	2	0.69

Animal 4	9.516792	1.195789	0	0.0625	1	0.5	0	0.125	0	0.0625	0	0	0	0.125	1	0.69
Animal 4	8.482926	1.294395	0	0.0625	1	0.5	0	0.125	0	0.0625	0	0	0	0.125	1	0.69
Animal 4	5.612307	1.738677	0	0.0625	1	0.5	1	0.125	0	0.0625	0	0	1	0.125	2	0.69
Animal 4	27.90162	6.011506	0	0.0625	1	0.5	0	0.125	0	0.0625	0	0	0	0.125	1	0.69
Animal 4	34.50132	9.238112	0	0.0625	0	0.5	0	0.125	0	0.0625	0	0	0	0.125	0	0.69
Animal 4	14.52677	3.790761	1	0.0625	1	0.5	0	0.125	1	0.0625	0	0	0	0.125	2	0.69
Animal 4	10.69079	2.161986	0	0.0625	0	0.5	0	0.125	0	0.0625	0	0	0	0.125	0	0.69
Animal 4	2.364823	0.617101	0	0.0625	0	0.5	0	0.125	0	0.0625	0	0	0	0.125	0	0.69
Animal 4	9.064093	0.752795	0	0.0625	0	0.5	0	0.125	0	0.0625	0	0	0	0.125	0	0.69
Animal 4	13.49965	2.640302	0	0.0625	1	0.5	0	0.125	0	0.0625	0	0	0	0.125	1	0.69
Animal 4	10.21108	2.535072	0	0.0625	0	0.5	0	0.125	0	0.0625	0	0	0	0.125	0	0.69
Animal 4	0	1.239941	0	0.0625	0	0.5	0	0.125	0	0.0625	0	0	0	0.125	0	0.69
Animal 4	8.765303	1.239941	0	0.0625	0	0.5	0	0.125	0	0.0625	0	0	0	0.125	0	0.69
Animal 5	13.32336	1.565931	0	0.066667	0	0.533333	0	0	0	0.066667	0	0	0	0	0	0.6
Animal 5	28.40927	3.274622	0	0.066667	0	0.533333	0	0	0	0.066667	0	0	0	0	0	0.6
Animal 5	29.51258	7.986397	0	0.066667	0	0.533333	0	0	0	0.066667	0	0	0	0	0	0.6
Animal 5	32.24981	4.982576	0	0.066667	1	0.533333	0	0	0	0.066667	0	0	0	0	1	0.6
Animal 5	21.58604	7.726635	0	0.066667	0	0.533333	0	0	0	0.066667	0	0	0	0	0	0.6
Animal 5	30.90553	5.56097	0	0.066667	1	0.533333	0	0	0	0.066667	0	0	0	0	1	0.6

Animal 5	29.99303	3.603555	0	0.066667	1	0.533333	0	0	0	0.066667	0	0	0	0	1	0.6
Animal 5	8.259645	2.400114	0	0.066667	0	0.533333	0	0	0	0.066667	0	0	0	0	0	0.6
Animal 5	36.33676	5.928169	0	0.066667	0	0.533333	0	0	0	0.066667	0	0	0	0	0	0.6
Animal 5	37.68311	1.950791	0	0.066667	1	0.533333	0	0	0	0.066667	0	0	0	0	1	0.6
Animal 5	14.61518	2.091343	0	0.066667	0	0.533333	0	0	0	0.066667	0	0	0	0	0	0.6
Animal 5	11.9495	2.729342	0	0.066667	1	0.533333	0	0	0	0.066667	0	0	0	0	1	0.6
Animal 5	17.18995	1.761673	0	0.066667	1	0.533333	0	0	0	0.066667	0	0	0	0	1	0.6
Animal 5	25.33076	5.085598	0	0.066667	1	0.533333	0	0	0	0.066667	0	0	0	0	1	0.6
Animal 5	36.90968	6.876705	1	0.066667	1	0.533333	0	0	1	0.066667	0	0	0	0	2	0.6
Animal 6	29.87565	7.395052	0	0.166667	0	0.166667	0	0	0	0	0	0	0	0	0	0.333
Animal 6	19.54197	6.13642	0	0.166667	0	0.166667	0	0	0	0	0	0	0	0	0	0.333
Animal 6	40.31247	12.34422	0	0.166667	1	0.166667	0	0	0	0	0	0	0	0	1	0.333
Animal 6	38.81967	11.54506	0	0.166667	0	0.166667	0	0	0	0	0	0	0	0	0	0.333
Animal 6	54.53166	21.07605	1	0.166667	0	0.166667	0	0	0	0	0	0	0	0	1	0.333
Animal 6	33.39222	10.78609	0	0.166667	0	0.166667	0	0	0	0	0	0	0	0	0	0.333
Animal 6	37.45432	10.31248	0	0.166667	0	0.166667	0	0	0	0	0	0	0	0	0	0.333
Animal 6	34.09935	12.69376	0	0.166667	0	0.166667	0	0	0	0	0	0	0	0	0	0.333
Animal 6	17.12304	3.705105	0	0.166667	1	0.166667	0	0	0	0	0	0	0	0	1	0.333
Animal 6	47.09206	12.56204	0	0.166667	0	0.166667	0	0	0	0	0	0	0	0	0	0.333

Animal 6	9.609494	2.145061	0	0.166667	0	0.166667	0	0	0	0	0	0	0	0	0	0.333
Animal 6	34.09935	12.69376	1	0.166667	0	0.166667	0	0	0	0	0	0	0	0	1	0.333
Animal 7	40.04168	14.64823	0	0	0	0	0	0.3	0	0	0	0	0	0	0	0.3
Animal 7	37.18874	11.62895	0	0	0	0	1	0.3	0	0	0	0	0	0	1	0.3
Animal 7	21.12916	7.875281	0	0	0	0	0	0.3	0	0	0	0	0	0	0	0.3
Animal 7	20.19706	7.465401	0	0	0	0	0	0.3	0	0	0	0	0	0	0	0.3
Animal 7	17.42196	2.891233	0	0	0	0	0	0.3	0	0	0	0	0	0	0	0.3
Animal 7	22.15891	8.648062	0	0	0	0	1	0.3	0	0	0	0	0	0	1	0.3
Animal 7	17.35531	3.680822	0	0	0	0	0	0.3	0	0	0	0	0	0	0	0.3
Animal 7	28.98801	8.625868	0	0	0	0	1	0.3	0	0	0	0	0	0	1	0.3
Animal 7	34.82114	13.58981	0	0	0	0	0	0.3	0	0	0	0	0	0	0	0.3
Animal 7	28.69909	9.341252	0	0	0	0	0	0.3	0	0	0	0	0	0	0	0.3
Animal 8	33.12729	14.66383	0	0	1	0.076923	0	0	0	0	0	0	0	0	1	0.077
Animal 8	23.75423	3.148788	0	0	0	0.076923	0	0	0	0	0	0	0	0	0	0.077
Animal 8	39.22133	11.34196	0	0	0	0.076923	0	0	0	0	0	0	0	0	0	0.077
Animal 8	2.880634	1.275116	0	0	0	0.076923	0	0	0	0	0	0	0	0	0	0.077
Animal 8	27.82008	6.187077	0	0	0	0.076923	0	0	0	0	0	0	0	0	0	0.077
Animal 8	5.464658	1.215319	0	0	0	0.076923	0	0	0	0	0	0	0	0	0	0.077
Animal 8	16.39398	3.645956	0	0	0	0.076923	0	0	0	0	0	0	0	0	0	0.077

Animal 8	19.8201	4.270254	0	0	0	0.076923	0	0	0	0	0	0	0	0	0	0.077
Animal 8	19.35287	1.794051	0	0	0	0.076923	0	0	0	0	0	0	0	0	0	0.077
Animal 8	3.579499	0.661547	0	0	0	0.076923	0	0	0	0	0	0	0	0	0	0.077
Animal 8	22.58939	7.08422	0	0	0	0.076923	0	0	0	0	0	0	0	0	0	0.077
Animal 8	26.80693	6.999228	0	0	0	0.076923	0	0	0	0	0	0	0	0	0	0.077
Animal 8	3.651531	1.136551	0	0	0	0.076923	0	0	0	0	0	0	0	0	0	0.077
Animal 9	0	5.532271	0	0	0	0.2	0	0	0	0	0	0	0	0	0	0.2
Animal 9	29.50168	6.227668	0	0	0	0.2	0	0	0	0	0	0	0	0	0	0.2
Animal 9	40.21332	11.46485	0	0	0	0.2	0	0	0	0	0	0	0	0	0	0.2
Animal 9	29.50493	9.255773	0	0	1	0.2	0	0	0	0	0	0	0	0	1	0.2
Animal 9	19.83646	6.781778	0	0	0	0.2	0	0	0	0	0	0	0	0	0	0.2
Animal 9	27.50454	8.189497	0	0	0	0.2	0	0	0	0	0	0	0	0	0	0.2
Animal 9	29.50061	10.80919	0	0	0	0.2	0	0	0	0	0	0	0	0	0	0.2
Animal 9	22.14998	6.65668	0	0	0	0.2	0	0	0	0	0	0	0	0	0	0.2
Animal 9	18.64283	7.479383	0	0	1	0.2	0	0	0	0	0	0	0	0	1	0.2
Animal 9	28.25072	7.825977	0	0	0	0.2	0	0	0	0	0	0	0	0	0	0.2
Animal 10	39.53113	11.6525	0	0.076923	0	0.076923	0	0	0	0.076923	0	0	0	0	0	0.154
Animal 10	42.79332	4.025945	0	0.076923	0	0.076923	0	0	0	0.076923	0	0	0	0	0	0.154
Animal 10	54.57407	9.263867	0	0.076923	0	0.076923	0	0	0	0.076923	0	0	0	0	0	0.154

Animal 10	36.32486	4.207705	0	0.076923	0	0.076923	0	0	0	0.076923	0	0	0	0	0	0.154
Animal 10	18.28394	3.622688	0	0.076923	0	0.076923	0	0	0	0.076923	0	0	0	0	0	0.154
Animal 10	60.08934	16.35103	0	0.076923	0	0.076923	0	0	0	0.076923	0	0	0	0	0	0.154
Animal 10	26.12648	5.416739	1	0.076923	1	0.076923	0	0	1	0.076923	0	0	0	0	2	0.154
Animal 10	21.54522	4.423315	0	0.076923	0	0.076923	0	0	0	0.076923	0	0	0	0	0	0.154
Animal 10	12.98843	1.297339	0	0.076923	0	0.076923	0	0	0	0.076923	0	0	0	0	0	0.154
Animal 10	4.806455	1.113666	0	0.076923	0	0.076923	0	0	0	0.076923	0	0	0	0	0	0.154
Animal 10	19.22582	4.454663	0	0.076923	0	0.076923	0	0	0	0.076923	0	0	0	0	0	0.154
Animal 10	29.94183	2.868421	0	0.076923	0	0.076923	0	0	0	0.076923	0	0	0	0	0	0.154
Animal 10	99.37673	14.58789	0	0.076923	0	0.076923	0	0	0	0.076923	0	0	0	0	0	0.154
Animal 11	11.36955	5.109145	0	0.090909	0	0.363636	0	0	0	0.090909	0	0	0	0	0	0.09
Animal 11	7.843399	5.242338	0	0.090909	0	0.363636	0	0	0	0.090909	0	0	0	0	0	0.09
Animal 11	18.1536	4.949462	1	0.090909	1	0.363636	0	0	1	0.090909	0	0	0	0	1	0.09
Animal 11	9.059684	0.701284	0	0.090909	0	0.363636	0	0	0	0.090909	0	0	0	0	0	0.09
Animal 11	23.55026	2.454274	0	0.090909	0	0.363636	0	0	0	0.090909	0	0	0	0	0	0.09
Animal 11	25.30867	4.630683	0	0.090909	1	0.363636	0	0	0	0.090909	0	0	0	0	0	0.09
Animal 11	18.1536	4.949462	0	0.090909	1	0.363636	0	0	0	0.090909	0	0	0	0	0	0.09
Animal 11	16.74479	10.00415	0	0.090909	1	0.363636	0	0	0	0.090909	0	0	0	0	0	0.09
Animal 11	14.32778	4.956084	0	0.090909	0	0.363636	0	0	0	0.090909	0	0	0	0	0	0.09

Animal 11	21.12487	7.804637	0	0.090909	0	0.363636	0	0	0	0.090909	0	0	0	0	0	0.09
Animal 11	27.11482	12.71583	0	0.090909	0	0.363636	0	0	0	0.090909	0	0	0	0	0	0.09
Animal 12	112.5811	8.063663	0	0	0	0	0	0	0	0	0	0	0	0	0	0
Animal 12	76.02489	15.54709	0	0	0	0	0	0	0	0	0	0	0	0	0	0
Animal 12	67.74345	9.154591	0	0	0	0	0	0	0	0	0	0	0	0	0	0
Animal 12	18.50734	3.237092	0	0	0	0	0	0	0	0	0	0	0	0	0	0
Animal 12	86.51255	18.63517	0	0	0	0	0	0	0	0	0	0	0	0	0	0
Animal 12	24.72623	2.610867	0	0	0	0	0	0	0	0	0	0	0	0	0	0
Animal 12	92.78593	20.52857	0	0	0	0	0	0	0	0	0	0	0	0	0	0
Animal 12	14.15572	1.238469	0	0	0	0	0	0	0	0	0	0	0	0	0	0
Animal 12	44.94227	12.10322	0	0	0	0	0	0	0	0	0	0	0	0	0	0
Animal 12	14.98076	4.034407	0	0	0	0	0	0	0	0	0	0	0	0	0	0
Animal 12	72.99863	13.52971	0	0	0	0	0	0	0	0	0	0	0	0	0	0
Animal 12	33.8269	5.09693	0	0	0	0	0	0	0	0	0	0	0	0	0	0
Animal 12	38.82953	5.632643	0	0	0	0	0	0	0	0	0	0	0	0	0	0
Animal 12	23.79123	5.276924	0	0	0	0	0	0	0	0	0	0	0	0	0	0
Animal 12	22.55127	3.397953	0	0	0	0	0	0	0	0	0	0	0	0	0	0
Animal 12	22.55127	3.397953	0	0	0	0	0	0	0	0	0	0	0	0	0	0
Animal 13	25.65	8.80	0	0	0	0	0	0	0	0	0	0	0	0	0	0

Animal 13	7.90	0.84	0	0	0	0	0	0	0	0	0	0	0	0	0	0
Animal 13	19.30	8.17	0	0	0	0	0	0	0	0	0	0	0	0	0	0
Animal 13	29.22	6.06	0	0	0	0	0	0	0	0	0	0	0	0	0	0
Animal 13	22.54	3.26	0	0	0	0	0	0	0	0	0	0	0	0	0	0
Animal 13	29.11	10.01	0	0	0	0	0	0	0	0	0	0	0	0	0	0
Animal 13	6.83	2.01	0	0	0	0	0	0	0	0	0	0	0	0	0	0
Animal 13	29.27	6.57	0	0	0	0	0	0	0	0	0	0	0	0	0	0
Animal 13	59.83	9.93	0	0	0	0	0	0	0	0	0	0	0	0	0	0
Animal 13	32.91	5.59	0	0	0	0	0	0	0	0	0	0	0	0	0	0
Animal 13	25.90	5.12	0	0	0	0	0	0	0	0	0	0	0	0	0	0
Animal 13	21.21	3.74	0	0	0	0	0	0	0	0	0	0	0	0	0	0
Animal 13	20.19	3.38	0	0	0	0	0	0	0	0	0	0	0	0	0	0
Animal 13	26.03	7.33	0	0	0	0	0	0	0	0	0	0	0	0	0	0
Animal 13	21.69	3.65	0	0	0	0	0	0	0	0	0	0	0	0	0	0
Animal 13	24.67	8.28	0	0	0	0	0	0	0	0	0	0	0	0	0	0

Supplemental Table 2. Placental Perfusion Domain Flow and Volume at 65gd, 100gd, and 145gd.

Animal Number	Gestational Age	Perfusion domain flow by MRI measurement (mL/min)	Average perfusion domain flow by gestational age (mL/min)	Perfusion domain volume by MRI measurement (mL)	Average perfusion domain volume by gestational age (mL)	Average Total Pathology Score at Term ([presence of CHIV at term+presence of PI at term+presence of MDV at term]/# perfusion domains at term)
Animal 1	65	6.810999835	17.2139004	0.56956338	2.55126129	1.417
Animal 1	65	9.200927386	17.2139004	1.63215966	2.55126129	1.417
Animal 1	65	10.25477129	17.2139004	0.80798526	2.55126129	1.417
Animal 1	65	21.12776964	17.2139004	5.27839551	2.55126129	1.417
Animal 1	65	17.53730004	17.2139004	3.33128349	2.55126129	1.417
Animal 1	65	49.80882369	17.2139004	5.51976087	2.55126129	1.417
Animal 1	65	5.756710909	17.2139004	0.71968086	2.55126129	1.417
Animal 1	100	26.55497342	20.42548358	5.30341509	4.357019373	1.417
Animal 1	100	38.6836401	20.42548358	10.02328527	4.357019373	1.417
Animal 1	100	31.17727643	20.42548358	8.1019287	4.357019373	1.417
Animal 1	100	13.7946318	20.42548358	2.90962998	4.357019373	1.417
Animal 1	100	16.13283913	20.42548358	2.60424393	4.357019373	1.417
Animal 1	100	10.9478075	20.42548358	2.69402007	4.357019373	1.417
Animal 1	100	23.92685613	20.42548358	7.23286623	4.357019373	1.417
Animal 1	100	9.672075511	20.42548358	1.83673152	4.357019373	1.417
Animal 1	100	9.267339823	20.42548358	1.38269973	4.357019373	1.417
Animal 1	100	33.11672948	20.42548358	3.97296213	4.357019373	1.417
Animal 1	100	11.40615008	20.42548358	1.86543045	4.357019373	1.417
Animal 1	145	17.80776492	12.43983711	2.80072122	2.476001858	1.417
Animal 1	145	37.82244845	12.43983711	8.42939085	2.476001858	1.417
Animal 1	145	10.28632031	12.43983711	2.27751765	2.476001858	1.417
Animal 1	145	17.80977906	12.43983711	3.17012796	2.476001858	1.417
Animal 1	145	8.499413413	12.43983711	4.21064814	2.476001858	1.417
Animal 1	145	4.606968068	12.43983711	0.64094277	2.476001858	1.417
Animal 1	145	10.72596397	12.43983711	0.9639897	2.476001858	1.417

Animal 1	145	7.21019675	12.43983711	2.26721547	2.476001858	1.417
Animal 1	145	4.933158354	12.43983711	0.68730258	2.476001858	1.417
Animal 1	145	6.464012929	12.43983711	1.03095387	2.476001858	1.417
Animal 1	145	10.672182	12.43983711	0.75721023	2.476001858	1.417
Animal 2	65	20.86132006	13.80847102	8.63984967	2.59099827	0.93
Animal 2	65	20.63089443	13.80847102	2.07883275	2.59099827	0.93
Animal 2	65	11.97189173	13.80847102	1.13986263	2.59099827	0.93
Animal 2	65	10.80603631	13.80847102	1.61744226	2.59099827	0.93
Animal 2	65	8.782213459	13.80847102	0.86317551	2.59099827	0.93
Animal 2	65	11.53743403	13.80847102	2.1119469	2.59099827	0.93
Animal 2	65	12.0695071	13.80847102	1.68587817	2.59099827	0.93
Animal 2	100	30.16949378	19.69648412	2.416597	2.130477455	0.93
Animal 2	100	14.54649245	19.69648412	0.647566	2.130477455	0.93
Animal 2	100	12.40496722	19.69648412	3.334963	2.130477455	0.93
Animal 2	100	28.9756122	19.69648412	3.625631	2.130477455	0.93
Animal 2	100	17.74764434	19.69648412	0.685095	2.130477455	0.93
Animal 2	100	29.0527778	19.69648412	2.500486	2.130477455	0.93
Animal 2	100	15.168092	19.69648412	2.117098	2.130477455	0.93
Animal 2	100	9.721139739	19.69648412	0.576186	2.130477455	0.93
Animal 2	100	13.97951744	19.69648412	2.039832	2.130477455	0.93
Animal 2	100	25.62287644	19.69648412	2.091343	2.130477455	0.93
Animal 2	100	19.27271194	19.69648412	3.400455	2.130477455	0.93
Animal 2	145	20.98500041	24.19786109	3.88171425	4.941253839	0.93
Animal 2	145	29.76877514	24.19786109	0.89187444	4.941253839	0.93
Animal 2	145	33.99257692	24.19786109	3.25916823	4.941253839	0.93
Animal 2	145	18.11809901	24.19786109	1.66085859	4.941253839	0.93
Animal 2	145	35.62768364	24.19786109	10.51705404	4.941253839	0.93
Animal 2	145	27.56534709	24.19786109	3.15099534	4.941253839	0.93
Animal 2	145	21.44441466	24.19786109	6.62871696	4.941253839	0.93
Animal 2	145	9.541079723	24.19786109	0.61886667	4.941253839	0.93
Animal 2	145	22.11752757	24.19786109	11.24998056	4.941253839	0.93
Animal 2	145	3.160070539	24.19786109	1.05450171	4.941253839	0.93

Animal 2	145	42.39303128	24.19786109	14.00654958	4.941253839	0.93
Animal 2	145	35.20877812	24.19786109	5.12974977	4.941253839	0.93
Animal 2	145	14.64981013	24.19786109	2.18626977	4.941253839	0.93
Animal 3	145	5.242669987	28.39513503	0.62033841	7.05061576	0.824
Animal 3	145	53.06415944	28.39513503	8.9996901	7.05061576	0.824
Animal 3	145	26.20787775	28.39513503	2.77496577	7.05061576	0.824
Animal 3	145	30.49684846	28.39513503	2.34227421	7.05061576	0.824
Animal 3	145	12.46576518	28.39513503	1.38269973	7.05061576	0.824
Animal 3	145	11.61877798	28.39513503	1.96771638	7.05061576	0.824
Animal 3	145	12.20927523	28.39513503	1.45996608	7.05061576	0.824
Animal 3	145	42.43996075	28.39513503	17.36726787	7.05061576	0.824
Animal 3	145	24.08170184	28.39513503	4.08555024	7.05061576	0.824
Animal 3	145	5.970059752	28.39513503	0.97355601	7.05061576	0.824
Animal 3	145	37.7307581	28.39513503	7.67218062	7.05061576	0.824
Animal 3	145	28.50539765	28.39513503	5.98041549	7.05061576	0.824
Animal 3	145	32.61715828	28.39513503	6.55292235	7.05061576	0.824
Animal 3	145	23.09456695	28.39513503	4.84570395	7.05061576	0.824
Animal 3	145	80.18204811	28.39513503	38.73398919	7.05061576	0.824
Animal 4	65	9.230524391	14.07866685	1.09055934	1.991816123	0.69
Animal 4	65	8.366402366	14.07866685	2.67267984	1.991816123	0.69
Animal 4	65	23.42069309	14.07866685	3.24003561	1.991816123	0.69
Animal 4	65	15.29704757	14.07866685	0.9639897	1.991816123	0.69
Animal 4	100	3.66769826	12.92993441	0.57250686	1.876626186	0.69
Animal 4	100	15.56967379	12.92993441	2.99131155	1.876626186	0.69
Animal 4	100	8.185626642	12.92993441	1.19873223	1.876626186	0.69
Animal 4	100	9.705145643	12.92993441	2.11047516	1.876626186	0.69
Animal 4	100	8.376396369	12.92993441	1.02874626	1.876626186	0.69
Animal 4	100	15.41846721	12.92993441	2.86547778	1.876626186	0.69
Animal 4	100	6.123855352	12.92993441	0.59531883	1.876626186	0.69
Animal 4	100	11.29261773	12.92993441	0.6696417	1.876626186	0.69
Animal 4	100	40.61871227	12.92993441	4.57858314	1.876626186	0.69
Animal 4	100	16.43966653	12.92993441	2.60718741	1.876626186	0.69

Animal 4	100	15.33915456	12.92993441	3.68597283	1.876626186	0.69
Animal 4	100	5.916074807	12.92993441	0.43710678	1.876626186	0.69
Animal 4	100	9.57318535	12.92993441	2.08839906	1.876626186	0.69
Animal 4	100	14.79280719	12.92993441	0.84330702	1.876626186	0.69
Animal 4	145	10.21108118	11.88215957	2.53507215	2.335973323	0.69
Animal 4	145	9.064092701	11.88215957	0.75279501	2.335973323	0.69
Animal 4	145	16.89159288	11.88215957	4.4078613	2.335973323	0.69
Animal 4	145	8.765302609	11.88215957	1.23994095	2.335973323	0.69
Animal 4	145	10.69078551	11.88215957	2.16198606	2.335973323	0.69
Animal 4	145	13.49964751	11.88215957	2.64030156	2.335973323	0.69
Animal 4	145	11.06470289	11.88215957	0.79547547	2.335973323	0.69
Animal 4	145	9.89889379	11.88215957	0.44446548	2.335973323	0.69
Animal 4	145	24.60242787	11.88215957	8.7936465	2.335973323	0.69
Animal 4	145	8.482926493	11.88215957	1.29439533	2.335973323	0.69
Animal 4	145	22.44922927	11.88215957	6.95470737	2.335973323	0.69
Animal 4	145	9.516792082	11.88215957	1.19578875	2.335973323	0.69
Animal 4	145	6.284680415	11.88215957	0.99489624	2.335973323	0.69
Animal 4	145	16.80783045	11.88215957	1.98832074	2.335973323	0.69
Animal 4	145	4.011243085	11.88215957	0.41723829	2.335973323	0.69
Animal 4	145	7.873324376	11.88215957	0.75868197	2.335973323	0.69
Animal 5	65	19.57847097	19.72460185	1.22228007	2.02511424	0.6
Animal 5	65	10.53024506	19.72460185	0.63211233	2.02511424	0.6
Animal 5	65	12.51579241	19.72460185	1.75210647	2.02511424	0.6
Animal 5	65	20.99827807	19.72460185	2.52992106	2.02511424	0.6
Animal 5	65	44.30596429	19.72460185	3.56308254	2.02511424	0.6
Animal 5	65	20.38526488	19.72460185	1.61302704	2.02511424	0.6
Animal 5	65	34.76985434	19.72460185	6.45284403	2.02511424	0.6
Animal 5	65	14.35882332	19.72460185	1.43788998	2.02511424	0.6
Animal 5	65	9.74208596	19.72460185	0.43637091	2.02511424	0.6
Animal 5	65	10.06123917	19.72460185	0.61150797	2.02511424	0.6
Animal 5	100	8.042947663	18.07449162	1.13691915	1.935127851	0.6
Animal 5	100	16.31869089	18.07449162	1.46658891	1.935127851	0.6

Animal 5	100	9.646839927	18.07449162	1.14501372	1.935127851	0.6
Animal 5	100	34.40854184	18.07449162	1.16561808	1.935127851	0.6
Animal 5	100	13.79319164	18.07449162	0.44372961	1.935127851	0.6
Animal 5	100	13.42770458	18.07449162	1.36503885	1.935127851	0.6
Animal 5	100	8.352420912	18.07449162	0.515109	1.935127851	0.6
Animal 5	100	47.00347705	18.07449162	4.42772979	1.935127851	0.6
Animal 5	100	19.87073967	18.07449162	5.50504347	1.935127851	0.6
Animal 5	100	22.58396141	18.07449162	1.60640421	1.935127851	0.6
Animal 5	100	24.27487318	18.07449162	4.6801332	1.935127851	0.6
Animal 5	100	10.8632558	18.07449162	2.07662514	1.935127851	0.6
Animal 5	100	17.51707523	18.07449162	0.69466128	1.935127851	0.6
Animal 5	100	6.939162877	18.07449162	0.86317551	1.935127851	0.6
Animal 5	145	13.32335644	21.35761844	1.56593136	3.78601242	0.6
Animal 5	145	28.40927344	21.35761844	3.2746215	3.78601242	0.6
Animal 5	145	36.90968066	21.35761844	6.87670515	3.78601242	0.6
Animal 5	145	21.58603506	21.35761844	7.726635	3.78601242	0.6
Animal 5	145	29.51258148	21.35761844	7.98639711	3.78601242	0.6
Animal 5	145	11.07782931	21.35761844	1.68146295	3.78601242	0.6
Animal 5	145	15.12916551	21.35761844	2.99131155	3.78601242	0.6
Animal 5	145	25.33076097	21.35761844	5.08559757	3.78601242	0.6
Animal 5	145	17.18994963	21.35761844	1.76167278	3.78601242	0.6
Animal 5	145	19.82769637	21.35761844	3.87950664	3.78601242	0.6
Animal 5	145	14.61517885	21.35761844	2.09134254	3.78601242	0.6
Animal 5	145	22.24420864	21.35761844	4.12896657	3.78601242	0.6
Animal 5	145	13.76607552	21.35761844	4.00018932	3.78601242	0.6
Animal 5	145	37.6831095	21.35761844	1.95079137	3.78601242	0.6
Animal 5	145	10.90495558	21.35761844	3.81842943	3.78601242	0.6
Animal 5	145	29.99303372	21.35761844	3.60355539	3.78601242	0.6
Animal 5	145	11.94949662	21.35761844	2.72934183	3.78601242	0.6
Animal 5	145	10.00559967	21.35761844	0.8536092	3.78601242	0.6
Animal 5	145	36.3367633	21.35761844	5.92816872	3.78601242	0.6
Animal 6	65	1.083156312	17.26297307	0.57839382	2.58314899	0.333

Animal 6	65	17.16001518	17.26297307	1.88088372	2.58314899	0.333
Animal 6	65	6.588753086	17.26297307	2.18111868	2.58314899	0.333
Animal 6	65	22.25861207	17.26297307	3.27167802	2.58314899	0.333
Animal 6	65	7.365471815	17.26297307	0.71158629	2.58314899	0.333
Animal 6	65	14.90343583	17.26297307	3.69480327	2.58314899	0.333
Animal 6	65	20.14474943	17.26297307	3.7897305	2.58314899	0.333
Animal 6	65	37.95785036	17.26297307	3.87729903	2.58314899	0.333
Animal 6	65	27.90471354	17.26297307	3.26284758	2.58314899	0.333
Animal 6	100	19.16173522	22.37481645	5.13931608	4.905782479	0.333
Animal 6	100	15.44636311	22.37481645	4.10468286	4.905782479	0.333
Animal 6	100	9.217519301	22.37481645	1.43715411	4.905782479	0.333
Animal 6	100	29.50674812	22.37481645	4.77506043	4.905782479	0.333
Animal 6	100	15.36540721	22.37481645	3.38941722	4.905782479	0.333
Animal 6	100	42.46050651	22.37481645	17.03612637	4.905782479	0.333
Animal 6	100	31.40777694	22.37481645	6.58162128	4.905782479	0.333
Animal 6	100	32.1377395	22.37481645	8.11149501	4.905782479	0.333
Animal 6	100	23.10804642	22.37481645	4.17679812	4.905782479	0.333
Animal 6	100	15.76716666	22.37481645	0.98238645	4.905782479	0.333
Animal 6	100	33.35792358	22.37481645	2.3842188	4.905782479	0.333
Animal 6	100	16.23697475	22.37481645	2.62337655	4.905782479	0.333
Animal 6	100	25.57293704	22.37481645	6.83696817	4.905782479	0.333
Animal 6	100	4.500585903	22.37481645	1.10233326	4.905782479	0.333
Animal 6	145	21.52759299	26.7764601	4.69852995	8.312440082	0.333
Animal 6	145	40.3124728	26.7764601	12.34421925	8.312440082	0.333
Animal 6	145	19.54197077	26.7764601	6.13641993	8.312440082	0.333
Animal 6	145	23.59903546	26.7764601	7.56989469	8.312440082	0.333
Animal 6	145	13.85528395	26.7764601	2.74258749	8.312440082	0.333
Animal 6	145	41.74027011	26.7764601	13.48261014	8.312440082	0.333
Animal 6	145	12.25096373	26.7764601	2.04498273	8.312440082	0.333
Animal 6	145	54.53166479	26.7764601	21.07605267	8.312440082	0.333
Animal 6	145	26.56870469	26.7764601	9.5000817	8.312440082	0.333
Animal 6	145	47.09205924	26.7764601	12.56203677	8.312440082	0.333

Animal 6	145	17.12303795	26.7764601	3.70510545	8.312440082	0.333
Animal 6	145	34.09935066	26.7764601	12.6937575	8.312440082	0.333
Animal 6	145	13.01854056	26.7764601	5.67282183	8.312440082	0.333
Animal 6	145	9.609493697	26.7764601	2.14506105	8.312440082	0.333
Animal 7	145	28.98800864	26.80010396	8.62586814	8.839491201	0.3
Animal 7	145	17.35531464	26.80010396	3.68082174	8.839491201	0.3
Animal 7	145	79.13894744	26.80010396	30.88593564	8.839491201	0.3
Animal 7	145	6.540186985	26.80010396	0.69318954	8.839491201	0.3
Animal 7	145	40.04167817	26.80010396	14.64822822	8.839491201	0.3
Animal 7	145	21.12915606	26.80010396	7.87528074	8.839491201	0.3
Animal 7	145	37.18873738	26.80010396	11.62895361	8.839491201	0.3
Animal 7	145	7.166316622	26.80010396	0.89555379	8.839491201	0.3
Animal 7	145	10.25563845	26.80010396	1.99567944	8.839491201	0.3
Animal 7	145	20.1970552	26.80010396	7.46540115	8.839491201	0.3
Animal 8	65	21.9026847	25.74843594	1.60714008	3.96854691	0.077
Animal 8	65	30.13153995	25.74843594	5.5852533	3.96854691	0.077
Animal 8	65	20.73245154	25.74843594	4.23346011	3.96854691	0.077
Animal 8	65	10.18444101	25.74843594	2.07368166	3.96854691	0.077
Animal 8	65	45.7910625	25.74843594	6.3431994	3.96854691	0.077
Animal 8	100	43.12166594	22.00598466	11.57744271	5.236377333	0.077
Animal 8	100	29.72496988	22.00598466	9.06223905	5.236377333	0.077
Animal 8	100	18.62263454	22.00598466	0.76604067	5.236377333	0.077
Animal 8	100	18.90498667	22.00598466	3.82725987	5.236377333	0.077
Animal 8	100	21.97853943	22.00598466	7.37488914	5.236377333	0.077
Animal 8	100	30.70518492	22.00598466	8.42497563	5.236377333	0.077
Animal 8	100	17.81775921	22.00598466	2.86621365	5.236377333	0.077
Animal 8	100	4.361850119	22.00598466	1.76829561	5.236377333	0.077
Animal 8	100	28.93653245	22.00598466	5.62131093	5.236377333	0.077
Animal 8	100	5.88572345	22.00598466	1.07510607	5.236377333	0.077
Animal 8	145	36.00791919	25.11446807	15.9389442	5.806081197	0.077
Animal 8	145	49.67871307	25.11446807	11.04835218	5.806081197	0.077
Animal 8	145	31.79664734	25.11446807	0.44299374	5.806081197	0.077

Animal 8	145	23.75422595	25.11446807	3.14878773	5.806081197	0.077
Animal 8	145	19.82009567	25.11446807	4.27025361	5.806081197	0.077
Animal 8	145	39.22133096	25.11446807	11.34196431	5.806081197	0.077
Animal 8	145	19.35287083	25.11446807	1.79405106	5.806081197	0.077
Animal 8	145	22.58938652	25.11446807	7.08422049	5.806081197	0.077
Animal 8	145	15.85233684	25.11446807	3.58957386	5.806081197	0.077
Animal 8	145	3.579498598	25.11446807	0.66154713	5.806081197	0.077
Animal 8	145	14.60612381	25.11446807	4.54620486	5.806081197	0.077
Animal 9	65	19.7095399	39.27876262	5.11650411	7.76146618	0.2
Animal 9	65	14.90986575	39.27876262	0.62916885	7.76146618	0.2
Animal 9	65	83.2168822	39.27876262	17.53872558	7.76146618	0.2
Animal 9	100	9.465591318	28.96835931	1.77933366	4.756998166	0.2
Animal 9	100	16.88005653	28.96835931	3.25475301	4.756998166	0.2
Animal 9	100	27.73715315	28.96835931	4.16281659	4.756998166	0.2
Animal 9	100	37.47533466	28.96835931	9.10124016	4.756998166	0.2
Animal 9	100	20.2043116	28.96835931	1.70648253	4.756998166	0.2
Animal 9	100	61.71298536	28.96835931	7.63023603	4.756998166	0.2
Animal 9	100	14.32503806	28.96835931	1.3907943	4.756998166	0.2
Animal 9	100	55.70603145	28.96835931	3.35041611	4.756998166	0.2
Animal 9	100	25.50174391	28.96835931	6.20706345	4.756998166	0.2
Animal 9	100	32.42298396	28.96835931	10.52882796	4.756998166	0.2
Animal 9	100	17.22072245	28.96835931	3.21501603	4.756998166	0.2
Animal 9	145	27.50453877	22.28228044	8.18949723	6.790073182	0.2
Animal 9	145	22.14997895	22.28228044	6.65668002	6.790073182	0.2
Animal 9	145	29.50061086	22.28228044	10.80919443	6.790073182	0.2
Animal 9	145	18.64283226	22.28228044	7.47938268	6.790073182	0.2
Animal 9	145	28.25072167	22.28228044	7.82597745	6.790073182	0.2
Animal 9	145	4.347953166	22.28228044	0.52320357	6.790073182	0.2
Animal 9	145	40.213323	22.28228044	11.4648546	6.790073182	0.2
Animal 9	145	17.20945657	22.28228044	6.9539715	6.790073182	0.2
Animal 9	145	14.25519246	22.28228044	3.56529015	6.790073182	0.2
Animal 9	145	29.50493048	22.28228044	9.25577286	6.790073182	0.2

Animal 9	145	13.52554665	22.28228044	1.96698051	6.790073182	0.2
Animal 10	100	6.45103742	13.28051314	0.61224384	2.52655155	0.154
Animal 10	100	40.31373263	13.28051314	8.75390952	2.52655155	0.154
Animal 10	100	5.451962659	13.28051314	0.97429188	2.52655155	0.154
Animal 10	100	14.64566521	13.28051314	3.67272717	2.52655155	0.154
Animal 10	100	12.97606858	13.28051314	0.82785375	2.52655155	0.154
Animal 10	100	4.786040095	13.28051314	0.61371558	2.52655155	0.154
Animal 10	100	5.561145156	13.28051314	1.13029632	2.52655155	0.154
Animal 10	100	13.44584656	13.28051314	1.24950726	2.52655155	0.154
Animal 10	100	20.16099686	13.28051314	4.24964925	2.52655155	0.154
Animal 10	100	10.10961869	13.28051314	2.97144306	2.52655155	0.154
Animal 10	100	8.241630382	13.28051314	0.52026009	2.52655155	0.154
Animal 10	100	19.26556328	13.28051314	2.58952653	2.52655155	0.154
Animal 10	100	15.63279474	13.28051314	2.80955166	2.52655155	0.154
Animal 10	100	22.5142157	13.28051314	4.41742761	2.52655155	0.154
Animal 10	100	14.05792008	13.28051314	5.71991751	2.52655155	0.154
Animal 10	100	7.575109148	13.28051314	1.25392248	2.52655155	0.154
Animal 10	100	9.235304423	13.28051314	2.34668943	2.52655155	0.154
Animal 10	100	17.29579368	13.28051314	2.72198313	2.52655155	0.154
Animal 10	100	4.609304442	13.28051314	0.56956338	2.52655155	0.154
Animal 10	145	14.48525631	22.85540862	1.80067389	4.003500735	0.154
Animal 10	145	24.03227627	22.85540862	5.56832829	4.003500735	0.154
Animal 10	145	15.45657464	22.85540862	1.06774737	4.003500735	0.154
Animal 10	145	55.2192216	22.85540862	7.5205914	4.003500735	0.154
Animal 10	145	16.34934043	22.85540862	2.04498273	4.003500735	0.154
Animal 10	145	12.98842899	22.85540862	1.29733881	4.003500735	0.154
Animal 10	145	27.80816795	22.85540862	5.02231275	4.003500735	0.154
Animal 10	145	21.54522252	22.85540862	4.42331457	4.003500735	0.154
Animal 10	145	26.12648198	22.85540862	5.41673907	4.003500735	0.154
Animal 10	145	18.28394224	22.85540862	3.62268801	4.003500735	0.154
Animal 10	145	36.42385067	22.85540862	9.934245	4.003500735	0.154
Animal 10	145	23.66548602	22.85540862	6.4167864	4.003500735	0.154

Animal 10	145	16.90067644	22.85540862	3.8633175	4.003500735	0.154
Animal 10	145	47.98505174	22.85540862	7.41977721	4.003500735	0.154
Animal 10	145	6.589018463	22.85540862	1.84409022	4.003500735	0.154
Animal 10	145	17.47458782	22.85540862	4.32470799	4.003500735	0.154
Animal 10	145	9.774541702	22.85540862	0.56367642	4.003500735	0.154
Animal 10	145	22.05653845	22.85540862	7.32779346	4.003500735	0.154
Animal 10	145	26.55031513	22.85540862	3.64402824	4.003500735	0.154
Animal 10	145	18.14410337	22.85540862	2.39304924	4.003500735	0.154
Animal 10	145	24.64922152	22.85540862	1.63289553	4.003500735	0.154
Animal 10	145	20.31068545	22.85540862	0.92793207	4.003500735	0.154
Animal 11	65	23.23013514	23.79350187	7.753862	5.191317528	0.09
Animal 11	65	26.74648806	23.79350187	3.43724877	5.191317528	0.09
Animal 11	65	25.08589663	23.79350187	4.52633637	5.191317528	0.09
Animal 11	65	18.37002329	23.79350187	1.97654682	5.191317528	0.09
Animal 11	65	43.69224571	23.79350187	12.53407371	5.191317528	0.09
Animal 11	65	5.636222379	23.79350187	0.9198375	5.191317528	0.09
Animal 11	100	11.87733802	17.30661246	4.28055579	2.669937052	0.09
Animal 11	100	19.69323979	17.30661246	0.76604067	2.669937052	0.09
Animal 11	100	25.40659937	17.30661246	3.90231861	2.669937052	0.09
Animal 11	100	18.41567877	17.30661246	5.67944466	2.669937052	0.09
Animal 11	100	9.73479791	17.30661246	0.71011455	2.669937052	0.09
Animal 11	100	23.25745203	17.30661246	2.22527088	2.669937052	0.09
Animal 11	100	15.73072542	17.30661246	1.30837686	2.669937052	0.09
Animal 11	100	10.61055041	17.30661246	0.56588403	2.669937052	0.09
Animal 11	100	31.50135659	17.30661246	4.91193225	2.669937052	0.09
Animal 11	100	6.420226003	17.30661246	3.78899463	2.669937052	0.09
Animal 11	100	17.72477276	17.30661246	1.23037464	2.669937052	0.09
Animal 11	145	27.11482462	19.27510298	12.7158336	6.351735492	0.09
Animal 11	145	17.22309694	19.27510298	1.29660294	6.351735492	0.09
Animal 11	145	11.36955319	19.27510298	5.10914541	6.351735492	0.09
Animal 11	145	21.12487315	19.27510298	7.80463722	6.351735492	0.09
Animal 11	145	31.63583661	19.27510298	5.78835342	6.351735492	0.09

Animal 11	145	14.32778186	19.27510298	4.95608445	6.351735492	0.09
Animal 11	145	7.843399159	19.27510298	5.24233788	6.351735492	0.09
Animal 11	145	9.05968398	19.27510298	0.70128411	6.351735492	0.09
Animal 11	145	16.74478884	19.27510298	10.00415265	6.351735492	0.09
Animal 11	145	36.30719148	19.27510298	9.89892324	6.351735492	0.09
Animal 12	65	21.17420731	15.4635028	2.42616339	2.255257583	0
Animal 12	65	18.003615	15.4635028	4.45127763	2.255257583	0
Animal 12	65	7.316635741	15.4635028	1.97581095	2.255257583	0
Animal 12	65	13.20383933	15.4635028	1.28998011	2.255257583	0
Animal 12	65	16.9244366	15.4635028	4.22757315	2.255257583	0
Animal 12	65	9.881124008	15.4635028	0.88893096	2.255257583	0
Animal 12	65	8.856176507	15.4635028	1.04346366	2.255257583	0
Animal 12	65	7.855355178	15.4635028	0.91321467	2.255257583	0
Animal 12	65	17.85425966	15.4635028	3.30332043	2.255257583	0
Animal 12	65	22.01497937	15.4635028	3.64697172	2.255257583	0
Animal 12	65	11.38871566	15.4635028	2.03394468	2.255257583	0
Animal 12	65	14.34841367	15.4635028	2.3695014	2.255257583	0
Animal 12	65	16.15558315	15.4635028	1.67263251	2.255257583	0
Animal 12	65	16.45849418	15.4635028	1.04787888	2.255257583	0
Animal 12	65	28.67184697	15.4635028	1.32162252	2.255257583	0
Animal 12	65	17.30836246	15.4635028	3.47183466	2.255257583	0
Animal 12	100	18.87904104	34.87900782	3.0832953	4.194786053	0
Animal 12	100	41.56069495	34.87900782	2.05528491	4.194786053	0
Animal 12	100	30.16722631	34.87900782	2.05602078	4.194786053	0
Animal 12	100	41.15673414	34.87900782	3.76397505	4.194786053	0
Animal 12	100	13.93745318	34.87900782	1.97728269	4.194786053	0
Animal 12	100	55.23378614	34.87900782	8.45073108	4.194786053	0
Animal 12	100	22.48705224	34.87900782	3.73233264	4.194786053	0
Animal 12	100	61.53184519	34.87900782	5.40202167	4.194786053	0
Animal 12	100	22.37571062	34.87900782	7.50072291	4.194786053	0
Animal 12	100	59.58773303	34.87900782	14.96391645	4.194786053	0
Animal 12	100	45.79905371	34.87900782	4.50058092	4.194786053	0

Animal 12	100	10.51596104	34.87900782	1.71604884	4.194786053	0
Animal 12	100	18.8764648	34.87900782	1.09203108	4.194786053	0
Animal 12	100	29.44615587	34.87900782	1.58579985	4.194786053	0
Animal 12	100	35.69955031	34.87900782	1.42464432	4.194786053	0
Animal 12	100	50.02894123	34.87900782	5.3792097	4.194786053	0
Animal 12	100	55.08662056	34.87900782	4.8273072	4.194786053	0
Animal 12	100	15.45211649	34.87900782	1.99494357	4.194786053	0
Animal 12	145	17.94460092	34.09863954	4.58079075	5.79107294	0
Animal 12	145	5.846627888	34.09863954	0.69613302	5.79107294	0
Animal 12	145	14.15571539	34.09863954	1.23846921	5.79107294	0
Animal 12	145	72.06390856	34.09863954	5.82293931	5.79107294	0
Animal 12	145	57.74798533	34.09863954	13.48481775	5.79107294	0
Animal 12	145	112.7563266	34.09863954	16.98976656	5.79107294	0
Animal 12	145	5.002632869	34.09863954	0.53571336	5.79107294	0
Animal 12	145	59.92303051	34.09863954	16.1376291	5.79107294	0
Animal 12	145	40.51722671	34.09863954	2.24072415	5.79107294	0
Animal 12	145	28.76456788	34.09863954	5.15035413	5.79107294	0
Animal 12	145	45.68435526	34.09863954	12.37071057	5.79107294	0
Animal 12	145	29.05139742	34.09863954	9.17261955	5.79107294	0
Animal 12	145	12.05657239	34.09863954	3.96192408	5.79107294	0
Animal 12	145	16.75960994	34.09863954	1.70942601	5.79107294	0
Animal 12	145	24.72623476	34.09863954	2.61086676	5.79107294	0
Animal 12	145	11.70544142	34.09863954	1.41066279	5.79107294	0
Animal 12	145	33.95447378	34.09863954	4.69705821	5.79107294	0
Animal 12	145	15.28214354	34.09863954	3.46006074	5.79107294	0
Animal 12	145	37.40290973	34.09863954	5.97820788	5.79107294	0
Animal 12	145	60.68107522	34.09863954	6.35276571	5.79107294	0
Animal 12	145	27.85500553	34.09863954	5.06131386	5.79107294	0
Animal 12	145	35.87953187	34.09863954	6.29463198	5.79107294	0
Animal 12	145	18.50733591	34.09863954	3.23709213	5.79107294	0
Animal 13	65	16.83	28.39	3.76	5.94	0
Animal 13	65	45.36	28.39	10.82	5.94	0

Animal 13	65	56.30	28.39	10.61	5.94	0
Animal 13	65	22.14	28.39	7.04	5.94	0
Animal 13	65	29.79	28.39	5.61	5.94	0
Animal 13	65	17.29	28.39	1.23	5.94	0
Animal 13	65	11.03	28.39	2.52	5.94	0
Animal 13	100	11.26	21.96	0.63	3.20	0
Animal 13	100	21.78	21.96	3.81	3.20	0
Animal 13	100	31.95	21.96	5.10	3.20	0
Animal 13	100	16.62	21.96	0.98	3.20	0
Animal 13	100	20.58	21.96	1.98	3.20	0
Animal 13	100	83.91	21.96	11.52	3.20	0
Animal 13	100	18.42	21.96	4.52	3.20	0
Animal 13	100	10.86	21.96	0.76	3.20	0
Animal 13	100	13.40	21.96	3.88	3.20	0
Animal 13	100	10.82	21.96	2.06	3.20	0
Animal 13	100	34.52	21.96	9.14	3.20	0
Animal 13	100	18.13	21.96	2.07	3.20	0
Animal 13	100	36.73	21.96	4.59	3.20	0
Animal 13	100	25.84	21.96	4.83	3.20	0
Animal 13	100	8.75	21.96	0.70	3.20	0
Animal 13	100	14.54	21.96	0.96	3.20	0
Animal 13	100	16.97	21.96	1.79	3.20	0
Animal 13	100	10.61	21.96	0.55	3.20	0
Animal 13	100	18.37	21.96	2.67	3.20	0
Animal 13	100	15.12	21.96	1.37	3.20	0
Animal 13	145	12.75	20.11	2.85	4.70	0
Animal 13	145	15.32	20.11	2.23	4.70	0
Animal 13	145	24.67	20.11	8.28	4.70	0
Animal 13	145	14.83	20.11	2.31	4.70	0
Animal 13	145	32.91	20.11	5.59	4.70	0
Animal 13	145	8.85	20.11	0.66	4.70	0
Animal 13	145	59.83	20.11	9.93	4.70	0

Animal 13	145	17.18	20.11	6.67	4.70	0
Animal 13	145	6.83	20.11	2.01	4.70	0
Animal 13	145	25.90	20.11	5.12	4.70	0
Animal 13	145	25.65	20.11	8.80	4.70	0
Animal 13	145	29.11	20.11	10.01	4.70	0
Animal 13	145	19.30	20.11	8.17	4.70	0
Animal 13	145	29.22	20.11	6.06	4.70	0
Animal 13	145	7.90	20.11	0.84	4.70	0
Animal 13	145	15.93	20.11	5.06	4.70	0
Animal 13	145	13.34	20.11	1.52	4.70	0
Animal 13	145	8.78	20.11	1.03	4.70	0
Animal 13	145	13.76	20.11	2.22	4.70	0
Animal 14	65	16.93984468	14.6534388	3.14510838	2.767791038	0.059
Animal 14	65	9.229569872	14.6534388	1.23184638	2.767791038	0.059
Animal 14	65	7.520181647	14.6534388	0.61371558	2.767791038	0.059
Animal 14	65	7.767453856	14.6534388	1.16414634	2.767791038	0.059
Animal 14	65	28.13014852	14.6534388	4.66615167	2.767791038	0.059
Animal 14	65	5.454469946	14.6534388	0.78370155	2.767791038	0.059
Animal 14	65	26.51289992	14.6534388	7.94813187	2.767791038	0.059
Animal 14	65	15.67294195	14.6534388	2.58952653	2.767791038	0.059
Animal 14	100	64.56574835	27.96780384	7.43596635	3.595166472	0.059
Animal 14	100	23.15594715	27.96780384	2.26574373	3.595166472	0.059
Animal 14	100	71.61909993	27.96780384	12.38542797	3.595166472	0.059
Animal 14	100	17.77294112	27.96780384	1.2362616	3.595166472	0.059
Animal 14	100	25.52956764	27.96780384	3.12229641	3.595166472	0.059
Animal 14	100	19.98921154	27.96780384	2.75656902	3.595166472	0.059
Animal 14	100	13.70662017	27.96780384	1.22375181	3.595166472	0.059
Animal 14	100	42.28674447	27.96780384	3.72865329	3.595166472	0.059
Animal 14	100	31.50347798	27.96780384	2.71683204	3.595166472	0.059
Animal 14	100	41.16193294	27.96780384	8.8598748	3.595166472	0.059
Animal 14	100	7.534167475	27.96780384	0.70128411	3.595166472	0.059
Animal 14	100	7.061196469	27.96780384	0.69466128	3.595166472	0.059

Animal 14	100	21.77849629	27.96780384	3.85007184	3.595166472	0.059
Animal 14	100	17.13555853	27.96780384	1.68440643	3.595166472	0.059
Animal 14	100	14.71634749	27.96780384	1.2656964	3.595166472	0.059

Supplemental Table 3. Trends in Perfusion Domain Flow and Volume Across Gestation.

Animal Number	Gestational Age	Perfusion domain flow by MRI measurement (mL/min)	Average perfusion domain flow by gestational age (mL/min)	Trend in average flow over gestation	Perfusion domain volume by MRI measurement (mL)	Average perfusion domain volume by gestational age (mL)	Trend in average volume over gestation	Average Total Pathology Score at Term ([presence of CHIV at term+presence of PI at term+presence of MDV at term]/# perfusion domains at term)	Average presence of PI per cotyledon (# cotyledons with PI/total # cotyledons)
Animal 1	65	6.810999835	17.2139	-0.06517	0.56956338	2.5512613	-0.00285	1.417	0.9166667
Animal 1	65	9.200927386	17.2139	-0.06517	1.63215966	2.5512613	-0.00285	1.417	0.9166667
Animal 1	65	10.25477129	17.2139	-0.06517	0.80798526	2.5512613	-0.00285	1.417	0.9166667
Animal 1	65	21.12776964	17.2139	-0.06517	5.27839551	2.5512613	-0.00285	1.417	0.9166667
Animal 1	65	17.53730004	17.2139	-0.06517	3.33128349	2.5512613	-0.00285	1.417	0.9166667
Animal 1	65	49.80882369	17.2139	-0.06517	5.51976087	2.5512613	-0.00285	1.417	0.9166667
Animal 1	65	5.756710909	17.2139	-0.06517	0.71968086	2.5512613	-0.00285	1.417	0.9166667
Animal 1	100	26.55497342	20.425484	-0.06517	5.30341509	4.3570194	-0.00285	1.417	0.9166667
Animal 1	100	38.6836401	20.425484	-0.06517	10.02328527	4.3570194	-0.00285	1.417	0.9166667
Animal 1	100	31.17727643	20.425484	-0.06517	8.1019287	4.3570194	-0.00285	1.417	0.9166667
Animal 1	100	13.7946318	20.425484	-0.06517	2.90962998	4.3570194	-0.00285	1.417	0.9166667
Animal 1	100	16.13283913	20.425484	-0.06517	2.60424393	4.3570194	-0.00285	1.417	0.9166667

Animal 1	100	10.9478075	20.425484	-0.06517	2.69402007	4.3570194	-0.00285	1.417	0.9166667
Animal 1	100	23.92685613	20.425484	-0.06517	7.23286623	4.3570194	-0.00285	1.417	0.9166667
Animal 1	100	9.672075511	20.425484	-0.06517	1.83673152	4.3570194	-0.00285	1.417	0.9166667
Animal 1	100	9.267339823	20.425484	-0.06517	1.38269973	4.3570194	-0.00285	1.417	0.9166667
Animal 1	100	33.11672948	20.425484	-0.06517	3.97296213	4.3570194	-0.00285	1.417	0.9166667
Animal 1	100	11.40615008	20.425484	-0.06517	1.86543045	4.3570194	-0.00285	1.417	0.9166667
Animal 1	145	17.80776492	12.439837	-0.06517	2.80072122	2.4760019	-0.00285	1.417	0.9166667
Animal 1	145	37.82244845	12.439837	-0.06517	8.42939085	2.4760019	-0.00285	1.417	0.9166667
Animal 1	145	10.28632031	12.439837	-0.06517	2.27751765	2.4760019	-0.00285	1.417	0.9166667
Animal 1	145	17.80977906	12.439837	-0.06517	3.17012796	2.4760019	-0.00285	1.417	0.9166667
Animal 1	145	8.499413413	12.439837	-0.06517	4.21064814	2.4760019	-0.00285	1.417	0.9166667
Animal 1	145	4.606968068	12.439837	-0.06517	0.64094277	2.4760019	-0.00285	1.417	0.9166667
Animal 1	145	10.72596397	12.439837	-0.06517	0.9639897	2.4760019	-0.00285	1.417	0.9166667
Animal 1	145	7.21019675	12.439837	-0.06517	2.26721547	2.4760019	-0.00285	1.417	0.9166667
Animal 1	145	4.933158354	12.439837	-0.06517	0.68730258	2.4760019	-0.00285	1.417	0.9166667
Animal 1	145	6.464012929	12.439837	-0.06517	1.03095387	2.4760019	-0.00285	1.417	0.9166667
Animal 1	145	10.672182	12.439837	-0.06517	0.75721023	2.4760019	-0.00285	1.417	0.9166667
Animal 2	65	20.86132006	13.808471	0.1285	8.63984967	2.5909983	0.03092	0.93	0.4285714
Animal 2	65	20.63089443	13.808471	0.1285	2.07883275	2.5909983	0.03092	0.93	0.4285714
Animal 2	65	11.97189173	13.808471	0.1285	1.13986263	2.5909983	0.03092	0.93	0.4285714
Animal 2	65	10.80603631	13.808471	0.1285	1.61744226	2.5909983	0.03092	0.93	0.4285714
Animal 2	65	8.782213459	13.808471	0.1285	0.86317551	2.5909983	0.03092	0.93	0.4285714
Animal 2	65	11.53743403	13.808471	0.1285	2.1119469	2.5909983	0.03092	0.93	0.4285714
Animal 2	65	12.0695071	13.808471	0.1285	1.68587817	2.5909983	0.03092	0.93	0.4285714
Animal 2	100	30.16949378	19.696484	0.1285	2.416597	2.1304775	0.03092	0.93	0.4285714
Animal 2	100	14.54649245	19.696484	0.1285	0.647566	2.1304775	0.03092	0.93	0.4285714
Animal 2	100	12.40496722	19.696484	0.1285	3.334963	2.1304775	0.03092	0.93	0.4285714
Animal 2	100	28.9756122	19.696484	0.1285	3.625631	2.1304775	0.03092	0.93	0.4285714
Animal 2	100	17.74764434	19.696484	0.1285	0.685095	2.1304775	0.03092	0.93	0.4285714
Animal 2	100	29.0527778	19.696484	0.1285	2.500486	2.1304775	0.03092	0.93	0.4285714
Animal 2	100	15.168092	19.696484	0.1285	2.117098	2.1304775	0.03092	0.93	0.4285714
Animal 2	100	9.721139739	19.696484	0.1285	0.576186	2.1304775	0.03092	0.93	0.4285714

Animal 2	100	13.97951744	19.696484	0.1285	2.039832	2.1304775	0.03092	0.93	0.4285714
Animal 2	100	25.62287644	19.696484	0.1285	2.091343	2.1304775	0.03092	0.93	0.4285714
Animal 2	100	19.27271194	19.696484	0.1285	3.400455	2.1304775	0.03092	0.93	0.4285714
Animal 2	145	20.98500041	24.197861	0.1285	3.88171425	4.9412538	0.03092	0.93	0.4285714
Animal 2	145	29.76877514	24.197861	0.1285	0.89187444	4.9412538	0.03092	0.93	0.4285714
Animal 2	145	33.99257692	24.197861	0.1285	3.25916823	4.9412538	0.03092	0.93	0.4285714
Animal 2	145	18.11809901	24.197861	0.1285	1.66085859	4.9412538	0.03092	0.93	0.4285714
Animal 2	145	35.62768364	24.197861	0.1285	10.51705404	4.9412538	0.03092	0.93	0.4285714
Animal 2	145	27.56534709	24.197861	0.1285	3.15099534	4.9412538	0.03092	0.93	0.4285714
Animal 2	145	21.44441466	24.197861	0.1285	6.62871696	4.9412538	0.03092	0.93	0.4285714
Animal 2	145	9.541079723	24.197861	0.1285	0.61886667	4.9412538	0.03092	0.93	0.4285714
Animal 2	145	22.11752757	24.197861	0.1285	11.24998056	4.9412538	0.03092	0.93	0.4285714
Animal 2	145	3.160070539	24.197861	0.1285	1.05450171	4.9412538	0.03092	0.93	0.4285714
Animal 2	145	42.39303128	24.197861	0.1285	14.00654958	4.9412538	0.03092	0.93	0.4285714
Animal 2	145	35.20877812	24.197861	0.1285	5.12974977	4.9412538	0.03092	0.93	0.4285714
Animal 2	145	14.64981013	24.197861	0.1285	2.18626977	4.9412538	0.03092	0.93	0.4285714
Animal 4	65	9.230524391	14.078667	-0.02726	1.09055934	1.9918161	0.004577	0.69	0.5
Animal 4	65	8.366402366	14.078667	-0.02726	2.67267984	1.9918161	0.004577	0.69	0.5
Animal 4	65	23.42069309	14.078667	-0.02726	3.24003561	1.9918161	0.004577	0.69	0.5
Animal 4	65	15.29704757	14.078667	-0.02726	0.9639897	1.9918161	0.004577	0.69	0.5
Animal 4	100	3.66769826	12.929934	-0.02726	0.57250686	1.8766262	0.004577	0.69	0.5
Animal 4	100	15.56967379	12.929934	-0.02726	2.99131155	1.8766262	0.004577	0.69	0.5
Animal 4	100	8.185626642	12.929934	-0.02726	1.19873223	1.8766262	0.004577	0.69	0.5
Animal 4	100	9.705145643	12.929934	-0.02726	2.11047516	1.8766262	0.004577	0.69	0.5
Animal 4	100	8.376396369	12.929934	-0.02726	1.02874626	1.8766262	0.004577	0.69	0.5
Animal 4	100	15.41846721	12.929934	-0.02726	2.86547778	1.8766262	0.004577	0.69	0.5
Animal 4	100	6.123855352	12.929934	-0.02726	0.59531883	1.8766262	0.004577	0.69	0.5
Animal 4	100	11.29261773	12.929934	-0.02726	0.6696417	1.8766262	0.004577	0.69	0.5
Animal 4	100	40.61871227	12.929934	-0.02726	4.57858314	1.8766262	0.004577	0.69	0.5
Animal 4	100	16.43966653	12.929934	-0.02726	2.60718741	1.8766262	0.004577	0.69	0.5
Animal 4	100	15.33915456	12.929934	-0.02726	3.68597283	1.8766262	0.004577	0.69	0.5
Animal 4	100	5.916074807	12.929934	-0.02726	0.43710678	1.8766262	0.004577	0.69	0.5

Animal 4	100	9.57318535	12.929934	-0.02726	2.08839906	1.8766262	0.004577	0.69	0.5
Animal 4	100	14.79280719	12.929934	-0.02726	0.84330702	1.8766262	0.004577	0.69	0.5
Animal 4	145	10.21108118	11.88216	-0.02726	2.53507215	2.3359733	0.004577	0.69	0.5
Animal 4	145	9.064092701	11.88216	-0.02726	0.75279501	2.3359733	0.004577	0.69	0.5
Animal 4	145	16.89159288	11.88216	-0.02726	4.4078613	2.3359733	0.004577	0.69	0.5
Animal 4	145	8.765302609	11.88216	-0.02726	1.23994095	2.3359733	0.004577	0.69	0.5
Animal 4	145	10.69078551	11.88216	-0.02726	2.16198606	2.3359733	0.004577	0.69	0.5
Animal 4	145	13.49964751	11.88216	-0.02726	2.64030156	2.3359733	0.004577	0.69	0.5
Animal 4	145	11.06470289	11.88216	-0.02726	0.79547547	2.3359733	0.004577	0.69	0.5
Animal 4	145	9.89889379	11.88216	-0.02726	0.44446548	2.3359733	0.004577	0.69	0.5
Animal 4	145	24.60242787	11.88216	-0.02726	8.7936465	2.3359733	0.004577	0.69	0.5
Animal 4	145	8.482926493	11.88216	-0.02726	1.29439533	2.3359733	0.004577	0.69	0.5
Animal 4	145	22.44922927	11.88216	-0.02726	6.95470737	2.3359733	0.004577	0.69	0.5
Animal 4	145	9.516792082	11.88216	-0.02726	1.19578875	2.3359733	0.004577	0.69	0.5
Animal 4	145	6.284680415	11.88216	-0.02726	0.99489624	2.3359733	0.004577	0.69	0.5
Animal 4	145	16.80783045	11.88216	-0.02726	1.98832074	2.3359733	0.004577	0.69	0.5
Animal 4	145	4.011243085	11.88216	-0.02726	0.41723829	2.3359733	0.004577	0.69	0.5
Animal 4	145	7.873324376	11.88216	-0.02726	0.75868197	2.3359733	0.004577	0.69	0.5
Animal 5	65	19.57847097	19.724602	0.02286	1.22228007	2.0251142	0.0229	0.6	0.5333333
Animal 5	65	10.53024506	19.724602	0.02286	0.63211233	2.0251142	0.0229	0.6	0.5333333
Animal 5	65	12.51579241	19.724602	0.02286	1.75210647	2.0251142	0.0229	0.6	0.5333333
Animal 5	65	20.99827807	19.724602	0.02286	2.52992106	2.0251142	0.0229	0.6	0.5333333
Animal 5	65	44.30596429	19.724602	0.02286	3.56308254	2.0251142	0.0229	0.6	0.5333333
Animal 5	65	20.38526488	19.724602	0.02286	1.61302704	2.0251142	0.0229	0.6	0.5333333
Animal 5	65	34.76985434	19.724602	0.02286	6.45284403	2.0251142	0.0229	0.6	0.5333333
Animal 5	65	14.35882332	19.724602	0.02286	1.43788998	2.0251142	0.0229	0.6	0.5333333
Animal 5	65	9.74208596	19.724602	0.02286	0.43637091	2.0251142	0.0229	0.6	0.5333333
Animal 5	65	10.06123917	19.724602	0.02286	0.61150797	2.0251142	0.0229	0.6	0.5333333
Animal 5	100	8.042947663	18.074492	0.02286	1.13691915	1.9351279	0.0229	0.6	0.5333333
Animal 5	100	16.31869089	18.074492	0.02286	1.46658891	1.9351279	0.0229	0.6	0.5333333
Animal 5	100	9.646839927	18.074492	0.02286	1.14501372	1.9351279	0.0229	0.6	0.5333333
Animal 5	100	34.40854184	18.074492	0.02286	1.16561808	1.9351279	0.0229	0.6	0.5333333

Animal 5	100	13.79319164	18.074492	0.02286	0.44372961	1.9351279	0.0229	0.6	0.5333333
Animal 5	100	13.42770458	18.074492	0.02286	1.36503885	1.9351279	0.0229	0.6	0.5333333
Animal 5	100	8.352420912	18.074492	0.02286	0.515109	1.9351279	0.0229	0.6	0.5333333
Animal 5	100	47.00347705	18.074492	0.02286	4.42772979	1.9351279	0.0229	0.6	0.5333333
Animal 5	100	19.87073967	18.074492	0.02286	5.50504347	1.9351279	0.0229	0.6	0.5333333
Animal 5	100	22.58396141	18.074492	0.02286	1.60640421	1.9351279	0.0229	0.6	0.5333333
Animal 5	100	24.27487318	18.074492	0.02286	4.6801332	1.9351279	0.0229	0.6	0.5333333
Animal 5	100	10.8632558	18.074492	0.02286	2.07662514	1.9351279	0.0229	0.6	0.5333333
Animal 5	100	17.51707523	18.074492	0.02286	0.69466128	1.9351279	0.0229	0.6	0.5333333
Animal 5	100	6.939162877	18.074492	0.02286	0.86317551	1.9351279	0.0229	0.6	0.5333333
Animal 5	145	13.32335644	21.357618	0.02286	1.56593136	3.7860124	0.0229	0.6	0.5333333
Animal 5	145	28.40927344	21.357618	0.02286	3.2746215	3.7860124	0.0229	0.6	0.5333333
Animal 5	145	36.90968066	21.357618	0.02286	6.87670515	3.7860124	0.0229	0.6	0.5333333
Animal 5	145	21.58603506	21.357618	0.02286	7.726635	3.7860124	0.0229	0.6	0.5333333
Animal 5	145	29.51258148	21.357618	0.02286	7.98639711	3.7860124	0.0229	0.6	0.5333333
Animal 5	145	11.07782931	21.357618	0.02286	1.68146295	3.7860124	0.0229	0.6	0.5333333
Animal 5	145	15.12916551	21.357618	0.02286	2.99131155	3.7860124	0.0229	0.6	0.5333333
Animal 5	145	25.33076097	21.357618	0.02286	5.08559757	3.7860124	0.0229	0.6	0.5333333
Animal 5	145	17.18994963	21.357618	0.02286	1.76167278	3.7860124	0.0229	0.6	0.5333333
Animal 5	145	19.82769637	21.357618	0.02286	3.87950664	3.7860124	0.0229	0.6	0.5333333
Animal 5	145	14.61517885	21.357618	0.02286	2.09134254	3.7860124	0.0229	0.6	0.5333333
Animal 5	145	22.24420864	21.357618	0.02286	4.12896657	3.7860124	0.0229	0.6	0.5333333
Animal 5	145	13.76607552	21.357618	0.02286	4.00018932	3.7860124	0.0229	0.6	0.5333333
Animal 5	145	37.6831095	21.357618	0.02286	1.95079137	3.7860124	0.0229	0.6	0.5333333
Animal 5	145	10.90495558	21.357618	0.02286	3.81842943	3.7860124	0.0229	0.6	0.5333333
Animal 5	145	29.99303372	21.357618	0.02286	3.60355539	3.7860124	0.0229	0.6	0.5333333
Animal 5	145	11.94949662	21.357618	0.02286	2.72934183	3.7860124	0.0229	0.6	0.5333333
Animal 5	145	10.00559967	21.357618	0.02286	0.8536092	3.7860124	0.0229	0.6	0.5333333
Animal 5	145	36.3367633	21.357618	0.02286	5.92816872	3.7860124	0.0229	0.6	0.5333333
Animal 6	65	1.083156312	17.262973	0.1179	0.57839382	2.583149	0.07181	0.333	0.1666667
Animal 6	65	17.16001518	17.262973	0.1179	1.88088372	2.583149	0.07181	0.333	0.1666667
Animal 6	65	6.588753086	17.262973	0.1179	2.18111868	2.583149	0.07181	0.333	0.1666667

Animal 6	65	22.25861207	17.262973	0.1179	3.27167802	2.583149	0.07181	0.333	0.1666667
Animal 6	65	7.365471815	17.262973	0.1179	0.71158629	2.583149	0.07181	0.333	0.1666667
Animal 6	65	14.90343583	17.262973	0.1179	3.69480327	2.583149	0.07181	0.333	0.1666667
Animal 6	65	20.14474943	17.262973	0.1179	3.7897305	2.583149	0.07181	0.333	0.1666667
Animal 6	65	37.95785036	17.262973	0.1179	3.87729903	2.583149	0.07181	0.333	0.1666667
Animal 6	65	27.90471354	17.262973	0.1179	3.26284758	2.583149	0.07181	0.333	0.1666667
Animal 6	100	19.16173522	22.374816	0.1179	5.13931608	4.9057825	0.07181	0.333	0.1666667
Animal 6	100	15.44636311	22.374816	0.1179	4.10468286	4.9057825	0.07181	0.333	0.1666667
Animal 6	100	9.217519301	22.374816	0.1179	1.43715411	4.9057825	0.07181	0.333	0.1666667
Animal 6	100	29.50674812	22.374816	0.1179	4.77506043	4.9057825	0.07181	0.333	0.1666667
Animal 6	100	15.36540721	22.374816	0.1179	3.38941722	4.9057825	0.07181	0.333	0.1666667
Animal 6	100	42.46050651	22.374816	0.1179	17.03612637	4.9057825	0.07181	0.333	0.1666667
Animal 6	100	31.40777694	22.374816	0.1179	6.58162128	4.9057825	0.07181	0.333	0.1666667
Animal 6	100	32.1377395	22.374816	0.1179	8.11149501	4.9057825	0.07181	0.333	0.1666667
Animal 6	100	23.10804642	22.374816	0.1179	4.17679812	4.9057825	0.07181	0.333	0.1666667
Animal 6	100	15.76716666	22.374816	0.1179	0.98238645	4.9057825	0.07181	0.333	0.1666667
Animal 6	100	33.35792358	22.374816	0.1179	2.3842188	4.9057825	0.07181	0.333	0.1666667
Animal 6	100	16.23697475	22.374816	0.1179	2.62337655	4.9057825	0.07181	0.333	0.1666667
Animal 6	100	25.57293704	22.374816	0.1179	6.83696817	4.9057825	0.07181	0.333	0.1666667
Animal 6	100	4.500585903	22.374816	0.1179	1.10233326	4.9057825	0.07181	0.333	0.1666667
Animal 6	145	21.52759299	26.77646	0.1179	4.69852995	8.3124401	0.07181	0.333	0.1666667
Animal 6	145	40.3124728	26.77646	0.1179	12.34421925	8.3124401	0.07181	0.333	0.1666667
Animal 6	145	19.54197077	26.77646	0.1179	6.13641993	8.3124401	0.07181	0.333	0.1666667
Animal 6	145	23.59903546	26.77646	0.1179	7.56989469	8.3124401	0.07181	0.333	0.1666667
Animal 6	145	13.85528395	26.77646	0.1179	2.74258749	8.3124401	0.07181	0.333	0.1666667
Animal 6	145	41.74027011	26.77646	0.1179	13.48261014	8.3124401	0.07181	0.333	0.1666667
Animal 6	145	12.25096373	26.77646	0.1179	2.04498273	8.3124401	0.07181	0.333	0.1666667
Animal 6	145	54.53166479	26.77646	0.1179	21.07605267	8.3124401	0.07181	0.333	0.1666667
Animal 6	145	26.56870469	26.77646	0.1179	9.5000817	8.3124401	0.07181	0.333	0.1666667
Animal 6	145	47.09205924	26.77646	0.1179	12.56203677	8.3124401	0.07181	0.333	0.1666667
Animal 6	145	17.12303795	26.77646	0.1179	3.70510545	8.3124401	0.07181	0.333	0.1666667
Animal 6	145	34.09935066	26.77646	0.1179	12.6937575	8.3124401	0.07181	0.333	0.1666667

Animal 6	145	13.01854056	26.77646	0.1179	5.67282183	8.3124401	0.07181	0.333	0.1666667
Animal 6	145	9.609493697	26.77646	0.1179	2.14506105	8.3124401	0.07181	0.333	0.1666667
Animal 8	65	21.9026847	25.748436	-0.00433	1.60714008	3.9685469	0.02249	0.077	0.0769231
Animal 8	65	30.13153995	25.748436	-0.00433	5.5852533	3.9685469	0.02249	0.077	0.0769231
Animal 8	65	20.73245154	25.748436	-0.00433	4.23346011	3.9685469	0.02249	0.077	0.0769231
Animal 8	65	10.18444101	25.748436	-0.00433	2.07368166	3.9685469	0.02249	0.077	0.0769231
Animal 8	65	45.7910625	25.748436	-0.00433	6.3431994	3.9685469	0.02249	0.077	0.0769231
Animal 8	100	43.12166594	22.005985	-0.00433	11.57744271	5.2363773	0.02249	0.077	0.0769231
Animal 8	100	29.72496988	22.005985	-0.00433	9.06223905	5.2363773	0.02249	0.077	0.0769231
Animal 8	100	18.62263454	22.005985	-0.00433	0.76604067	5.2363773	0.02249	0.077	0.0769231
Animal 8	100	18.90498667	22.005985	-0.00433	3.82725987	5.2363773	0.02249	0.077	0.0769231
Animal 8	100	21.97853943	22.005985	-0.00433	7.37488914	5.2363773	0.02249	0.077	0.0769231
Animal 8	100	30.70518492	22.005985	-0.00433	8.42497563	5.2363773	0.02249	0.077	0.0769231
Animal 8	100	17.81775921	22.005985	-0.00433	2.86621365	5.2363773	0.02249	0.077	0.0769231
Animal 8	100	4.361850119	22.005985	-0.00433	1.76829561	5.2363773	0.02249	0.077	0.0769231
Animal 8	100	28.93653245	22.005985	-0.00433	5.62131093	5.2363773	0.02249	0.077	0.0769231
Animal 8	100	5.88572345	22.005985	-0.00433	1.07510607	5.2363773	0.02249	0.077	0.0769231
Animal 8	145	36.00791919	25.114468	-0.00433	15.9389442	5.8060812	0.02249	0.077	0.0769231
Animal 8	145	49.67871307	25.114468	-0.00433	11.04835218	5.8060812	0.02249	0.077	0.0769231
Animal 8	145	31.79664734	25.114468	-0.00433	0.44299374	5.8060812	0.02249	0.077	0.0769231
Animal 8	145	23.75422595	25.114468	-0.00433	3.14878773	5.8060812	0.02249	0.077	0.0769231
Animal 8	145	19.82009567	25.114468	-0.00433	4.27025361	5.8060812	0.02249	0.077	0.0769231
Animal 8	145	39.22133096	25.114468	-0.00433	11.34196431	5.8060812	0.02249	0.077	0.0769231
Animal 8	145	19.35287083	25.114468	-0.00433	1.79405106	5.8060812	0.02249	0.077	0.0769231
Animal 8	145	22.58938652	25.114468	-0.00433	7.08422049	5.8060812	0.02249	0.077	0.0769231
Animal 8	145	15.85233684	25.114468	-0.00433	3.58957386	5.8060812	0.02249	0.077	0.0769231
Animal 8	145	3.579498598	25.114468	-0.00433	0.66154713	5.8060812	0.02249	0.077	0.0769231
Animal 8	145	14.60612381	25.114468	-0.00433	4.54620486	5.8060812	0.02249	0.077	0.0769231
Animal 9	65	19.7095399	39.278763	-0.2095	5.11650411	7.7614662	-0.00947	0.2	0.2
Animal 9	65	14.90986575	39.278763	-0.2095	0.62916885	7.7614662	-0.00947	0.2	0.2
Animal 9	65	83.2168822	39.278763	-0.2095	17.53872558	7.7614662	-0.00947	0.2	0.2
Animal 9	100	9.465591318	28.968359	-0.2095	1.77933366	4.7569982	-0.00947	0.2	0.2

Animal 9	100	16.88005653	28.968359	-0.2095	3.25475301	4.7569982	-0.00947	0.2	0.2
Animal 9	100	27.73715315	28.968359	-0.2095	4.16281659	4.7569982	-0.00947	0.2	0.2
Animal 9	100	37.47533466	28.968359	-0.2095	9.10124016	4.7569982	-0.00947	0.2	0.2
Animal 9	100	20.2043116	28.968359	-0.2095	1.70648253	4.7569982	-0.00947	0.2	0.2
Animal 9	100	61.71298536	28.968359	-0.2095	7.63023603	4.7569982	-0.00947	0.2	0.2
Animal 9	100	14.32503806	28.968359	-0.2095	1.3907943	4.7569982	-0.00947	0.2	0.2
Animal 9	100	55.70603145	28.968359	-0.2095	3.35041611	4.7569982	-0.00947	0.2	0.2
Animal 9	100	25.50174391	28.968359	-0.2095	6.20706345	4.7569982	-0.00947	0.2	0.2
Animal 9	100	32.42298396	28.968359	-0.2095	10.52882796	4.7569982	-0.00947	0.2	0.2
Animal 9	100	17.22072245	28.968359	-0.2095	3.21501603	4.7569982	-0.00947	0.2	0.2
Animal 9	145	27.50453877	22.28228	-0.2095	8.18949723	6.7900732	-0.00947	0.2	0.2
Animal 9	145	22.14997895	22.28228	-0.2095	6.65668002	6.7900732	-0.00947	0.2	0.2
Animal 9	145	29.50061086	22.28228	-0.2095	10.80919443	6.7900732	-0.00947	0.2	0.2
Animal 9	145	18.64283226	22.28228	-0.2095	7.47938268	6.7900732	-0.00947	0.2	0.2
Animal 9	145	28.25072167	22.28228	-0.2095	7.82597745	6.7900732	-0.00947	0.2	0.2
Animal 9	145	4.347953166	22.28228	-0.2095	0.52320357	6.7900732	-0.00947	0.2	0.2
Animal 9	145	40.213323	22.28228	-0.2095	11.4648546	6.7900732	-0.00947	0.2	0.2
Animal 9	145	17.20945657	22.28228	-0.2095	6.9539715	6.7900732	-0.00947	0.2	0.2
Animal 9	145	14.25519246	22.28228	-0.2095	3.56529015	6.7900732	-0.00947	0.2	0.2
Animal 9	145	29.50493048	22.28228	-0.2095	9.25577286	6.7900732	-0.00947	0.2	0.2
Animal 9	145	13.52554665	22.28228	-0.2095	1.96698051	6.7900732	-0.00947	0.2	0.2
Animal 11	65	23.23013514	23.793502	-0.05181	7.753862	5.1913175	0.01764	0.09	0.3636364
Animal 11	65	26.74648806	23.793502	-0.05181	3.43724877	5.1913175	0.01764	0.09	0.3636364
Animal 11	65	25.08589663	23.793502	-0.05181	4.52633637	5.1913175	0.01764	0.09	0.3636364
Animal 11	65	18.37002329	23.793502	-0.05181	1.97654682	5.1913175	0.01764	0.09	0.3636364
Animal 11	65	43.69224571	23.793502	-0.05181	12.53407371	5.1913175	0.01764	0.09	0.3636364
Animal 11	65	5.636222379	23.793502	-0.05181	0.9198375	5.1913175	0.01764	0.09	0.3636364
Animal 11	100	11.87733802	17.306612	-0.05181	4.28055579	2.6699371	0.01764	0.09	0.3636364
Animal 11	100	19.69323979	17.306612	-0.05181	0.76604067	2.6699371	0.01764	0.09	0.3636364
Animal 11	100	25.40659937	17.306612	-0.05181	3.90231861	2.6699371	0.01764	0.09	0.3636364
Animal 11	100	18.41567877	17.306612	-0.05181	5.67944466	2.6699371	0.01764	0.09	0.3636364
Animal 11	100	9.73479791	17.306612	-0.05181	0.71011455	2.6699371	0.01764	0.09	0.3636364

Animal 11	100	23.25745203	17.306612	-0.05181	2.22527088	2.6699371	0.01764	0.09	0.3636364
Animal 11	100	15.73072542	17.306612	-0.05181	1.30837686	2.6699371	0.01764	0.09	0.3636364
Animal 11	100	10.61055041	17.306612	-0.05181	0.56588403	2.6699371	0.01764	0.09	0.3636364
Animal 11	100	31.50135659	17.306612	-0.05181	4.91193225	2.6699371	0.01764	0.09	0.3636364
Animal 11	100	6.420226003	17.306612	-0.05181	3.78899463	2.6699371	0.01764	0.09	0.3636364
Animal 11	100	17.72477276	17.306612	-0.05181	1.23037464	2.6699371	0.01764	0.09	0.3636364
Animal 11	145	27.11482462	19.275103	-0.05181	12.7158336	6.3517355	0.01764	0.09	0.3636364
Animal 11	145	17.22309694	19.275103	-0.05181	1.29660294	6.3517355	0.01764	0.09	0.3636364
Animal 11	145	11.36955319	19.275103	-0.05181	5.10914541	6.3517355	0.01764	0.09	0.3636364
Animal 11	145	21.12487315	19.275103	-0.05181	7.80463722	6.3517355	0.01764	0.09	0.3636364
Animal 11	145	31.63583661	19.275103	-0.05181	5.78835342	6.3517355	0.01764	0.09	0.3636364
Animal 11	145	14.32778186	19.275103	-0.05181	4.95608445	6.3517355	0.01764	0.09	0.3636364
Animal 11	145	7.843399159	19.275103	-0.05181	5.24233788	6.3517355	0.01764	0.09	0.3636364
Animal 11	145	9.05968398	19.275103	-0.05181	0.70128411	6.3517355	0.01764	0.09	0.3636364
Animal 11	145	16.74478884	19.275103	-0.05181	10.00415265	6.3517355	0.01764	0.09	0.3636364
Animal 11	145	36.30719148	19.275103	-0.05181	9.89892324	6.3517355	0.01764	0.09	0.3636364
Animal 12	65	21.17420731	15.463503	0.2213	2.42616339	2.2552576	0.04379	0	0
Animal 12	65	18.003615	15.463503	0.2213	4.45127763	2.2552576	0.04379	0	0
Animal 12	65	7.316635741	15.463503	0.2213	1.97581095	2.2552576	0.04379	0	0
Animal 12	65	13.20383933	15.463503	0.2213	1.28998011	2.2552576	0.04379	0	0
Animal 12	65	16.9244366	15.463503	0.2213	4.22757315	2.2552576	0.04379	0	0
Animal 12	65	9.881124008	15.463503	0.2213	0.88893096	2.2552576	0.04379	0	0
Animal 12	65	8.856176507	15.463503	0.2213	1.04346366	2.2552576	0.04379	0	0
Animal 12	65	7.855355178	15.463503	0.2213	0.91321467	2.2552576	0.04379	0	0
Animal 12	65	17.85425966	15.463503	0.2213	3.30332043	2.2552576	0.04379	0	0
Animal 12	65	22.01497937	15.463503	0.2213	3.64697172	2.2552576	0.04379	0	0
Animal 12	65	11.38871566	15.463503	0.2213	2.03394468	2.2552576	0.04379	0	0
Animal 12	65	14.34841367	15.463503	0.2213	2.3695014	2.2552576	0.04379	0	0
Animal 12	65	16.15558315	15.463503	0.2213	1.67263251	2.2552576	0.04379	0	0
Animal 12	65	16.45849418	15.463503	0.2213	1.04787888	2.2552576	0.04379	0	0
Animal 12	65	28.67184697	15.463503	0.2213	1.32162252	2.2552576	0.04379	0	0
Animal 12	65	17.30836246	15.463503	0.2213	3.47183466	2.2552576	0.04379	0	0

Animal 12	100	18.87904104	34.879008	0.2213	3.0832953	4.1947861	0.04379	0	0
Animal 12	100	41.56069495	34.879008	0.2213	2.05528491	4.1947861	0.04379	0	0
Animal 12	100	30.16722631	34.879008	0.2213	2.05602078	4.1947861	0.04379	0	0
Animal 12	100	41.15673414	34.879008	0.2213	3.76397505	4.1947861	0.04379	0	0
Animal 12	100	13.93745318	34.879008	0.2213	1.97728269	4.1947861	0.04379	0	0
Animal 12	100	55.23378614	34.879008	0.2213	8.45073108	4.1947861	0.04379	0	0
Animal 12	100	22.48705224	34.879008	0.2213	3.73233264	4.1947861	0.04379	0	0
Animal 12	100	61.53184519	34.879008	0.2213	5.40202167	4.1947861	0.04379	0	0
Animal 12	100	22.37571062	34.879008	0.2213	7.50072291	4.1947861	0.04379	0	0
Animal 12	100	59.58773303	34.879008	0.2213	14.96391645	4.1947861	0.04379	0	0
Animal 12	100	45.79905371	34.879008	0.2213	4.50058092	4.1947861	0.04379	0	0
Animal 12	100	10.51596104	34.879008	0.2213	1.71604884	4.1947861	0.04379	0	0
Animal 12	100	18.8764648	34.879008	0.2213	1.09203108	4.1947861	0.04379	0	0
Animal 12	100	29.44615587	34.879008	0.2213	1.58579985	4.1947861	0.04379	0	0
Animal 12	100	35.69955031	34.879008	0.2213	1.42464432	4.1947861	0.04379	0	0
Animal 12	100	50.02894123	34.879008	0.2213	5.3792097	4.1947861	0.04379	0	0
Animal 12	100	55.08662056	34.879008	0.2213	4.8273072	4.1947861	0.04379	0	0
Animal 12	100	15.45211649	34.879008	0.2213	1.99494357	4.1947861	0.04379	0	0
Animal 12	145	17.94460092	34.09864	0.2213	4.58079075	5.7910729	0.04379	0	0
Animal 12	145	5.846627888	34.09864	0.2213	0.69613302	5.7910729	0.04379	0	0
Animal 12	145	14.15571539	34.09864	0.2213	1.23846921	5.7910729	0.04379	0	0
Animal 12	145	72.06390856	34.09864	0.2213	5.82293931	5.7910729	0.04379	0	0
Animal 12	145	57.74798533	34.09864	0.2213	13.48481775	5.7910729	0.04379	0	0
Animal 12	145	112.7563266	34.09864	0.2213	16.98976656	5.7910729	0.04379	0	0
Animal 12	145	5.002632869	34.09864	0.2213	0.53571336	5.7910729	0.04379	0	0
Animal 12	145	59.92303051	34.09864	0.2213	16.1376291	5.7910729	0.04379	0	0
Animal 12	145	40.51722671	34.09864	0.2213	2.24072415	5.7910729	0.04379	0	0
Animal 12	145	28.76456788	34.09864	0.2213	5.15035413	5.7910729	0.04379	0	0
Animal 12	145	45.68435526	34.09864	0.2213	12.37071057	5.7910729	0.04379	0	0
Animal 12	145	29.05139742	34.09864	0.2213	9.17261955	5.7910729	0.04379	0	0
Animal 12	145	12.05657239	34.09864	0.2213	3.96192408	5.7910729	0.04379	0	0
Animal 12	145	16.75960994	34.09864	0.2213	1.70942601	5.7910729	0.04379	0	0

Animal 12	145	24.72623476	34.09864	0.2213	2.61086676	5.7910729	0.04379	0	0
Animal 12	145	11.70544142	34.09864	0.2213	1.41066279	5.7910729	0.04379	0	0
Animal 12	145	33.95447378	34.09864	0.2213	4.69705821	5.7910729	0.04379	0	0
Animal 12	145	15.28214354	34.09864	0.2213	3.46006074	5.7910729	0.04379	0	0
Animal 12	145	37.40290973	34.09864	0.2213	5.97820788	5.7910729	0.04379	0	0
Animal 12	145	60.68107522	34.09864	0.2213	6.35276571	5.7910729	0.04379	0	0
Animal 12	145	27.85500553	34.09864	0.2213	5.06131386	5.7910729	0.04379	0	0
Animal 12	145	35.87953187	34.09864	0.2213	6.29463198	5.7910729	0.04379	0	0
Animal 12	145	18.50733591	34.09864	0.2213	3.23709213	5.7910729	0.04379	0	0
Animal 13	65	16.83	28.39	-0.1006	3.76	5.94	-0.01322	0	0
Animal 13	65	45.36	28.39	-0.1006	10.82	5.94	-0.01322	0	0
Animal 13	65	56.30	28.39	-0.1006	10.61	5.94	-0.01322	0	0
Animal 13	65	22.14	28.39	-0.1006	7.04	5.94	-0.01322	0	0
Animal 13	65	29.79	28.39	-0.1006	5.61	5.94	-0.01322	0	0
Animal 13	65	17.29	28.39	-0.1006	1.23	5.94	-0.01322	0	0
Animal 13	65	11.03	28.39	-0.1006	2.52	5.94	-0.01322	0	0
Animal 13	100	11.26	21.96	-0.1006	0.63	3.20	-0.01322	0	0
Animal 13	100	21.78	21.96	-0.1006	3.81	3.20	-0.01322	0	0
Animal 13	100	31.95	21.96	-0.1006	5.10	3.20	-0.01322	0	0
Animal 13	100	16.62	21.96	-0.1006	0.98	3.20	-0.01322	0	0
Animal 13	100	20.58	21.96	-0.1006	1.98	3.20	-0.01322	0	0
Animal 13	100	83.91	21.96	-0.1006	11.52	3.20	-0.01322	0	0
Animal 13	100	18.42	21.96	-0.1006	4.52	3.20	-0.01322	0	0
Animal 13	100	10.86	21.96	-0.1006	0.76	3.20	-0.01322	0	0
Animal 13	100	13.40	21.96	-0.1006	3.88	3.20	-0.01322	0	0
Animal 13	100	10.82	21.96	-0.1006	2.06	3.20	-0.01322	0	0
Animal 13	100	34.52	21.96	-0.1006	9.14	3.20	-0.01322	0	0
Animal 13	100	18.13	21.96	-0.1006	2.07	3.20	-0.01322	0	0
Animal 13	100	36.73	21.96	-0.1006	4.59	3.20	-0.01322	0	0
Animal 13	100	25.84	21.96	-0.1006	4.83	3.20	-0.01322	0	0
Animal 13	100	8.75	21.96	-0.1006	0.70	3.20	-0.01322	0	0
Animal 13	100	14.54	21.96	-0.1006	0.96	3.20	-0.01322	0	0

Animal 13	100	16.97	21.96	-0.1006	1.79	3.20	-0.01322	0	0
Animal 13	100	10.61	21.96	-0.1006	0.55	3.20	-0.01322	0	0
Animal 13	100	18.37	21.96	-0.1006	2.67	3.20	-0.01322	0	0
Animal 13	100	15.12	21.96	-0.1006	1.37	3.20	-0.01322	0	0
Animal 13	145	12.75	20.11	-0.1006	2.85	4.70	-0.01322	0	0
Animal 13	145	15.32	20.11	-0.1006	2.23	4.70	-0.01322	0	0
Animal 13	145	24.67	20.11	-0.1006	8.28	4.70	-0.01322	0	0
Animal 13	145	14.83	20.11	-0.1006	2.31	4.70	-0.01322	0	0
Animal 13	145	32.91	20.11	-0.1006	5.59	4.70	-0.01322	0	0
Animal 13	145	8.85	20.11	-0.1006	0.66	4.70	-0.01322	0	0
Animal 13	145	59.83	20.11	-0.1006	9.93	4.70	-0.01322	0	0
Animal 13	145	17.18	20.11	-0.1006	6.67	4.70	-0.01322	0	0
Animal 13	145	6.83	20.11	-0.1006	2.01	4.70	-0.01322	0	0
Animal 13	145	25.90	20.11	-0.1006	5.12	4.70	-0.01322	0	0
Animal 13	145	25.65	20.11	-0.1006	8.80	4.70	-0.01322	0	0
Animal 13	145	29.11	20.11	-0.1006	10.01	4.70	-0.01322	0	0
Animal 13	145	19.30	20.11	-0.1006	8.17	4.70	-0.01322	0	0
Animal 13	145	29.22	20.11	-0.1006	6.06	4.70	-0.01322	0	0
Animal 13	145	7.90	20.11	-0.1006	0.84	4.70	-0.01322	0	0
Animal 13	145	15.93	20.11	-0.1006	5.06	4.70	-0.01322	0	0
Animal 13	145	13.34	20.11	-0.1006	1.52	4.70	-0.01322	0	0
Animal 13	145	8.78	20.11	-0.1006	1.03	4.70	-0.01322	0	0
Animal 13	145	13.76	20.11	-0.1006	2.22	4.70	-0.01322	0	0

REFERENCES

1. Alexander BT. Placental insufficiency leads to development of hypertension in growth-restricted offspring. Hypertension 2003; 41:457-462.
2. Brosens I, Pijnenborg R, Vercruysse L, Romero R. The "Great Obstetrical Syndromes" are associated with disorders of deep placentation. American Journal of Obstetrics and Gynecology 2011; 204:193-201.
3. Krishna U, Bhalerao S. Placental insufficiency and fetal growth restriction. Journal of Obstetrics and Gynaecology India 2011; 61:505-511.
4. Roberts DJ, Post MD. The placenta in pre-eclampsia and intrauterine growth restriction. Journal of Clinical Pathology 2008; 61:1254-1260.
5. Fox H. The histopathology of placental insufficiency. Journal of Clinical Pathology 1976; 29:1–8.
6. Roberts DJ. Placenta Pathology, a Survival Guide. Archives of Pathology & Laboratory Medicine 2008; 132:641–651.
7. Newnham JP, O'dea MR-A, Reid KP, Diepeveen DA. Doppler flow velocity waveform analysis in high risk pregnancies: a randomized controlled trial. BJOG: An International Journal of Obstetrics and Gynaecology 1991; 98:956–963.
8. Kofinas AD, Penry M, Nelson LH, Meis PJ, Swain M. Uterine and Umbilical Artery Flow Velocity Waveform Analysis in Pregnancies Complicated by Chronic Hypertension or Preeclampsia. Southern Medical Journal 1990; 83:150–155.
9. Fadl S, Moshiri M, Fligner CL, Katz DS, Dighe M. Placental Imaging: Normal Appearance with Review of Pathologic Findings. RadioGraphics 2017; 37:979–998.

10. Hashem LB, Salem DS, Hamed ST, Hussein AM. Role of MRI versus ultrasound in the assessment of placental abnormalities and diseases. The Egyptian Journal of Radiology and Nuclear Medicine 2016; 47:641–658.

11. Vázquez-Boland JA, Krypotou E, Scortti M. Listeria Placental Infection. MBio 2017; 8.

12. Tabata T, Petitt M, Fang-Hoover J, Zydek M, Pereira L. Persistent Cytomegalovirus Infection in Amniotic Membranes of the Human Placenta. The American Journal of Pathology 2016; 186:2970–2986.

13. Mcdonagh S, Maidji E, Ma W, Chang HT, Fisher S, Pereira L. Viral and Bacterial Pathogens at the Maternal-Fetal Interface. The Journal of Infectious Diseases 2004; 190:826–834.

14. Hirsch AJ, Roberts VHJ, Grigsby PL, Haese N, Schabel MC, Wang X, Lo JO, Liu Z, Kroenke CD, Smith JL, Kelleher M, Broeckel R, et al. Zika virus infection in pregnant rhesus macaques causes placental dysfunction and immunopathology. Nature Communications 2018; 9.

15. Millischer AE, Deloison B, Silvera S, Ville Y, Boddaert N, Balvay D, Siauve N, Cuenod CA, Tsatsaris V, Sentilhes L, Salomon LJ.. Dynamic contrast enhanced MRI of the placenta: A tool for prenatal diagnosis of placenta accreta? Placenta 2017; 53:40-47.

16. Yankeelov T, Gore J. Dynamic Contrast Enhanced Magnetic Resonance Imaging in Oncology: Theory, Data Acquisition, Analysis, and Examples. Current Medical Imaging Reviews 2007; 3(2):91-107.

17. Tofts PS. T1-Weighted DCE Imaging Concepts: Modelling, Acquisition and Analysis. 2010.

18. Choyke P, Dwyer A, Knopp M. Functional tumor imaging with dynamiccontrast-

enhanced magnetic resonance imaging. Journal of Magnetic Resonance Imaging 2003; 17(5):509-520.

28. Frias AE, Schabel MC, Roberts VHJ, Tudorica A, Grigsby PL, Oh KY, Kroenke CD. Using dynamic contrast-enhanced MRI to quantitatively characterize maternal vascular organization in the primate placenta. Magnetic Resonance in Medicine 2014; 73:1570–1578.

29. Hirsch AJ, Roberts VHJ, Grigsby PL, Haese N, Schabel MC, Wang X, Lo JO, Liu Z, Kroenke CD, Smith JL, Kelleher M, Broeckel R, et al. Zika virus infection in pregnant rhesus macaques causes placental dysfunction and immunopathology. Nature Communications 2018; 9.

30. Chalouhi GE, Deloison B, Siauve N, Aimot S, Balvay D, Cuenod CA, Ville Y, Clément O, Salomon LJ. Dynamic contrast-enhanced magnetic resonance imaging: definitive imaging of placental function?. Seminars in Fetal and Neonatal Medicine 2011; 16:22-28.

31. Prola-Netto J, Woods M, Roberts VHJ, Sullivan EL, Miller CA, Frias AE, Oh KY. Gadolinium Chelate Safety in Pregnancy: Barely Detectable Gadolinium Levels in the Juvenile Nonhuman Primate after in Utero Exposure. Radiology 2018; 286:122–128.

32. Rogosnitzky M, Branch S. Gadolinium-based contrast agent toxicity: a review of known and proposed mechanisms. BioMetals 2016; 29:365–376.

33. Oh KY, Roberts VHJ, Schabel MC, Grove KL, Woods M, Frias AE. Gadolinium Chelate Contrast Material in Pregnancy: Fetal Biodistribution in the Nonhuman Primate. Radiology 2015; 276:110–118.

34. Ray JG, Vermeulen MJ, Bharatha A, Montanera WJ, Park AL. Association Between

MRI Exposure During Pregnancy and Fetal and Childhood Outcomes. Jama 2016; 316:952–961.

35. Siauve N, Chalouhi GE, Deloison B, Alison M, Clement O, Ville Y, Salomon LJ. Functional imaging of the human placenta with magnetic resonance. American Journal of Obstetrics and Gynecology 2015; 213.

19. AMAG Pharmaceuticals. Feraheme: Highlights of Prescribing Information; 2018. https://www.accessdata.fda.gov/drugsatfda_docs/label/2009/022180lbl.pdf. Accessed August 2, 2020.

20. Toth GB, Varallyay CG, Horvath A, Bashir MR, Choyke PL, Daldrup-Link HE, Dosa E, Finn JP, Gahramanov S, Harisinghani M, Macdougall I, Neuwelt A, et al. Current and potential imaging applications of ferumoxytol for magnetic resonance imaging. Kidney International 2017; 92:47–66.

21. Vasanawala SS, Nguyen K-L, Hope MD, Bridges MD, Hope TA, Reeder SB, Bashir MR. Safety and technique of ferumoxytol administration for MRI. Magnetic Resonance in Medicine 2016; 75:2107–2111.

22. Auerbach M, Landy HJ. Anemia in pregnancy; 2019. https://www.uptodate.com/contents/anemia-in-pregnancy?topicRef=7148&source=see_link. Accessed August 2, 2020.

23. Nguyen SM, Wiepz GJ, Schotzko M, Simmons HA, Mejia A, Ludwig KD, Zhu A, Brunner K, Hernando D, Reeder SB, et al. Impact of ferumoxytol magnetic resonance imaging on the rhesus macaque maternal-fetal interface. Biology of Reproduction 2020; 102: 434-333.

24. Macdonald JA, Corrado PA, Nguyen SM, Johnson KM, Francois CJ, Magness RR,

Shah DM, Golos TG, Wieben O. Uteroplacental and Fetal 4D Flow MRI in the Pregnant Rhesus Macaque. Journal of Magnetic Resonance Imaging 2018; 49:534–545.

25. Zhu A, Reeder SB, Johnson KM, Nguyen SM, Golos TG, Shimakawa A, Muehler MR, Francois CJ, Bird IM, Fain SB, Shah DM, Wieben O, et al. Evaluation of a motion-robust 2D chemical shift-encoded technique for R2* and field map quantification in ferumoxytol-enhanced MRI of the placenta in pregnant rhesus macaques. Journal of Magnetic Resonance Imaging 2019; 51:580–592.

26. Zhu A, Reeder SB, Johnson KM, Nguyen SM, Fain SB, Bird IM, Golos TG, Wieben O, Shah DM, Hernando D. Quantitative ferumoxytol-enhanced MRI in pregnancy: A feasibility study in the nonhuman primate. Magnetic Resonance Imaging 2020; 65:100–108.

27. Ludwig KD, Fain SB, Nguyen SM, Golos TG, Reeder SB, Bird IM, Shah DM, Wieben OE, Johnson KM. Perfusion of the placenta assessed using arterial spin labeling and ferumoxytol dynamic contrast enhanced magnetic resonance imaging in the rhesus macaque. Magnetic Resonance in Medicine 2018; 81:1964–1978.

36. De Rijk EPCT, Esch EV. The Macaque Placenta—A Mini-Review. Toxicologic Pathology 2008; 36:108S–118S.

37. Stouffer RL, Woodruff TK. Nonhuman Primates: A Vital Model for Basic and Applied Research on Female Reproduction, Prenatal Development, and Women's Health. ILAR Journal 2017; 58:281–294.

38. Joffe TH, Tarantal AF, Rice K, Leland M, Oerke A-K, Rodeck C, Geary M, Hindmarsh P, Wells JC, Aiello LC. Fetal and infant head circumference sexual dimorphism in primates. American Journal of Physical Anthropology 2004; 126:97–110.

39. Abbink P, Larocca RA, Barrera RADL, Bricault CA, Moseley ET, Boyd M, Kirilova M, Li Z, Nganga D, Nanayakkara O, Nityanandam R, Mercado NB, et al. Protective efficacy of multiple vaccine platforms against Zika virus challenge in rhesus monkeys. Science 2016; 353:1129–1132.

40. Dudley DM, Aliota MT, Mohr EL, Weiler AM, Lehrer-Brey G, Weisgrau KL, Mohns MS, Breitbach ME, Rasheed MN, Newman CM, Gellerup DD, Moncla LH, et al. A rhesus macaque model of Asian-lineage Zika virus infection. Nature Communications 2016; 7.

41. Nguyen SM, Antony KM, Dudley DM, Kohn S, Simmons HA, Wolfe B, Salamat MS, Teixeira LBC, Wiepz GJ, Thoong TH, Aliota MT, Weiler AM, et al. Highly efficient maternal-fetal Zika virus transmission in pregnant rhesus macaques. PLoS Pathogens 2017; 13.

42. Khong TY, Mooney EE, Ariel I, Balmus NCM, Boyd TK, Brundler M, Derricott H, Evans MJ, Faye-Peterson OM, Gillan JEHeazell AE, Heller DS, et al. Sampling and Definitions of Placental Lesions: Amsterdam Placental Workshop Group Consensus Statement. Archives of Pathology & Laboratory Medicine 2016; 140(7):698-713.

43. Dimasuay KG, Boeuf P, Powell TL, Jansson T. Placental Responses to Changes in the Maternal Environment Determine Fetal Growth. Frontiers in Physiology 2016; 7:12.

44. Roland MCP, Friis CM, Godang K, Bollerslev J, Haugen G, Henriksen T. Maternal Factors Associated with Fetal Growth and Birthweight Are Independent Determinants of Placental Weight and Exhibit Differential Effects by Fetal Sex. PLoS One 2014; 9(2).

Chapter 6:

Concluding Remarks

Prior to FDA studies that can result in wide approval of a new procedure, animal studies can provide initial insights on potential value and safety. This thesis showcases the process of investigating the potential safety and efficacy of ferumoxytol MRI in the identification of placental pathology (summarized in Figure 1). We hypothesized that ferumoxytol DCE MRI could be applied to pregnancy for the imaging of placental pathology through monitoring of placental functional information in a rhesus macaque model. In Chapter 2, ZIKV virus is utilized to develop an infection model in rhesus macaques that is disruptive of normal pregnancy and introduces a variety of pathology to the placenta. In Chapter 3, both MRI and MRI with ferumoxytol are applied to normal macaque pregnancy to confirm that no pathology or other evidence of pregnancy disruption is seen due to these procedures. In Chapter 4, methods are described for placental imaging with ferumoxytol and the matching of the resulting functional data to placenta biopsies to relate function with pathology. In chapter 5, ferumoxytol MRI is finally applied to the ZIKV -infected macaque pregnancy model to determine the potential value of resulting images.

While we show that MRI with ferumoxytol can be used to identify changes in average placental cotyledon size and flow in correlation to higher presence of placental infarctions or levels of general pathology, our experiments are far from exhaustive. Pathology could manifest in a variety of ways, from countless infections, disorders, or other abnormalities. Furthermore, while ZIKV is a serious infection that can result in miscarriage and severe fetal defects, the number of cases has diminished in much of the world and the virus is currently circulating at a

much lower level than was seen during the 2015 outbreak. The results seen in this thesis should represent a proof of concept, that MRI can be used to assess placental function in relation to levels of pathology, and the concept should be applied to additional placental ailments. This would help determine if MRI is only effective in identifying placenta functional values affected by the particular pathologies relevant to infections like ZIKV. If more common, less severe infections can also be identified using ferumoxytol MRI, the value of the procedure would be greatly strengthened and there would be more reason to apply the procedure to human pregnancies.

Our studies, while showcasing interesting new data concerning DCE MRI in pregnancy, also gave rise to a few questions that must be investigated prior to the use of ferumoxytol in human pregnancies. The most important of these questions is in relation to the safety of the use of ferumoxytol in pregnancy. In Chapter 3, we studied iron concentrations in fetal tissues and levels of placenta-related hormones in maternal blood, both by mass spectrometry. This method allows for sensitive identification of specific material in samples, the results of which suggest that there is no significant difference in these values between animals that did or did not receive ferumoxytol, but the number of subjects we had was very low – only four which received ferumoxytol and four acting as controls. It is difficult to definitively state results with only four subjects per treatment group, as inter-subject variation can affect baseline readings. Additional experimentation utilizing more subjects should take place to expand the subject pool.

A major limitation in our studies stems from the use of our animal model. Due to the expense, availability, and ethics surrounding the use of primates in research, the minimum number of macaques are assigned to a project to elucidate results. While other animal models, such as mice, allow for larger numbers of subjects with more efficient data and tissue collection

due to shorter gestation, these models have far fewer similarities to human pregnancy. Therefore, despite the low subject numbers, our use of macaques provides results that are more applicable to humans. Regardless, due to the relatively small number of subjects in our studies, our initial findings would benefit from additional research in macaques.

An appropriate next research project should be designed in such a way to test repeatability and answer the questions that arose during the studies showcased here: a study testing the efficacy of ferumoxytol MRI in a different, more common pathology-inducing model such as preeclampsia or listeriosis infection, in rhesus macaques. As completed in Chapter 3, maternal blood samples should be collected before and after ferumoxytol injection, and fetal tissue should be collected to investigate fetal iron levels following use of ferumoxytol for imaging. This data can be compared to the findings in Chapter 3 to either support or challenge ferumoxytol's safety profile for use in pregnancy. The imaging data from these animals would help determine the sensitivity of the ferumoxytol DCE procedure in assessing pathology from a non- ZIKV infection.

In the investigation of new imaging methods utilizing an animal model, the animal is anesthetized, and fetal motion is diminished. This is not the case however, when imaging humans. Pregnant women will be fully awake and image collection will be subject to fetal movement which will affect the degree of detail captured by the images. Small vasculature, including uterine vessels that feed blood into the placenta will not be reliably captured and this will limit the type of information that can be collected. However, this showcases a benefit of the use of DCE imaging over non-contrast MRI in pregnancy. DCE MRI is reflective of whole-organ perfusion rather than the movement of blood through particular vessels and may be robust

enough for data collection despite fetal movement. The target being imaged is larger and will not be lost when slightly displaced by fetal repositioning during the scan time.

After more definitively showing safety with the use of ferumoxytol and effectiveness in imaging a variety of placental pathologies in the macaque model, human studies can be prepared. The similarities in macaque and human pregnancy and placentation would suggest similar imaging results, but it is possible that particular infections might manifest differently in each model. Initial human imaging experiments will have to take place with a small subject pools with normal pregnancy and known placental infection to confirm the ability to capture meaningful DCE imaging information in pregnancy humans, and to confirm variation in imaging data of normal vs pathological placentas. After this checkpoint, research could take place to define imaging hallmarks of particular placental pathologies in humans to further develop a procedure with, and determine the limits of, ferumoxytol DCE MRI as a clinical diagnostic tool. Under current limitations involving fetal movement that will prevent vessel-specific investigation, pathology that affects the rate at which the placenta is perfused, or the structure or volume of the placental blood space are most likely to be successfully identified by the DCE MRI methods.

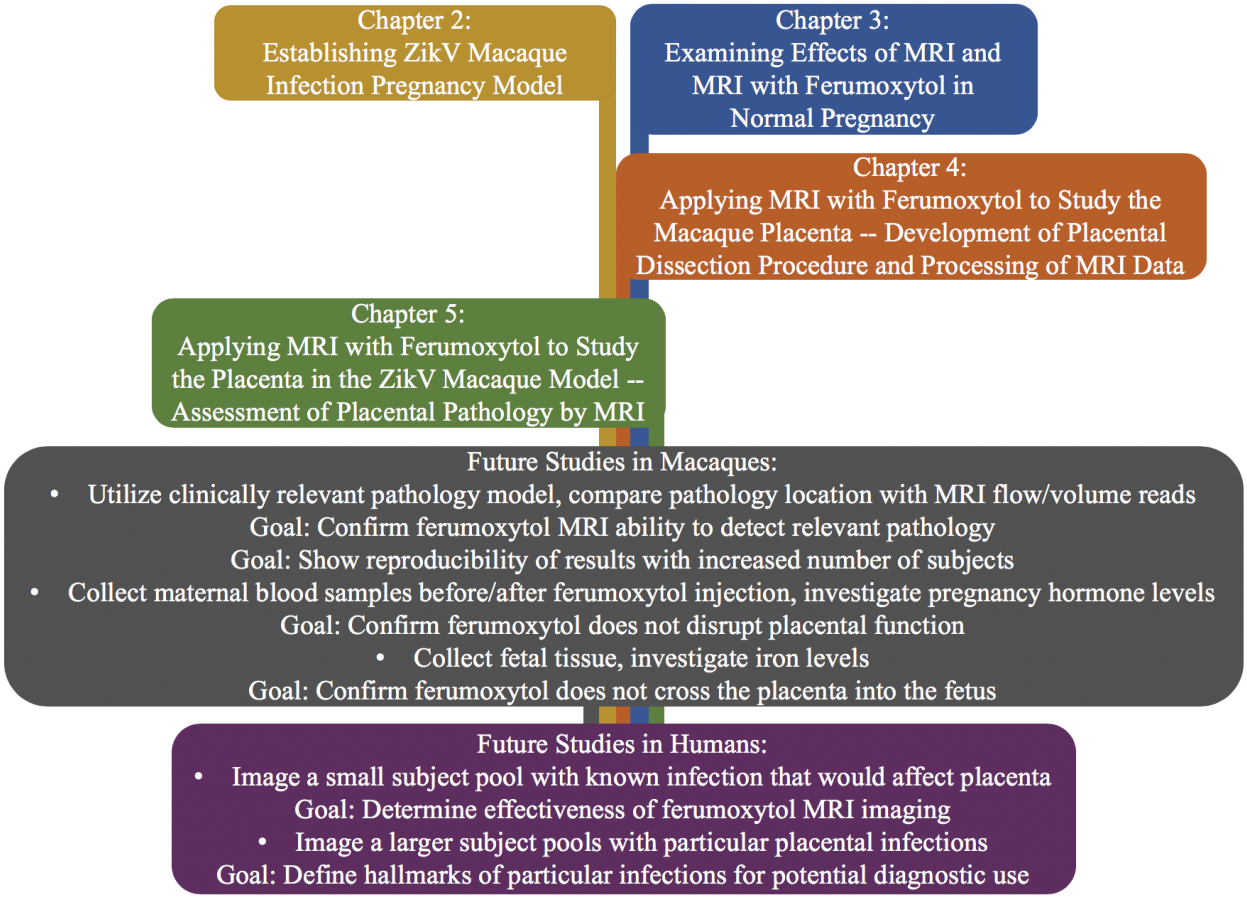

Figure 1. Study Goals and Future Research Opportunities. Chart depicting the goals of the studies described in the chapters of this thesis. The information learned in each chapter contribute to our understanding of MRI in pregnancy and contribute to appropriate establishment of future studies.

Following clinical validation, there is still a long road ahead for the use of MRI as a diagnostic tool in pregnancy. MRI is an incredibly expensive procedure utilizing highly-specialized equipment that must be routinely maintained. The use of MRI in pregnancy diagnostics would not be feasible for the average American without health insurance covering the procedure. Often, medical insurance coverage is dictated by what is medically necessary. It may be difficult to convince health insurance agencies of the necessity of this expensive imaging

when ultrasound is widely available and much more affordable, but it may be a goal worth perusing. Should the ferumoxytol MRI procedure be successful for use in identification of human placenta pathology, patients with factors that can make ultrasound difficult to read – obese patients or patients with prior abnormally invasive placentas – would benefit from a method that could clearly assess pregnancy health and weigh potential risks. The identification of abnormal uterine blood flow by doppler ultrasound, on an inability to derive standard ultrasound readings due to preexisting conditions for example, would be reason to refer a patient for the more intensive MRI procedure to further examine the pregnancy in order to intervene and prevent potentially catastrophic outcomes.

The placenta is an extremely important, but chronically understudied organ. The application of safe contrast MRI in the placenta has potential to increase our understanding of the physiological effects of different infections on the maternal-fetal interface. Commonly, investigation of quantitative placental perfusion takes place post-delivery with devices that simulate blood passage through the placenta manually. This, however, only provides detailed data at a single timepoint, where DCE MRI can be applied throughout pregnancy to understand placental changes through time. The use of DCE MRI for the study of perfusion would also allow more flexibility on data collection, as imaging sessions can be scheduled rather than depending on quick collection and testing of the organ following delivery, whenever that may occur. Furthermore, DCE MRI with a contrast agent that does not cross the placental barrier, as is suggested in our ferumoxytol data, provides the unique benefit of visualizing only maternal blood movement in the placenta. As non-contrast MRI modalities utilize the movement of hydrogen molecules in the blood to collect information, the maternal and fetal blood pools cannot be distinguished. Completing MR imaging with and without contrast could provide total

and maternal-only blood movement in the placenta, furthering our understanding of normal and abnormal placental growth and function.

The use of stronger magnetic fields produces higher resolution images, which provide improved detail about the tissue of interest. DCE MRI is a dynamic method that collects images over time, where imaging resolution is sacrificed for capture speed. In the use of a more powerful magnetic field, a sharper image in these dynamic datasets is possible. This might provide a degree of detail that better visualizes the placental bed vessels that bring maternal blood to the placenta, which play a direct role in the organ's health. However, due to prudent safety efforts surrounding imaging during pregnancy, and uncertainties surrounding the in utero affect of a stronger magnetic field, its adoption is unlikely. Instead, the supplementation of current pregnancy monitoring methods and other imaging efforts with DCE MRI should be pursued in efforts to identify and treat placental insufficiency. Doppler ultrasound is a standard method used to measure blood flow through vessels in pregnancy – a measurement that is not attained with DCE MRI. Despite relatively low image quality, doppler is used to identify pregnancies that have potential for adverse outcomes. If data from doppler ultrasound is combined with unique data collected during DCE MRI, a data set can be achieved that can assist in the understanding of vessel blood flow and placental perfusion, leading to a better understanding of the placenta in disease and more targeted treatment options.

Completing multiple types of MRI scans in a single imaging session will not substantially increase the procedure time while greatly improving the quantity and context of data being collected. Coupling anatomical MRI with DCE MRI can be used to calculate a placental organ volume versus interior blood volume to determine if the relationship between these measures changes in the presence of placental pathology, which may serve as a hallmark of infection for

use of MRI as a diagnostic tool. Additionally, Blood Oxygen Level Dependent (BOLD) is a type of MRI that creates images based on the location of oxygenated vs deoxygenated hemoglobin. In combination with the cotyledon and perfusion maps developed using DCE MRI data, BOLD can be used to analyze the oxygenation levels of blood in the cotyledons, matching cotyledon oxygenation to perfusion rates to better reflect the health and function of these placental functional groups. The addition of anatomical and BOLD data provides context for the DCE MRI data, improving its usefulness for analysis of placental health.

Currently, there is no contrast agent deemed fully safe for clinical placental imaging, but the use of contrast imaging could provide valuable functional placental detail not otherwise achievable by current non-contrast methods. Combining contrast MRI data with current non-contrast methods holds great potential to dramatically improve research and treatment of placental disorders. The work in this thesis takes the first steps in investigation of ferumoxytol as a safe contrast choice. If contrast MRI can be applied routinely to at-risk women, problematic pregnancies may be efficiently identified prior to symptom manifestation and resources can be appropriately allocated to care for the mother and growing fetus. This would prevent potentially life-threatening situations and expensive intervention later in pregnancy, reducing maternal mortality rates and revolutionizing standards of care for the pregnant population.

Appendix A:

Perfusion of the Placenta assessed using Arterial Spin Labeling and Ferumoxytol Dynamic Contrast Enhanced Magnetic Resonance Imaging in the Rhesus Macaque

Publication: Kai D. Ludwig, Sean B. Fain, Sydney M. Nguyen, Thaddeus G. Golos, Scott B. Reeder, Ian M. Bird, Dinesh M. Shah, Oliver E. Wieben, and Kevin M. Johnson. 2019. Perfusion of the placenta assessed using arterial spin labeling and ferumoxytol dynamic contrast enhanced magnetic resonance imaging in the rhesus macaque. Magnetic Resonance Imaging. doi: 10.1002/mrm.27548.

ABSTRACT

Purpose: To investigate the correspondence between arterial spin labeling (ASL) flow-sensitive alternating inversion recovery (FAIR) and ferumoxytol dynamic contrast enhanced (DCE) magnetic resonance imaging (MRI) for the assessment of placental intervillous perfusion.

Methods: Ten pregnant macaques in late 2nd trimester were imaged at 3T using a 2D ASL FAIR, with and without outer volume saturation (OVS) pulses used to control the bolus width, and a 3D ferumoxytol DCE MRI acquisition. ASL tagged/control pairs were averaged, subtracted, and normalized to create perfusion ratio maps. Contrast arrival time and uptake slope were estimated by fitting DCE data to a sigmoid function. Macaques (N=4) received interleukin-1β to induce inflammation and disrupt perfusion.

Results: FAIR tag modification with OVS reduced median ASL ratio percentage compared to conventional FAIR (0.64±1.42% vs. 0.71±2.00%;p<0.05). Extended ferumoxytol arrival times

(34±25sec) were observed across the placenta. No significant DCE signal change was measured in fetal tissue (-0.6±3.0%;p=0.52) or amniotic fluid (1.9±8.8%;p=0.59). High ASL ratio was significantly correlated with early arrival time and high uptake slope (p<0.05) but ASL signal was not above noise in late-DCE-enhancing regions. No significant differences were observed in perfusion measurements between the interleukin-1β and controls (p>0.05).

Conclusion: ASL FAIR and ferumoxytol DCE MRI are feasible methods to detect early blood delivery to the macaque placenta. OVS reduced high macrovascular ASL signal. Interleukin-1β exposure did not alter placental intervillous perfusion. An endogenous-labeling perfusion technique is limited due to extended transit times for flow within the placenta beyond the immediate vicinity of the maternal spiral arteries.

INTRODUCTION

The placenta supplies nutrients and oxygen to the fetus while removing waste products and consists of a complex, maternal-fetal interface. Maternal blood is delivered to the placenta via spiral arteries which conduct blood from the maternal arteries to the intervillous space surrounding the placental chorionic villi [1]. Fetal blood circulates separately within the villi that are floating in the maternal blood in the intervillous space or anchored to the maternal decidua. Abnormal placental function can be life threatening and have long-term effects both for maternal and fetal health [2]. For example, deficiencies in perfusion impede the nutrient exchange affecting placental function and fetal development [3]. Potentially in response to the reduced nutrient exchange, 3-7% of first-time mothers develop pre-eclampsia (a hypertensive disorder of pregnancy) [4] and in some cases growth restriction of the fetus may result.

Despite its crucial role in fetal development, the placenta is poorly understood, due in part to the limited non-invasive methods to study the placenta throughout pregnancy [5]. Ultrasound is a primary imaging modality for the assessment of placenta and fetal health due to its low cost, strong safety profile, and real-time image capabilities. Unfortunately, ultrasound provides a limited number of image contrasts and thus may be insensitive in detecting early functional precursors to pregnancy complications.

Magnetic resonance imaging (MRI) is an emerging modality for the longitudinal monitoring of placental health in utero. It has an excellent safety profile and can acquire 3D volumes in any orientation with multiple contrasts including functional measures. Quantitative, non-contrast-enhanced perfusion MRI methods like arterial spin labeling (ASL) are promising approaches for the safe evaluation of placental perfusion [6]. For example, ASL with flow-sensitive alternating inversion recovery (FAIR) acquires images with a global and slice-selective inversion to tag inflowing blood outside a slice of interest resulting in perfusion contrast [7]. The FAIR labeling scheme is effective for assessment of multi-directional flow into the tissue of interest (e.g. placenta) without the need to locate the feeding arteries. Prior work has investigated FAIR in human placentas demonstrating feasibility of the FAIR scheme to quantify placental perfusion in healthy human mothers [8] and detecting low perfusion in the basal plate of the placenta, a sign that is predictive of "small for gestational age" neonates [6].

Despite the success of initial placenta ASL, perfusion quantification is potentially complicated by the unique maternal vascular network perfusing the placenta that lacks a traditional capillary bed and contains multiple arterial input sources. ASL has contributions from both perfused blood signal that has left the vasculature and from blood signal remaining within the vasculature. To mitigate vascular signal, the timing of ASL tagging must be adapted to the vascular

system. In the case of FAIR ASL, saturation pulses can be played out after a specified delay time to allow for a post-label delay as was first introduced in the brain with inferior saturation RF [9, 10]. The post-labeling delay must match the transit time of blood from its tag location to location of perfusion for accurate quantification. Vascular spaces of the intervillous circulation are relatively large, potentially leading to long blood transit times. Long transit times will prohibit ASL analysis in regions since the persistence of the ASL signal transit times relies on the bolus transit times. This is among other confounders including the T_1 time of labeled blood, variation in labeling efficiency, low signal to noise ratio (SNR), and the contributions from fetal circulations. Dynamic contrast enhanced (DCE) MRI offers an alternative, and potentially more robust, technique to measure maternal placenta perfusion. DCE MRI collects of a series of T_1-weighted images, with high temporal resolution, throughout the injection of a T_1-shortening contrast agent, which enhances local signal [11]. Perfusion can be assessed through tracer kinetic modeling of the signal-time curves in the tissue of interest [12]. DCE has relatively high SNR and has demonstrated agreement with ASL in the measurement of renal blood flow [13] and relative pulmonary blood flow [14]. It is also potentially more robust in slow perfusing organs (e.g. placenta, liver) comparatively with ASL. Gadolinium-based contrast agent (GBCA) DCE MRI in the rhesus macaque has been demonstrated for the estimation of contrast arrival times, and detection of placental spiral artery locations [15, 16]. While GBCA's have shown efficacy in measuring perfusion, they are known to cross the placenta and are contraindicated in humans due to concerns for teratogenicity and known long-term sequalae of in utero GBCA exposure [17].

Ferumoxytol, an ultra-small superparamagnetic iron oxide nanoparticle (SPION), offers an FDA-approved alternative to GBCA's. Although approved for intravenous iron supplementation to treat anemia, there is evidence supporting its off-label use as an intravascular agent contrast

agent for dynamic susceptibility contrast (DSC) and DCE MRI. Ferumoxytol, being of large molecular size, and due to entrapment by macrophages on the maternal side, is unlikely to cross the placental barrier. Phagocytosis of SPIONs by macrophages allows MRI of SPIONs to be used as a biomarker macrophage infiltration in infection and inflammation [18]. Further, the T_1 shortening properties of ferumoxytol enable both visualization of the vasculature and perfusion measurements in the placental tissue.

Limited studies currently exist that evaluate non-contrast perfusion methods, such as ASL, with reference contrast methods, such as ferumoxytol DCE, specifically in the placenta. The rhesus macaque (*Macaca mulatta*) is a suitable experimental model to develop MR imaging methodologies during gestation with a placental villous organization and number of offspring similar to humans [19]. The objective of this work is to evaluate the potential of two variants of ASL MRI with FAIR, with and without outer volume saturation (OVS) pulses, to assess placental intervillous perfusion without contrast reagents, then compare with a "gold-standard" reference, ferumoxytol DCE MRI in animals receiving interleukin-1β (IL-1β) and healthy controls. Intra-amniotic fluid injection of IL-1β has previously been shown to induce chorioamnionitis and preterm labor in the rhesus macaque [20, 21]. The induced inflammation response could potentially disrupt perfusion. We hypothesize that acute inflammation may also perturb placental intervillous perfusion, measurable by MRI methods.

METHODS

Animal Population

All procedures were approved by the Institutional Animal Care and Use Committee at the University of Wisconsin-Madison. Ten healthy, pregnant rhesus macaques (*Macaca mulatta*)

underwent MRI in the late second trimester (mean±standard deviation (SD)=99.2±5.9 days) based on an average 166-day macaque pregnancy length [22] with an average maternal weight of 8.93±1.03 kg. Table 1 summarizes the characteristics of the animal and treatment groups studied. Animals were divided into three treatment groups: no intervention, saline injection, or IL-1β (human IL-1β, PeproTech, Rocky Hill, NJ, USA) treated. Animals received an intra-amniotic injection of 10 µg of IL-1β in 0.5 mL sterile saline (*N*=4), 0.5 mL saline (*N*=3), or no injection (*N*=3). We performed the IL-1β infusion to induce an inflammation response and promote immune cell trafficking, but that is not the focus of the work presented here.

Animal Number	Intervention	Gestational Age [days]	Maternal Weight [kg]
1	None	91	9.9
2		99	10.02
3		106	10.04
4	Saline	98	8.56
5		100	9.06
6		104	7.09
7	IL-1β	93	8.56
8		93	9.77
9		99	7.63
10		109	8.65
All		99.2 ± 5.9	8.93 ± 1.03

Table 1. Summary of the animal characteristics in this study (*N* = 10). Trimester calculations based on an average 166-day gestational cycle for rhesus macaque. The mean ± SD of the gestational age and maternal weight is shown for each intervention group along with the all animals grouped together.

Imaging Acquisitions

All imaging was performed on a clinical 3.0T MRI system (Discovery MR750, GE Healthcare, Waukesha, WI, USA) with a 32-channel phased array torso coil (Neocoil, Pewaukee, WI). Rhesus macaques were sedated with 1.5% isoflurane supplemented with O_2 using a portable anesthesia system and imaged in a right-lateral position.

Anatomical MRI

A stack of 2D, T_2-weighted anatomical MR images was acquired using a single-shot fast spin echo (SSFSE) data readout with a repetition time (TR)=3.0-4.0 sec, echo time (TE)=100.3 ms, receiver bandwidth (BW)=651 Hz/voxel, matrix=256×128, in-plane spatial resolution=0.70 mm, slice thickness=2.0 mm, with 40-70 slices in both the sagittal and axial orientation with complete coverage of the placenta.

ASL MRI

Pulsed ASL FAIR imaging [7] was performed using a 2D, single-slice, respiratory-triggered acquisition with an SSFSE data readout (TR=5.0-7.0 sec, TE=49.2 ms, BW=651 Hz/voxel, matrix=128×128, field-of-view (FOV)=18×18 cm, in-plane spatial resolution=0.70 mm, readout slice thickness=4 mm, selective inversion slice thickness=14 mm, and 2 dummy scans for a total scan time of ~6 minutes depending on respiratory rate). Images were acquired under free breathing conditions with the 2.0 sec inversion time (TI) chosen such that tagging and imaging occurred at end-expiration resulting in a variable TR between animals. Control and FAIR tagged images were alternated until 40 total images (20 control/tag pairs) were acquired. A proton density weighted image (M_0) was obtained prior to the control/tag pairs using no magnetization preparation. ASL FAIR imaging was performed with and without outer volume saturation (OVS) using RF pulses applied above and below the ASL imaging plane, similar to the QUIPSS II approach [9]. OVS pulses were used to limit the temporal width of the ASL bolus by saturation the late-arriving FAIR-labeled spins. This has the objective of reducing sensitivity to bolus arrival time and minimizing hyper-intense signal from the macrovasculature. OVS pulses were applied

1.0 sec after the inversion preparation using flip=90°, 100 mm superior-to-inferior coverage, and 10 ms quadratic phase RF pulses resulting in a bolus width of TI_1=1.0 sec. The ASL FAIR pulse sequence with OVS pulses added will be denoted, +OVS, and without, -OVS, throughout the manuscript. Fig 1 shows diagrams of the two ASL FAIR pulse sequences and their theoretical ASL signal as a function of transit time.

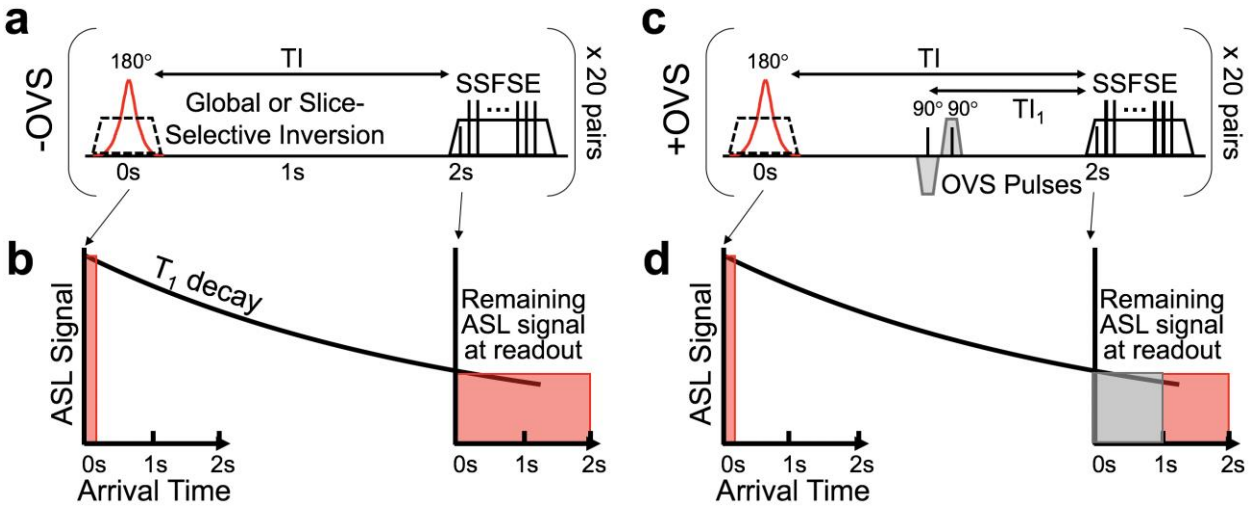

Figure 1. Simplified MRI pulse sequence diagrams are shown for both the ASL FAIR acquisitions without (a, -OVS) and with (c, +OVS) outer volume saturation (OVS) RF pulses. Inverted or FAIR labeled spins are represented by the red color while saturated spins are represented by the gray color. The theoretical ASL signal is shown for the –OVS (**b**) and +OVS (**d**) cases as a function of the blood spins arrival time from labeling region to the placental tissue at two time points during the pulse sequence: immediately after inversion (0 sec) and at imaging readout (TI = 2.0 sec). The remaining ASL signal is governed by assuming a T_1 decay of labeled blood and constant blood flow from the labeling region into the imaging slice. The OVS pulses serve to saturate macrovascular signal in the imaging region and this is depicted as removing the ASL signal with the +OVS schematic.

DCE MRI

DCE was acquired with a 3D T_1-weighted spoiled gradient echo with differential subsampling with Cartesian ordering (DISCO) [23] with 2 point fat/water separation (TR=4.8 ms, TE_1/TE_2,=1.2/2.4 ms, BW=1116 Hz/voxel, matrix=256×128×128, FOV=22×15.4×12.8 cm, spatial resolution=0.86×0.86×1.0 mm, temporal resolution=5 sec, total scan time=200-300 sec, flip=12°, ARC acceleration factor=2x2) throughout injection of 4 mg/kg ferumoxytol (Feraheme^{TM}, AMAG Pharmaceuticals, Waltham, MA, USA) diluted 5:1 with saline and infused intravenously over 20 sec allowing for direct measurement of contrast arrival time to placental tissue.

Magnetic Resonance Angiography

High resolution ferumoxytol-enhanced magnetic resonance angiogram (MRA) data were acquired with a respiratory gated 3D, T_1-weighted ultrashort echo time (UTE) acquisition with center-out radial trajectory [24] (TR=4.4 ms, TE=0.13 ms, BW=694 Hz/voxel, matrix=360×360×360, FOV=18×18×18 cm, spatial resolution =0.5×0.5×0.5 mm, flip=10°, scan time=5:33) both pre- and post-injection of ferumoxytol. Volume rendering was performed on the complex subtracted MRA data using Horos DICOM viewer (Horos Project).

Image Analysis

MRI data reconstruction and analysis was performed using custom scripts in MATLAB (MathWorks, Natick, MA) unless otherwise noted. Image segmentation of the placental tissue was performed using the M_0 image. All ASL FAIR tagged/control pair images were co-registered to the M_0 image using MelastiX, a collection of MATLAB wrappers for the image registration suite

Elastix [25, 26]. DCE volumetric data were resampled and registered to the ASL slice using the Advanced Normalization Tools (ANTs) [27]. Supporting Information Figure S1 shows the entire image registration pipeline between the DCE and ASL data with step-wise explanations.

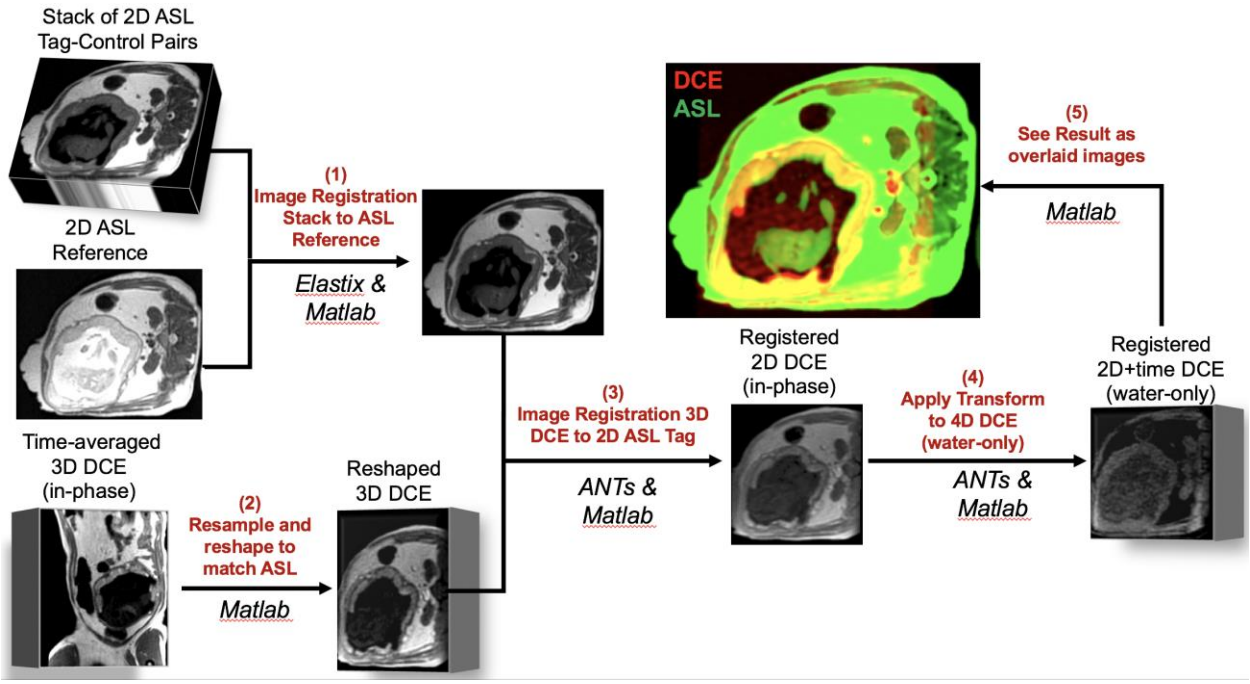

Supporting Information Figure S1. Schematic showing the registration pipeline between the 4D (3D+time) ferumoxytol DCE data set and the 2D, single slice ASL FAIR data set. The stack of 2D ASL images (tag and control pairs) are registered individually to the 2D proton density weighted ASL reference image with Elastix by calling the program through MATLAB. The 4D in-phase DCE data is first time-averaged to produce a 3D, high-SNR DCE data set which is subsequently resampled to match the resolution of the ASL data and reshaped to the orientation (axial) of the ASL data; all within MATLAB. The reshaped 3D DCE in-phase DCE data set is registered to the mean, 2D FAIR-tagged ASL slice using MATLAB calls to the Advanced Normalization Tools (ANTs). This results in a 2D DCE slice registered to the ASL slice. The resulting transform or deformation field from ANTs is then applied to each time frame of the 3D,

water-only DCE data set, again using MATLAB calls to ANTs. The output is a 3D, water-only DCE data set (2D slice over time) whose registration results are qualitatively verified in MATLAB as seen in the overlay color image above with ASL in green and DCE in red.

ASL data was processed by separately averaging then subtracting the FAIR tagged and control pairs to create an ASL signal difference image (ΔM). ASL ratio maps were created using Eq. 1 below by normalizing ΔM to M_0.

$$ASL\ Ratio\ Map = \ 100\% \cdot \frac{\Delta M / M_0}{TI_1} \quad [1]$$

For comparisons between ASL FAIR -OVS and +OVS, the ratio maps were divided by the ASL bolus width (TI_1=TI=2 sec in the -OVS case) to account for the FAIR tagged inflow duration.

Conventional ASL analysis in organs with traditional capillary beds (e.g. brain, kidney, etc.) entails fitting the ASL signal to a single-parameter implementation of the general kinetic model [28]. Given the unusual maternal vascular circulation within the intervillous space of the placenta, absolute quantification of ASL data could have substantial errors. We have chosen to represent the ASL signal as an ASL ratio map, in units of percentage. This is a semi-quantitative parameter of the perfusion signal and will be proportional to the blood delivery to the placental intervillous space.

DCE data was analyzed with a semi-quantitative method. The signal intensity (SI) from the DCE data over time (t) was fit to the generalized sigmoid-shaped logistic function (i.e. S-shaped curve with plateau),

$$SI(t) = \ SI_0 + (SI_{max} - SI_0) / \Big(1 + \exp\big(-s(t-d)\big)\Big) \quad [2]$$

on a per voxel basis to determine the contrast delay time (d), a contrast uptake steepness factor (s), the maximum signal intensity (SI_{max}), and baseline signal intensity (SI_0) for every placental voxel. This fitting function choice closely matched the observed ferumoxytol DCE signal-time curves within the placental tissue with no appreciable contrast agent washout. Unlike alternative tracer-kinetic models, this approach is not sensitive to accurate measurement of the arterial input function, which is challenging to estimate in the placenta due to the multiple arterial inputs. The general shape of the sigmoid-shaped function and derivative ($\frac{d}{dt}SI(t)$) are shown for simulated data in Supporting Information Figure S2a along with in vivo DCE data, the sigmoid-shaped fit, and estimated parameters in Supporting Information Figure S2b. The contrast delay times were shifted relative to the injection time to derive the contrast arrival time (i.e. delay time from contrast injection to 50% maximum enhancement). The relative blood flow (rBF) was estimated to be equivalent to the slope of the contrast uptake curve.

$$SI(t) = SI_0 + (SI_{max} - SI_0)/\left(1 + \exp\left(-s(t-d)\right)\right)$$

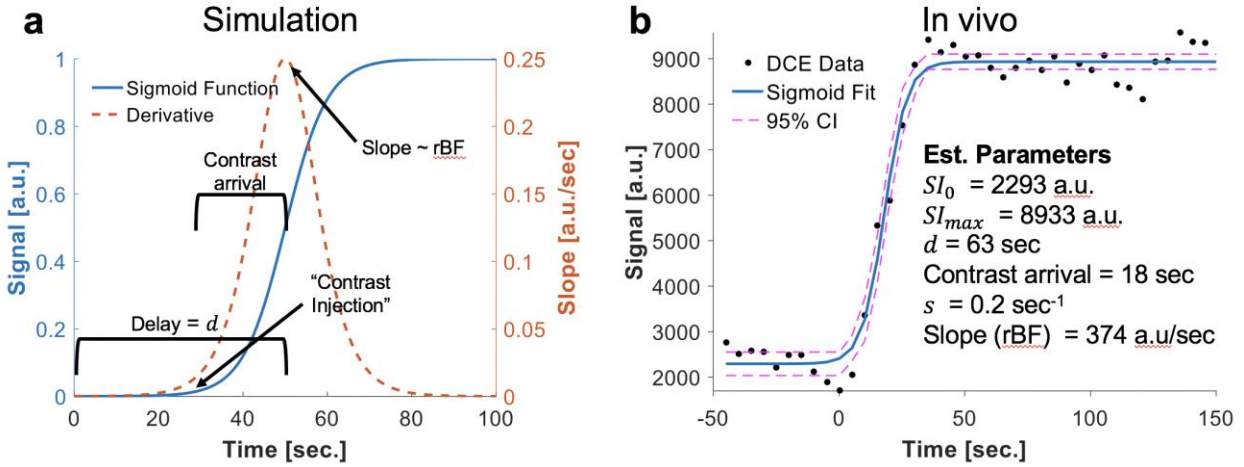

Supporting Information Figure S2. A simulated logistic function (a) shows the general sigmoid-shape of the fitting curve (solid line) along with its derivative (dotted line). The delay

time (d) is estimated from the beginning of the acquisition to the point of inflection (50% max enhancement) along the sigmoid-shaped fit. The contrast arrival time is adjusted based on the contrast injection time point. The inflection point is also the location for the measurement of the uptake curve slope which is assumed to be proportional to the relative blood flow (rBF). In vivo DCE data from a single voxel within the placental tissue is plotted throughout the injection of ferumoxytol (**b**). The data was fit to the logistic function and is plotted (solid line) along with the 95% confidence intervals (CI) (dotted line). The resulting estimated parameters are shown on the graph.

To determine the fetal change in SI (ΔSI) from the ferumoxytol contrast, ROIs were manually drawn on a single slice containing both fetal tissue and amniotic fluid. The percent ΔSI was calculated using Eq. 3 below

$$\Delta SI = 100\% \cdot \left(SI_f - SI_i\right)/SI_i \quad [3]$$

using the SI from the initial (SI_i) and final (SI_f) time frame in the DCE data.

Statistical Analysis

A Wilcoxon rank-sum test was performed between the distributions of the ASL FAIR ratio percentages within the placenta using either +OVS or –OVS tag modifications by combining data from all animals. A Wilcoxon rank-sum test was performed between the grouped ASL FAIR +OVS ratio percentage and DCE arrival times as well as the grouped ASL FAIR +OVS ratio percentage and DCE uptake slope. To determine a significant change in the DCE signal intensity, a paired, two-sided Student t-test was performed between SI_i and SI_f averaged across all animals. Statistical significance was defined as a p-value<0.05.

RESULTS

The 3D volume renderings of the MRA, shown in Fig. 2a demonstrate the highly vascular nature of the rhesus placenta in the uterine space, and the ability of ferumoxytol enhanced MRA to visualize the placental vasculature. Maternal blood supply to the placenta and growing fetus, originates in the uterine arteries prior to delivery to the placenta through the radial and spiral arteries. The major feeding arteries and draining veins are highlighted. The rhesus macaque placenta is typically bi-lobed (i.e., two separate placental discs, with the primary disc having the insertion of the umbilical cord, and connected to the secondary disc by several arteries and veins) and differs from typical single lobed human placental anatomy in this respect. Fig. 2b shows T_2-weighted anatomical MR images of the macaque placenta with the placental tissue separately outlined. Several other anatomical features are highlighted to orient the reader.

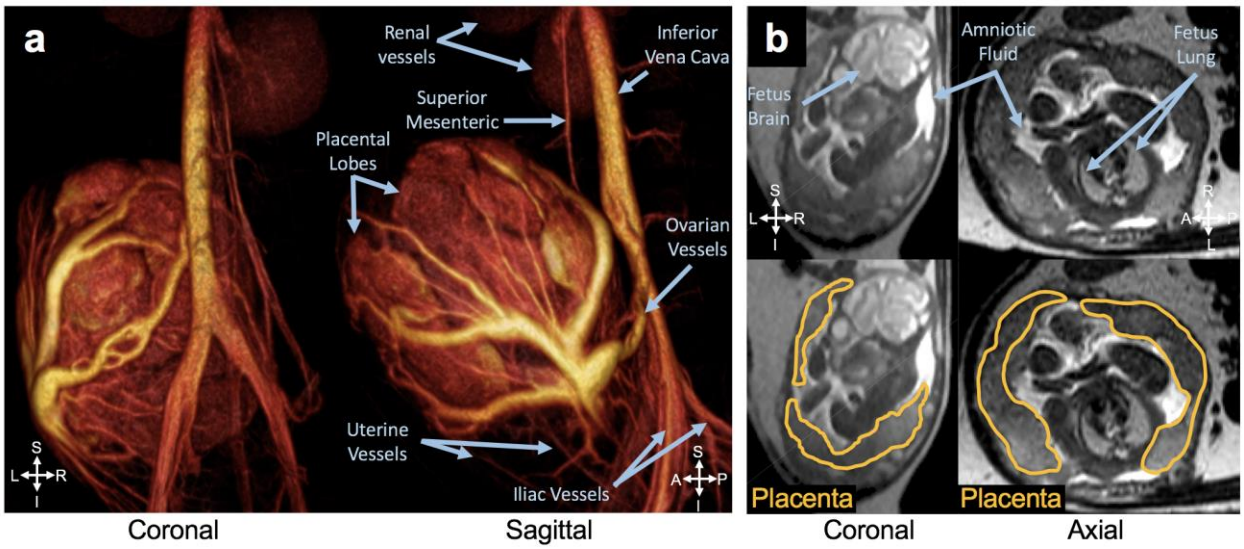

Figure 2. Coronal and sagittal views (a) of a volume rendered 3D MR ferumoxytol angiogram (MRA) of the rhesus placenta and major blood vessels. The rhesus placenta is a bi-lobular system with blood being supplied from both the left and right uterine and ovarian arteries. Draining

vessels are primarily observable in the 3D MRA. Coronal and axial views (**b**), top and bottom row of an anatomical 2D multi-slice T_2-weighted MR image with the primary and secondary placental lobes outlined. The fetus and bright amniotic fluid are readily observable between the placental lobes in the T_2-weighted anatomical images.

Fig. 3a (top row) shows the averaged FAIR tagged, control, and ASL perfusion ratio map (color) overlaid on the M_0 image (gray) from the ASL FAIR –OVS acquisition. The ratio map shows focal signal enhancements within the placenta and in its surrounding vasculature. Fig. 3a (bottom row) shows the ratio map from the +OVS acquisition depicting similar localized regions of high perfusion with predominately noise elsewhere. A histogram distribution of the ratio percentages within the placenta for the two FAIR acquisitions is displayed in Fig. 3b showing a reduction in the median ratio percentage and saturation of high ASL ratio voxels (>10%). The ASL ratios for both FAIR acquisitions in each of the ten individual macaques and all animals grouped together are shown as box-and-whisker plots in Fig. 4a. Fig. 4b shows a voxel-wise density plot of the ASL ratio between the two FAIR variants with voxels having reduced ASL ratio with addition of OVS pulses circled. OVS pulses significantly (p<0.05) reduced the median ASL ratio (+OVS=0.64±1.42%) compared to without OVS pules (–OVS=0.71±2.00%). Table 2 summarizes the placental perfusion values (median±SD and quartile values (5%-95%)) of the ASL ratio for all interventions.

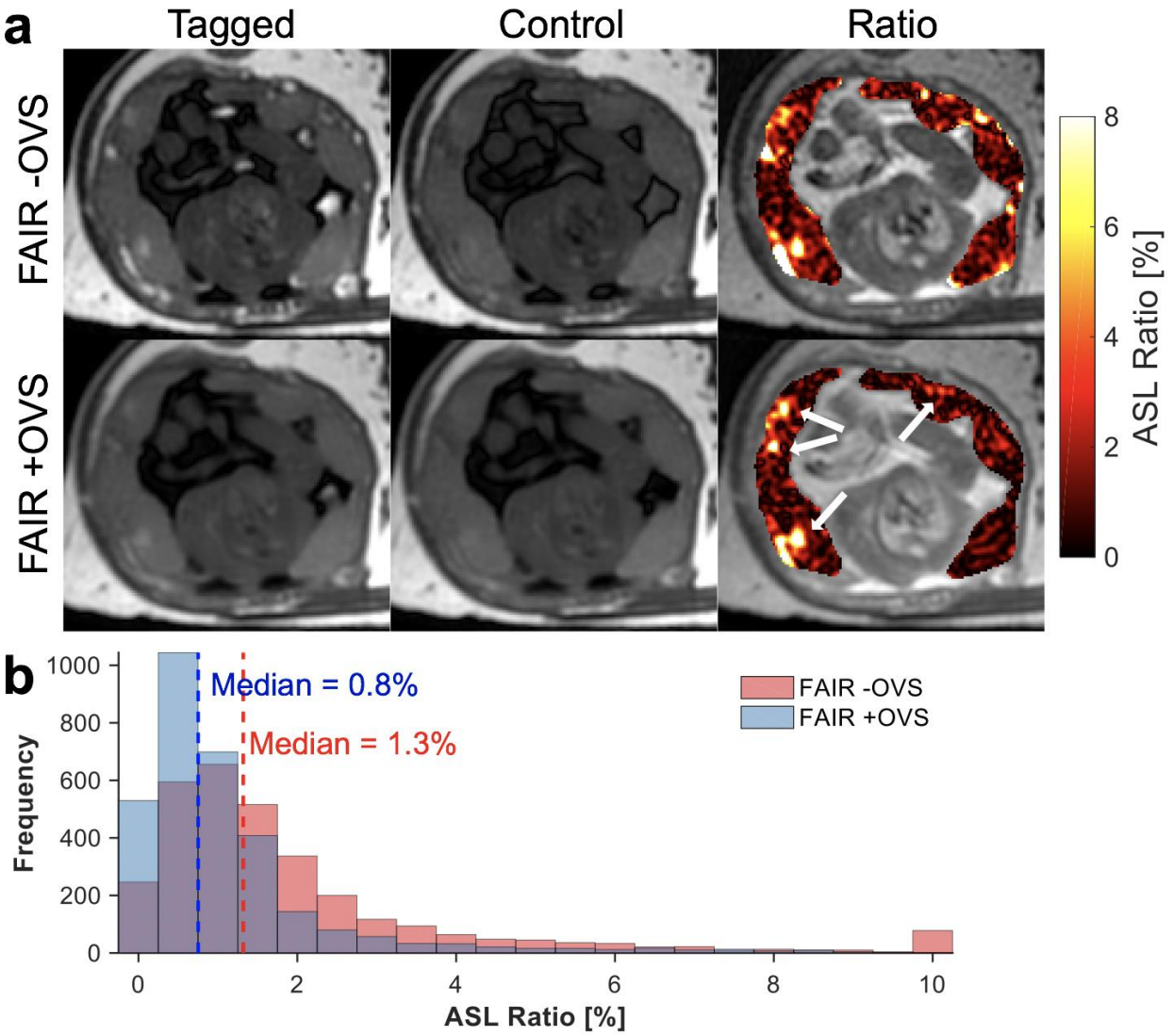

Figure 3. Representative ASL FAIR images (a, top row) show the FAIR tagged (left column), control (center column), and the perfusion ratio percentage map (right column), shown in color scale, overlaid on a proton density weighted image, shown in gray scale. OVS pulses were added to the ASL FAIR after FAIR tagging (**a**, bottom row) to reduce macrovascular signal on the periphery of placental tissue. Several localized perfusion regions within the placenta remain in the +OVS ratio map and these regions are highlighted by the white arrows. A histogram plot of the ASL ratio percentage (**b**) within the placental tissue for both ASL acquisitions is shown for one case ($N = 1$).

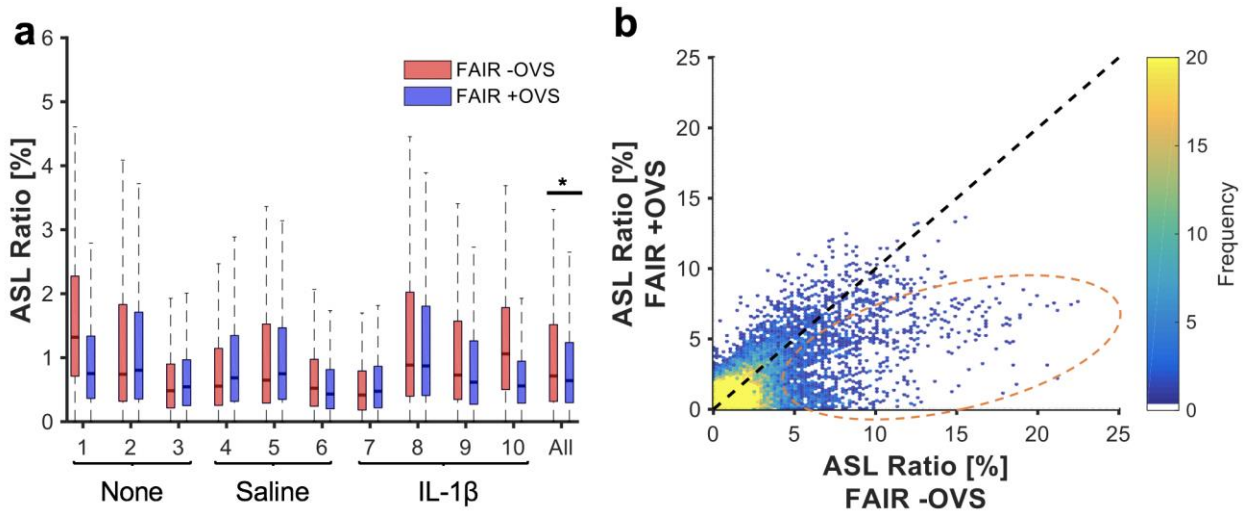

Figure 4. A comparison between the distributions of the ASL ratio percentages within the placental tissue for each individual macaques and for all macaques grouped together is shown as a box-and-whisker plot (a) for the two ASL FAIR pulse sequences: with (+OVS) or without (-OVS) the addition of OVS RF pulses. A voxel-wise density plot (**b**) of the ASL FAIR ratio percentage for corresponding spatial locations in either the +OVS or –OVS variant. The region with voxels having reduced ASL ratio with addition of OVS pulses are circled. An identity line (black-dotted line) is also plotted for reference.

	ASL Ratio [%]			
	FAIR -OVS		FAIR +OVS	
Intervention	Median ± SD	Quartiles [5 - 95%]	Median ± SD	Quartiles [5 - 95%]
None (*N*=3)	0.81 ± 2.37	[0.07 – 6.11]	0.69 ± 1.47	[0.06 – 4.07]
Saline (*N*=3)	0.57 ± 1.83	[0.05 – 4.93]	0.61 ± 1.56	[0.06 – 4.71]
IL-1β (*N*=4)	0.75 ± 1.73	[0.06 – 4.62]	0.62 ± 1.26	[0.06 – 3.45]
All (*N*=10)	0.71 ± 2.00	[0.06 – 5.21]	0.64 ± 1.42	[0.06 – 4.01]

Table 2. Summary of the ASL perfusion measurements within the rhesus macaque placenta for the three subgroups. The median ± SD and quartile values [5% and 95%] from the ASL ratio percentage for both FAIR acquisitions are tabulated.

Heterogeneous contrast arrival times and localized regions of contrast in-flow are observable in the volumetric maximum-intensity projections (MIPs) (Fig. 5a) and single slice DCE MRI series (Fig. 5b) of corresponding time-frames. The DCE signal enhancement curve and fits for voxels representing 'early-enhancing' and 'late-enhancing' placental regions or fetal regions are shown in Fig. 5c. Differences in enhancement time within placental regions is approximately 10's of seconds. From the sigmoid-shaped fits, contrast arrival time (Fig. 5d) and relative blood flow (uptake curve slope) maps (Fig. 5e) are derived. Table 3 summarizes the ferumoxytol DCE measurements for all interventions. The median contrast arrival time from the time of injection for all cases was 34±25 sec and ranged from 14-87 sec (5-95% quartile) with a median relative blood flow of 102±39 sec^{-1}.

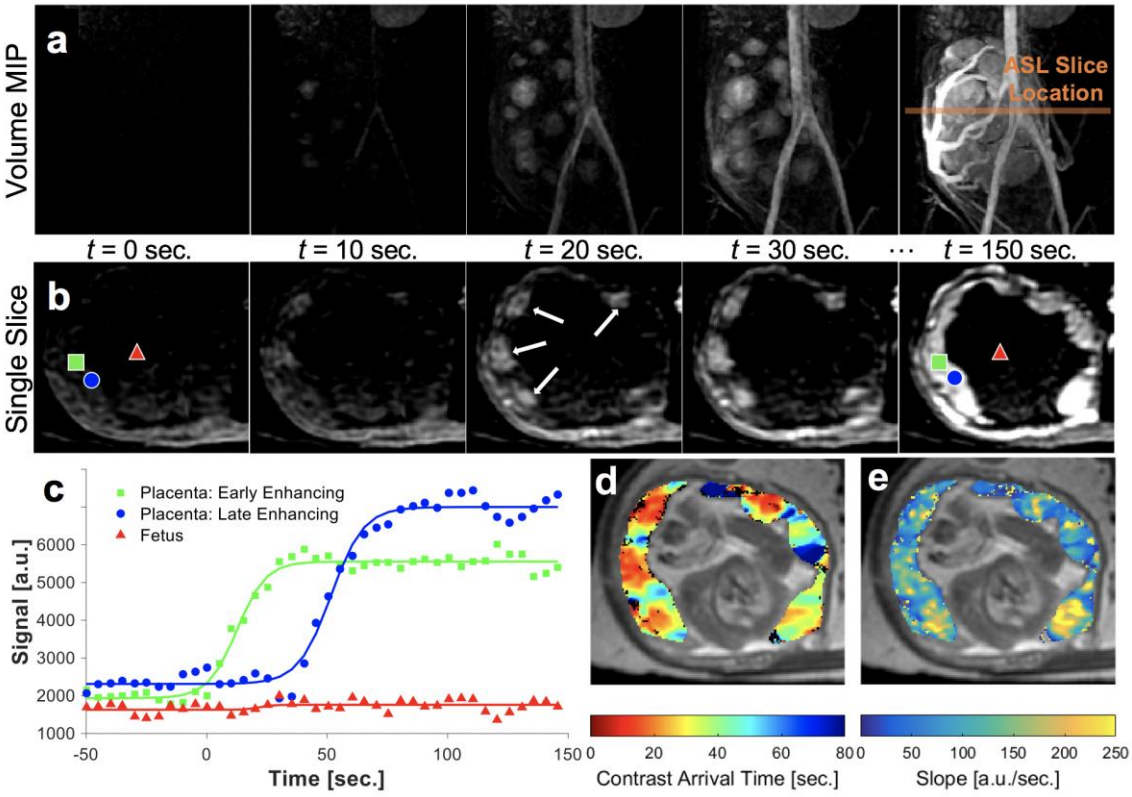

Figure 5. Dynamic contrast enhanced (DCE) MR images acquired throughout the injection of ferumoxytol. Maximum intensity projection (MIP) images (**a**) of the whole placenta and major

vessels from a T_1-weighted DCE time series shown at 10 second time frames. The location of the ASL slices (orange line) is denote on the MIPs. The corresponding axial slice (**b**), matching the location of the ASL slice, is shown at corresponding time frames. Regions of early contrast arrival are highlighted (white arrows). The DCE signal enhancement and sigmoid curve fits (**c**) are shown for single voxels in two locations within the placenta, early (■) and late enhancing (●), and for a single voxel within the fetus (▲). The voxel locations are also highlighted in the final DCE time series image. Parameter maps derived from the fitted DCE data show the contrast arrival time (**d**) and the estimated relative blood flow (**e**) to the placental tissue. Parameter maps are shown (color scale) overlaid on an anatomical reference image (gray scale).

	DCE Parameter			
	Contrast Arrival Time [sec]		Relative Blood Flow [sec^{-1}]	
Intervention	Median ± SD	Quartiles [5 - 95%]	Median ± SD	Quartiles [5 - 95%]
None (*N*=3)	33 ± 31	[11 - 107]	112 ± 34	[21 - 288]
Saline (*N*=3)	35 ± 21	[16 - 76]	85 ± 34	[17 - 252]
IL-1β (*N*=4)	33 ± 23	[16 - 72]	106 ± 50	[15 - 388]
All (*N*=10)	34 ± 25	[14 - 87]	102 ± 39	[17 - 336]

Table 3. Summary of the ferumoxytol DCE measurements of the contrast arrival time and relative blood flow within the rhesus macaque placenta for the three interventions. The median ± SD and quartile values [5% and 95%] for the DCE parameters are tabulated.

No ferumoxytol signal enhancement was observable within the fetus or amniotic fluid. The percent change in the signal intensity was calculated for both from the 4D DCE data. A non-significant relative signal change was measured to be -0.6±3.0% for fetal tissue (p=0.52) and 1.9±8.8% for the amniotic fluid (p=0.59) across all animals in the study.

A regional comparison for one case in Fig. 6 shows the parametric maps of perfusion: ASL (FAIR +OVS) ratio (a), DCE contrast arrival times (b), and DCE relative blood flow (c) within the

placental tissue. Spatial similarities can be observed between voxels exhibiting high ASL ratio, early contrast arrival, and high relative blood flow. Locations within placental tissue that display long contrast arrival times also show low ASL ratio percentage which are likely dominated by noise (<0.5% ASL ratio). These trends can be observed in the voxel-wise density plots of ASL ratio and contrast arrival times (Fig. 6d) and between ASL ratio and uptake slope (Fig. 6e) in the placental tissue for the single case. The circled region in Fig. 6d shows many voxels with high ASL ratio having short contrast arrival times while voxels with long contrast arrival times tended to have very low ASL ratio. The highlighted region in Fig. 6e showed a slight association between voxels with high ASL ratio coinciding with voxels with high uptake slope.

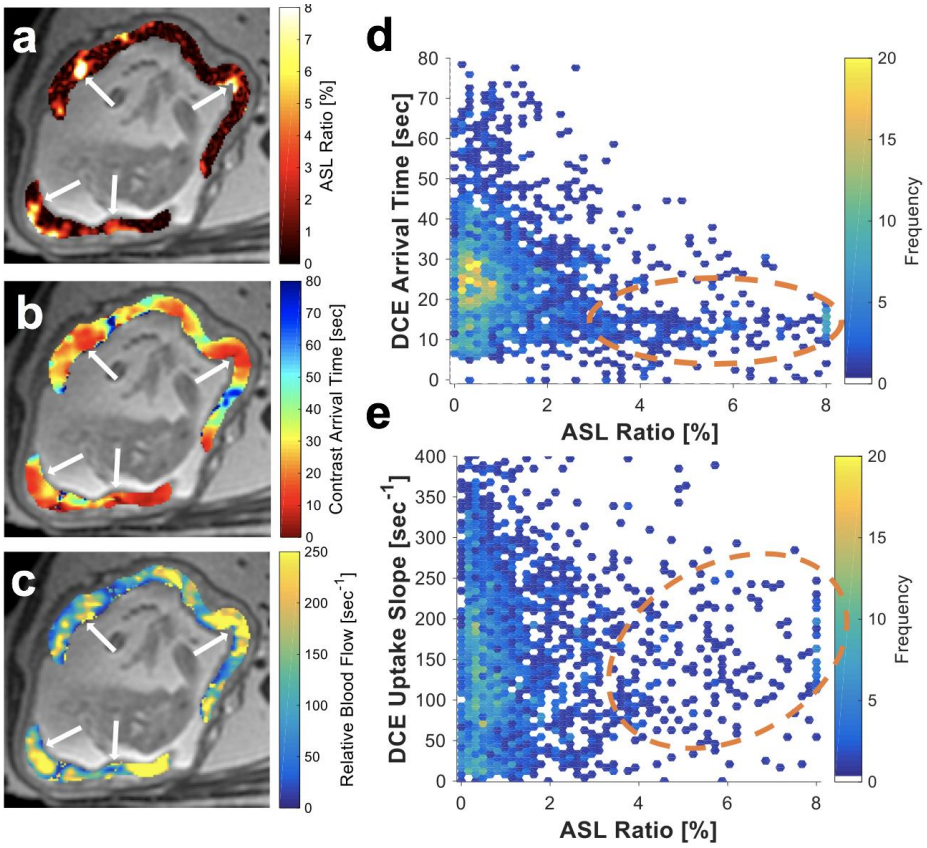

Figure 6. A regional comparison between the parametric maps of perfusion: ASL (FAIR +OVS) ratio (a), DCE contrast arrival times (b), and DCE relative blood flow (c) within the

placental tissue. Spatial similarities between voxels with high ASL ratio percentage, early contrast arrival, and high relative blood flow are indicated by the white arrows. The parameter maps are shown in color scale overlaid on an anatomical reference image in gray scale. A voxel-wise density plot (**d**) between ASL ratio and uptake slope is shown for a representative case (N =1). The region with voxels having both high ASL ratio and early contrast arrival times is circled. A second voxel-wise density plot (**e**) between ASL ratio and uptake slope shows a circled region with a slight association between voxels with high ASL ratio coinciding with voxels with high uptake slope.

The voxels with early contrast arrival were significantly ($p<<0.05$) correlated with voxels with high ASL ratio percentage, which can be seen in the box-and-whiskers plots (Fig. 7a). Fig. 7b shows a voxel-wise density plot for all placental voxels across the entire group of monkeys studied demonstrating a large frequency of voxels with early DCE arrival time and high ASL signal. Further, Fig. 7c shows a box-and-whiskers plot where voxels with high uptake slope were also significantly ($p<<0.05$) correlated with voxels with high ASL ratio percentage. The voxel-wise density plot for all voxels and all animals is shown in Fig. 7d.

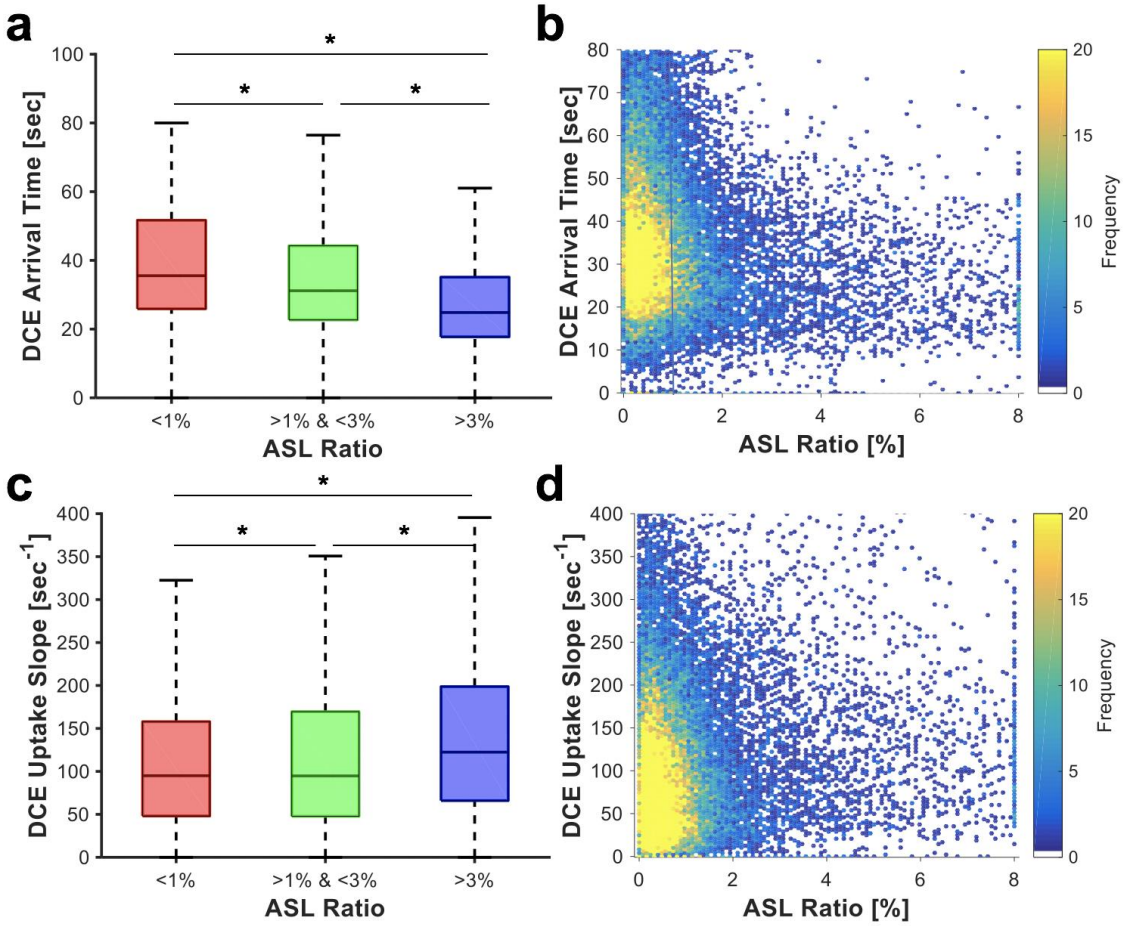

Figure 7. Box-and-whisker plots (a) comparing the ASL ratio percentage versus either the DCE contrast arrival time or the DCE uptake slope (b) for all macaques (*N* = 10). A Wilcoxon rank-sum test shows statistically significant differences between the three groups. The voxel-wise density plots are shown for the ASL ratio percentage versus either the DCE arrival time (**c**) or the DCE uptake slope (**d**). (* = $p < 0.05$)

DISCUSSION

In this work, ASL FAIR and ferumoxytol DCE MRI were shown to be feasible to detect early blood delivery to the placenta in a pregnant rhesus macaque model. Regions of intense ASL perfusion signal were correlated spatially to early arrival times and increased slope of contrast

agent uptake on DCE MRI. Likely, both ASL FAIR and ferumoxytol DCE MRI can identify the locations of the maternal decidual spiral arteries entering the placental intervillous space. We performed IL-1β infusions to induce inflammation and potentially disrupt perfusion. However, no statistically significant differences were observed between the IL-1β injected group and the control groups in the ASL ratio or DCE contrast arrival time and relative blood flow. Sub-analysis of the groups should be considered preliminary due to low numbers.

The heterogeneous nature of intervillous perfusion signal in ASL FAIR suggests that a voxel-wise interpretation at distal regions from the spiral arteries may be confounded by the limits of the FAIR inversion tagging duration and delay. This observation is corroborated by the extended transit time across the placental region from ferumoxytol DCE images. While some of this variation may be compensated in ASL by labeling closer to placental regions and with a tighter bolus to limit dispersion, these adaptations will not address the extended transit times. Thus, the unique intervillous space of the placenta that leads to extended transit times is likely the reason for the low correlation between ASL and DCE observed in our study. In ASL FAIR, and ASL generally, for any signal difference to occur, spins must travel from the labeling region to the imaging voxel within a post-label delay period. In this work, this delay was 2.0 sec, a typical value used for ASL at 3.0T. Extending the post-label delay would theoretically allow for ASL with reduced transit time dependence but with the tradeoff that the magnetic-inversion label will decay exponentially according to the T_1 of blood (T_1=~1.6 sec at 3T [29]) degrading SNR.

The contrast arrival times and relative blood flow were estimated using a simplified, semi-quantitative approach based on the empirical uptake curves behaving in a sigmoidal fashion since limited literature exists for absolute quantification of ferumoxytol DCE MRI data. Most animals showed similar regions of high ASL ratios, early contrast arrival time, and higher uptake slope.

Blood delivery through the spiral arteries should have the highest velocity and slow down upon entering the intervillous space. In some animals, regions with high ASL ratio and early arrival time are adjacent to regions with higher uptake slope. Additionally, some regions with high uptake slope do not coincide with regions having early contrast arrival time or high ASL signal. This may be physiological with more complex flow patterns within the intervillous space being measured such as a narrow portion of the placental tissue where ferumoxytol contrast quickly fills. Regions with high ASL signal and long contrast arrival times may be potentially from fetal perfusion. ASL FAIR analysis ignores contributions from fetal circulations and may overestimate placental perfusion as a result. The distribution of DCE arrival times within the placenta were substantially longer than the 2.0 sec ASL TI. In distal portions of the placenta with late enhancment, the contrast arrival times are upwards of 70 seconds from the injection time to completely fill. The contrast arrival is much faster in early enhancing regions. These times preclude measurement by spatially-based ASL methods due to loss of ASL label. The early contrast arrival portions may be able to predict the locations of ASL and vice versa but distal portions with slow uptake, noise predominates the ASL ratio images. The ASL data is likely uninformative beyond the immediate vicinity of the spiral arteries.

Additional saturation RF pulses (e.g. QUIPSS II and Q2TIPS) have previously been shown to minimize systematic error caused by variable transit time of labeled blood and remove contaminating macro-vascular signal for brain applications [9, 10]. Here, we have applied saturation pulses to the tagging region above and below the imaging slice to limit the ASL bolus width. A controlled ASL bolus width is recommended for quantification, allowing transport of the tagged magnetization into the extravascular space and to avoid intravascular signal. In the case of the placenta, blood is delivered to the tissue via spiral arteries after which it enters the intervillous

space, a blood compartment. There the magnetization is subject to motion within the intervillous space, and exchange with the placenta tissue and fetal circulation. With our ASL timing, using OVS would allow for measurements insensitive to a 1s difference in the bolus arrival time. This is significantly less that the heterogeneity observed in DCE. Thus, the major effect of the OVS was to suppress the macro-vasculature signal, particularly on the periphery of the placenta. A fraction of the observed ASL signal is still intravascular residing in the intervillous space. OVS did additionally lower the median ASL signal, which is expected due to the shorter bolus width, a reduction of partial volume artifacts from large vessels, and off-resonance magnetization transfer. The endogenous, non-invasive nature of ASL is advantageous for safety and cost reasons when translating to human patients. While placental ASL perfusion has been investigated in humans [6, 8, 30], animal studies with reference standards are limited. Currently, no ASL perfusion studies exist in the rhesus macaque placenta for which to compare these results. In humans however, ASL FAIR has been shown to be sensitive to detect a greater proportion of low perfusion voxels in intrauterine growth restricted patients versus controls [8, 30] and reduced perfusion in the basal region of the placenta in mothers who delivered small for gestational age neonates [6]. Given the comparisons in this study and these results, it is conceivable that the distribution of early arriving blood is sufficient to determine the overall health of the placenta. Spatially-based ASL methods may still prove valuable in measuring blood flow to the intervillous space near the vicinity of spiral arteries. Spiral artery remodeling during pregnancy is essential to maximize the delivery of maternal blood to the intervillous space at suitably low velocity [31]. Maladaptation of the spiral arteries has been associated with several gestational complications including pre-eclampsia and intrauterine growth restriction [32, 33]. However, in defining the pathogenesis, the ASL signal may not fully represent the perfusion signal.

FAIR ASL does have limitations with respect to imaging the placenta. In FAIR, the labeling plane and imaging plane are identical. Thus, there is potential for the imaging slab to intersect with the feeding arteries and potential for tagging of venous, fetal, and intervillous flow. An axial/transverse slab was chosen in this work. This puts the ASL plane roughly orthogonal to the feeding uterine arteries but may intersect with in-plane spiral arteries. Alternative ASL variants have been explored to measure placental perfusion in humans including pseudo-continuous ASL (pCASL) [34] and velocity-selective ASL (VSASL) [35, 36]. pCASL utilizes a train of short RF pulses to invert the magnetization of blood as it flows through a thin labeling plane. Recent work applying pCASL in the human placenta at 3T [37] shows localized perfused regions with high signal intensity, similar to the results presented here. pCASL showed promise to estimate the placental blood flow and arterial transit time in healthy subjects imaged in the second trimester. While pCASL shows higher SNR than pulsed ASL methods (e.g. FAIR), the labeling technique suffers from extended arterial blood delay times between the labeling and imaging location (i.e. placenta). Furthermore, the feeding arteries must be located to place the labeling plane, which is difficult for the placenta.

The extended arrival time across the placental region from ferumoxytol DCE MRI, median=34 sec from the injection time, are qualitatively similar to that observed by others using GBCA's in the rhesus macaque [15, 38] and iron in mice [39]. Though not specifically reported on a voxel-wise basis, the contrast arrival times to the placenta appear to be approximately 10's of sec, with distant portions taking upwards of 1 min. In humans, Burchell demonstrated 2-3 sec arrival times of contrast dye into the intervillous space after injected through an aorta catheter [40] measure by X-ray. Diffusion of the dye took roughly 30 sec in late-gestational stage women with the diffusion rate depending on the spiral artery and location within the placenta. Similarly, Borell

et al. quoted “first seen” dye contrast into the intervillous space in humans of 3-11 sec and qualitatively described slow filling at more distal portions of the placenta [41]. The longer arrival times reported in this study are likely due to the 20 sec venous infusion resulting in contrast dispersion. Additionally, arrival time was calculated at the 50% enhancement hence, slow enhancement would lead to extended estimates of the contrast arrival.

We have shown non-significant enhancement of the fetal tissue and amniotic fluid throughout the DCE acquisition providing evidence that ferumoxytol is not immediately taken up into these tissues. MRI contrast agents, primarily GBCA, have previously been used to enhance placental visualization and identify maternal decidual spiral arteries in humans [42], the rhesus macaque [15, 16, 38, 43, 44] and a variety of small animal models [45-50]. However, most GBCA’s exchange with the extravascular space. Recently, GBCA’s were shown to be at nearly undetectable levels in the fetal and placental tissue in non-human primates [51] after intravenous infusion for DCE MRI, but they have previously been observed in the bladder of the fetus [38]. Ferumoxytol can be administered during pregnancy similar to other intravenous iron preparations but is safer and produces fewer allergic and idiosyncratic reactions [52]. Pregnancy is a physiological iron-deficient state and as such presents an imaging opportunity with efficient iron delivery by ferumoxytol without risk of iron overload [53]. Further, its long intravascular half-life (~14-15 hrs.) compared to GBCA makes ferumoxytol a useful agent for consideration as a vascular MRI T_1 shortening contrast agent.

MRI techniques to measure tissue perfusion based on motion rather than spatial-labeling of blood exist such as, previously mentioned, VSASL, and intravoxel incoherent motion (IVIM). VSASL tags blood based on flow velocity using flow-sensitizing gradients [35, 36]. VSASL is insensitive to the large transit delays observed in the placenta as has been recently demonstrated

[54, 55] and allows for 3D imaging coverage. VSASL demonstrated greater global placental perfusion with differences in regional variation in pregnancies with fetal congenital heart disease compared to controls suggesting VSASL may provide viable biomarkers in early pregnancy detection of dysfunction [55]. IVIM relies on collecting diffusion-weighted MR images with varying degrees of weighting followed by signal modeling of the fast (perfusion) and slow (diffusion) components of water. This technique assumes blood motion is incoherent over a voxel and of higher degree than surrounding tissue [56]. IVIM has been applied to placenta imaging in healthy subjects [57] and demonstrated promise in detecting differences in the perfusion fraction in pregnancies with fetal growth restriction [58], small for gestational age fetuses [59], and in early and late preeclampsia [60] compared to controls. In initial comparisons of placental perfusion, IVIM demonstrated a higher predictive power to reduced birthweight than ASL FAIR [6]. VSASL or IVIM may be better alternatives to ASL FAIR due to reduced dependence on the long transit time. However, strategies for the mitigation of maternal and fetal motion are crucial for motion-based perfusion techniques since encoding of bulk-motion will confound interpretation of the measured signals.

Bulk-motion can also be problematic for pulsed ASL (e.g. FAIR) and DCE MRI acquisitions confounding resulting and/or creating image artifacts, however, IVIM and VSASL are sensitive to much lower levels of motion. In this study, maternal respiratory motion was considered the potentially primary source of bulk motion. Due to anesthesia, negligible fetal motion was qualitatively observed throughout the duration of the ASL and DCE acquisition. The DCE acquisition used a respiratory-gated, acquisition known as DISCO [23] that reconstructs images using pseudo-randomly acquired segmented portions of k-space. The pseudorandom sampling, similar to radial, reduces motion blurring and other motion-related artifacts. These

effects are likely small though given the regularity of maternal breathing under anesthesia and were not observable in image. A 2.0 sec TI was chosen to coincide with the maternal respiratory rate ensuring the labeling and imaging region were in an identical respiratory phase and physical location. Furthermore, image registration was performed to mitigate remaining maternal motion. More advanced motion management techniques, reviewed elsewhere [61], may be needed in clinical settings where anesthesia is not commonly used and fetal motion is potentially more significant.

There are several limitations to the current study. The ASL FAIR data represents a single slice acquisition where volumetric coverage of the placenta would be desirable. With dispersion and bolus delays from multiple inputs into the placenta, (i.e. uterine arteries), we have limited the ASL FAIR approach to a single delay time. Thus, a limited representation of entire placental perfusion is shown. Long acquisition times may have contributed to through-plane placental tissue movement between the ASL and DCE acquisitions. Therefore, errors in the volume-to-slice registration of placental tissue may have result in spatial differences between the ASL signal, contrast arrival time, and relative blood flow. Our DCE-fitting algorithm with a sigmoid-shaped function may overestimate contrast arrival times in locations with ‘jets’ of blood. These unusual flow patterns, such as Borell’s jets first demonstrated by MRI using a GBCA [38], would lead to partial enhancements such that the uptake curve would not be sigmoid-shaped, and the contrast arrival time may be overestimated as a result. Perfusion variations may also manifest from different arterial pressures, cardiac outputs, gestational ages as well as positioning.

In conclusion, +OVS reduced the highest ASL FAIR ratio signal compared to -OVS when controlling for labeling duration. ASL FAIR and ferumoxytol DCE MRI are feasible to detect regions of early blood delivery in the placenta in a pregnant rhesus macaque model. In this

small, preliminary study, placental intervillous perfusion, as measured by ASL and DCE, was not altered by the IL-1β exposure compared to controls. An endogenous labeling perfusion technique is potentially advantageous when translating to human mothers but is possibly limited due to the extended transit times for placental tissues beyond the immediate vicinity of the maternal spiral arteries.

ACKNOWLEDGEMENTS

The authors thank our collaborators and colleagues. We gratefully acknowledge the University of Wisconsin-Madison School of Medicine and Public Health and Departments of Medical Physics, Radiology, and Obstetrics and Gynecology for research support and AMAG Pharmaceuticals, Inc. Waltham, MA for the generous gift of ferumoxytol. In addition, the authors wish to acknowledge support from GE Healthcare who provides research support to UW-Madison. Further, Dr. Reeder is a Romnes Faculty Fellow, and has received an award provided by the University of Wisconsin-Madison Office of the Vice Chancellor for Research and Graduate Education with funding from the Wisconsin Alumni Research Foundation.

REFERENCES

1. Zaidi, S.F., et al., *Comprehensive Imaging Review of Abnormalities of the Placenta.* Ultrasound Q, 2016. **32**(1): p. 25-42.
2. Gandhi, S., M. Ohliger, and L. Poder, *State-of-the-Art Imaging of the Placenta.* Current Radiology Reports, 2015. **3**(12): p. 1-13.
3. Krishna, U. and S. Bhalerao, *Placental Insufficiency and Fetal Growth Restriction.* Journal of Obstetrics and Gynaecology of India, 2011. **61**(5): p. 505-511.

4. Uzan, J., et al., *Pre-eclampsia: pathophysiology, diagnosis, and management.* Vascular Health and Risk Management, 2011. **7**: p. 467-474.

5. Guttmacher, A.E., Y.T. Maddox, and C.Y. Spong, *The Human Placenta Project: placental structure, development, and function in real time.* Placenta, 2014. **35**(5): p. 303-4.

6. Derwig, I., et al., *Association of placental perfusion, as assessed by magnetic resonance imaging and uterine artery Doppler ultrasound, and its relationship to pregnancy outcome.* Placenta, 2013. **34**(10): p. 885-91.

7. Kim, S.-G., *Quantification of relative cerebral blood flow change by flow-sensitive alternating inversion recovery (FAIR) technique: Application to functional mapping.* Magnetic Resonance in Medicine, 1995. **34**(3): p. 293-301.

8. Gowland, P.A., et al., *In vivo perfusion measurements in the human placenta using echo planar imaging at 0.5 T.* Magnetic Resonance in Medicine, 1998. **40**(3): p. 467-473.

9. Wong, E.C., R.B. Buxton, and L.R. Frank, *Quantitative imaging of perfusion using a single subtraction (QUIPSS and QUIPSS II).* Magn Reson Med, 1998. **39**(5): p. 702-8.

10. Luh, W.M., et al., *QUIPSS II with thin-slice TI1 periodic saturation: a method for improving accuracy of quantitative perfusion imaging using pulsed arterial spin labeling.* Magn Reson Med, 1999. **41**(6): p. 1246-54.

11. Khalifa, F., et al., *Models and methods for analyzing DCE-MRI: A review.* Medical Physics, 2014. **41**(12): p. 124301.

12. Sourbron, S.P. and D.L. Buckley, *Classic models for dynamic contrast-enhanced MRI.* NMR Biomed, 2013. **26**(8): p. 1004-27.

13. Cutajar, M., et al., *Comparison of ASL and DCE MRI for the non-invasive measurement of renal blood flow: quantification and reproducibility.* European Radiology, 2014. **24**(6): p. 1300-8.

14. Lin, Y.R., et al., *Comparison of arterial spin labeling and first-pass dynamic contrast-enhanced MR imaging in the assessment of pulmonary perfusion in humans: the inflow spin-tracer saturation effect.* Magn Reson Med, 2004. **52**(6): p. 1291-301.

15. Frias, A.E., et al., *Using dynamic contrast-enhanced MRI to quantitatively characterize maternal vascular organization in the primate placenta.* Magn Reson Med, 2015. **73**(4): p. 1570-8.

16. Schabel, M.C., et al., *Functional imaging of the nonhuman primate Placenta with endogenous blood oxygen level–dependent contrast.* Magnetic Resonance in Medicine, 2015: p. n/a-n/a.

17. Ray, J.G., et al., *Association Between MRI Exposure During Pregnancy and Fetal and Childhood Outcomes.* Jama, 2016. **316**(9): p. 952-61.

18. Neuwelt, A., et al., *Iron-Based Superparamagnetic Nanoparticle Contrast Agents for MRI of Infection and Inflammation.* American Journal of Roentgenology, 2015. **204**(3): p. W302-W313.

19. Golos, T.G., et al., *On the role of placental Major Histocompatibility Complex and decidual leukocytes in implantation and pregnancy success using non-human primate models.* Int J Dev Biol, 2010. **54**(2-3): p. 431-43.

20. Presicce, P., et al., *Neutrophil Recruitment and Activation in Decidua with Intra-Amniotic IL-1beta in the Preterm Rhesus Macaque.* Biology of Reproduction, 2015. **92**(2): p. 56.

21. Sadowsky, D.W., et al., *Preterm labor is induced by intraamniotic infusions of interleukin-1beta and tumor necrosis factor-alpha but not by interleukin-6 or interleukin-8 in a nonhuman primate model.* Am J Obstet Gynecol, 2006. **195**(6): p. 1578-89.

22. Silk, J., et al., *Gestation length in rhesus macaques (Macaca mulatta).* International Journal of Primatology, 1993. **14**(1): p. 95-104.

23. Saranathan, M., et al., *DIfferential Subsampling with Cartesian Ordering (DISCO): a high spatio-temporal resolution Dixon imaging sequence for multiphasic contrast enhanced abdominal imaging.* J Magn Reson Imaging, 2012. **35**(6): p. 1484-92.

24. Johnson, K.M., et al., *Optimized 3D ultrashort echo time pulmonary MRI.* Magnetic Resonance in Medicine, 2013. **70**(5): p. 1241-1250.

25. Klein, S., et al., *elastix: A Toolbox for Intensity-Based Medical Image Registration.* IEEE Transactions on Medical Imaging, 2010. **29**(1): p. 196-205.

26. Shamonin, D., et al., *Fast Parallel Image Registration on CPU and GPU for Diagnostic Classification of Alzheimer's Disease.* Frontiers in Neuroinformatics, 2014. **7**(50).

27. Avants, B.B., et al., *A reproducible evaluation of ANTs similarity metric performance in brain image registration.* Neuroimage, 2011. **54**(3): p. 2033-44.

28. Buxton, R.B., et al., *A general kinetic model for quantitative perfusion imaging with arterial spin labeling.* Magnetic Resonance in Medicine, 1998. **40**(3): p. 383-396.

29. Ingram, E., et al., *R1 changes in the human placenta at 3 T in response to a maternal oxygen challenge protocol.* Placenta, 2016. **39**: p. 151-3.

30. Francis, S.T., et al., *Non-invasive mapping of placental perfusion.* Lancet, 1998. **351**(9113): p. 1397-9.

31. Espinoza, J., et al., *Normal and abnormal transformation of the spiral arteries during pregnancy.* J Perinat Med, 2006. **34**(6): p. 447-58.

32. Olofsson, P., R.N. Laurini, and K. Marsal, *A high uterine artery pulsatility index reflects a defective development of placental bed spiral arteries in pregnancies complicated by hypertension and fetal growth retardation.* Eur J Obstet Gynecol Reprod Biol, 1993. **49**(3): p. 161-8.

33. Aardema, M.W., et al., *Uterine artery Doppler flow and uteroplacental vascular pathology in normal pregnancies and pregnancies complicated by pre-eclampsia and small for gestational age fetuses.* Placenta, 2001. **22**(5): p. 405-11.

34. Dai, W., et al., *Continuous flow-driven inversion for arterial spin labeling using pulsed radio frequency and gradient fields.* Magn Reson Med, 2008. **60**(6): p. 1488-97.

35. Duhamel, G., C. de Bazelaire, and D.C. Alsop, *Evaluation of systematic quantification errors in velocity-selective arterial spin labeling of the brain.* Magn Reson Med, 2003. **50**(1): p. 145-53.

36. Wong, E.C., et al., *Velocity-selective arterial spin labeling.* Magnetic Resonance in Medicine, 2006. **55**(6): p. 1334-1341.

37. Shao, X., et al., *Measuring human placental blood flow with multidelay 3D GRASE pseudocontinuous arterial spin labeling at 3T.* J Magn Reson Imaging, 2018. **47**(6): p. 1667-1676.

38. Panigel, M., G. Wolf, and A. Zeleznick, *Magnetic resonance imaging of the placenta in rhesus monkeys, Macaca mulatta.* J Med Primatol, 1988. **17**(1): p. 3-18.

39. Deloison, B., et al., *SPIO-enhanced magnetic resonance imaging study of placental perfusion in a rat model of intrauterine growth restriction.* BJOG: An International Journal of Obstetrics & Gynaecology, 2012. **119**(5): p. 626-633.

40. Burchell, R.C., *Arterial blood flow into the human intervillous space.* Am J Obstet Gynecol, 1967. **98**(3): p. 303-11.

41. Borell, U., et al., *Influence of Uterine Contractions on the Uteroplacental Blood Flow at Term.* Am J Obstet Gynecol, 1965. **93**: p. 44-57.

42. Marcos, H.B., R.C. Semelka, and S. Worawattanakul, *Normal placenta: gadolinium-enhanced dynamic MR imaging.* Radiology, 1997. **205**(2): p. 493-6.

43. Lo, J.O., et al., *Novel Detection of Placental Insufficiency by Magnetic Resonance Imaging in the Nonhuman Primate.* Reprod Sci, 2017: p. 1933719117699704.

44. Panigel, M., et al., *Fast scan magnetic resonance imaging and Doppler ultrasonography of uteroplacental hemodynamics in the rhesus monkey (Macaca mulatta).* J Med Primatol, 1993. **22**(7-8): p. 393-9.

45. Taillieu, F., et al., *Placental perfusion and permeability: simultaneous assessment with dual-echo contrast-enhanced MR imaging in mice.* Radiology, 2006. **241**(3): p. 737-45.

46. Yadav, B.K., et al., *A longitudinal study of placental perfusion using dynamic contrast enhanced magnetic resonance imaging in murine pregnancy.* Placenta, 2016. **43**: p. 90-97.

47. Shetty, A.N., et al., *A liposomal Gd contrast agent does not cross the mouse placental barrier.* Scientific Reports, 2016. **6**: p. 27863.

48. Ghaghada, K.B., et al., *Pre-clinical evaluation of a nanoparticle-based blood-pool contrast agent for MR imaging of the placenta.* Placenta, 2017. **57**: p. 60-70.

49. Tomlinson, T.M., et al., *Magnetic resonance imaging of hypoxic injury to the murine placenta.* Am J Physiol Regul Integr Comp Physiol, 2010. **298**(2): p. R312-9.

50. Alison, M., et al., *Measurement of placental perfusion by dynamic contrast-enhanced MRI at 4.7 T.* Invest Radiol, 2013. **48**(7): p. 535-42.

51. Prola-Netto, J., et al., *Gadolinium Chelate Safety in Pregnancy: Barely Detectable Gadolinium Levels in the Juvenile Nonhuman Primate after in Utero Exposure.* Radiology, 2017: p. 162534.

52. Avni, T., et al., *The safety of intravenous iron preparations: systematic review and meta-analysis.* Mayo Clin Proc, 2015. **90**(1): p. 12-23.

53. MC, M., et al., *Williams Obstetrics*. 20th Edition ed, ed. C. F. 1997: Appleton and Lange.

54. Zun, Z., et al., *Three-Dimensional Placental Perfusion Imaging Using Velocity-Selective Arterial Spin Labeling.* In Proceedings of the 24th Annual Meeting of ISMRM, Singapore, Singapore, 2016: p. 0974.

55. Zun, Z., et al., *Non-Invasive Placental Perfusion Imaging in Pregnancies Complicated by Fetal Heart Disease Using Velocity-Selective Arterial Spin Labeled MRI.* Sci Rep, 2017. **7**(1): p. 16126.

56. Le Bihan, D., et al., *Separation of diffusion and perfusion in intravoxel incoherent motion MR imaging.* Radiology, 1988. **168**(2): p. 497-505.

57. Capuani, S., et al., *Diffusion and perfusion quantified by Magnetic Resonance Imaging are markers of human placenta development in normal pregnancy.* Placenta, 2017. **58**: p. 33-39.

58. Sohlberg, S., et al., *Magnetic resonance imaging-estimated placental perfusion in fetal growth assessment.* Ultrasound Obstet Gynecol, 2015. **46**(6): p. 700-5.

59. Siauve, N., et al., *Assessment of human placental perfusion by intravoxel incoherent motion MR imaging.* J Matern Fetal Neonatal Med, 2017: p. 1-8.

60. Sohlberg, S., et al., *Placental perfusion in normal pregnancy and early and late preeclampsia: A magnetic resonance imaging study.* Placenta, 2014. **35**(3): p. 202-206.

61. Malamateniou, C., et al., *Motion-Compensation Techniques in Neonatal and Fetal MR Imaging.* American Journal of Neuroradiology, 2013. **34**(6): p. 1124-1136.

Appendix B:

Quantitative Ferumoxytol-enhanced MRI in Pregnancy: A Feasibility Study in the Nonhuman Primate

Publication: Ante Zhu, Scott B. Reeder, Kevin M. Johnson, Sydney M. Nguyen, Sean B. Fain, Ian M. Bird, Thaddeus G. Golos, Oliver Wieben, Dinesh M. Shah, and Diego Hernando. 2020. Quantitative ferumoxytol-enhanced MRI in pregnancy: A feasibility study in the nonhuman primate. Magnetic Resonance Imaging. doi: 10.1016/j.mri.2019.20.006.

ABSTRACT

Objectives: To assess the feasibility of ferumoxytol-enhanced MRI in pregnancy with a nonhuman primate model.

Materials and methods: In this prospective study, eleven pregnant rhesus macaques at day 98 ± 5 of gestation were divided into three groups, untreated control (UC) ($n = 3$), saline control (SC) ($n = 4$) and interleukin 1 beta (IL-1β) treated (IT) ($n = 4$), which were administered with either saline or IL-1β into the amniotic fluid. All animals were imaged at multiple time points before and after ferumoxytol administration (4 mg/kg). Longitudinal R2* and susceptibility of tissues were obtained using region-of-interest analysis and the longitudinal changes were assessed using linear mixed models and Student's *t*-test.

Results: In fetuses, a slope of 0.3 s^{-1}/day ($P = 0.008$), 0.00 ppm/day ($P = 0.699$) and − 0.2 s^{-1}/day ($P = 0.023$) was observed in liver R2*, liver susceptibility, and lung R2*, respectively. In placentas, R2* and susceptibility increased immediately after ferumoxytol administration ($P < 0.001$) and decreased to baseline within two days. The mean change from baseline showed

no significant difference between the SC group and the IT group at all scan time points. In maternal livers, R2* increased immediately after ferumoxytol administration, further increased at one-day, and then decreased but remained elevated ($P < 0.001$). The mean change from baseline showed no significant difference between the SC group and the IT group at all scan time points. **Conclusions:** This work demonstrates the feasibility of quantitative ferumoxytol-enhanced MRI to measure dynamics of ferumoxytol delivery and washout in the placenta. Stable MRI measurements indicated no evidence of iron deposition in fetal tissues of nonhuman primates after maternal ferumoxytol exposure.

INTRODUCTION

Preeclampsia is an inflammatory condition of human pregnancy that can lead to peripheral edema, hypertension, seizures and maternal death [1-2]. Maternal vascular dysfunction at the maternal-fetal interface in preeclampsia leads to insufficient placental perfusion and activation of the uteroplacental inflammatory response [3-4]. Altered immune cell (e.g. macrophage) activation and distribution within the maternal-fetal interface may also play an important role in the development of adverse pregnancy outcomes [5]. Evaluation of macrophage distribution may enable early assessment of the developing pathophysiologic conditions in preeclampsia and/or inflammation-induced fetal growth restriction before their clinical manifestation. Thus, evaluation of macrophage distribution and activity is highly desirable for identifying immune cell homing in pregnancy.

Ferumoxytol is an FDA-approved iron compound for treatment of anemia [6] which recently has received substantial interest as an off-label contrast agent in MRI [7-8]. Ferumoxytol particles are phagocytosed by macrophage in the reticuloendothelial system or sites with activated

inflammation responses [9]. Importantly, the presence of ferumoxytol affects MR contrast parameters, including R2* (=1/T2*) and magnetic susceptibility. Quantitative R2* mapping and quantitative susceptibility mapping (QSM) have been used for detection of ferumoxytol [10-12] and characterization of microscopic iron distribution [13-14]. Ferumoxytol-enhanced MRI has been shown to enable non-invasive assessment of macrophages in applications including pancreatic inflammation in type I diabetes, high-grade gliomas, and inflammation after myocardial infarction [15-17]. Therefore, ferumoxytol-enhanced MRI may enable sensitive detection of macrophage homing in inflammation at the maternal-fetal interface.

However, the use of ferumoxytol for the assessment of macrophage distribution in pregnancy, and the safety of the ferumoxytol use, including the potential uptake in the fetus after maternal administration, have not been investigated. Unlike gadolinium-based contrast agents with an approximate diameter of 0.4 nm [9], which cross the placenta into the fetal circulation [18-19], ferumoxytol with an approximate diameter of 30 nm [9] may not transport directly into fetal circulation [20]. The nonhuman primate has the most similar placentation, physiology and immunology with the human reproductive system [21-23]. Thus, quantification of iron accumulation at the maternal-fetal interface and in the fetus after ferumoxytol exposure in nonhuman primates would constitute an important step towards evaluating the feasibility and safety of ferumoxytol-enhanced MRI in human pregnancy.

The hypothesis for this work was that maternal ferumoxytol exposure will not lead to increased iron deposition in fetal tissues. Further, we hypothesize that ferumoxytol will be taken up by macrophages in the placenta or the decidua, the endometrium of pregnancy, in inflammation with macrophage homing and will be detectable by MRI. Therefore, the purpose of this study was

to assess the feasibility of ferumoxytol-enhanced R2* mapping and QSM in a pregnant nonhuman primate model.

METHODS

Animals and Experimental Procedure

This prospective animal study was approved by our institution's animal care and use committee. Interleukin 1 beta (IL-1β), a pro-inflammatory cytokine, was used to generate inflammation at the maternal-fetal interface. Eleven pregnant rhesus macaques at day 98±5 of gestation (average term pregnancy=165 days), equivalent to the late second trimester of human pregnancy, were obtained. Animals were divided into three groups, i.e., untreated control (UC) (*n*=3), saline control (SC) (*n*=4), and IL-1β treated (IT) (*n*=4). For all procedures and MRI scans, the animal was anesthetized by administration of up to 10mg/kg ketamine and the sedation was prolonged by delivering oxygen with 1.5% isoflurane through inhalation. The animal was monitored during all procedures, and subsequently until fully recovery from the anesthesia. Veterinarian staff were alerted for treatment if the recovery took more than 90 minutes, or if there were symptoms of compromised health.

Each animal in the UC group was imaged first as baseline (Day 0-pre). Subsequently, ferumoxytol (AMAG Pharmaceuticals, Waltham, MA, USA) was administered intravenously at a dose of 4 mg/kg, diluted 5:1 with sterile saline. Immediately after ferumoxytol administration, the animal was imaged again (Day 0-post) and follow-up MRI scans were performed afterwards at four time points within 25 days (Day 1-25), as shown in the flow chart of Figure 1. Animal information, drug dose, ferumoxytol administration, and scan time points are detailed in Supporting Information Table S1.

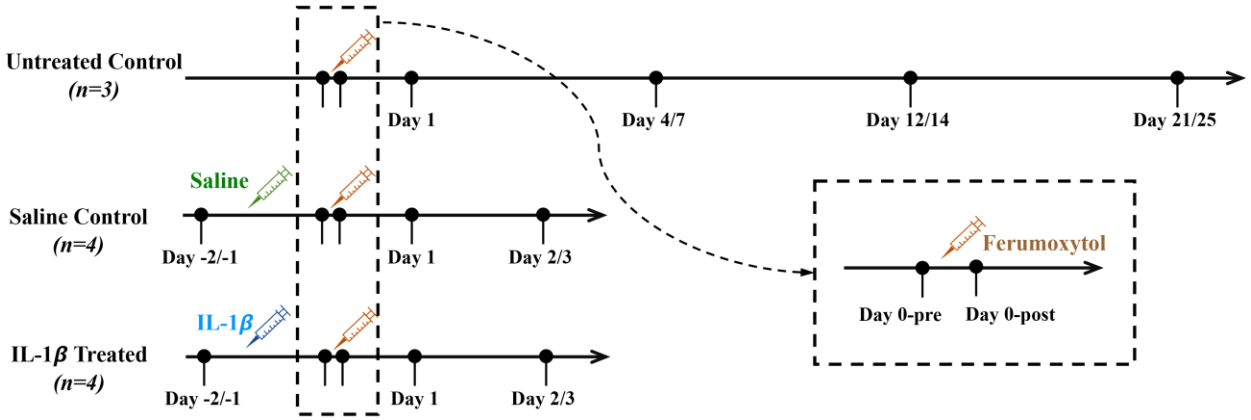

Figure 1. Flow chart of the MRI scan time points relative to the administration of ferumoxytol, saline and IL-1β for all eleven animals.

Rhesus No.	Groups	Gestational Age (days)	Maternal Weight (kg)	Scan Time Points	Drug Administration	Ferumoxytol Administration	Administration Rate (ml/s)
1	UC	102	7.0	Day 0 pre/post, 1, 4, 12, 25	N/A	Hand Administrated over 10 mins.	0.009
2	UC	106	10.0	Day 0 pre/post, 1, 7, 14, 21	N/A	Administrated with a power injector over 20s.	0.39
3	UC	91	9.9	Day 0 pre/post, 1, 7, 14, 21	N/A	Administrated with a power injector over 20s.	0.39
4	IT	92	9.8	Day -1, Day 0 pre/post, 1, 3	10 μg IL-1β in 0.5mL sterile saline	Administrated with a power injector over 20s.	0.39
5	SC	103	7.1	Day -1, Day 0 pre/post, 1, 3	0.5mL Saline	Administrated with a power injector over 20s.	0.27
6	IT	98	7.6	Day -1, Day 0 pre/post, 1, 2	10 μg IL-1β in 0.5mL sterile saline	Administrated with a power injector over 20s.	0.30
7	IT	92	8.6	Day -1, Day 0 pre/post, 1, 2	10 μg IL-1β in 0.5mL sterile saline	Administrated with a power injector over 20s.	0.33
8	SC	99	9.1	Day -1, Day 0 pre/post, 1, 3	0.5mL Saline	Administrated with a power injector over 20s.	0.36
9	SC	96	8.6	Day -2, Day 0 pre/post, 1, 2	0.5mL Saline	Administrated with a power injector over 20s.	0.33
10	SC	98	10.0	Day -2, Day 0 pre/post, 1, 2	0.5mL Saline	Administrated with a power injector over 20s.	0.39
11	IT	109	8.7	Day -1, Day 0 pre/post, 1, 2	10 μg IL-1β in 0.5mL sterile saline	Administrated with a power injector over 20s.	0.36

Note – UC=untreated control, IT=interleukin 1beta treated, SC=saline control, IL-1β=interleukin 1beta, No.=number
Day -2/-1: Two or one day before ferumoxytol administration; Day 0 pre/post: Before and immediately after ferumoxytol administration; Day 1/2/4/7/12/14/21/25: 1/2/4/7/12/14/21/25 days after ferumoxytol administration.

Table S1. Animal information, drug dose, ferumoxytol administration.

Each animal in either the SC or IT group was imaged first as baseline (Day -2/-1). On the same day after the baseline imaging, animals were administered either saline (0.5 mL) or IL-1β (10 μg IL-1β in 0.5mL saline) into the amniotic using a needle inserted through an aseptically prepared site of the abdominal wall and introduced until the tip touched the uterus wall. Subsequent scans were started one or two days later, in order to allow for inflammation to develop. The animals were then imaged before and immediately after ferumoxytol administration (Day 0 pre/post) and follow-up scans were performed afterwards within three days (Day 1-3), as shown in the flow chart of Figure 1. Animal information, drug dose, ferumoxytol administration and scan time points are detailed in Supporting Information Table S1. Histology and iron quantification analysis on placental and fetal tissues were performed after the last MRI scan.

MRI Acquisition

MRI scans were performed on a 3.0T MRI system (Discovery 750, GE Healthcare, Waukesha, WI, USA) using a 32-channel torso coil (Neocoil, Pewaukee, WI, USA) with the animal in the left lateral decubitus position. An axial 3D multi-echo spoiled gradient-echo (SGRE) acquisition of the maternal pelvis covering the uterus cavity was obtained to evaluate the ferumoxytol distribution at the maternal-fetal interface. Additionally, the ferumoxytol distribution in the maternal reticuloendothelial system including the maternal liver was also evaluated in this study. For this purpose, an axial 3D multi-echo SGRE radial ultra-short TE (UTE-SGRE) acquisition of the maternal abdomen covering the maternal liver was performed. Respiratory-gating [24] was used in both acquisitions. Scan parameters are detailed in Table 1.

	# TE	TE_{init}/ΔTE (ms)	TR (ms)	Flip Angle (°)	Field of View (mm^3)	Acquired Resolution (mm^3)	Reconstructed Resolution (mm^3)	Parallel Imaging Acceleration Phase/Slice	Scan Time (minutes)
Maternal pelvic MRI: SGRE	8	1.6/1.3	12.9	9	160×160×140	1.1×1.1×1.9	0.6×0.6×1.9	1.5 / 1.0	4:51
Maternal abdominal MRI: UTE-SGRE	3	0.1/0.2	2.8	3	180×180×180	1.4×1.4×1.4	1.4×1.4×1.4	1.0 / 1.0	5:30

SGRE=spoiled gradient-echo, UTE=ultra-short echo time

Table 1. Scan parameters of maternal pelvic MRI (SGRE) and maternal abdominal MRI (UTE-SGRE) of the animal.

Imaging Reconstruction and Data Analysis

R2* maps of the maternal pelvis were generated from the SGRE images using a chemical shift-encoded reconstruction [25]. R2* maps of the maternal abdomen were obtained by using monoexponential fit of echoes in the UTE-SGRE images. In each animal at each scan time point, R2* of the amniotic fluid, the fetal liver, the fetal lung, the two separate placental discs, and the maternal liver were measured in oval regions of interest (ROIs). Information on ROIs is detailed in Supporting Information Table S2.

Parameters	Position	Region of Interest size (cm^2)
Amniotic fluid R2*	A region with homogenous R2*	~0.6
Fetal liver R2*	Right lobe of the liver	~0.1
Fetal lung R2*	Central region in one of the fetal lungs	~0.1
Placental R2*	Two ROIs in two separate placental discs	~0.6
Maternal liver R2*	Right lobe of the liver avoiding large vessels or bile ducts and the dome of the liver	~0.6
Fetal liver susceptibility	One ROI in the fetal liver and one in the adjacent amniotic fluid	~0.1
Placental susceptibility	One ROI in one of the placental discs and one in the adjacent amniotic fluid	~0.1

Table S2. Scan time points of maternal pelvic and abdominal MRI.

Susceptibility maps of the maternal pelvis were generated from the SGRE images using a QSM reconstruction [26]. All susceptibility measurements were calculated relative to the adjacent amniotic fluid, which was used as a susceptibility reference as no ferumoxytol uptake was observed as shown below. The fetal liver susceptibility was measured by calculating the difference between the susceptibility values in the fetal liver and the amniotic fluid. The placental susceptibility was measured by calculating the difference between the susceptibility values in one of the placental discs and the amniotic fluid. Information on ROIs is detailed in Supporting

Information Table S2. Susceptibilities of the fetal lung and the maternal liver were not obtained due to the lack of adjacent susceptibility reference and the limited range of echo times in UTE-SGRE, respectively.

Statistical Analysis

To investigate the longitudinal variation of R2* and susceptibility measurements of the fetal liver and R2* measurements of the fetal lung, a linear mixed-effects model was used. The model included the time interval of each scan to the baseline scan as a fixed continuous factor, the animal groups as a fixed classification factor, the interaction of the animal group and the time interval as a fixed factor, and animal as a random classification factor.

To investigate the longitudinal variation of placental R2* and susceptibility measurements, and maternal liver R2*, respectively, a linear-mixed effects model was used in each animal group, including the scan time point as a fixed classification factor and animal as a random classification factor. The changes at each scan time point from baseline were calculated for placental R2* as $\Delta R2^*_p = R2^*_{p,TimePoint} - R2^*_{p,Baseline}$, for placental susceptibility as $\Delta\chi_p = \chi_{p,TimePoint} - \chi_{p,Baseline}$, and for maternal liver R2* as $\Delta R2^*_l = R2^*_{l,TimePoint} - R2^*_{l,Baseline}$. To investigate the inter-group difference on the longitudinal variation of MRI measurements, Student's t-test with conservative Bonferroni correction for multiple comparison was used to compare $\Delta R2^*_p$ at each time point between the SC and IT groups, as well as $\Delta\chi_p$ and $\Delta R2^*_l$. Statistical analyses were performed in Matlab (MathWorks, Natick, MA, USA). Statistical significance was selected as a *P* value less than 0.05.

RESULTS

One animal in the UC group (Rhesus #9) and one in the IT group (Rhesus #4) which had a history of ocular swelling not associated with ferumoxytol were noted to have moderate periocular swelling/edema following the ferumoxytol administration. They were treated with 10 mg diphenhydramine hydrochloride and recovered without further medical intervention. No complications were observed in all the other animals during or after ferumoxytol administration. 3D SGRE acquisitions of the maternal pelvis were successfully obtained without apparent motion artifacts in the reconstructed R2* and susceptibility maps, except for the Day 0-pre acquisition in Rhesus #2 when the respiratory gating failed. 3D UTE-SGRE MRI of maternal abdomen was successfully obtained at most time points as listed in Supporting Information Table S3.

Rhesus No.	Groups	Day -2	Day -1	Day 0-pre	Day 0-post	Day 1	Day 2	Day 3	Day 4	Day 7	Day 12	Day 21	Day 25
1	UC			✓	✓	✓			✓		✓		✓
2	UC			✓○	✓○	✓○				✓○		✓○	
3	UC			✓○	✓○	✓○				✓○		✓○	
4	IT		✓○	✓○	✓○	✓○		✓○					
5	SC		✓○	✓○	✓○	✓○		✓○					
6	IT		✓○	✓○	✓	✓○	✓○						
7	IT		✓○	✓○	✓○	✓○	✓○						
8	SC		✓○	✓○	✓○	✓○		✓○					
9	SC	✓		✓○	✓	✓○	✓○						
10	SC	✓○		✓○	✓○	✓○	✓○						
11	IT		✓○	✓○	✓	✓○	✓○						

Note – ✓: maternal pelvic images acquired, ○: maternal abdominal images acquired, UC=untreated control, IT=IL-1β treated, SC=saline control, IL-1β=interleukin 1beta, No.=number

Table S3. Scan time points of maternal pelvic and abdominal MRI.

The MRI scan time points for Rhesus #3 in the UC group, Rhesus #4 in the IT group and Rhesus #5 in the SC group are shown at the top of Figures 2 and 3. Anatomic images, R2* maps, and susceptibility maps are shown at each scan time point for each animal. The fetal liver (red lines), the fetal lung (pink lines), the maternal liver (white lines), the uterine cavity (yellow lines), the two separate placental discs (orange lines), and the amniotic fluid (green arrows) are delineated and indicated in Figures 2 and 3. Placental R2* and susceptibility measurements of animals in all groups increased substantially after ferumoxytol administration (Day 0-post) and decreased towards baseline at Day 1 and afterwards. Maternal liver R2* in Rhesus #3 increased immediately after ferumoxytol administration (Day 0-post), further increased at one-day follow-up (Day 1), and subsequently decreased but remained elevated three weeks afterwards (Days 7-21).

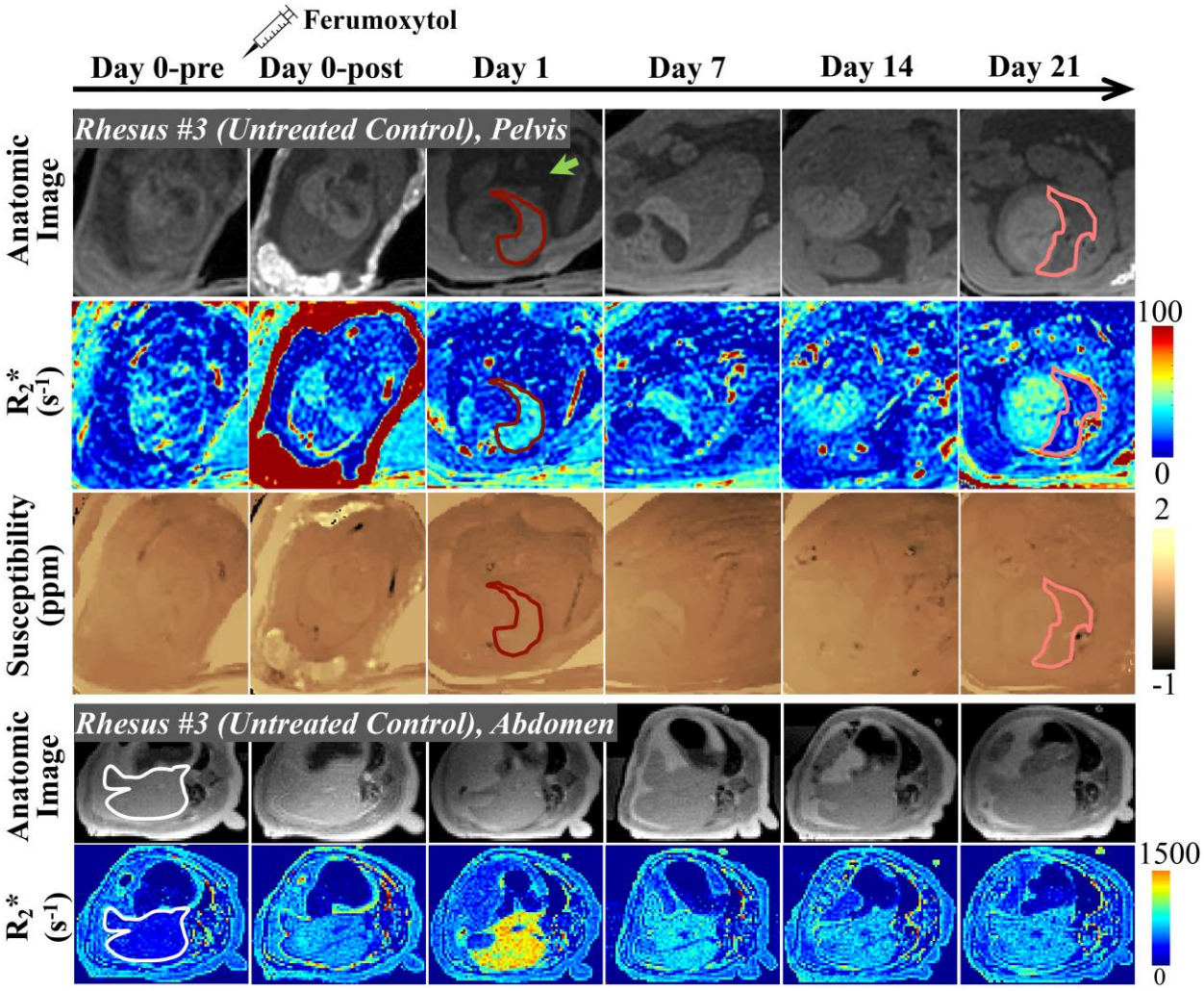

Figure 2. Longitudinal axial anatomic image (1st and 4th row), R2* (2nd and 5th row) and susceptibility (3rd row) maps of fetal liver (red lines), fetal lung (pink lines) and maternal liver (white lines) of Rhesus #3 (day 91 of gestation) in the untreated control group. Stable R2* and susceptibility of fetal tissues after maternal ferumoxytol administration were observed. Maternal liver R2* increased after ferumoxytol administration, further increased at one-day follow-up (Day 1), and remained elevated at seven-, fourteen, and twenty-one day follow-up.

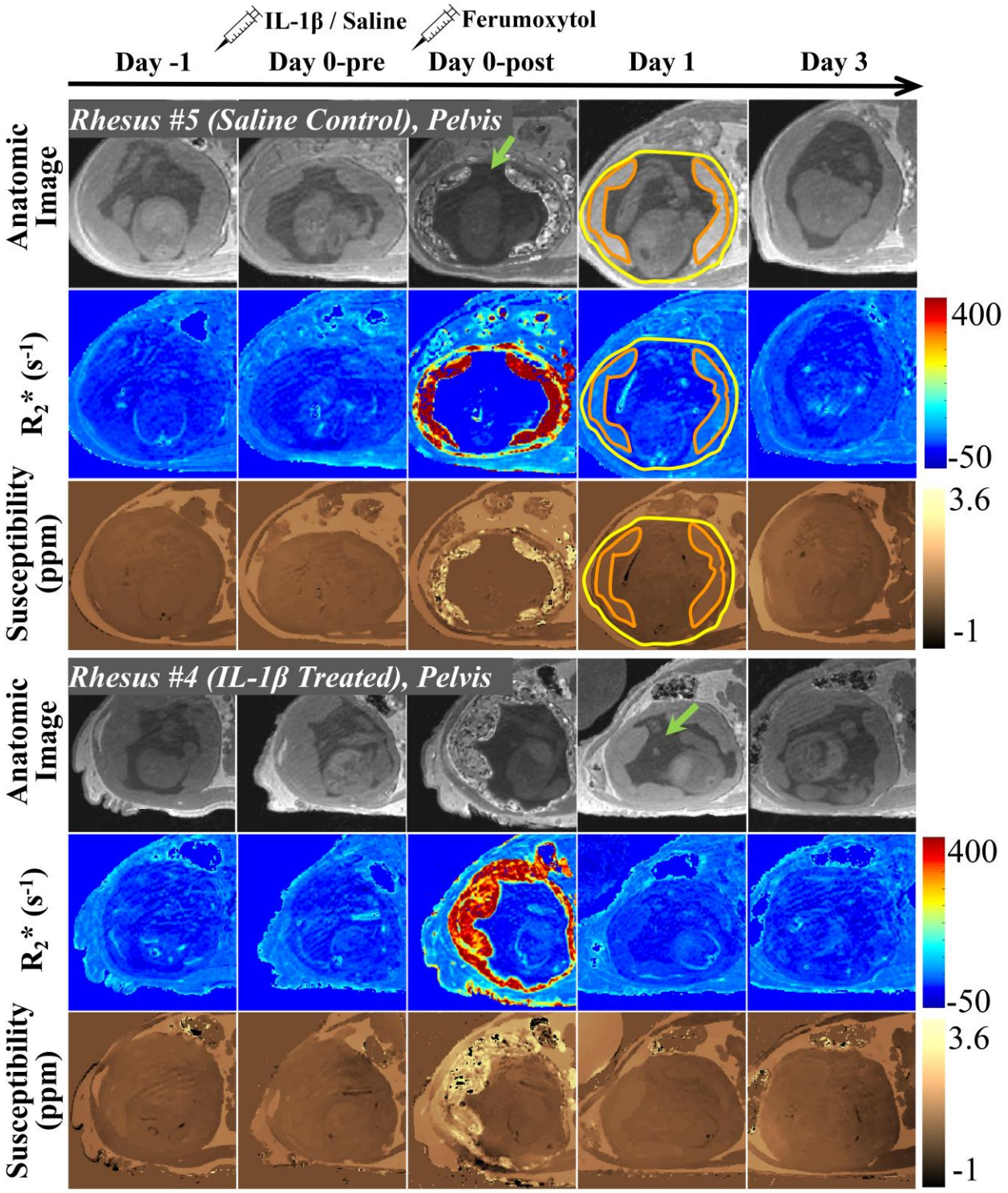

Figure 3. Placental R2* and susceptibility of Rhesus #5 (day 103 of gestation, bottom three rows) in the saline control group and Rhesus #4 (day 92 of gestation, top three rows) in the interleukin 1 beta (IL-1β) treated group increased after ferumoxytol administration (at Day

0-post) and decreased towards baseline at Day 1 and afterwards. The amniotic fluid is indicated by green arrow. The uterus cavity and the two separate placental discs are delineated by yellow lines and orange lines, respectively.

Longitudinal measurements and changes from baseline in R2* of the amniotic fluid, R2* and susceptibility of fetal liver and R2* of fetal lung in all animals are summarized in Figure 4 and Table 2. Stable R2* measurements of the amniotic fluid before and after ferumoxytol administration indicated no ferumoxytol deposition there. It further indicated the amniotic fluid to be a reliable reference tissue for the susceptibility measurement. In the UC group, a slope of 0.3 s^{-1}/day (P=0.008) and a slope of 0.00 ppm/day (P=0.699) were observed in fetal liver R2* and susceptibility, respectively. A slope of -0.2s^{-1}/day (P=0.023) was observed in fetal lung R2*. An intercept of -0.09ppm (P=0.003) was observed in susceptibility of fetal liver in the IT group compared to the measurements in the UC group. The remaining measurements of R2* and susceptibility in the fetal liver and the fetal lung in the SC and IT groups were not significantly different from the reference, i.e., the UC group. Based on previous published calibrations in phantoms [27-30], the additional iron deposition after maternal ferumoxytol exposure, indicated by the MRI measurements, is less than 9.0, 7.0 and 4.3 micrograms iron per gram of tissue in the amniotic fluid, the fetal liver and the fetal lung, respectively (see Supporting Information S1).

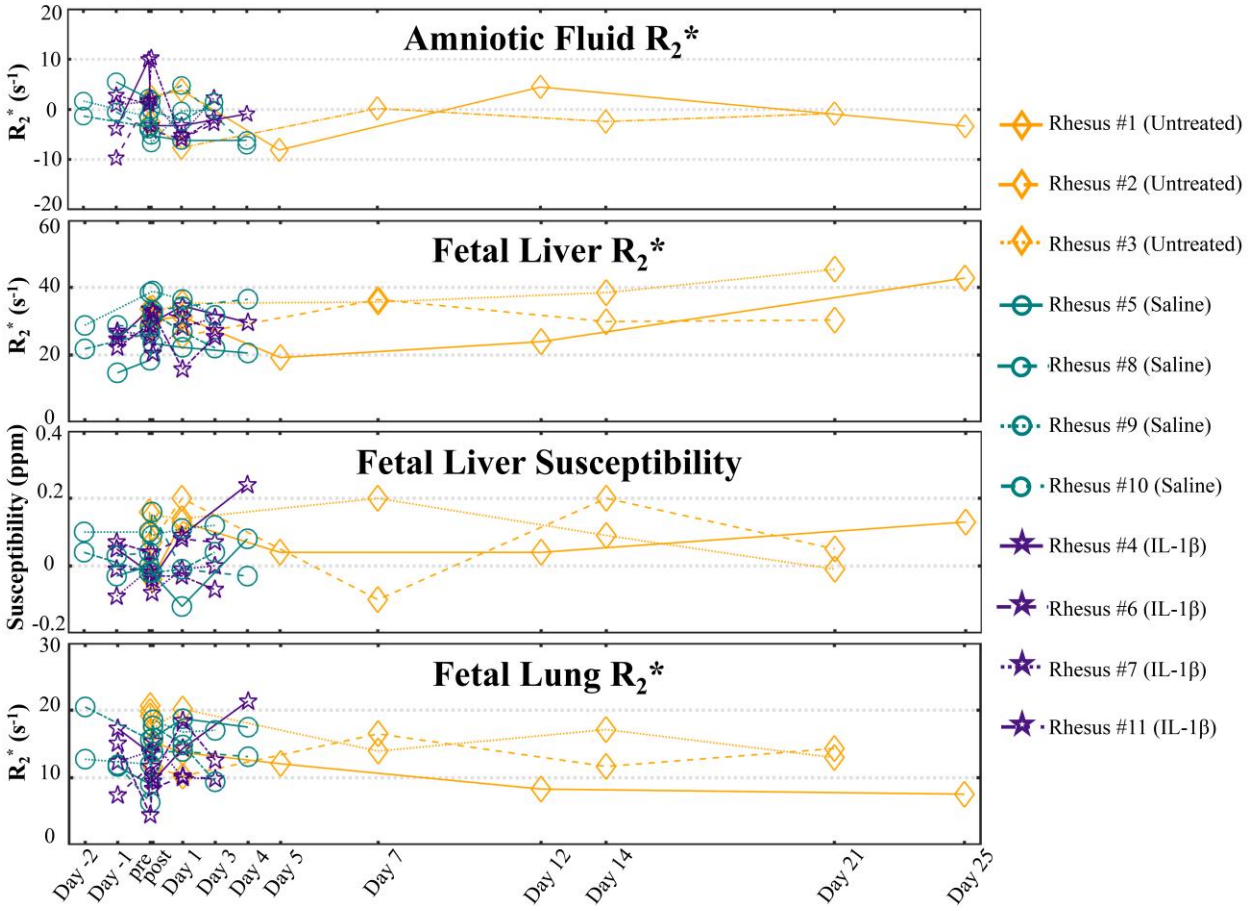

Figure 4. Stable R2* measurements of the amniotic fluid indicate no ferumoxytol uptake, suggesting the amniotic fluid as a reliable reference tissue for the susceptibility measurement.

Fetal liver R2* and susceptibility measurements and fetal lung R2* measurements in all animals are not significantly increased over time after maternal ferumoxytol administration at Day 0-post.

	Estimated Change in Fetal Liver R2* (s^{-1})	*P* value	Estimated Change in Fetal Liver Susceptibility (ppm)	*P* value	Estimated Change in Fetal Lung R2* (s^{-1})	*P* value
UC Group (reference)	Intercept: 30.0 (25.1, 35.0)	<0.001	Intercept: 0.09 (0.05, 0.14)	<0.001	Intercept: 16.3 (14.0, 18.5)	<0.001
	Slope: 0.3 (0.1, 0.6)	0.008	Slope: 0.00 (-0.00, 0.00)	0.699	Slope: -0.2 (-0.4, 0.0)	0.023
SC Group	Intercept: -2.3 (-8.7, 4.2)	0.489	Intercept: -0.06 (-0.11, 0.00)	0.046	Intercept: -2.0 (-4.8, 0.8)	0.081
	Slope: 0.9 (-0.8, 2.2)	0.365	Slope: 0.00 (-0.03, 0.02)	0.886	Slope: 0.4 (-0.8, 1.6)	0.544
IT Group	Intercept: -2.7 (-9.2, 3.8)	0.411	Intercept: -0.09 (-0.15, -0.03)	0.003	Intercept: 4.5 (-0.6, 9.5)	0.081
	Slope: 0.3 (-1.5, 2.1)	0.765	Slope: 0.03 (0.00, 0.06)	0.057	Slope: 1.0 (-0.5, 2.4)	0.186

Data in parentheses are 95% confidence intervals, IL-1β=interleukin 1beta, UC=untreated control, IT= interleukin 1beta treated, SC=saline control

Table 2. Longitudinal variation of R2* and susceptibility measurements of the fetal liver and R2* measurements of the fetal lung over time in all animals.

Longitudinal measurements and changes from baseline in placental R2* and susceptibility and R2* of maternal liver in the UC group are summarized in Figure 5 and Table 3. Example ROIs are shown in a previous study [31]. Placental R2* and susceptibility increased significantly after ferumoxytol administration at Day 0-post (P<0.001). Placental R2* and susceptibility at Day 1 decreased back to the baseline and showed no significant differences at all four follow-up scans (P=0.395, P=0.627, P=0.905 and P=0.559 in R2*, respectively, and P=0.172, P=0.859, P=0.974 and P=0.948 in susceptibility, respectively). Maternal liver R2* increased after ferumoxytol administration at Day 0-post (P<0.001), further increased at one-day follow-up (P<0.001) and decreased but remained elevated at all three follow-up scans (P<0.001).

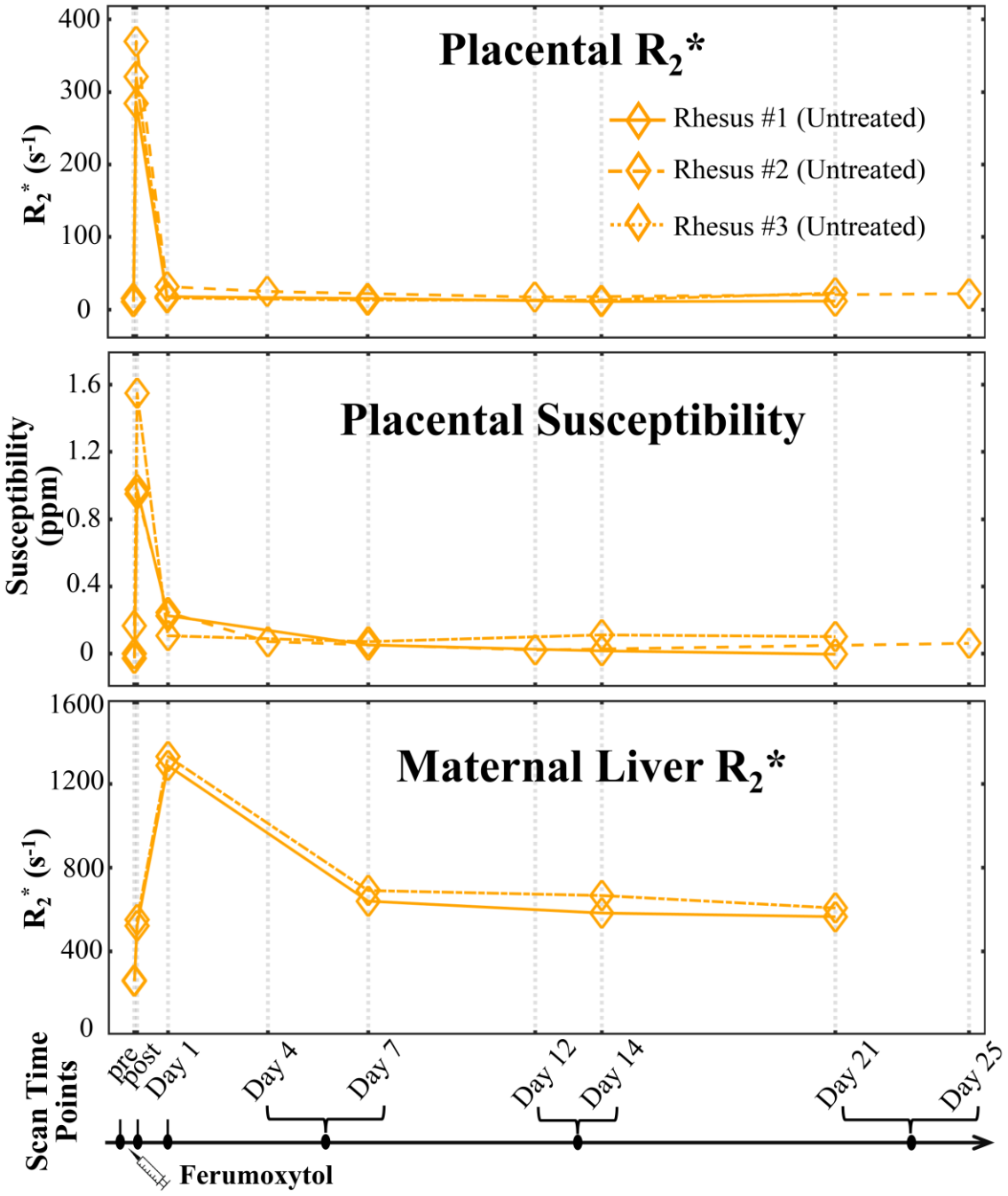

Figure 5. Longitudinal measurements of placental R2* and susceptibility and maternal liver R2* in the untreated control group. Both the placental R2* and susceptibility increased significantly after ferumoxytol administration at Day 0-post and decreased back to the baseline at follow-up scans. Maternal liver R2* increased after ferumoxytol administration and remained elevated at follow-up scans.

	Estimated Change in Placental R2* (s^{-1})		Estimated Change in Placental Susceptibility (ppm)		Estimated Change in Maternal Liver[Π] R2* (s^{-1})	
	Intercept	*P* value	Intercept	*P* value	Intercept	*P* value
Day 0-pre vs. Day 0-post	312.8 (289.6, 335.9)	<0.001	1.1 (0.9, 1.3)	<0.001	276.8 (217.1, 301.0)	<0.001
Day 0-pre vs. Day 1	9.4 (-13.8, 32.6)	0.395	0.2 (-0.1, 0.4)	0.172	1049.4 (1013.8, 1085.0)	<0.001
Day 0-pre vs. Day 4/7	5.3 (-17.9, 28.5)	0.627	0.0 (-0.2, 0.2)	0.859	405.2 (369.6, 440.8)	<0.001
Day 0-pre vs. Day 12/14	1.3 (-21.9, 24.5)	0.905	0.0 (-0.2, 0.2)	0.974	364.7 (329.0, 400.3)	<0.001
Day 0-pre vs. Day 21/25	6.4 (-16.8, 29.6)	0.559	0.0 (-0.2, 0.2)	0.948	326.2 (290.6, 361.8)	<0.001

Data in parentheses are 95% confidence intervals, vs.=versus, [Π]Data of Rhesus #1 in the untreated control group were not available at all scan time points and thus not included.

Table 3. Estimated change of placental R2* and susceptibility measurements at scan time points after ferumoxytol administration from the baseline in the untreated control group.

Longitudinal measurements and changes from baseline in placental R2* and susceptibility and maternal R2* in the SC and IT groups are summarized in Figure 6 and Table 4. After administration of either saline or IL-1β measured at Day 0-pre, placental R2* and susceptibility did not significantly change. Immediately after ferumoxytol administration, placental R2* and susceptibility in both groups increased significantly ($P<0.001$). At one-day follow-up, placental R2* and susceptibility decreased towards baseline but remained elevated in both groups. At two- or three- day follow-up, placental R2* and susceptibility further decreased towards baseline in both groups. At all time points, the mean change of either placental R2* or susceptibility from baseline showed no significant difference between the SC group and the IT group. Based on previous published calibrations in phantoms [27-29,32], the maximum increase of R2* at Day 2/3 relatively to the baseline in all animals indicated a maximum iron concentration of 16.3 micrograms iron per gram of placental tissue (see Supporting Information S2).

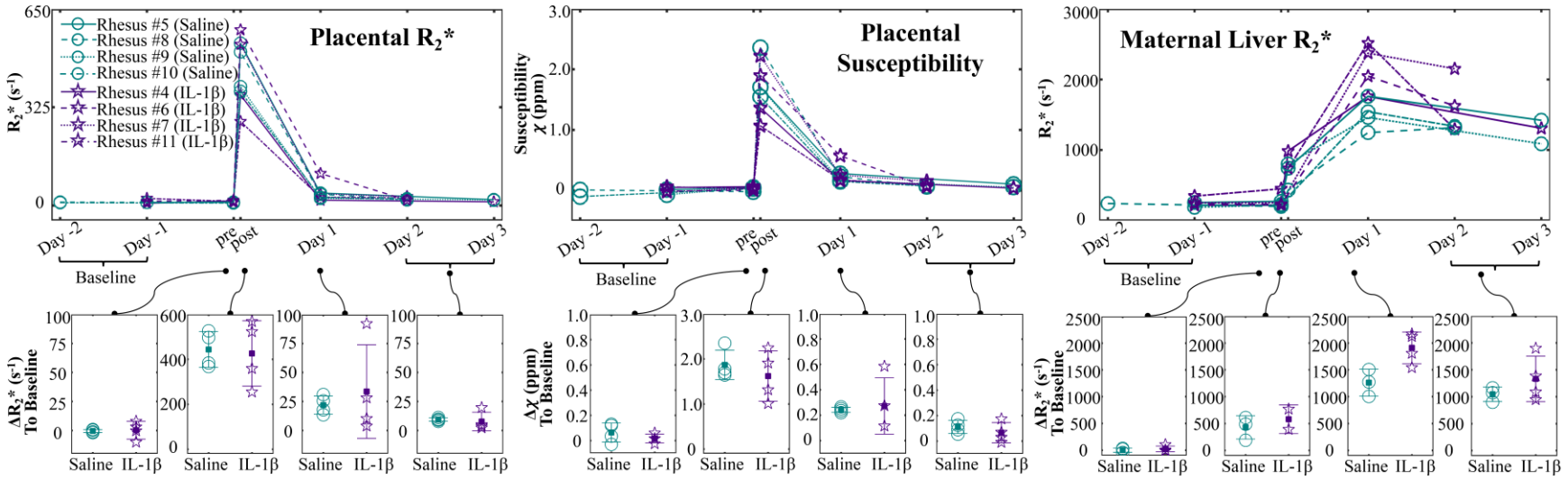

Figure 6. Placental R2* and susceptibility (χ) measurements of all animals in the saline control group and the interleukin 1 beta (IL-1β) treated group increased after ferumoxytol administration at Day 0-post and decreased back to the baseline at follow-up scans. The difference of measurements at each scan time point compared to that at baseline, i.e., ΔR2* and $\Delta\chi$, showed no difference between the saline control group and the IL-1β treated group. Maternal liver R2* in both groups immediately increased after ferumoxytol administration, further increased at Day 1, and remained elevated at Day 2 or Day 3.

	Saline control (*n*=4)		IL-1β treated (*n*=4)		SC vs. IT
	Estimated Change Placental ΔR2* (s^{-1})	***P* value**	**Estimated Change Placental ΔR2* (s^{-1})**	***P* value**	***P* value**[Π]
Day 0-pre vs. Day -1/-2	-0.5 (-47.3, 46.4)	0.984	0.2 (-82.1, 82.5)	0.996	0.867
Day 0-post vs. Day -1/-2	444.0 (397.1, 490.8)	<0.001	426.3 (343.9, 508.6)	<0.001	0.824
Day 1 vs. Day -1/-2	21.9 (-24.9, 68.8)	0.338	33.6 (-48.7, 115.9)	0.398	0.598
Day 2/3 vs. Day -1/-2	9.4 (-37.4, 56.3)	0.677	7.7 (-74.7, 90.0)	0.845	0.733
	Estimated Change Placental Δχ (ppm)	***P* value**	**Estimated Change Placental Δχ (ppm)**	***P* value**	***P* value**[Π]
Day 0-pre vs. Day -1/-2	0.06 (-0.15, 0.28)	0.541	0.02 (-0.31, 0.34)	0.917	0.339
Day 0-post vs. Day -1/-2	1.87 (1.60, 2.13)	<0.001	1.62 (1.29, 1.95)	<0.001	0.385
Day 1 vs. Day -1/-2	0.24 (-0.02, 0.51)	0.031	0.27 (-0.05, 0.60)	0.095	0.818
Day 2/3 vs. Day -1/-2	0.11 (-0.11, 0.33)	0.293	0.07 (-0.26, 0.39)	0.671	0.402
	Estimated Change Maternal Liver ΔR2* (s^{-1})	***P* value**	**Estimated Change Maternal Liver ΔR2* (s^{-1})**	***P* value**	***P* value**[Π]
Day 0-pre vs. Day -1/-2	3.5 (-211.9, 218.8)	0.972	24.6 (-317.9, 367.1)	0.879	0.591
Day 0-post vs. Day -1/-2	429.8 (214.5, 645.2)	0.001	598.9 (179.5, 1018.4)	0.009	0.534
Day 1 vs. Day -1/-2	1261.4 (1046.0, 1476.7)	<0.002	1910.3 (1567.8, 2252.8)	<0.001	0.028
Day 2/3 vs. Day -1/-2	1046.9 (831.6, 1262.3)	<0.001	1331.4 (988.9, 1673.9)	<0.001	0.320

Data in parentheses are 95% confidence intervals, IL-1β=interleukin 1beta, vs.=versus, SC=saline control, IT= IL-1β treated

[Π]Data were compared by using the Student's t-test with conservative Bonferroni correction for multiple comparison. Threshold for statistical significance was set to *P*<0.0125 after correction.

Table 4. Estimated change of placental R2* and susceptibility (χ) measurements at scan time points before and after ferumoxytol administration from the baseline in the saline control group and the untreated control group.

Maternal liver R2* was not significantly altered after administration of either saline or IL-1β measured at Day 0-pre. Immediately after ferumoxytol administration, maternal liver R2* increased significantly in both groups ($P<0.009$). At one-day follow-up, maternal liver R2* further increased in both groups. At two- or three- day follow-up, maternal liver R2* decreased but remained elevated in both groups. At all time points, the mean change of maternal liver R2* from baseline showed no significant difference between the SC group and the IT group.

DISCUSSION

This work demonstrated the feasibility of R2* mapping and QSM to measure the ferumoxytol delivery and washout from the placental tissues. Additionally, stable R2* and tissue susceptibility were observed in fetal tissues before and after ferumoxytol administration in nonhuman primates, indicating no increased iron deposition in the fetus after maternal exposure.

The elevated maternal liver R2* immediately after ferumoxytol administration and the further increase of R2* at one-day follow-up were likely due to the presence of ferumoxytol in the blood pool [9,33]. Maternal liver R2* decreased subsequently over the following three weeks, but did not return to the baseline over this time span. This suggests iron uptake in the maternal liver as expected to occur following ferumoxytol administration in treatment of anemia [33].

The elevated placental R2* and susceptibility immediately after ferumoxytol administration were also likely due to the presence of ferumoxytol in the blood pool [9,34]. At one-day follow-up, placental R2* and susceptibility remained elevated, most likely due to the remaining ferumoxytol in the blood pool [9,34]. Further, the lack of significantly elevated placental R2* at one-, two- or three- day follow-up, compared to the elevated maternal liver R2*, indicated a lack of ferumoxytol uptake in the placenta.

Importantly, the lack of significant amount of iron deposit in fetal tissues, compared to the iron uptake in the maternal liver, suggests that ferumoxytol does not cross into the amniotic cavity and may not enter the fetal circulation. This is an important observation towards evaluating the safety implications for the use of ferumoxytol in pregnancy. However, delayed effects of elevated iron content in the maternal body (as shown in maternal liver R2*) on the fetus are unknown. To further investigate the safety of the ferumoxytol use in pregnancy, future studies are needed to assess iron contents in offspring with in utero exposure to ferumoxytol. In addition, ferumoxytol administration in animals at different gestation stages also need to be studied.

In the UC group, slightly elevated R2* measurements were observed in the fetal liver over time after maternal ferumoxytol exposure. However, a previous study has shown an increase of human fetal liver R2* over gestation stage in normal fetuses without maternal ferumoxytol exposure [35]. It cannot be determined from the current study whether the elevated fetal liver R2* is due to the normal development of the reticuloendothelial system over gestation stage [36-37], or due to the maternal exposure of ferumoxytol. Quantification of iron content in fetuses without maternal ferumoxytol exposure is under separate study [38].

Tissue R2* and susceptibility measurements were both obtained as potential imaging biomarkers of iron content in this study. In the placenta, both R2* and susceptibility measurements showed consistent behavior after ferumoxytol administration, even though R2* and susceptibility may have different dependence on the presence of iron [39]. The fact that R2* and susceptibility can be obtained as separate measurements from the same 3D SGRE data may enable a comprehensive evaluation of iron content and microscopic iron distributions [14] in a single acquisition.

This study has several limitations. The IL-1β treatment was ineffective at inducing the pathology reported in a previous study [40] where neutrophil and macrophage infiltration of the decidua parietalis was demonstrated. However, in this previous study the decidua basalis or the placenta itself was not evaluated; it is possible that the inflammatory response on the maternal side is limited to fetal membranes. With the MRI techniques in this study, it was not possible to resolve the thin fetal membranes and decidual parietalis. The potential use of ferumoxytol-enhanced MRI for the detection of macrophage homing to the decidua basalis and placenta needs further validation in an effective macrophage homing inflammation model. Additionally, a larger population of animals is needed to capture the biological variation on the iron biodistribution after maternal ferumoxytol exposure.

In conclusion, this study demonstrated the feasibility of longitudinal tracking of placental iron content in ferumoxytol-enhanced MRI. Additionally, this study suggested ferumoxytol may not cross the placenta and hence enter into the amniotic cavity or into the fetal circulation after maternal ferumoxytol exposure in nonhuman primates at late second trimester. Upon successful detection of macrophage homing in an effective inflammation model and being proven safe, ferumoxytol-enhanced MRI may enable assessment of the inflammation at the maternal-fetal interface in human pregnancy.

ACKNOWLEDGEMENTS

The authors thank GE Healthcare who provides research support to University of Wisconsin-Madison. The authors thank Samir D. Sharma for the guidance on image reconstruction, and Colin Longhurst for advice on statistical analyses. Additionally, the authors thank AMAG Pharmaceuticals Inc. for providing ferumoxytol used in animal studies. Further, Dr. Reeder is a

Romnes Faculty Fellow, and has received an award provided by the University of Wisconsin-Madison Office of the Vice Chancellor for Research and Graduate Education with funding from the Wisconsin Alumni Research Foundation. This work was supported by the National Institutes of Health (U01-HD087216, R01-DK117354, R01-DK100651, K24-DK102595, and P51-OD011106).

SUPPLEMENTARY DATA

S1. Iron concentration based on R2* measurements at 3.0T

- Liu et al [27] reported R2* relaxivity of ferumoxytol as follows:

$$R2^* = 1562\times[\text{Iron}]+2 \quad [1]$$

where [Iron] is the iron concentration with units of mg/mL, R2* has units of s^{-1}, and the slope 1562 has units of $s^{-1}\cdot mL/mg$. Note that ferumoxytol consists of 30 mg/mL elemental iron.

- Barick et al [28] and Laurent et al [29] reported R2 relaxivity of ferumoxytol (Advanced Magnetics, Cambridge, MA) as follows:

$$R2 = 84.9\times[\text{Iron}] \quad [2]$$

where [Iron] is the iron concentration with units of mM, R2 has units of s^{-1}, and the slope 84.9 has units of $s^{-1}\cdot mM^{-1}$. Based on phantom experiments by Knobloch et al (https:/doi.org/10.1097/RLI.0000000000000434), we assume that in ferumoxytol R2*≈R2. As the molecular weight of iron is 55.85g/mol, Equation 2 can be rewritten as,

$$R2 = 84.9\times[\text{Iron}]/55.85\times1000 = 1520\times[\text{Iron}] \quad [3]$$

where [Iron] has units of mg/mL and the slope 1520 has units of s^{-1}·mL/mg. The slopes in Equations 1-3 have similar values. We used a slope of 1562s^{-1}·mL/mg in the following calculations.

- The maximum increase in R2* in the amniotic fluid among all animals over all scan time points after ferumoxytol administration was 13.7s^{-1}. Assuming the change in R2* was due to the presence of ferumoxytol, then 13.7s^{-1} corresponds to an iron concentration of 0.009mg/mL based on the above equations. Assuming that amniotic fluid has a density of 1g/cm^3, an iron concentration of 0.009mg/mL corresponds to 9.0 micrograms iron per gram of tissue.

- The maximum change in fetal liver R2* after ferumoxytol administration among all animals at all scan times was 11.8s^{-1}. Assuming the change in fetal liver R2* was due to the presence of ferumoxytol, then 11.8s^{-1} corresponds to an iron concentration of 0.008mg/mL based on the above equations. Using the approximated density 1.15g/cm^3 for fetal liver tissue [32], an iron concentration of 0.008mg/mL corresponds to 7.0 micrograms iron per gram of tissue.

- The maximum change in fetal lung R2* after ferumoxytol administration among all animals at all scan times was 7.1s^{-1}. Assuming the change in fetal lung R2* was due to the presence of ferumoxytol, then 7.1s^{-1} corresponds to an iron concentration of 0.005mg/mL based on the above equations. Using the approximated density 1.15g/cm^3 for fetal lung tissue [30], an iron concentration of 0.005mg/mL corresponds to 4.3 micrograms iron per gram of tissue.

- The maximum change in placental R2* after ferumoxytol administration among all animals at Day 2/3 was 25.0s^{-1}. Assuming the change of placental R2* was due to the presence of ferumoxytol, then 25.0s^{-1} corresponds to an iron concentration of 0.016mg/mL based on the above equations. Using the approximated density 0.98g/cm^3 for the placental tissue [32], an iron concentration of 0.016mg/mL corresponds to 16.3 micrograms iron per gram of tissue.

S2. Iron concentration based on susceptibility measurements at 3.0T

- Liu et al [27] reported the susceptibility of the ferumoxytol as follows:

$$\chi = 32.0 \times [\text{Iron}] \quad [4]$$

where [Iron] is the iron concentration with units of mg/mL, χ is the susceptibility with units of ppm, and the slope 32.0 has units of ppm·mL/mg.

The maximum change in fetal liver susceptibility after ferumoxytol administration among all animals at all scan times was 0.19ppm. Assuming the change in fetal liver susceptibility was due to the presence of ferumoxytol, then 0.19ppm corresponds to an iron concentration of 0.006mg/mL based on the above equation. Using the approximated density 1.15g/cm^3 for fetal liver tissue [30], an iron concentration of 0.006mg/mL corresponds to 5.2 micrograms iron per gram of tissue.

REFERENCES

1. LaMarca B, Cornelius DC, Harmon AC, Amaral LM, Cunningham MW, Faulkner JL, et al. Identifying immune mechanisms mediating the hypertension during preeclampsia. Am J Physiol Regul Integr Comp Physiol 2016;311:R1-R9.

2. Kohi S, Ranjan S, Hoffman J, Kashif M, Daniel EA, Bock F, et al. Maternal extracellular vesicles and platelets promote preeclampsia via inflammasome activation in trophoblasts. Blood 2016;128(17):2153-2164.

3. Taylor BD, Tang G, Ness RB, Olsen J, Hougaard DM, Skogstrand K, et al. Mid-pregnancy circulating immune biomarkers in women with preeclampsia and normotensive controls. Pregnancy hypertension 2016;6(1):72-78.

4. Jonsson Y, Rubèr M, Matthiesen L, Berg G, Nieminen K, Sharma S, et al. Cytokine mapping of sera from women with preeclampsia and normal pregnancies. J Reprod Immunol 2006;70(1-2):83-91.

5. Faas MM, Spaans F, De Vos P. Monocytes and macrophages in pregnancy and pre-eclampsia. Front Immunol 2014; 5:298.

6. Spinowitz BS, Kausz AT, Baptista J, Noble SD, Sothinathan R, Bernardo MV, et al. Ferumoxytol for treating iron deficiency anemia in CKD. JASN 2008; 19:1599-1605.

7. Bashir MR, Bhatti L, Martin D, Nelson RC. Emerging applications for ferumoxytol as a contrast agent in MRI. J Magn Reson Imaging 2015; 41:884-98.

8. Vasanawala SS, Nguyen KL, Hope MD, Bridges MD, Hope TA, Reeder SB, et al. Safety and technique of ferumoxytol administration for MRI. Magn Reson Med 2016; 75:2107-2111.

9. Toth GB, Varallyay CG, Horvath A, Bashir MR, Choyke PL, Daldrup-Link HE, et al. Current and potential imaging applications of ferumoxytol for magnetic resonance imaging. Kidney Int 2017; 92(1):47-66.

10. Rivera-Rivera LA, Schubert T, Knobloch G, Turski PA, Wieben O, Reeder SB, et al. Comparison of ferumoxytol-based cerebral blood volume estimates using quantitative R1 and R2* relaxometry. Magn Reson Med 2018;79(6):3072-3081.

11. Stirrat CG, Alam SR, MacGillivray TJ, Gray CD, Forsythe R, Dweck MR, et al. Ferumoxytol-enhanced magnetic resonance imaging methodology and normal values at 1.5 and 3T. J Cardiovasc Magn Reson 2016; 18(1):p.46.

12. Hernando D, Cook RJ, Diamond C, Reeder SB. Magnetic susceptibility as a B0 field strength independent MRI biomarker of liver iron overload. Magn Reson Med 2013; 70(3):648-656.

13. Ghugre NR, Wood JC. Relaxivity-iron calibration in hepatic iron overload: probing underlying biophysical mechanisms using a Monte Carlo model. Magn Reson Med 2011;65(3):837-47.

14. Colgan T, Knobloch G, Reeder S, Hernando D. Sensitivity of quantitative relaxometry and susceptibility mapping to microscopic iron distribution. Magn Reson Med 2019. https://doi.org/10.1002/mrm.27946.

15. Iv M, Samgbabadi P, Holdsworth S, Gentles A, Rezaii P, Harsh G, et al. Quantification of macrophages in high-grade gliomas by using ferumoxytol-enhanced MRI: a pilot study. Radiology 2018;290(1):198-206.

16. Gaglia JL, Harisinghani M, Aganj I, Wojtkiewicz GR, Hedgire S, Benoist C, et al. Noninvasive mapping of pancreatic inflammation in recent-onset type-1 diabetes patients. Proc Natl Acad Sci USA 2015; 112(7):2139-2144.

17. Stirrat CG, Alam SR, MacGilivray TJ, Gray CD, Dweck MR, Raftis J, et al. Ferumoxytol-enhanced magnetic resonance imaging assessing inflammation after myocardial infarction. Heart 2017; 103:1528-1535.

18. Oh KY, Roberts VH, Schabel MC, Grove KL, Woods M, Frias AE. Gadolinium chelate contrast material in pregnancy: fetal biodistribution in the nonhuman primate. Radiology 2015; 276(1):110-118.

19. Prola-Netto, Woods M, Roberts VH, Sullivan EL, Miller CA, Frias AE, et al. Gadolinium chelate safety in pregnancy: barely detectable gadolinium levels in the juvenile nonhuman primate after in utero exposure. Radiology 2017; 286(1):122-128.

20. Myllynen PK, Loughran MJ, Howard CV, Sormunen R, Walsh AA, Vähäkangas. Kinetics of gold nanoparticles in the human placenta. Reprod Toxicol 2008;26(2):130-7.

21. Golos TG. Pregnancy initiation in the rhesus macaque: Towards functional manipulation of the maternal-fetal interface. Reprod Biol Endocrinol 2004;2(1):35.

22. Van Esch EV, Cline JM, Buse E, Wood CE, de Rijk EP, Weinbauer GF. Summary comparison of female reproductive system in human and the cynomolgus monkey (macaca fascicularis). Toxicol Pathol 2008;36:171S-172S.

23. Blankenship TN, Enders AC, King BF. Trophoblastic invasion and the development of uteroplacental arteries in the macaque: immunohistochemical localization of cytokeratins, desmin, type IV collagen, laminin, and fibronectin. Cell Tissue Res 1993;272:227-236.

24. Johnson KM, Fain SB, Schiebler ML, Nagle S. Optimized 3D ultrashort echo time pulmonary MRI. Magn Reson Med 2013; 70:1241-1250.

25. Yu H, Shimakawa A, McKenzie CA, Brodsky E, Brittain JH, Reeder SB. Multiecho water-fat separation and simultaneous R2* estimation with multifrequency fat spectrum modeling. Magn Reson Med 2008; 60(5):1122-1134.

26. Sharma SD, Hernando D, Horng DE, Reeder SB. Quantitative susceptibility mapping in the abdomen as an imaging biomarker of hepatic iron overload. Magn Reson Med 2015; 74(3):673-683.

27. Liu S, Brisset J, Hu J, Haacke EM, Ge Y. Susceptibility weighted imaging and quantitative susceptibility mapping of the cerebral vasculature using ferumoxytol. J Magn Reson Imaging 2018; 47:621-633.

28. Barick KC, Aslam M, Lin YP, Bahadur D, Prasad PV, Dravid VP. Novel and efficient MR active aqueous colloidal Fe_3O_4 nanoassemblies. J Mater Chem 2009; 19:7023-7029.

29. Laurent S, Forge D, Port M, Roch A, Robic C, Vander Elst L, et al. Magnetic iron oxide nanoparticles: synthesis, stabilization, vectorization, physicochemical characterizations, and biological applications. Chem Rev 2008; 108:2064-2110.

30. Breeze AC, Gallagher FA, Lomas DJ, Smith GC, Lees CC. Postmortem fetal organ volumetry using magnetic resonance imaging and comparison to organ weights at conventional autopsy. Ultrasound Obstet Gynecol 2008; 31:187-193.

31. Zhu A, Reeder SB, Johnson KM, Nguyen SM, Golos TG, Shimakawa A, et al. Evaluation of a Motion-robust 2D Chemical Shift-Encoded Technique for R2* and Field Map Quantification in Ferumoxytol-Enhanced MRI of the Placenta in Pregnant Rhesus Macaques. J Magn Reson Imaging 2019. https://doi.org/10.1002/jmri.26849.

32. Palomba S, Russo T, Falbo A, Di Cello A, Tolino A, Tucci L, et al. Macroscopic and microscopic findings of the placenta in women with polycystic ovary syndrome. Human Reproduction 2013; 28:2838-2847.

33. Storey P, Lim RP, Chandarana H, Rosenkrantz AB, Kim D, Stoffel DR, et al. MRI assessment of hepatic iron clearance rates after administration in healthy adults. Invest Radiol 2012; 47:717-724.

34. Landry R, Jacobs PM, Davis R, Shenouda M, Bolton WK. Pharmacokinetic study of ferumoxytol: a new iron replacement therapy in normal subjects and hemodialysis patients. Am J Nephrol 2005; 25:400-410.

35. Morris DM, Ross JA, McVicar A, Semple SI, Haggarty P, Gilbert FJ, et al. Changes in foetal liver T2* measurements by MRI in response to maternal oxygen breathing: application to diagnosing foetal growth restriction. Physiol Meas 2010; 31:1137-1146.

36. Fernández KS, de Alarcón PA. Development of the hematopoietic system and disorders of hematopoiesis that present during infancy and early childhood. Pediatr Clin North Am 2013; 60:1273-89.

37. Pahal GS, Jauniaux E, Kinnon C, Thrasher AJ, Rodeck CH. Normal development of human fetal hematopoiesis between eight and seventeen weeks' gestation. Am J Obstet Gynecol 2000; 183:1029-1034.

38. Nguyen SM, Wiepz GJ, Schotzko ML, Simmons HA, Mejia A, Ludwig KD, et al. Impact of ferumoxytol magnetic resonance imaging on the rhesus macaque maternal-fetal interface. 2019. https://BIORXIV/2019/699835.

39. Simchick S, Liu Z, Nagy T, Xiong M, Zhao Q. Assessment of MR-based R2* and quantitative susceptibility mapping for the quantification of liver iron concentration in a mouse model at 7T. Magn Reson Med 2018;80:2081-2093.

40. Presicce P, Senthamaraikannan P, Alvarez M, Rueda CM, Cappelletti M, Miller LA, et al. Neutrophil recruitment and activation in decidua with intra-amniotic IL-1beta in the preterm rhesus macaque. Bio Reprod 2015;92(2):56.

Thank you.